Property-performance correlations in the oxidative coupling of methane: the importance of carbonate formation and stability

vorgelegt von

M. Sc.

Huan Wang

geb. in Shandong, V. R. China

von der Fakultät II - Mathematik und Naturwissenschaften

der Technischen Universität Berlin

zur Erlangung des akademischen Grades

Doktor der Naturwissenschaften

Dr. rer. nat.

genehmigte Dissertation

Promotionsausschuss:

Vorsitzender:	Prof. Dr. Arne Thomas
Gutachter:	Prof. Dr. Reinhard Schomäcker
Gutachter:	Prof. Dr. Thomas Risse
Gutachter:	Dr.-Ing. Ralph Krähnert

Tag der wissenschaftlichen Aussprache: 23.05.2018

Berlin 2018

Abstract

The oxidative coupling of methane is a “dream reaction” in heterogeneous catalysis to achieve direct conversion for natural gas towards value-added and easily transportable C_2 products with high economic relevance. Although extensive academic papers and patents have been reported over the last three decades, no economically viable industrial-scale application is yet achieved because of the limitation of C_2 yields. An important reason is that so far the complex reaction network is still not totally understood. There is no clear property-performance relationship established which is valid for catalysts with widely varying compositions. This work presents an experimental approach to reveal quantitative property-performance correlations for a large variety of catalysts by studying model catalyst systems.

In order to investigate the influence of catalyst porosity, porous silicon carbide (SiC) was employed as a suitable substitute of mesoporous SiO_2 for Mn-Na_2WO_4/SiO_2 catalyst. Experimental results show that the pore structure and high surface area of Mn/Na/W/SiC catalyst could be preserved during calcination in nitrogen, but not during calcination in air and under conditions of OCM catalysis, which is attributed to Na-promoted bulk oxidation of SiC. For Mn/Na/W/SiC catalysts, CH_4 conversion and C_2 yield scale roughly linear with the specific surface area of used catalysts. Compared to Mn/Na/W/SiO_2 with similar composition, Mn/Na/W/SiC shows a higher CH_4 conversion and C_2 yield per unit of surface area, suggesting a higher surface coverage with active sites on SiC supported catalysts.

To establish property-performance correlations, descriptors of catalysts were experimentally generated, validated and then correlated in this work. Catalysts composed of alkali or alkaline earth carbonate on various oxide and carbonate supports as well as selected typical OCM catalysts were prepared and characterized. Property-descriptors, mainly focused on carbonate formation and stability were defined and generated on the basis of IR and TGA-MS results. Based on TGA-MS data, all catalysts have more than one kind of carbonate species with different thermal stability. The oxide support could facilitate carbonate transfer from highly stable carbonate to carbonate species with lower stability, which tends to decompose at relatively low temperatures. OCM activity of all catalysts was then tested and performance-descriptors regarding to C_2 yield were defined and generated from performance data. It was observed that oxide supports strongly influence CH_4 conversion and C_2 yield of oxide-supported carbonate catalysts. The presence of CO_2 in OCM feed resulted in a significant shift of OCM performance to higher temperatures, which is attributed to the stabilization effect of CO_2 on carbonate species.

The generated property-descriptors and performance-descriptors of studied catalysts were correlated and the proposed correlations were evaluated by linear regression analysis. It is the first time to report a quantitative and universal volcano-like property-performance correlation between C_2 yield and carbonate stability. It reveals that carbonate species with intermediate stability would be essential to achieve good OCM performance. The isolated sites surrounded by carbonate are one possible critical path to generate selective oxygen species and to suppress total oxidation on the oxide. Furthermore, this volcano-like correlation could be extended to typical OCM catalysts. The concept of carbonate stability behaves much better than basicity concepts, because it reflects certain chemical reactivity involved in OCM catalysis and is part of the proposed reaction mechanism.

Zusammenfassung

Die oxidative Kopplung von Methan ist eine "Traumreaktion" in der heterogenen Katalyse, um eine direkte Umwandlung von Erdgas in wertgesteigerte und leicht transportierbare C_2-Produkte mit hoher wirtschaftlicher Relevanz zu erreichen. Obwohl in den letzten drei Jahrzehnten umfangreiche wissenschaftliche Arbeiten und Patente gemeldet wurden, ist aufgrund der Begrenzung der C_2-Ausbeute noch keine wirtschaftlich sinnvolle großtechnische Anwendung möglich. Ein wichtiger Grund ist, dass das komplexe Reaktionsnetzwerk noch nicht vollständig verstanden ist. Es wurde bisher kein eindeutiges Eigenschafts-Performance-Verhältnis abgeleitet, das für Katalysatoren mit sehr unterschiedlichen Zusammensetzungen gültig ist. Diese Arbeit präsentiert einen experimentellen Ansatz zur Aufdeckung quantitativer Eigenschafts-Performance-Korrelationen für eine Vielfalt von Katalysatoren durch die Untersuchung von Modellkatalysatorsystemen.

Um den Einfluss der Katalysatorporosität zu untersuchen, wurde poröses Siliciumcarbid (SiC) als geeigneter Ersatz von mesoporösem SiO_2 für den Mn-Na_2WO_4/SiO_2-Katalysator eingesetzt. Experimentelle Ergebnisse zeigen, dass die Porenstruktur und die hohe Oberfläche des Mn/Na/W/SiC-Katalysators während der Kalzinierung in Stickstoff erhalten werden konnten, jedoch nicht während der Kalzinierung in Luft und unter den Bedingungen der OCM-Katalyse, was auf die durch Na geförderte Massenoxidation von SiC zurückgeführt wird. Für Mn/Na/W/SiC-Katalysatoren skalieren der CH_4-Umsatz und die C_2-Ausbeute ungefähr linear mit der spezifischen Oberfläche der verwendeten Katalysatoren. Im Vergleich zu Mn/Na/W/SiO_2 mit ähnlicher Zusammensetzung zeigt Mn/Na/W/SiC einen höheren CH_4-Umsatz und C_2-Ausbeute pro Flächeneinheit, was auf eine höhere Oberflächenbedeckung mit aktiven Stellen auf SiC-Trägerkatalysatoren hindeutet.

Um Eigenschafts-Performance-Korrelationen zu etablieren, wurden Deskriptoren von Katalysatoren experimentell generiert, überprüft und dann in dieser Arbeit korreliert. Es wurden Katalysatoren bestehend aus Alkali- oder Erdalkalicarbonat auf verschiedenen Oxid- und Carbonatträgern sowie ausgewählte typische OCM-Katalysatoren hergestellt und charakterisiert. Auf der Basis von IR- und TGA-MS-Ergebnissen wurden Eigenschaftsdeskriptoren definiert und generiert, die sich hauptsächlich auf die Carbonatbildung und -stabilität konzentrierten. Basierend auf TGA-MS-Daten haben alle Katalysatoren mehr als eine Art von Carbonat-Spezies mit unterschiedlicher thermischer Stabilität. Der Oxidträger könnte den Karbonattransfer von hochstabilem Carbonat zu Carbonatarten mit geringerer Stabilität erleichtern, die zur Zersetzung bei relativ niedrigen Temperaturen neigen. Anschließend wurden die OCM-Aktivität aller Katalysatoren getestet und Performance-Deskriptoren für die C_2-Ausbeute definiert und aus Performance-Daten generiert. Es wurde beobachtet, dass Oxidträger den CH_4-Umsatz und die C_2-Ausbeute von oxidgeträgerten Carbonatkatalysatoren stark beeinflussen. Die Anwesenheit von CO_2 im OCM-Feed führte zu einer signifikanten Verschiebung der OCM-Performance hin zu höheren Temperaturen, was auf den Stabilisierungseffekt von CO_2 auf Carbonatspezies zurückzuführen ist.

Die generierten Eigenschafts- und Performance-Deskriptoren der untersuchten Katalysatoren wurden korreliert und die vorgeschlagenen Korrelationen wurden mittels linearer Regressionsanalyse ausgewertet. Es ist das erste Mal, dass ein quantitativer und universeller vulkanähnlicher Zusammenhang zwischen C_2-Ausbeute und Carbonatstabilität festgestellt werden konnte. Es zeigt, dass Carbonatspezies mit mittlerer Stabilität unerlässlich sind, um eine gute OCM-Performance zu erzielen. Isolierte, von Carbonat umgebene Zentrensind ein möglicher kritischer Weg, um selektive Sauerstoffspezies zu erzeugen und die Totaloxidation durch das Oxid zu unterdrücken. Außerdem könnte diese vulkanartige Korrelation auf typische OCM-Katalysatoren ausgedehnt werden. Das Konzept der Carbonatstabilität verhält sich viel besser als Basizitätskonzepte, weil es eine bestimmte chemische Reaktivität, die an der OCM-Katalyse beteiligt ist, widerspiegelt und Teil des vorgeschlagenen Reaktionsmechanismus ist.

Table of Contents

Acronyms

a	activity
a	Smith basicity value
A_{BET}	specific surface area by Brunauer-Emmett-Teller theory
at%	atomic percentage
B_C	carbon balance
C_2	hydrocarbons containing two C atoms (OCM context: C_2H_6, C_2H_4)
C_{2+}	hydrocarbons containing two or more C atoms
CO_x	CO and CO_2
ΔG	Gibbs enthalpy
EDX	energy dispersive X-ray spectroscopy
EPR	electron paramagnetic resonance
F-center	color center (anionic vacancy with electron charge)
FID	flame ionization detector
FT-IR	Fourier-transform infra red spectroscopy
GC	gas chromatograph
ΔH	enthalpy
HREELS	high resolution electron energy loss spectroscopy
ICP-OES	inductively coupled plasma - optical emission spectroscopy
K	equilibrium constant
MIESR	matrix isolation electron spin resonance
milli-Q	ultrapure grade (water)
mol%	molar percentage
MS	mass spectrometer
$\dot{n}$	molar flow
NLDFT	non-local density functional theory
OCM	oxidative coupling of methane
ODH	oxidative dehydrogenation
p	pressure
R	gas constant
r	ionic radius
R^2	R squared
RSD	residual standard deviation
RSS	residual sum of squares
ΔS	reaction entropy
S_{C2}	sum of selectivity of C_2H_6 and C_2H_4
SEM	scanning electron microscopy
T	temperature
TCD	thermal conductivity detector
ΔT_{dec}	shift of decomposition temperature
T_{dec}	decomposition temperature
$T_{dec,\ 1st\ CO2}$	mass loss temperature of carbonate decompostion when first CO_2 peak appearing in MS
$T_{dec,\ inter\ CO2}$	mass loss temperature of carbonate decompostion when CO_2 peak appearing within/closest to the range of 400 ~ 550 °C in MS
$T_{dec,\ last\ CO2}$	mass loss temperature of carbonate decompostion when last CO_2 peak appearing in MS
$T_{1st\ H2O}$	mass loss temperature when first H_2O peak appearing in MS
$T_{last\ H2O}$	mass loss temperature when last H_2O peak appearing in MS
TGA	thermogravimetric analysis
T_{melt}	melting point
$T_{Tammann}$	Tammann temperature
TPD	temperature programmed desorption
wt%	weight percentage
X_{CH4}	conversion of CH_4
X_{O2}	conversion of O_2
XPS	X-ray photoelectron spectroscopy
XRD	X-ray diffraction
Y_{C2}	sum of yield of C_2H_6 and C_2H_4
Z	charge number of the atomic core
$\sigma_{left,\ carb}$	wavenumber of the left characteristic peak for CO_3^{2-} in IR
$\Delta\sigma_{left,\ carb}$	wavenumber shift of the left characteristic peak for CO_3^{2-} in IR compared to pure carbonate
$\Delta\nu_{as}$	splitting of asymmetric stretching vibration of C=O bond in CO_3^{2-}
Λ	Optical basicity value

1. Introduction

1.1. Motivation

In today's perspective, with dramatically fluctuating prices and declining reserves of crude oil all over the world, natural gas is drawing intensive attention as a promising resource of clean fossil energy and as a feedstock for diversified chemicals production.[1] In particular, owing to recent technological breakthrough in the so-called "shale gas revolution" in U.S., shale gas has become the crucial nonconventional source of natural gas.[2, 3] Unfortunately, most of natural gas resources are located in depopulated areas where gas transportation in pipelines over a long distance is not an economically viable solution. Therefore, an alternative option is to extensively convert natural gas on-site to transportable high-density energy forms. In fact, much effect has been devoted to this direction since decades initially motivated by the successive oil crises in the 1970s. More importantly, intensive research has become more and more evident in the 21st century to convert methane (CH_4), the primary component of natural gas, to high value-added chemicals such as olefins, aromatics, and methanol.[4-6]

Although methane is the most potential promising substitute to crude oil as environmentally viable and cheap carbon source for chemical manufacturing industry, around 90% of its global production is simply combusted for heating and electrical power generation.[7] The reason is that methane, with strong C-H bonds (425 kJ/mol), contains no functional group, magnetic moment or polar distribution, which might facilitate chemical attack. As a result, oxidation agents and/or input of energy are required for activation of methane by splitting of the C-H bond. The existing technologies for methane in industrial processes are shown in Fig. 1.1. For example, methane is utilized as feedstock for production of hydrocyanic acid via the Andrussow or Degussa processes.[8] It is also converted to methylhalogens or carbon disulphide on large scale.[9] The largest industrial methane-based process is methane steam reforming to syngas, a mixture of carbon monoxide and hydrogen.[10, 11] Starting from syngas, a variety of products such as higher hydrocarbons, oxygenates as well as ammonia can be produced using the well-established technologies, e.g., Fischer-Tropsch synthesis (FTS).[12, 13] However, the reforming reaction is strongly endothermic and high carbon dioxide emissions. Moreover, the indirect route conversion of methane requires additional facilities and large quantities of heat supply. Therefore, efficient direct route of methane to hydrocarbons without going through the intermediate syngas production step is potentially more economical and more environmentally friendly.

Oxidative coupling of methane (OCM), considered as "dream-reaction", provides a direct route to convert methane to higher hydrocarbons, e.g., ethane and ethylene. Pioneering work can be traced to Keller and Bhasin in the 1980s,[14] which initiated a worldwide surge of research efforts in this direction. Although extensive research on this topic with roughly 2700 scientific papers and 400 patents published in the last 30 years, no large-scale industrial application has been established yet. A C_2 yield of above 30% should be reached to achieve the economically viable goal.[15] Up to now, however, such C_2 yields were only obtained within laboratory scale under certain conditions with relatively short time-on-stream. Nevertheless, the pioneering US company Siluria Technologies Inc. started in 2015 the operation of a pilot plant on claiming the commercial viability of industrial application of the OCM reaction.[16] But there is only limited information available on the employed nanowire

catalysts according to a few of their published patents.[17-19] A superior catalytic behavior operating at lower temperatures than the conventional materials is even doubtable.[20]

The main challenge is the selectivity control during reaction process because almost all intermediates and/or products including hydrocarbons and oxygenates are more reactive than the reactant methane. They readily undergo further oxidation in the presence of oxygen.[21] An upper bound of C_2 yield of about 25% has been predicted by Ying et al.[22] based on assumed fundamental kinetics. This barrier would be possibly overcome through deeper understanding of the OCM reaction. So far, however, many fundamental aspects, for example, the essential features for an optimal catalyst composition, contribution of surface and gas phase reactions, and the nature of active sites still remain unknown.[21, 23]

OCM reaction can be catalyzed by a surprisingly large number of catalysts with different elemental composition, which is highly unusual for heterogeneous catalysis, since typically catalyst compositions comprise a pool of few elements.[24-26] There is no generally accepted quantitative concept that is valid for a wide range of OCM catalysts.

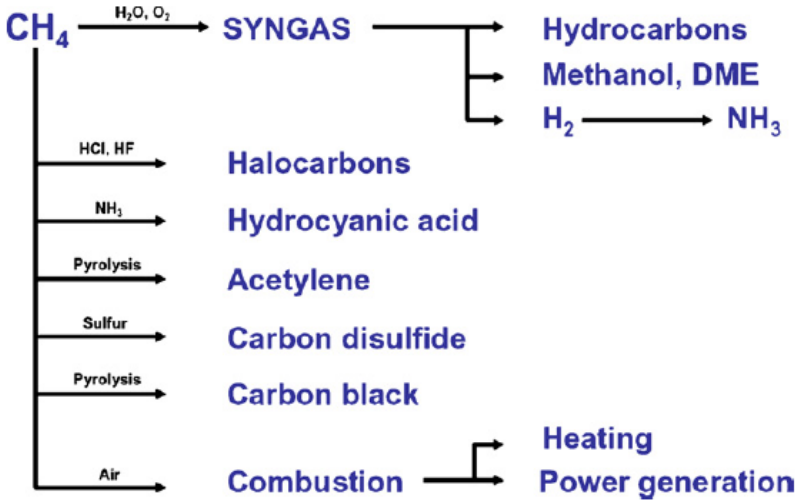

Fig. 1.1: Methane conversion on industrial scale. Figure unchanged adapted from Holmen's paper[4], with permission from Elsevier.

1.2. OCM reaction fundamentals

1.2.1. Overall thermodynamics of OCM

CH_4 is known as the most stable alkane molecule. The coupling of methane without an oxidant is a highly endothermic reaction (1.1) and would not thermodynamically proceed due to thermodynamic constraint.[27]

$$2CH_4 \rightarrow C_2H_6 + H_2 \qquad \Delta_r G^\circ(1000K) = 71.0\ kJ/mol \qquad (1.1)$$

By introducing an oxidizing agent, typically oxygen, the process becomes exothermic and the thermodynamic restrictions can be overcome. The overall OCM pathways are presented by reaction (1.2) and (1.3), respectively.

$$2CH_4 + ½O_2 \rightarrow C_2H_6 + H_2O \qquad \Delta_r G^\circ(1000K) = -121.6\ kJ/mol \qquad (1.2)$$

$$2CH_4 + O_2 \rightarrow C_2H_4 + 2H_2O \qquad \Delta_r G^\circ(1000K) = -152.5\ kJ/mol \qquad (1.3)$$

Both coupling reactions are exergonic and thermodynamically feasible. However, introducing oxidizing agent also poses the major challenge of further oxidation towards CO_x by-products. From a thermodynamic point of view, CH_4 combustion (1.4) and even C_2 product combustion (1.5) reactions are thermodynamically favored compared to the coupling reactions for CH_4.

$$CH_4 + 2O_2 \rightarrow CO_2 + 2H_2O \qquad \Delta_r G^\circ(1000\mathrm{K}) = -800.6\ \mathrm{kJ/mol} \qquad (1.4)$$

$$C_2H_4 + 3O_2 \rightarrow 2CO_2 + 2H_2O \qquad \Delta_r G^\circ(1000\mathrm{K}) = -1291.6\ \mathrm{kJ/mol} \qquad (1.5)$$

To facilitate the formation of C_2 product and suppress the occurrence of combustions, the reaction must be controlled kinetically. Therefore, suitable catalysts are necessary.

1.2.2. Simplified reaction network

Although the above overall reaction seems to be simple, the complex reaction network contains a large amount of possible elementary chemical reactions and is still not totally understood yet. Various reaction networks have been proposed through extensive research in the perspective of micro kinetic model simulation, intermediate substance experimental detection and so on. Among these options, the simplified scheme (Fig. 1.2) summarized by Fleischer et al.[28] on the basis of previous report [29-31] is herein adopted for general discussion.

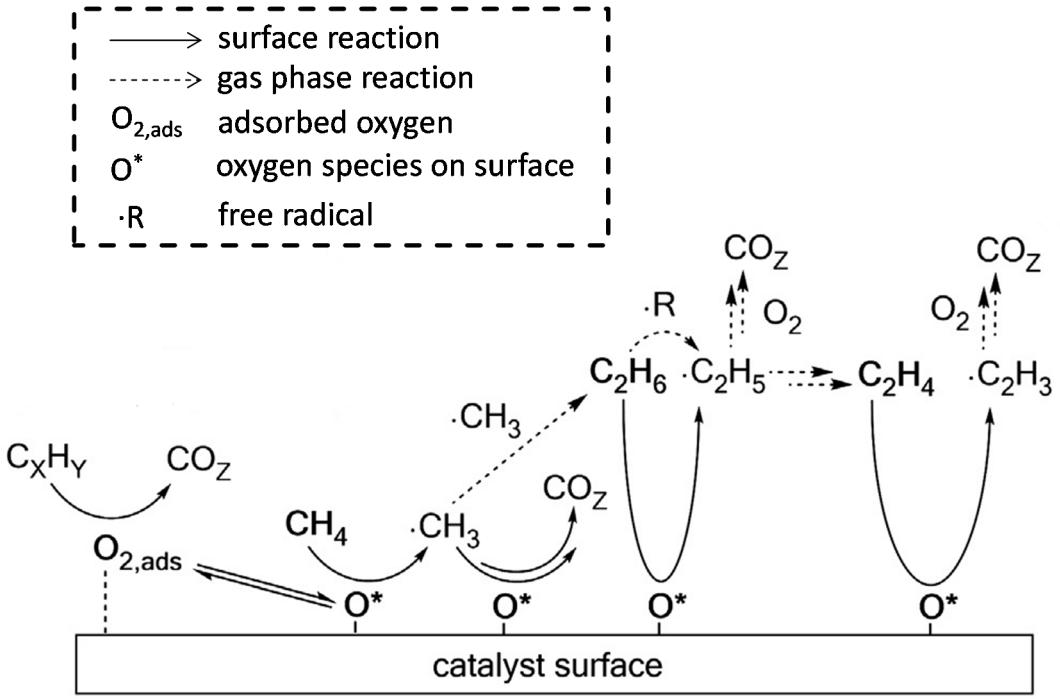

Fig. 1.2: Simplified reaction network, summarized by Fleischer et al.[28] on the basis of previous report [29-31] with permission from Elsevier.

OCM process is considered to be a homogeneous-heterogeneous reaction network composed of gas phase and surface reactions in parallel, which have a strong influence on each other. It is commonly claimed that the reaction is initiated by CH_4 activation on a certain active surface oxygen species (O*) and with the formation of methyl radicals ($\dot{CH_3}$) as a result. According to Sun[31] and Lee[30], there are two pathways for reaction of the formed methyl radicals. On one hand, methyl radicals couple in the gas phase to form C_2H_6 as primary product along a selective pathway. C_2H_6 undergoes further (oxidative)

dehydrogenation to form C_2H_4 as a secondary product. On the other hand, methyl radicals react with oxygen species along an unselective pathway to form oxygenated intermediates towards CO_x products finally. In addition, a third reaction pathway is the further oxidation of C_2 products to CO_x products according to Beck.[29] Isotopic labeling experiments illustrate that this pathway is more evident at higher conversions when higher reaction temperature is employed.[32]

The consecutive oxidation of C_2 coupling product explains why C_2 selectivity commonly decreases with the increase of CH_4 conversion and the observation of a "universal" limit to obtainable performance consequently. Besides, the loss of C_2 selectivity is also partly related to the relatively high concentrations of gas-phase oxygen required to obtain a considerable level of conversion.[33, 34]

It is known that, in principle, several hundred elementary reaction steps including approximately 40 species may appear in high-temperature gas-phase reactions of methane and oxygen from the literature. The massive amount of possibilities make it not readily reachable to simulate reaction kinetic by the available computer programs.[35-37] On the other hand, radical chemistry involved in the real OCM reaction network is by no means easy to monitor with current techniques. The definition and direct experimental evidence for the presence and relevance of the reactions of gas phase radicals and their contributions to OCM catalysis has not yet been provided in literature.[38, 39] All above complexity has so far impeded to reveal the comprehensive OCM mechanism as well as the active species of a catalyst.

1.2.3. Nature of active species

A variety of catalysts have been reported to that are able to catalyze OCM reaction (see Fig. 1.3). Thus, the concept on mechanism and active species should be applicable for many different catalysts. However, it is still a controversial topic regarding to the nature of active species for CH_4 activation.

Until now, the existing research works seem to show a diversity of active oxygen species responsible for CH_4 activation.[27] O^- was proposed to be the active oxygen species for typical Li-MgO catalyst[38, 40] as well as several other alkali element doped oxides, e.g., Li-ZnO[41] and Na-CaO[42] catalysts. For reducible oxide catalysts, e.g., PbO and Bi_2O_3, lattice oxygen O^{2-} is proposed as the active oxygen species formed by electron transfer from the reduced metal species to the gas phase oxygen.[38] There were also evidence to suggest peroxide species (O_2^{2-}) either directly or indirectly responsible for CH_4 activation for various catalysts containing alkali,[43, 44] alkaline earth[45-47] and rare earth elements.[48, 49] Specifically, the decomposition of peroxide ($O_2^{2-} + O_2 \rightarrow 2O_2^-$) may generate superoxide (O_2^-) species observed by means of electron paramagnetic resonance study (EPR) over La_2O_3 catalyst,[50] which was proposed as active species as well.

In addition to CH_4 activation, oxygen and its activation also play an important role in OCM reaction. The above proposed oxygen species arises from the interaction between oxygen and catalysts, while there might be equilibrium between each of oxygen species.[51, 52] These oxygen species are considered to be involved in different reaction pathway and may determine the product selectivity. The electrophilic oxygen species (O^-, O_2^- and O_2^{2-}) is reported to effectively improve the C_2 selectivity, whereas lattice oxygen O^{2-} is typically responsible for total oxidation, which is proposed through observation of the correlation between C_2 selectivity and the relative amount of electrophilic oxygen species to lattice

oxygen.[53, 54] The argument is problematic, as oxygen species are commonly quantified through X-ray photoelectron spectroscopy (XPS) and O_2-Temperature programmed decomposition (O_2-TPD) techniques which are not upon direct monitoring at OCM conditions. Closer investigation by temporal analysis of products (TAP) experiments enables people to direct monitor the time-dependent behaviors of reactants and products. Two different oxygen species, which are weakly and strongly bound on catalyst surface, are proposed to be responsible for total and selective oxidation of CH_4, respectively.[28, 29]

The Mn-Na_2WO_4/SiO_2 is most frequently investigated catalysts in recent years, which is promising for industrial application. Because this kind of catalyst not only has an appropriate performance (CH_4 conversions of 20 - 35% and C_2 selectivities of 70 - 80%) but also is stable for long periods at high temperatures required for the OCM.[32, 55, 56] It was firstly proposed by Li et al.[55] that the active species is associated with the formation of surface cluster species of tetrahedral WO_4 species with one W=O bond and three W-O-Si bonds. The following work reported by the same group,[57] however, concluded that the tetrahedral WO_4 species are distorted and the distortion is responsible for the activity. An oxygen spill-over mechanism was proposed later,[58] showing that a redox cycle would be complete where activation of CH_4 takes place on W^{6+} sites and the activation of gas phase O_2 on Mn^{3+} sites. In addition to metal element, SiO_2 support was also considered to have critical influence on OCM performance. Palermo et al.[59] observed a phase transition from the amorphous silica to α-cristobalite phase with the presence of Na during calcination for Mn-Na_2WO_4/SiO_2 catalysts, which exhibited significantly high C_2 selectivity at high CH_4 conversion level. Furthermore, the catalyst with α-cristobalite produced during phase transition behaves better than that with α-cristobalite as starting material. The author proposed that α-cristobalite formation during calcination may have a positive influence on dispersing and stabilizing active species, possibly WO_4. On the other hand, Na_2WO_4 becomes a liquid phase at typical OCM temperature (above 750 °C) since it has a theoretical melting point of is 698 °C.[60, 61] Meanwhile, a glass phase may form caused by SiO_2 being a typical glass former with Na being a typical glass modifier.[62] Both arguments suggest the formation of a complex molten phase under OCM reaction. Due to its high mobility, electron and mass transfer as well as formation and regeneration of active species could be substantially enhanced.

In addition, the generation of active species is sometime attributed to defect site of catalysts in the literature. Baerns et al.[63] observed a similar dependence of C_2 selectivity and oxygen-ion conductivity on the Ca content for CaO-CeO_2 catalysts. They indirectly concluded that highly mobile oxygen defects has a positive effect on C_2 product formation considering that oxygen defects promote the transformation of adsorbed oxygen species into lattice oxygen and enhance the oxygen-ion conductivity. The availability of oxygen defects was also emphasized by the same author as a beneficial catalyst feature for the OCM reaction in a review article.[64] Kondratenko et al.[65] reported that C_2H_6 formation rate over SrO catalyst is higher by using N_2O compared to O_2 as oxidant, which is proposed to be related with higher N_2O decomposition rate influenced by hydroxyl defects or anion vacancies measured by electron paramagnetic resonance (EPR) spectra. Wu et al.[66, 67] reported that C_2H_6 production over pure and Li-doped MgO film changes in concert with the concentration of F-center defects (oxygen vacancies with a captured electron charge) that were experimentally determined by high resolution electron energy loss spectroscopy (HREELS). They suggested that F-centers are responsible for CH_4 activation rather than oxygen species.

One more recent work reported by Schlögl et al.[68] found that the consumption rate of CH_4 as well as production rates of C_2 products are correlated with the monoatomic step edges on

surface, which was verified by TEM images and quantified by analysis of the vibration spectra with CO as a probe. They claimed that OCM performance are not associated with substance MgO itself but rather with its surface geometrical defect structure. But this concept on the basis of simple MgO model catalyst could not be generally transferred to other more relevant OCM catalysts.

1.3. Catalysts for OCM

Since the pioneering works of Keller and Bhasin[14], a wide variety of materials have been evaluated for their performance in OCM with the objective of developing an active, selective and stable catalyst. A huge body of oxide materials, such as alkali, alkaline earth, rare earth metal as well as modified or mixed as perovskite, have shown to be good catalysts for the OCM reaction. Fig. 1.3 depicts a few of representative catalysts providing C_2 yield above 25% from the literature. A brief review on frequently tested catalysts with good performance is shown as follows.

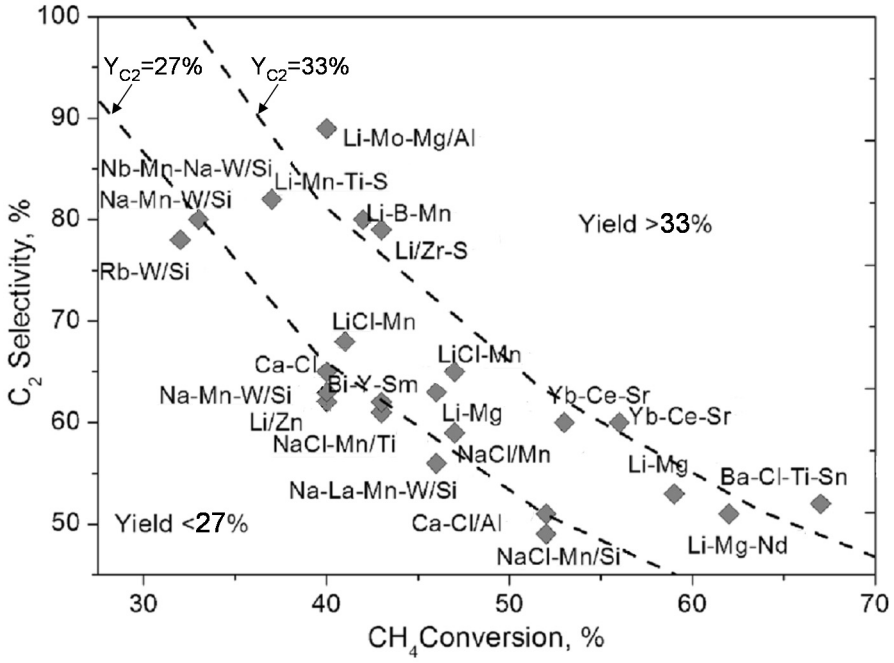

Fig. 1.3: CH_4 conversion versus C_2 selectivity of exemplary OCM catalysts with high C_2 yield reported in literature, adapted from Zavyalova et al.[69] with permission from John Wiley and Sons. Lower and upper dashed line represents for Y_{C2} = 27% and Y_{C2} = 33%, respectively. All shown catalysts were tested in fixed bed reactors in co-feed mode at atmospheric pressure. Reaction conditions differ for different catalysts, with temperatures in the range of 670 °C - 950 °C, CH_4 / O_2 ratio in range 1.7 - 9.0, and contact times in range 0.2 - 5.5 s.

1.3.1. Non-reducible oxide

Non-reducible oxide usually contains main-group (especially group IA and IIA) elements. Their oxides are characterized by a fixed stoichiometry, large band gaps and high formation energies for defects.[70] The most well-known catalysts based on this oxide is lithium-doped MgO (Li/MgO), initially studied by Lunsford and co-workers.[38] The presence of monovalent Li ions is capable of replacing divalent Mg ions in the crystal structure, creating Li substitutional defects with a localized electronic hole (so-called $[Li^+O^-]$ center) as a result, which was believed to be responsible for the initial abstraction of hydrogen from CH_4.[71]

Following the seminal investigations of Lunsford, a diversified combination of dopant and non-reducible oxide was reported as well OCM catalysts built on the synergetic effect.

Choudhary el al[72] investigated MgO doped with a series of alkali element (Li, Na, K, Rb and Cs) regarding to surface properties as well as catalytic performance, where Li/MgO showed the best performance. It was also observed that C_2 product formation rate is related to the surface density of strong basic sites influenced by the doped alkali metals. Korf et al.[73] reported that a number of other additives to Li/MgO system, e.g. transition metal and rare earth metal, gave rise to little or no difference in C_2 selectivity compared to Li/MgO, while considerably lowering the temperatures required to achieve the optimum C_2 yields. In addition to MgO, other alkaline earth oxides, CaO[42, 74-76], SrO[74, 77] and BaO[74, 77], were employed as the host oxide and exhibited considerable OCM performance.

In spite of good initial performance of Li/MgO catalyst, it suffers from an intrinsic instability and exhibited a severe activity loss with long-term test, which was observed by many research groups.[23, 78, 79] Korf and co-workers[80, 81] claimed that the catalyst deactivation is due to a loss of Li as the volatile species LiOH or Li_2SiO_3 by reaction with the laboratory reactors made of quartz glass. Furthermore, they found that C_2 selectivity is not affected by CO_2 addition by assuming that CO_2 temporarily poisoned the Li-containing active site and simultaneously stabilized it against deactivation.[82] The inferior stability of Li/MgO catalysts prevents its industrial application because OCM reaction typically is operated at high temperature and for long-term period.

Another problematic aspect is the doubt on active center [Li^+O^-] because pure MgO were also reported to be active and selective in OCM reaction.[83] Ardizzone et al.[84] observed systematical binding energy shifts in X-ray photoelectron spectroscopy (XPS) spectra for all MgO prepared by different precursors. It is attributed to the existence of F-center defects, which is considered to be responsible for CH_4 activation. Mellor et al.[85] studied isotope oxygen exchange activity of MgO samples with different crystallite sizes and termination crystallographic planes. They demonstrated that surface crystallographic plane with low-coordination site could be associated with activity.

1.3.2. Reducible oxide

Reducible oxides consist of transition metals and a few of group IIIA, IVA and VA metals plus oxygen. They commonly feature an intrinsic redox potential, because the cation is able to change oxidation state and the process is compensated by the insertion of defects as a result in order to keep the compound charge neutral.[70] The formed defects may be connected with the catalytic activity.

In some earlier reported papers, Hinsen and Baerns et al.[27, 86] investigated catalysts based on supported Pb , Bi, Sb , Sn, and Mn oxides tested on a fixed bed reactor with co-feed of CH_4 and air. Within these catalysts, PbO/Al_2O_3 was found to be the most active. However, significant deactivation was observed after several days of operation due to severe loss of Pb from the support. In a later review,[87] Jones et al. summarized the catalysts screening work by the Atlantic Richfield Company, which was mainly focused on a series of reducible oxide on SiO_2 support. Sodium-promoted manganese oxide on SiO_2 support was noted as a “well-performance” catalyst, showing similar conversion and selectivity upon simultaneous and sequential feed operation process. Emesh et al.[88] investigated quantities of group IIIA, IVA and VA metals on Al_2O_3 promoted by alkali elements and found that Bi_2O_3 is more active and selective than Ga_2O_3, In_2O_3,Tl_2O_3, GeO_2, and Sb_2O_4. A bifunctional mechanism was proposed, where CH_4 and O_2 activation is associated with Al_2O_3 support and Bi_2O_3 through a redox cycle, respectively.

However, one negative aspect regarding to reducible oxide catalysts is that the cation with multiple oxidation state may be much possibly reduced by methyl radicals through electron transfer. Consequently, the resulting methoxide and formate ions are intermediates for the formation of CO_x and H_2O, which is unfavorable for coupling reaction.[40] Tong et al.[89] defined a sticking coefficient (the ratio of the number of the methyl radicals reacted on a metal oxide to the number of the collisions between methyl radicals and the metal oxide) in an attempt to quantitatively describe the difference of reaction ability of metal oxides with methyl radicals. They found that the sticking coefficient of transition metal oxides is higher than non-reducible oxide MgO, which supports the argument on the consumption of methyl radicles by reducible oxide catalysts.

1.3.3. Rare earth oxide

Rare earth elements contain lanthanides, actinides as well as scandium and yttrium. Rare earth oxides are widely used in fabrication of optics, conductors, ferroelectric materials, glass and catalysts due to their unique optical, electronic and chemical properties.[90, 91] Initial work using rare earth oxides as catalysts for OCM reaction was reported by Otsuka et al.[92] They observed that Sm_2O_3 is the most active and selective catalysts through a wide screening of rare earth oxides without supports on a co-feed measurement. Later, reactions between methyl radicals and lanthanide oxide series was investigated by Tong et al.[93] via detection of relative formation rate of methyl radicals. They found that La_2O_3, Nd_2O_3, Sm_2O_3, Eu_2O_3, and Yb_2O_3 react with methyl radicals to only a small extent, while CeO_2, Pr_6O_{11} and Tb_4O_7 with multiple oxidation state react extensively with methyl radicals. This reaction of oxide with methyl radicals could be suppressed by the addition of Na_2CO_3.

One apparent advantage of using rare earth oxides as catalysts in OCM reaction is to reach comparable performance at relatively lower reaction temperatures. For example, Noon et al.[94] reported a kind of La_2O_3-CeO_2 nanofibers exhibiting OCM ignition at 470 °C (feed-gas temperature) with a CH_4/O_2 ratio ~ 7 and resulting in C_{2+} yield ~ 20% and C_{2+} selectivity ~ 70% at 520 °C (feed-gas temperature). Similarly, Huang et al.[95] prepared a La_2O_3 nanorod catalyst and it showed a CH_4 conversion onset of 450 °C, with exhibiting C_2 yield ~ 11% at 800 °C. Through TEM, N_2-physisorption, O_2-TPD, CO_2-TPD characterization and calculation by density functional theory (DFT), they claimed that the larger surface area, stronger surface basic sites, larger amount of electron deficient oxygen species on the surface as well as a well-defined surface are factors preferred for CH_4 activation at lower temperature. A more recent work, reported by Hou et al.[54] showed that $La_2O_2CO_3$ is able to active CH_4 with comparable C_2 selectivity (X_{CH4} ~ 29.7%, S_{C2} ~ 48.4%) at even surprisingly lower temperatures (420 °C) than the previous reported La_2O_3. They proposed a structural sensitivity in $La_2O_2CO_3$ catalyst with relatively loose atomic configuration at the exposed facets, resulting more defects or vacancies available on surface to be responsible for improvement of CH_4 conversion. Another promising aspect is from the only one case of OCM industrial application invented by the pioneering US company Siluria Technologies Incorporation. Due to inadequate published information,[17-19] the only known aspect is that La_2O_3 nanowire-type catalyst was utilized and showed superior catalytic behavior at lower temperatures.

1.3.4. Mn-Na_2WO_4/SiO_2

Mn-Na_2WO_4/SiO_2 is a compound system, first reported to be a OCM catalyst by the group of Li,[55] exhibiting superior catalytic activity, selectivity (CH_4 conversions of 20 - 30% with C_2

selectivities of 70 - 80%) and a remarkable stability under high temperature. The performance of Mn-Na_2WO_4/SiO_2 catalysts has been unanimously confirmed by different research groups.[32, 56, 96] Therefore, it is considered to be a suitable candidate for industrial application.

Earlier works regarding to Mn-Na_2WO_4/SiO_2 mainly focused on the catalyst preparation approach, catalysts composition optimization and preliminary exploration of active center. For example, Wang et al.[97] studied catalysts prepared by three different preparation procedures, which are incipient wetness impregnation, mixed slurry and sol-gel method. By XPS measurement, Na, W and Mn are mainly distributed on the surface of catalyst prepared by the incipient wetness impregnation method, but more uniform between the surface and bulk on the catalysts prepared by other two methods. However, the assumption of higher amount of metal element on surface responsible for higher activity cannot be supported by the fact that catalysts prepared by incipient wetness impregnation and mixed slurry method exhibit similar catalytic performance and stability. Ji et al.[98] reported that the OCM reaction was found to proceed without dramatic performance change with the contents of Na, W, and Mn in variation range between 0.4 - 2.3%, 2.2 - 8.9% and 0.5 - 3.0%, respectively. In addition, several groups proposed the nature of active center and possible reaction mechanism regarding to Mn-Na_2WO_4/SiO_2 system through detailed investigation on structural properties and catalytic performance, as discussed in section 1.2.3. In spite of great effort spent on this aspect, unfortunately there is up to now still no agreement reached due to the intrinsic complexity of this catalyst system.

In recent years, more investigations regarding to role of the silica support rather than metal elements were reported. Yildiz et al.[99] found an enhanced OCM performance of Mn-Na_2WO_4/SiO_2 catalysts when ordered mesoporous SiO_2 (SBA-15) was used as the support material instead of conventional SiO_2. Both, a better dispersion of Mn-Na_2WO_4 precursors in the pore system of support and the high surface area of SBA-15 might have contributed to this improvement. Later reported by the same group,[62] they investigated 13 kinds of SiO_2 as precursor for Mn-Na_2WO_4/SiO_2 catalyst and observed apparent difference of OCM performance influenced by the starting SiO_2 materials. Moreover, it was confirmed by in-situ XRD analysis that a phase transition happens during reaction. For example, Na_2WO_4 phase present in fresh catalysts was no longer detected as crystalline phase at reaction temperature due to occurrence of melting. The amount of crystalline SiO_2, cristobalite and tridymite tends phases, tends to change with temperature while a new quartz phase forms as a result. However, no clear structure-activity correlation was unraveled from the above studies.

In addition to lab-scale investigation, a few of papers with regard to scale-up attempts explored the possibility of practical application of Mn-Na_2WO_4/SiO_2 catalysts. Simon et al.[61] reported that a large amount of catalyst (~ 200 g) was successfully prepared through a fluidized bed processing with sequential operation, which is close to industrial application in reactors of appropriate size and fluid dynamics. The obtained catalyst was tested in a packed-bed tubular reactor and showed a relatively lower performance (X_{CH4} ~ 7% with S_{C2} ~ 76%) compared to the typical Mn-Na_2WO_4/SiO_2 catalyst made in lab-scale. Sadjadi et al.[60] reported a detailed investigation of Mn-Na_2WO_4/SiO_2 catalyst performed on a fluidized-bed reactor on a miniplant scale. They found the OCM performance is strongly influenced by reaction temperature, feed composition, fluidization velocity and particle size of catalysts. An optimal C_2 yield of 19.4% was reached at 820 °C with CH_4/O_2 ~ 2 by using a catalyst with particle size of 250 - 500 µm.

Usually OCM operation using Mn-Na_2WO_4/SiO_2 as catalyst requires fairly high temperature to reach an appreciable performance. Therefore, it is also a promising objective to reach a comparable performance at lower reaction temperature in order to suppress poor heat transfer and save energy supply cost. A very recent paper in 2017, reported by Wang et al.[100], gives a first insight into this idea. They explored a TiO_2-doped Mn-Na_2WO_4/SiO_2 catalyst, exhibiting a remarkable improvement in activity and selectivity at low reaction temperature (at 720 °C, X_{CH4} ~ 26% with S_{C2+C3} ~ 76%, CH_4:O_2:N_2 ~ 5:1:4). In-situ XRD analysis revealed that under the identical reaction condition, the $MnTiO_3$ ↔ Mn_2O_3 cycle requires much less time than the $MnWO_4$ ↔ Mn_2O_3 cycle. A catalytic recycle was proposed that $MnTiO_3$ triggers the low-temperature Mn^{2+} ↔ Mn^{3+} cycle for O_2 activation while working synergistically with Na_2WO_4 to achieve selectively converting methane.

The frequently studied OCM catalyst, non-reducible oxide, reducible oxide, rare earth oxide and Mn-Na_2WO_4/SiO_2 are briefly reviewed above. In addition, the anion additives to the catalytic system have been reported to play an important role as well. For example, Burch et al.[101] found that through a pulse injection of chlorinated gaseous additives (CH_2Cl_2 and $CHCl_3$) during the reaction, C_2 selectivity for Li/MgO and MnO_2 catalyst was slightly and substantially increased. They proposed that this beneficial effect is attributed to the suppression of the total oxidation by the chlorine containing promoters. Lunsford et al.[102] examined a series of Li/MgO catalyst with varied amount of Cl^-. CH_4 conversion increases with Cl^- content, and meanwhile, dramatic change of C_2H_4/C_2H_6 ratio occurred at Cl/Li ~ 1. They claimed that the chlorine promoter could either modify the existing active center in a way or create new centers, where one is responsible for CH_4 activation, while another type is especially active for oxidative dehydrogenation of C_2H_6. However, the promoting effect of chlorine is limited dependent on reaction conditions, such as temperature, time-on-stream and extent of produced water.

In general, for heterogeneous catalysis reaction, the typical catalyst is composed of a certain elemental composition.[8, 26] However, a large diversity in catalyst composition is shown above for OCM reaction, which is highly unusual. One possible explanation is that the crucial physicochemical properties possessed by “well-performing” OCM catalysts may be achieved by a number of elements.

1.4. Catalyst design regarding to support porosity

Heterogeneous catalytic reactions usually take place on the external and internal surfaces (pores) of the catalyst. For gas-solid reaction, gradients regarding to reactant/product concentration and temperature tend to appear in the gas-solid boundary layer surrounding the catalyst solids and inside the pores if mass diffusion and heat transfer between the bulk of gas, external and internal surface of the catalyst are not sufficiently fast.[8] Such gradients typically have a negative effect on the activity and selectivity of the catalyst. The adverse effect can be minimized by elaborate design of catalyst as well reactors and matching operation conditions. In this section, the perspective of catalyst design regarding to the function of support porosity would be mainly introduced.

1.4.1. General role of support porosity

Supported catalysts is commonly utilized and played a crucial role in industrial catalysis process. The support is able to provide high surface area as well as porosity and facilitate the loading and dispersion of the active component. During catalytic reaction, the presence of support could efficiently suppress the sintering of active component, such as metal

nanoparticles. Furthermore, especially for transition and noble metal typically having high surface energy, a favorable metal-support interaction enables less severe agglomeration of metal particles.[103, 104] Therefore, the nature of the support material for a given metal has a critical effect on the catalytic properties of entire catalyst.

The most frequently used commercial supports are binary oxides including Al_2O_3, SiO_2, TiO_2 (anatase), ZrO_2 (tetragonal), MgO and ternary oxides, typically amorphous SiO_2 - Al_2O_3 and zeolites. One of the common features is that they are porous materials with relatively high surface area. According to the definition by IUPAC, porous materials are divided into three categories: microporous (pore size < 2 nm), mesoporous (2 - 50 nm), and macroporous (> 50 nm) materials.[105] Zeolites are the most well-known example among microporous materials, which have wide application in petrochemical industry.[106] However, conventional zeolites exhibit significant drawbacks due to the limitation of pore size. Mass transfer is severely restricted when large reactant molecules are involved as is frequently the case in the synthesis of fine chemicals.[107, 108]

The direct solution is to enlarge the pore size of materials into mesopore range. Since the first report of mesoporous silica, MCM-41, by scientists in Mobil Oil Corporation in 1992,[109] people have done extensive research in the field of mesoporous materials. Quantities of papers focused on a diversity of aspects, such as preparation, surface modification, application as host materials and in catalysis.[110-112] The pore system of mesoporous materials with the narrow pore size distribution is an ideal space to stabilize nanoparticles with high dispersion. Accordingly, various catalytically active materials, not only noble metal particles but also metal oxides, can be supported on mesoporous materials and show distinct catalytic behaviors. Some examples are given in the following with regard of improvement of catalytic performance due to mesoporous materials utilization.

Chiche et al.[113] examined mesoporous aluminosilicates, zeolites and amorphous silica-alumina materials in the oligomerization reaction of butene. The mesoporous catalyst exhibited higher selectivity and good stability with time on stream for the production of branched dimers. They claimed that an open porosity improves mass diffusion and leads to a low concentration of reactive species on the surface with short residence times. Under the same experimental conditions, contrarily, zeolites and amorphous silica-alumina suffer from a fast deactivation due to rapid pore blocking by strongly adsorbed hydrocarbon residue. Corma et al.[111] investigated platinum nanoparticle supported on mesoporous silica-alumina over hydrogenation of aromatics reaction compared to conventional supports, such as commercial zeolite, γ-alumina and silica. Pt on mesoporous support presented a superior overall hydrogenation activity and highest sulfur tolerance. The high metal dispersion and the interaction between Pt clusters and moderate acidic sites in mesoporous support were proposed to account for the observed performance. Wingen et al.[114] prepared iron oxide supported on MCM-41 and observed substantially higher activity over the oxidation of SO_2 in highly concentrated gas streams than that of iron oxide supported on a commercial amorphous silica support. Besides, the MCM-41 supported one presented a remarkable long-term stability up to 750 °C.

1.4.2. Porous SiC material used in methane conversion reaction

Catalytic conversion of CH_4 typically requires high temperatures or aggressive reactants for ignition because CH_4 is not easy to be activated.[21] Specifically for OCM reaction, catalysts tend to encounter great challenges to rigorous conditions, such as high temperature applied and high content of water produced during the reaction. Although mesoporous silica is

considered to be a superior support for various catalytic reactions as introduced in section 1.4.1, its relatively low hydrothermal stability and amorphous framework limit its application in OCM reaction.[115, 116] For the typically Mn-Na_2WO_4/SiO_2 catalyst employed in OCM reaction, the SiO_2 component is usually a crystalline phase (e.g., α-cristobalite) and with low surface area.[59] Very few of attempts using materials other than SiO_2 for Mn-Na_2WO_4 active element were reported. For example, Yildiz et al.[117] reported a systematic screening through a wide range of materials as support. All Mn-Na_2WO_4 catalysts on different support were investigated in a parallel reactor system in terms of catalytic activity, enabling a direct comparison in between. They found that among all tested samples, silicon carbide (SiC), TiO_2-rutile and Fe_2O_3-based support materials show catalytic performances higher than the reference Mn-Na_2WO_4/SiO_2 at lower CH_4 conversion level. However, all above data were obtained at time-on-stream ~ 16 h. The lack of long-term operation test made it difficult to evaluate their catalytic stability.

It is a great challenge and opportunity for Mn-Na_2WO_4 type catalysts to incorporate higher surface area and porosity, which may increases the number of accessible active sites via a better dispersion and improves mass transfer between reactants and catalysts. Yildiz et al.[99] reported an enhanced OCM performance of Mn-Na_2WO_4/SiO_2 catalysts when ordered mesoporous silica (SBA-15) was used as the support material. Both, a better dispersion of metal precursors in the support pore system and the high surface area of SBA-15 might have contributed to this improvement. However, the mesostructure of SBA-15 collapsed during thermal treatments and under OCM reaction conditions. It remains unclear regarding to the contribution of porosity to the catalytic processes.

As introduced above, SiC might be a promising candidate as support materials for Mn-Na_2WO_4 type catalysts.[117] Generally, SiC possesses a three dimensional structure of Si and C atoms, where each atom is surrounded tetrahedrally by four of the other kind. It exists in more than 250 polymorphs and some of them are variations of the same chemical compound that are identical in two dimensions and differ in the third.[118] Two major kinds of silicon carbide are alpha silicon carbide (α-SiC) having hexagonal crystal structure (similar to Wurtzite) and β-modification (β-SiC or 3C-SiC) having zinc blende crystal structure (similar to diamond), respectively. In fact, SiC is usually demonstrated as a material with superior stability at high temperature, chemical inertness and high mechanical strength, which are all required for a good heterogeneous catalyst support.[119] In order to be used as an efficient catalyst carrier, SiC is expected to possess a high surface area. Several approaches, including carbothermal reduction,[120, 121] magnesiothermic reduction,[122, 123] chemical vapor deposition (CVD)[124] and pyrolysis of pre-ceramic polymers,[125, 126] were reported to prepare mesoporous SiC materials whose surface area is varied from less than 20 $m^2\ g^{-1}$ to above 900 $m^2\ g^{-1}$.

The successful synthesis of SiC with high surface area paves the way for its utilization as support for catalyst. However, catalytic methane conversion with SiC supported catalysts was seldom investigated. Hoffmann et al.[127] reported that mesoporous β-SiC prepared via hard templating and corresponding Ni/SiC catalyst exhibited higher conversion and stability in dry reforming of methane at 800 °C than conventional SiO_2 as a support. They found that the passivation layer on the surface of SiC support is able to largely prevent the transition of active nickel species to inactive nickel silicide, which has a beneficial effect on higher conversion over the whole time on stream. Leroi et al.[128] reported that β-SiC supported Ni catalyst exhibited comparable activity but better stability than Ni/γ-Al_2O_3 over the partial oxidation of methane at 900 °C. Ni/γ-Al_2O_3 showed significant deactivation after 30 h, which is attributed to higher amount of carbon deposition through methane decomposition due to

"hot spot" effect on the catalyst surface. On the contrary, much less amount of carbon was observed in Ni/β-SiC catalyst, where SiC could suppress carbon deposition by rapid heat evacuation out of the catalyst bed due to its excellent heat conductivity. On the other side, the extrudate shape showed no macroscopic morphology change after the catalytic test for Ni/β-SiC catalyst whereas the Ni/γ-Al_2O_3 was totally collapsed, with only small granules and fine powder remaining afterwards. This reveals the excellent mechanical strength of SiC support, which is usually indispensable for industrial application.

To our knowledge, even less studies was conducted concerning SiC as support for OCM reaction. Liu el al.[129] firstly reported that a preparation of monolithic foam SiC supported Mn-Na_2WO_4 catalyst. It showed no better performance than the Mn-Na_2WO_4/SiO_2 reference, but less increase of catalyst bed temperature was detected as a result of well thermal conductivity of SiC support. However, the comparison is questionable as the Mn-Na_2WO_4/SiO_2 reference was in powder form which was different from the used Mn-Na_2WO_4/SiC. Yildiz et al.[117] ever mentioned SiC materials when they carried out support variation for Mn-Na_2WO_4 type catalysts for OCM, where SiC supported catalyst showed lower CH_4 conversion and similar C_2 selectivity at 750 °C compared to SiO_2 supported catalyst. No available data could be found to comment on the stability of these catalysts. Serres et al.[130] investigated mesoporous SiC-supported Mn-Na_2WO_4 type catalysts and C_2 yield about 6% at 10% CH_4 conversion level were reached, despite the unusual high loading of 19.5 and 41.0 wt% of tungsten. Unfortunately, these catalysts provided an extremely low surface area (< 1 m^2 g^{-1}). Moreover, neither the stability and transformation of the support during OCM nor the role of porosity were investigated in detail.

In summary, all above descriptions point out a promising direction for OCM catalyst design if the character of mesoporosity and high stability can be combined in a facile fashion. Porous SiC material as support is potential to achieve this target.

1.5. Concept for a unified explanation of OCM across all active catalysts

The chemical composition of a catalyst plays a crucial role on catalytic performance. Broadly speaking, a suitable catalyst should be composed of a certain elemental composition for each heterogeneous catalysis reaction.[8] However, a huge body of catalysts with various elemental compositions have been studied in OCM reaction and may become potential candidates, as shown in Fig. 1.3. Furthermore, even for an identical catalyst, the difference of reaction conditions (i.e., reactant partial pressures, operating temperature, total pressure, contact time and reactor type) would result in distinct conversion and selectivity, which dramatically increases the complexity of an unbiased comparison. This is also perhaps a reason why until now there is still no commonly accepted suitable catalyst composition and no universal property-performance correlation established.

1.5.1. The concept of basicity

Basicity has been claimed by various researchers to be an important property of catalyst in OCM reaction.[72, 74, 77, 83, 131, 132] Basicity can be expressed in different ways from literatures, such as Lewis acid-base, Brønsted acid-base, Smith scale,[133] optical basicity,[134] or the ionic-covalent parameter[135]. CO_2 was also used in OCM literature as a measure of basicity, typically via temperature programmed desorption of CO_2 (CO_2-TPD), which reflects the interaction between CO_2 and the surface. It is typically used to measure the number and strength of basic sites of catalysts by considering CO_2 as an acidic probes. To our

knowledge, however, no clear quantitative correlation between OCM performance and strength of catalyst basicity has ever been reported.

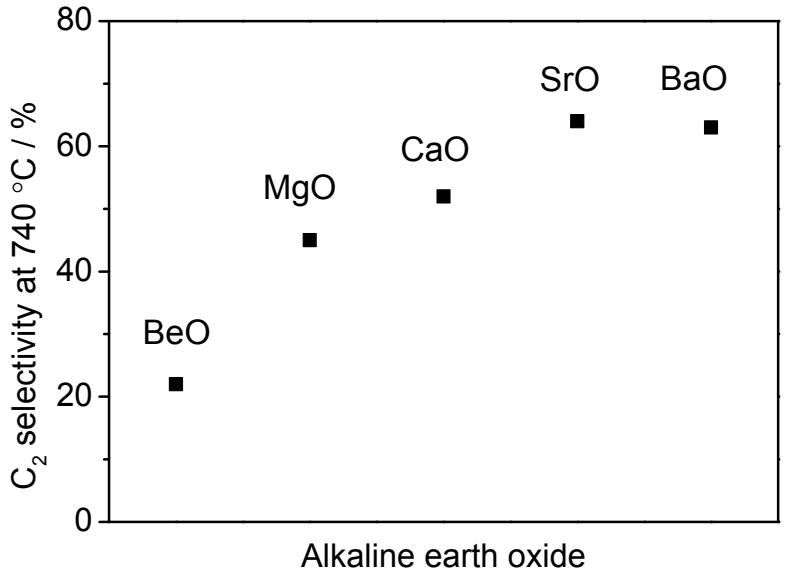

Fig. 1.4: C_2 selectivities at 740 °C for a series of alkaline earth oxide catalysts in Carreiro's paper.[77] The data of C_2 selectivity was abstracted from Table 1 shown in the paper, where no methane conversions were given.

Carreiro et al.[77] studied the OCM performance of a series of alkaline earth oxides. They found that C_2 selectivities increased from BeO to BaO, where bulk basicity of these materials was assumed to increase concomitantly. However, performance data in terms of CH_4 conversions were not clearly given, and catalyst activity was only expressed as a rate constant for a pseudo-first-order reaction calculated from the rate of O_2 conversion. Comparison of C_2 selectivities at inconsistent CH_4 conversion level is not meaningful. In addition, no experimental measurement about catalyst basicity was conducted and thus no clear quantitative correlation between OCM performance and catalyst basicity was presented in their paper.

Maitra et al.[74] investigated the OCM performance of a series of alkaline earth as well as rare earth oxide catalysts. They also experimentally measured decomposition temperatures ($T_{0.5}$) of corresponding carbonates, which were employed as a measure for catalyst basicity. They found that for the alkaline earth series, C_2 selectivities tested at several reaction temperatures showed a consistent increase with the increase of basicity. Compared to alkaline earth oxide, no straight-forward basicity-selectivity correlation was observed for the rare earth series, where the basicity did not change uniformly across the periodic table. However, C_2 selectivities were compared at different CH_4 conversion level based on their given data, which is quite misleading. Although catalyst basicity was expressed by measured decomposition temperature of carbonates, the author only stated a qualitative correlation without a quantitative fashion between OCM performance and catalyst basicity.

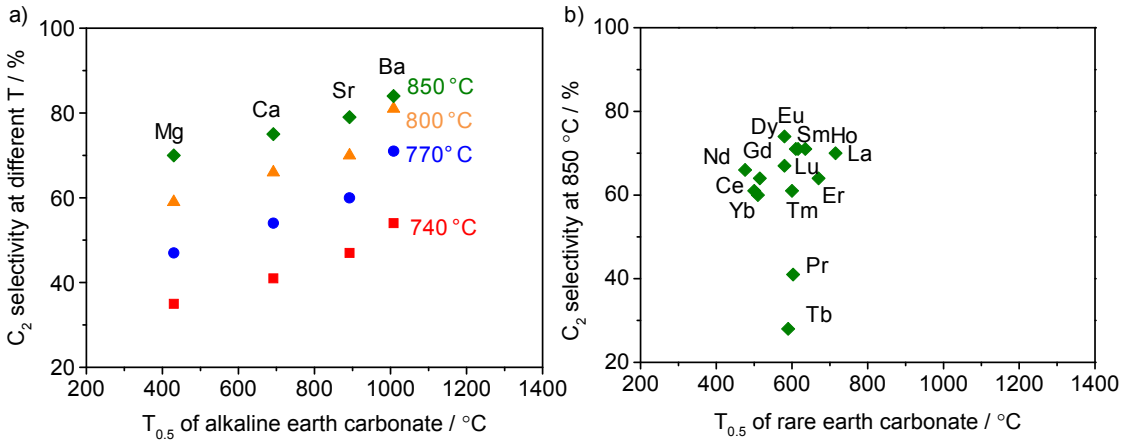

Fig. 1.5: (a) Correlation between C_2 selectivity at 740, 770, 880 and 850 °C for alkaline earth oxide catalysts and decomposition temperature of corresponding carbonates ($T_{0.5}$), (b) correlation between C_2 selectivity at 850 °C for rare earth oxide catalysts and decomposition temperature of corresponding carbonates ($T_{0.5}$) in Maitra's paper.[74] $T_{0.5}$ was defined by the author as the temperature corresponding to 50% of a total mass loss due to carbonate decomposition. The values of C_2 selectivity and $T_{0.5}$ were abstracted from Table 2 and Table 4 shown in the paper.

Choudhary et al.[72] determined the number of basic sites for a series of alkali metal promoted MgO catalysts by monitoring the desorbed CO_2 when temperatures was elevated from 50 to 900 °C. Considering the CO_2 desorption occurred in a very broad temperature range, the author attributed desorbed CO_2 at 50 ~ 900 °C and 500 ~ 900 °C to "total" and "strong" basic sites, respectively. They found that C_2 product formation rate per unit surface area increased exponentially with the increase of surface density of strong basic sites but not total basic sites. However, the comparison of performance parameter they defined is questionable because the information of C_2 formation may lose its original characters after normalization by catalyst surface area which was quite different based on the given data in this paper. Besides, the temperature range of CO_2 desorption corresponding to strong basic sites was broad and arbitrarily defined by the author, which could not clearly reflect the strength of catalyst basicity.

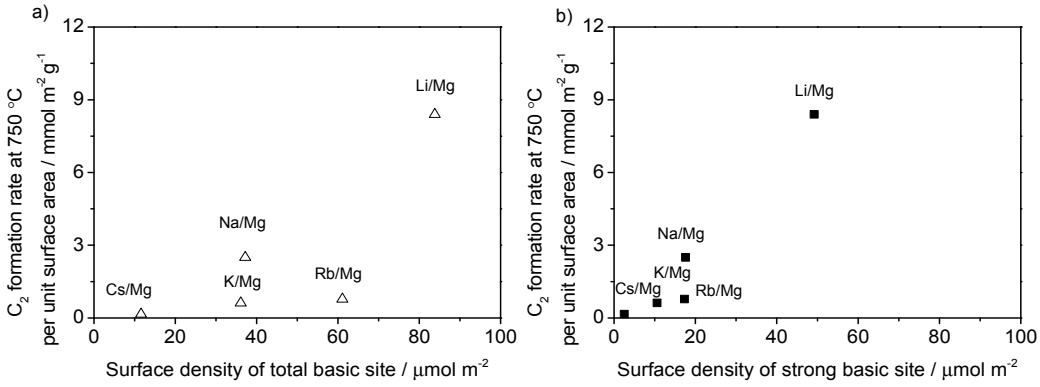

Fig. 1.6: Correlation between C_2 formation rate at 750 °C per unit surface area and surface density of (a) total basic sites and (b) strong basic sites for 0.1% alkali-promoted MgO catalysts in Choudhary's paper.[72] The performance and basicity values were abstracted from Table 2 and Table 4 shown in the paper. The author attributed CO_2 desorption at 50 ~ 900 °C and 500 ~ 900 °C to "total" and "strong" basic sites, respectively.

In a later publication by the same author,[136] the basicity and acidity strength distribution for a series of alkaline-earth promoted La_2O_3 catalysts was measured by CO_2-TPD and NH_3-TPD, respectively. They found that Sr-La_2O_3 catalyst containing a larger number of strong basic

sites and acid sites with intermediate strength exhibited the best OCM performance in terms of C_{2+} yield. However, the author did not attribute “strong” or “intermediate” basic/acid sites to a definite numerical temperature range of CO_2 or NH_3 desorption. Only the total number of basic or acid sites were presented corresponding to probe molecules desorption at whole temperature range. Although catalyst basicity/acidity was experimentally measured, no clear quantitative correlation between OCM performance and the number or strength of catalyst basicity was shown in this paper.

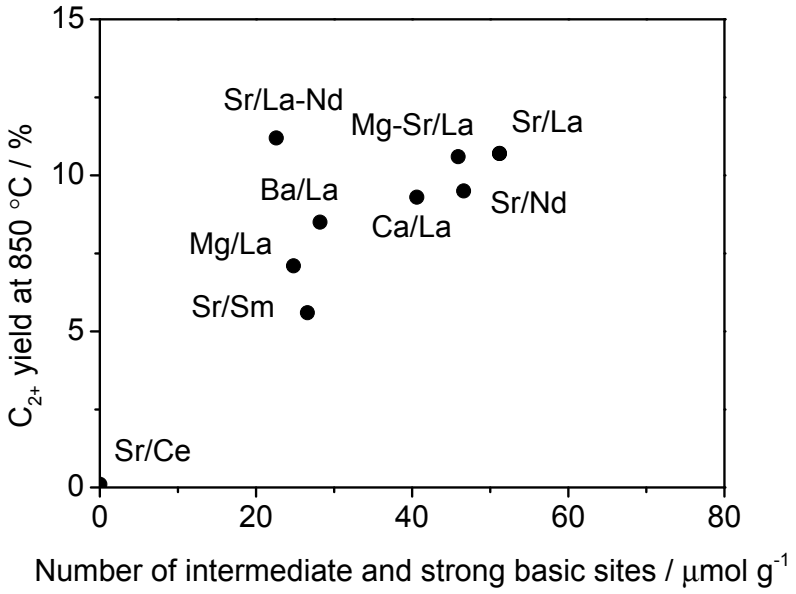

Fig. 1.7: Correlation between C_2 yield at 850 °C and number of intermediate and strong basic sites for alkaline earth oxides deposited on commercial Al_2O_3-SiO_2 support precoated with rare earth oxides in Choudhary’s paper.[131] The performance and basicity values were abstracted from Table 1, Table 2, Table 5 and Table 6 shown in the paper. The author attributed CO_2 desorption at 550 ~ 750 °C and 750 ~ 950 °C to “intermediate” and “strong” basic sites, respectively.

They also investigated a series of alkaline earth oxides deposited on commercial Al_2O_3-SiO_2 support precoated with rare earth oxides in another paper.[131] The basicity properties of catalysts were measured by CO_2-TPD in a similar fashion. Differently, the author proposed four kinds of basic sites present in catalysts with different strength (“weak”, “intermediate”, “strong” and “very strong”), which were considered to correspond with the desorption of CO_2 at 50 ~ 500 °C, 500 ~ 750 °C, 750 ~ 950 °C and above 950 °C, respectively. They observed a correlation between C_{2+} yield and the sum of number of intermediate and strong basic sites in catalysts. However, the quantitative correlation presented in this paper was not significant. Besides, the author arbitrarily defined the basicity strength by CO_2 desorption at certain temperature range and focused on the number of basic sites with different strength. But no unambiguous quantitative correlation between OCM performance and the strength of catalyst basicity was presented in this paper.

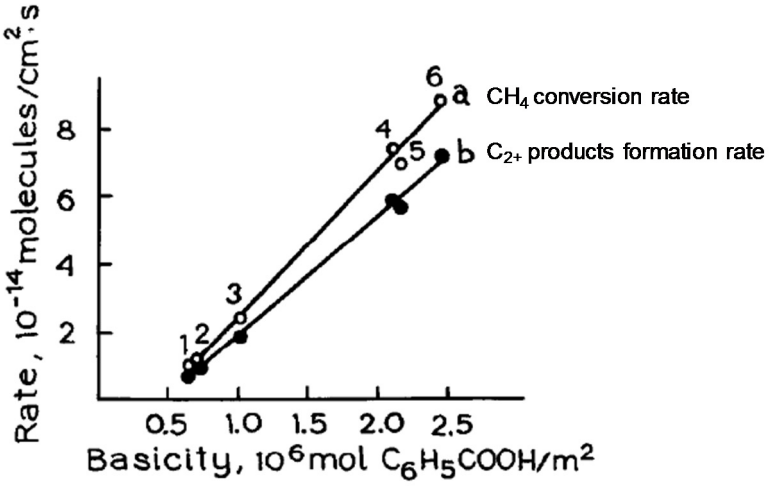

Fig. 1.8: Correlation between (a) CH_4 conversion rate, (b) C_{2+} products formation rate at 750 °C per unit surface area and concentration of basic sites for PbO-MgO catalysts doped with (1) 5% P, (2) 5% W, (3) no additives, (4) 5% Na, (5) 5% Li and (6) 5% K, adapted from Sokolovskii et al.,[132] with permission from Elsevier. The number of basic sites were measured by the adsorption of benzoic acid.

Sokolovskii et al.[132] determined the concentration of base sites for PbO-MgO catalysts doped with 5% P, W, Na, Li, K or no additives by the adsorption of benzoic acid from dry heptane. They found that the overall conversion rate of CH_4 as well as the formation rate of C_{2+} products increased with the increase of the concentration of basic sites in catalysts. However, both CH_4 conversion rate and C_{2+} products formation rate were normalized by surface area in this paper, which may be questionable to be utilized as catalytic performance parameters. Direct comparison of CH_4 conversion and C_2 yield would be more appropriate, but no clear values were given by the author. In addition, the basicity was only experimentally measured in terms of numbers as a whole, but basicity strength of these basic sites was not considered in the correlation with OCM performance shown in this paper.

In summary, people have done various research work attempting to build the correlation between OCM performance and catalyst basicity. Most of previous papers only stated an ambiguous qualitative correlation by presenting data tables where the catalyst basicity and corresponding catalytic performance were somehow compared. In those papers exhibiting clear quantitative correlation, the authors typically only focused on the number of basic sites and its influence on catalytic performance. Until now, however, no clear and universal quantitative correlation between OCM performance and strength of catalyst basicity has ever been reported.

1.5.2. Statistical evaluation of OCM dataset with respect to catalyst properties

A meta-analysis is a statistical technique referring to a large collection of analysis results from individual studies for the target of integrating the findings.[137] It is a powerful tool capable of unraveling sophisticated relationship and causalities hidden in the multiple data which is conducted and reported from independent experiments.

Zavyalova and Baerns et al.[69] in 2011 firstly reported an important breakthrough for statistical analysis of past catalytic data on OCM reaction. A substantial contribution is that they created a reliable dataset by manually collecting information on catalyst composition, reaction conditions as well as the respective catalyst performance originally from 421 publications including research papers and patents. Through statistical analysis, they suggested that a promising OCM catalyst should consist of host basic metal oxide (MgO or

La_2O_3) with dopants having positive effects on both C_2 selectivity (Cs, Na, Sr, Ba) and catalyst activity (Mn, W, Cl^-). They also tried to identify correlations between descriptors representing "catalyst composition" and "catalyst performance", but failed to evidence consistent robust trends, because their proposed descriptors did not capture the essential properties for OCM reaction.

Kondratenko et al.[138] reported an experimental approach in order to validate the strategy for generating OCM catalysts based on statistical model. But the validation failed mainly due to inappropriate selection of catalysts. Catalysts with diversified prediction values of C_2 yield should be designed and experimentally testified, but the author only synthesized and tested the expected well-performing catalysts (La_2O_3 or MgO as host oxide). Thus, all data points representing predicted and measured C_2 yield of catalysts were concentrated in a very narrow region (see Fig. A1.1), which failed to validate the statistical prediction.

Several challenges could not be solved in the above statistical analysis methods.[69] The reaction condition parameters, such as temperature, CH_4 / O_2 ratio, contact time, that are well-known parameters to affect conversion and selectivity, were scattered but not taken in to consideration. The analysis was established on the supposed existence of direct correlations between catalyst composition and performance, while no descriptors of physico-chemical catalyst properties were encoded in the dataset or statistical model, therefore no clear property-performance relationships could be derived. Besides, the statistical analysis was performed through a formal mathematical way without incorporation of chemical knowledge and intuition.

In order to deal with these challenges and explore the property-performance correlation in the language of “chemist”, Schmack[139] proposed a new meta-analysis approach to evaluate large catalytic dataset and seek for correlations between the physico-chemical properties and the catalytic performance. The approach is generally composed of the initial formulation of a chemical hypothesis, i.e. a proposed property-performance correlation, and a subsequent assessment if the hypothesis is reflected in a statistically significant way by the available experimental data. A brief introduction regarding to method, model and observed effects is shown in the following, because it provides a starting point for the experimental approach followed in this thesis.

Firstly, the OCM dataset compiled by Zavyalova et al., the only accessible and sufficiently large set of catalytic data, was refined through a few of catalytic data corrections and certain element assignment focusing on general categories "cation" and "anion". Secondly, the "descriptor rules" was postulated that computes values for arbitrary descriptors. The so-called “descriptor” was based on physico-chemical properties of individual chemical elements and chemical compounds formed by each element from literatures. The descriptors involve the molar mass of an element, its position in the periodic table of elements, the ability to form a carbonate as well as the carbonates decomposition temperature.

Furthermore, properties of the stoichiometry of the most stable oxide (potentially formed) and its melting point ($T_{melt,oxide}$) were incorporated. Associated with melting point, the Tammann temperature ($T_{Tammann}$)[140] was encoded as a measure to describe the onset of sintering and loss of surface area. Thirdly, a certain chemical hypothesis was proposed with the implementation of “selection rules” which assigns each catalyst into one of at least two distinct "property groups" based on the “descriptor rules”. Through the classification at different levels, very hierarchically nested hypotheses were formulated that stepwise divide the initial large dataset of catalysts via objective quantitative criteria but not empirical group assignment carried out by individual researchers. Fourthly, a multiple regression analysis

was performed to quantitatively compare the performance (C_2 yield) difference between catalysts assigned to two different property groups while compensating the effect of differences in the OCM test conditions. Equation (1.6) illustrates the regression typically used for the mentioned comparison.

$$Y_i = \beta_0 + \beta_{group} \times D_{group,i} + \beta_T \times \Delta T_i + \beta_{CH4/O2} \times \Delta p_{CH4/O2,i} + U_i \qquad (1.6)$$

where the dummy variable $D_{group,i}$ [1] describes which of the two compared property groups each catalyst i is assigned to. The regression procedure was targeted to adjust all β values in order to minimize the sum of squares of the residuals U_i between experimental (Y_i) and computed yield values over all entries in the two groups. The derived β values quantifies, most importantly, the effect of assignment to either one of the two compared catalyst groups (β_{group}) on Y_{C2}. Meanwhile, the effect of temperature (β_T) and pressure ratio ($\beta_{CH4/O2}$) were also quantified to describe the influence of test condition as a representative. Therefore, the obtained β_{group} is considered to be a quantitative measure (in terms of corrected C_2 yield) for the influence of catalyst physico-chemical properties on OCM catalytic performance. Fifthly, a statistical significance test related to each β regression coefficient was performed to check whether the two compared catalyst groups are indeed different in their C_2 yield. Finally, by assembling the property groups into one hierarchical model with corresponding regression results, a final model with tree-like structure was presented as depicted in Fig. 1.9, where the correlation between physico-chemical properties and catalytic performance was established.

On Level 1, catalysts containing at least one component that is known to form a carbonate compound (1b) show higher average Y_{C2} than those containing no component can form carbonate (1a). On Level 2, the terminology “Support” is defined by the two criteria: (i) among all the oxides possibly formed by cations, at least one possesses a Tammann temperature higher than the actual tested OCM temperature (ii) the mass content of this oxide, assuming that it exists in the most stable form, reaches above 50 wt% of the entire catalyst’s constituents. After selection by the rule of “Support”, the assigned “Supported” property group (2b), where one cation fulfills the “Support” criteria and another cation is present capable of forming a carbonate, exhibits higher average Y_{C2} than other property groups (2a, 2c and 2d). On Level 3, the additional ability of above “Support” cation to form a carbonate is considered. The “Supported” group (2b) on Level 2 is further divided into two subgroups, where catalysts with “Support” cation capable of forming also a carbonate ("Carbonate-supported", 3a) shows higher average Y_{C2} than those with “Support” cation lack of ability to form a carbonate ("Inert-supported", 3b). On Level 4, the stability of the potentially formed carbonates in catalysts is incorporated by a quantitative criterion that compares the decomposition temperature of a carbonate to the actual test temperature. The assigned "carbonate thermodynamically stable" subgroup contains catalysts with the cation forming the most stable carbonate, whose decomposition temperature is higher than the measured OCM temperature corrected with a certain offset due to experimental uncertainties and dependence of carbonate decomposition equilibrium on CO_2 partial pressure. These groups typically show higher average than the “carbonate thermodynamically not stable” group, where none of cation can form a carbonate decomposing at higher temperature than the test OCM temperature.

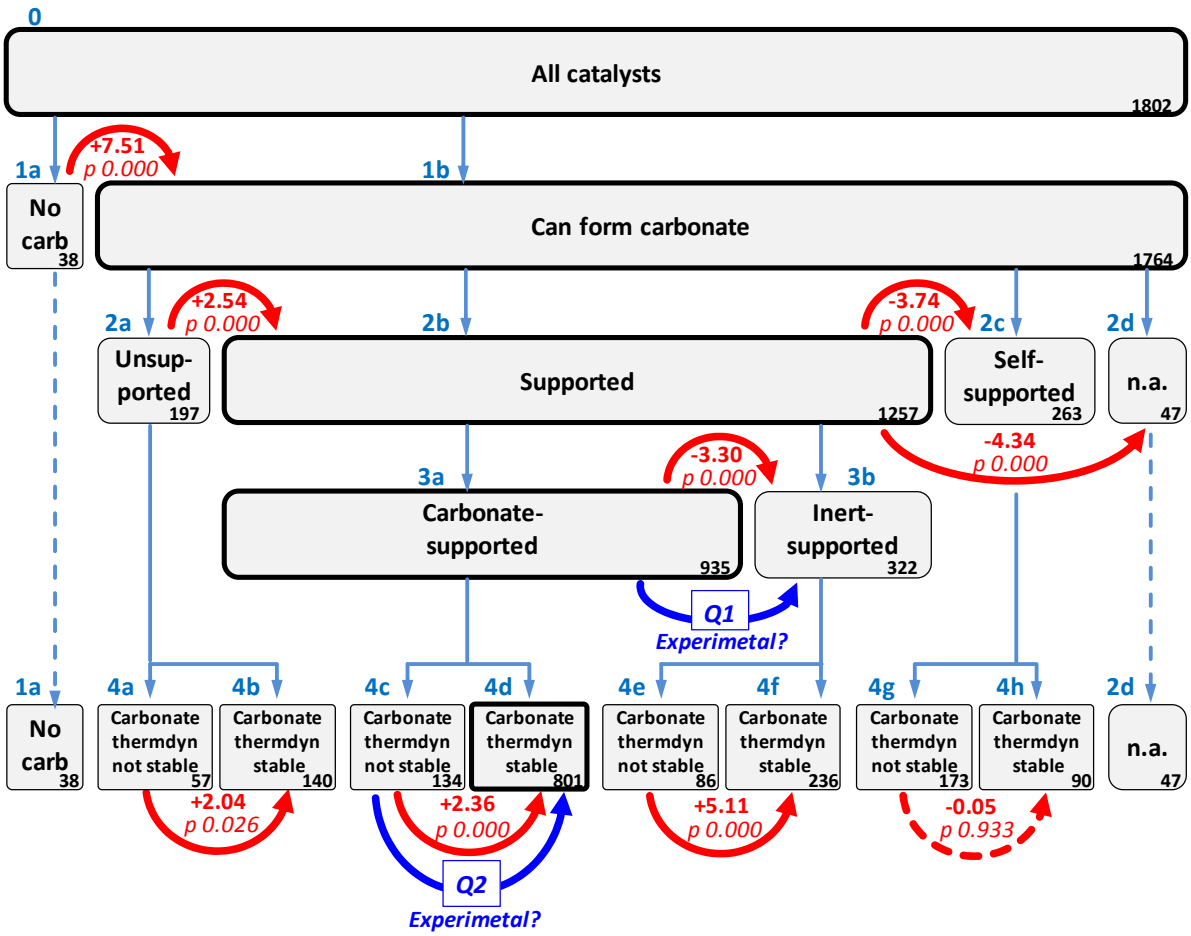

Q1: The effect of support cation which can form a carbonate or not on OCM performance?

Q2: The effect of cations which can form stable carbonate or not at OCM temperature on OCM performance?

Q3: Difference between metal oxide and carbonate with same cation used as support material for catalysts?

Fig. 1.9: Tree representation of the final model and corresponding regression results, adapted from the thesis of Schmack.[139] The box width scales with the approximate number of catalysts (N) assigned to the corresponding property group (level 1 to 3). Red arrows indicate the direction of regression analysis that compares two property groups and provide the obtained respective β_{group} regression coefficients (~ $\Delta\bar{Y}_{C2}$) and p-values. The path towards the group with the highest OCM performance (4d) is marked by boxes with bold frames. Three questions are proposed as a starting point for the experimental approach in this thesis.

Evaluable information concerning not only catalysts composition but also physico-chemical properties can be extracted from the statistical analysis for the purpose of designing a well-performing catalyst. A good catalyst should comprise at least two elements. One can form a thermally stable (non-sintering) oxide under OCM conditions, which could provide sufficient surface area for CH_4 activation and suppress non-selective oxidation. Another element is able to form a thermodynamically stable carbonate at the temperatures of OCM reaction, which probably facilitates the formation of C_2 products. Therefore, carbonate stability could be one important factor that controls OCM performance.

The concept of carbonate and its stability would be take into consideration of catalyst design in this thesis. Three questions are proposed considering this statistical analysis as a starting point for the experimental approach. First question is about the effect of support cation which can form a carbonate or not on OCM performance, where the statistical trend would be validated by experimental results of catalysts between “Carbonate-supported” and “Inert-supported” groups. Second question is regarding to the influence of supported cation can

form a stable carbonate at OCM temperature or not on catalytic performance. The statistical trend would be validated by experimental data of catalysts “Carbonate thermdyn not stable” and “Carbonate thermdyn stable” groups. Third question is about the kind of support materials and to investigate whether there is difference when oxide or carbonate with same cation is used as a support for catalyst. It would be studied by comparison between oxide-supported and carbonate-supported catalysts.

1.5.3. Carbonate stability in OCM

In Schmack’s statistical analysis,[139] the carbonate formation ability of element is considered to play a crucial role on catalyst performance. Generally, OCM catalysts usually contain metal oxides. These metal oxides have possibility to form carbonate species with considerable thermal stability under OCM conditions due to the inevitable presence of by-product CO_2. A decomposition/formation equilibrium of carbonate is expected to exist in the catalytic system, which may influence the proceeding of OCM reaction.

The concept of carbonate stability

The formation of carbonate can be expressed by the reaction between a base and an oxo-acid. Specifically, a basic oxide has a tendency to form a carbonate with CO_2, as shown in Equation 1.7. Therefore, oxide basicity can be used as a measure to evaluate the corresponding carbonate stability.[74]

$$\underset{\text{base}}{\mathrm{MO}} + \underset{\text{acid}}{\mathrm{CO_2}} \rightarrow \underset{\text{salt}}{\mathrm{MCO_3}} \qquad (1.7)$$

In a quantitative way to express the basicity, Smith[133] proposed a basicity scale, a measure in terms of tendency to behave as an O^{2-} donor. It was constructed for a wide range of oxides on the basis of reaction enthalpies (ΔH^0) between oxides and certain inorganic species (H_2O, CO_2, P_4O_{10}, SO_3) towards the corresponding salts (hydroxides, carbonates, phosphates, sulfates). He postulated that the reaction enthalpy between an oxo-acid (A) and an oxo-base (B) equals to the difference between the defined characteristic basicity scale $a(A)$ and $a(B)$, as shown in Equation 1.8.

$$\frac{-\Delta H^0}{kJ\ mol^{-1}} = [a(A) - a(B)]^2 \qquad (1.8)$$

where a is the Smith basicity value. The basicity scale difference between the two substances becomes larger when the reaction is more exothermic. The basicity scale of water was chosen to be a benchmark with value of 0, $a(\mathrm{H_2O}) = 0$, as water is commonly the weakest encountered acidic oxide. In this way, stronger basic oxide possesses more negative Smith basicity value. A more direct bridge between oxide basicity and carbonate could be established if CO_2 would have been used a benchmark. But this is not the case for the definition by Smith scale. Nevertheless, Smith basicity scale provides a quantitative possibility to express the oxide basicity related to reaction enthalpy. A selection of Smith basicity scale values is given in Table A1.1.

In general, carbonate stability can be expressed by the decomposition / formation equilibrium (1.9) and the equilibrium constant (1.10).

$$\mathrm{MCO_3} \rightleftharpoons \mathrm{MO} + \mathrm{CO_2} \qquad (1.9)$$

$$K = \frac{\mathrm{a_{MO}} \times p_{\mathrm{CO_2}}}{\mathrm{a_{MCO_3}}} = \exp\left(\frac{-\Delta G}{RT}\right) = \exp\left(\frac{-(\Delta H - T\Delta S)}{RT}\right) \quad (1.10)$$

where $\mathrm{a_{MO}}$ and $\mathrm{a_{MCO_3}}$ means the oxide and carbonate activity (note: not Smith basicity a) of in the condensed phase. $p_{\mathrm{CO_2}}$ is the equilibrium pressure of CO_2.[141] The reaction entropy (ΔS) values are similar for all carbonates decomposition, as it is caused by formation of CO_2. Hence, the proceeding of carbonate decomposition is mainly influenced by reaction enthalpy (ΔH). In others words, carbonate stability mostly depends on the reaction enthalpy.

Both Smith basicity scale and carbonate decomposition equilibrium are highly related to reaction enthalpy. Therefore, it is reasonable to assess carbonate stability with Smith basicity scale in a quantitative way.

In addition to Smith basicity scale based on reaction enthalpy, carbonate stability is also influenced by the polarizing power of cation, usually expressed by Z/r^2, where Z is the charge number of the atomic core and r is the ionic radius.[141-143] A selection of polarizing power values of cations is given in Table A1.2. Higher Z/r^2 means stronger electrostatic force between a positive charge (cation) and a negative charge (carbonate anion). Cations with high Z/r^2 tend to easily attract electrons in the outermost shell of the carbonate anion and subsequently induce its deformation through breaking C-O bond when the polarizing power of cation is sufficiently high. That is to say, carbonate stability is negatively related to the polarizing power of cation.

Both Smith basicity scale and polarizing power seem to be related to carbonate stability. However, carbonate stability can be evaluated by the decomposition temperature of carbonate in a more direct and measurable way.[74] Thermogravimetric analysis (TGA) is frequently employed to evaluate the thermal stability of a material, in which mass change is typically measured as a function of increasing temperature. If the material is thermally stable in a certain temperature range, there will be no mass change observed. Beyond this temperature range, mass change will be detected indicating the material begin to degrade. Additionally, the heat flow during the whole ramping process is usually monitored as well to reflect the involved phase transition. Luckily, quantities of research have been done to investigate the thermal decomposition of carbonate involving nearly all elements in the periodic table.[141, 144, 145] These reports provide an available source to search for the decomposition temperature of a certain carbonate. In Table A1.3, carbonate decomposition temperatures (T_{dec}) were extracted from previous reports and archived here in the order of atomic number.

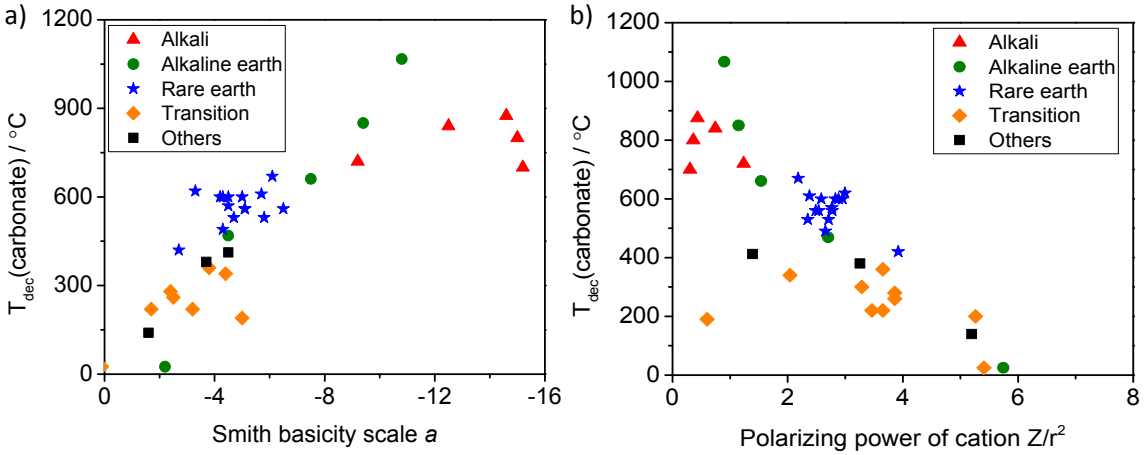

Fig. 1.10: Correlation between decomposition temperatures of carbonates (see Table A1.3) and Smith basicity scale (See Table A1.1) or polarizing power of cation (See Table. A1.2). Alkali metal (▲), alkaline earth metal (●), rare earth metal (★), transition metal (◆) and other (■) elements.

There may be interconnection between carbonate decomposition temperature, basicity of oxides and polarizing power of cations. Fig. 1.10 a illustrates the correlation between carbonate decomposition temperature and Smith basicity scale of the corresponding oxide. In general, a rational linear correlation is obtained over a wide range of element, revealing that carbonate decomposition temperature roughly increases with the basicity of corresponding oxide. For example, transition metal oxides (orange diamond) possess low basicity (Smith scale typically 0 ~ -4) and thus their corresponding carbonates are quite thermally unstable. Rare earth metal oxides (blue star) have intermediate basicity (Smith scale typically -4 ~ -8) and the carbonates formed by these element also exhibit intermediate thermal stability. Differently, the basicity of alkaline earth metal oxides show a consistent increase with the atomic number of element and their respective carbonates exhibit the correspondingly increased thermal stability as well. However, for alkali metal oxides with strong basicity, which are Cs and Rb (Smith scale < -14), they seems to deviate from the primary trend. The reason is that these corresponding carbonates begin to decompose upon melting.[141] The formed molten phase improves mass transfer, especially the removal of produced CO_2 from the bulk and thus facilitates the decomposition of carbonates. Additionally, other oxides containing main group metal element, such as Pb, Bi and Ga (black square), locate in the area of low basicity and carbonate decomposition temperature.

Fig. 1.10 b depicts the correlation between carbonate decomposition temperature and polarizing power of the cation. Similarly, an approximately linear correlation is obtained over a huge body of cations, exhibiting that carbonate decomposition temperature roughly decreases with polarizing ability of the cation. For example, alkali cations possess lower polarizing power and therefore, carbonates with these cations are typically stable. Rare earth cations have intermediate polarizing power and their corresponding carbonates exhibit intermediate thermal stability as well. For carbonates with transition metal cations possessing higher polarizing power, they are usually quite unstable.

Therefore, Smith basicity scale, polarizing power of cations and carbonate decomposition temperature provide the approach to evaluate the stability of a carbonate. Importantly, the carbonate decomposition temperature is a more experimentally measurable parameter, which can be directly derived from thermogravimetric analysis. Furthermore, this measure is

facile to be applied to more complex composition of carbonate, which is typically the case for catalysts in OCM reaction.

Contribution of carbonate to OCM

Metal oxides are commonly involved in OCM catalysts, which have a tendency to form carbonate species under OCM conditions when they contact with the by-product CO_2. The carbonate stability as well as the formation/decomposition equilibrium can be mediated by self-produced reaction atmosphere, operation temperature, CO_2-containing feed and so on. Many groups have investigated catalysts related to carbonate formation and tried to elucidate the contribution of carbonate to OCM. But unfortunately, it still remains unclear and controversial.

Aika et al.[146] found that pure $SrCO_3$ and $BaCO_3$ containing no additives were effective catalysts for OCM reaction, with remarkable C_2 yield (8.5% and 15.3% at 750 °C, respectively). The carbonates are considered to possess radical centers which abstract hydrogen abstraction from CH_4 at the elevated temperature. This is an exemplary report to claim for the direct contribution of carbonate to OCM. However, there was no powerful evidence to prove the existence of carbonate after OCM reaction, which weakens their argument.

Another direct contribution of carbonate to OCM was proposed by Tong et al.[93]. They suggested that carbonate is able to suppress the unselective oxidation of methyl radical reaction with catalysts surface through partially covering the surface. They achieved to measure the amount of methyl radical via an advanced setup combined with matrix isolation electron spin resonance (MIESR). It enabled the separated generation of methyl radicals by a Sm_2O_3 and detection of $\dot{C}H_3$ passing through various lanthanide oxides catalysts located in the middle. Extremely low amount of $\dot{C}H_3$ was detected when CeO_2 was employed, thus behaving as an effective $\dot{C}H_3$ scavenger. Furthermore, they tested CeO_2 as catalyst in a separate OCM co-feed experiment by using a fixed bed reactor, and found that pure CeO_2 exhibited no selectivity towards C_2 products although appreciable amount of CH_4 conversion was converted (X_{CH4} ~ 20%). But when Na_2CO_3 was doped with CeO_2, the C_{2+} selectivity was significantly improved (S_{C2+} ~ 60%) for the Na_2CO_3-CeO_2 catalyst at similar CH_4 conversion level. Much more amount of $\dot{C}H_3$ was also detected for CeO_2 after doping with Na_2CO_3. The authors suggested that Na_2CO_3 could partially cover the catalyst surface and decrease the reaction rate of methyl radical with surface, therefore providing more opportunity for the radicals to escape into gas phase where they probably couple towards C_2 product. Similar positive effect on C_2 selectivity was also reported when La_2O_3[147] , Yb_2O_3[147] and Pr_6O_{11}[148] are promoted by sodium salts.

On the other hand, carbonates are considered to play an indirect role in OCM catalysis. The presence of carbonate species was proposed to form and stabilize oxygen species (e.g., peroxide) at high temperatures. An equilibrium between carbonate and peroxide species associated with gas phase oxygen was described by Appleby et al. when they investigated molten alkali carbonate phase such as pure Li_2CO_3[149] and Li_2CO_3-K_2CO_3 eutectic melt[150], as shown in Equation (1.11).

$$2\,CO_3^{2-} + O_2 \rightleftharpoons 2\,O_2^{2-} + 2\,CO_2 \qquad (1.11)$$

The carbonate ion is in favor of peroxide formation. A following study of by Moneuse et al.[43] claimed that decomposition of carbonate in a Na_2CO_3-K_2CO_3 eutectic melt increases the concentration of oxygen ions and makes the melt more basic. The peroxide species,

preferably formed from carbonate decomposition, could be stabilized in this basic media, which was also proved by in-situ Raman spectroscopy[151] and voltammetry characterization[152]. Hence, the carbonate ion also functions as a stabilizer for peroxide species. The typical OCM reaction condition involves the presence of oxygen in feed and high operation temperatures. The above equilibrium between carbonate and peroxide species shown in Equation (1.11) is expected to exist in catalysts during OCM reaction. The formation of peroxides ions, related to carbonate, would be either direct or indirect responsible for CH_4 activation,[44, 45, 49] as introduced specifically in section 1.2.3.

The stabilization effect on active species by carbonate was also suggested from a different perspective. Korf and co-workers[80, 81] investigated the deactivation mechanism of Li/MgO catalysts through systematic characterization and claimed that the deactivation is due to a loss of Li as a volatile species LiOH or as a silicate Li_2SiO_3 by reaction with the laboratory reactors made of quartz glass. In a following study from the same group,[82] they tested OCM activity and stability for Li/MgO catalysts in a typical feed (CH_4, O_2 and N_2) and a CO_2-containing feed, separately. In the former case, the initial activity dropped dramatically after the first 2 h. In CO_2-containing feed, however, the CH_4 conversion was a bit lower than the initial level detected in none CO_2-containing feed while the stability was enhanced because there was no deactivation observed in 20 h. When CO_2 was removed from the feed, it was found that the catalyst activity returned to the same level as the result tested in typical feed. They concluded that carbonate formation may efficiently stabilize active component Li involved in catalysis through the formation/decomposition equilibrium of Li_2CO_3, which suppress the severe loss either by hydroxide LiOH evaporation or irreversible formation of Li_2SiO_3.

The presence of carbonate might also contribute to improved catalyst selectivity through the isolation of active sites. The primary concept of active site isolation, originally proposed by Grasselli[153] with regard to oxygen atoms, means that oxygen atoms must be distributed over the surface of a selective oxidation catalyst in an arrangement which provides stoichiometric sufficient oxygen amount for partial oxidation, but insufficient amount for complete oxidation. One approach to introduce site isolation is to modify the oxide surface by reaction with a reagent that renders the surface partially deactivated. The idea has also been achieved in a later study on oxydehydrogenation (ODH) of alkanes.[154] Connecting ODH with OCM is rational by the concept of active site isolation because for both reactions it is accepted that the initial activation step is the formation of alkyl radicals on oxygen species. Wang et al.[155] studied the surface composition of Mn-Na_2WO_4/SiO_2 catalysts by XPS and observed that the presence of Na (mainly in the form of Na_2CO_3) decreased the amount of Mn element in surface region. They suggested that Mn-containing active species are dispersed in catalyst, probably due to a Na_2CO_3 phase on surface responsible for the dispersion. Based on this argument, one could speculate that the carbonate, with the assumption of inactive itself, covers the catalyst surface and undergoes partial decomposition at OCM reaction temperature. As a result, active species could then appear on the sites without coverage of carbonate and these sites are surrounded by the remaining carbonate species. In this way, active site isolation could be achieved with the contribution of carbonate in catalysts.

On the contrary, carbonate is considered to be an inactive species and has negative effect on OCM catalysis, which is typically associated with the presence of CO_2 in feed or generated from combustion reaction. CO_2 is often regarded as a OCM catalyst poison, as it adsorbs on basic sites of catalyst responsible for methane activation.[40] The extent of CO_2 poison effect depends on the basicity of the catalyst. It was observed that CO_2 addition with a

certain amount in feed resulted in a decrease of CH_4 conversion for catalysts, such as Li/MgO[82, 156, 157] and Na_2WO_4/SiO_2[158]. The formation of carbonate species was confirmed by in-situ FT-IR[159] and Raman spectroscopy[47]. Especially for catalysts containing strongly basic oxide, e.g. SrO and BaO,[131] CH_4 conversion exhibited no significant increase although they possessed high basicity determined by CO_2-TPD. The reason is that strong basic sites tend to be blocked by CO_2 adsorption under OCM conditions. However, CO_2 showed less effect on activity over Sm_2O_3,[160] La_2O_3 and CeO_2,[161] which are mostly rare earth meal oxide catalysts. They speculated that these oxides with intermediate basicity are able to form carbonates which decompose at the temperatures lower than the OCM operation temperature, as depicted in Fig. 1.10. The active sites would be not permanently blocked by the formed carbonate, but again released under OCM conditions. Hence, the presence of carbonate and its negative effect are highly related to the carbonate stability.

Table 1.1: Possible contributions of carbonate on OCM reaction.

Positive effect	Direct	responsible for hydrogen abstraction	[146]
		inhibition of unselective oxidation of methyl radicals	[93, 147]
	Indirect	stabilization of peroxide species	[45, 49, 75, 149]
		stabilization of catalysts against loss of active components	[80-82]
		generation of isolated active sites	[153, 155]
Negative effect	Direct	poison to active sites with carbonate formation	[131, 157, 158]
	Indirect	-	-

In summary, various possible contribution of carbonate on OCM reaction was reviewed above from positive and negative perspectives via a direct or indirect route, as shown in Table 1.1. Actually all the explanations do not exclude each other. The complexity of practical OCM reaction makes it impossible to be interpreted from a single effect of carbonates, especially when the formation/decomposition equilibrium of carbonate species can be self-mediated under reaction conditions. Synergetic influence of carbonates related to carbonate stability should be taken into consideration for the observed OCM performance.

1.6. Aims of the thesis

The oxidative coupling of methane (OCM) is regarded as a “dream reaction” to achieve direct conversion for natural gas towards value-added and easily transportable C_2 products with high economic relevance.

On one hand, Mn-Na_2WO_4/SiO_2 catalyst is considered to be a suitable candidate for industrial application. But when mesoporous SiO_2 is employed as support, it suffers from severe loss of surface area and porosity ought to be beneficial to the reaction. Therefore, a mesoporous material with high thermal stability under OCM conditions should be incorporated for Mn-Na_2WO_4 compound to preserve the surface area and porosity of the catalyst. To achieve this, silicon carbide (SiC) is to be employed as support due to its well-known high stability, chemical inertness and high mechanical strength. The proper approach has to be explored to obtain a new mesporous Mn-Na_2WO_4/SiC catalyst. OCM performance between mesoporous SiC and conventional SiO_2 supported Mn-Na_2WO_4/SiC catalyst should be reasonably compared. The reason to explain the possible distinct behaviors has to be unraveled.

On the other hand, no general quantitative correlation between catalyst properties and OCM performance is presented so far, although a huge body of catalysts with various composition have been studied. In order to solve this problem, it is highly required to generate proper descriptors and test them for possible correlations on the basis of experimental studies by investigation of exemplary catalysts. Considering that catalysts with the ability to form carbonates are of high interest, a series of catalyst containing alkali and alkaline earth carbonate on metal oxide support would be prepared and tested inspired by the statement from statistical analysis[139]. Afterwards, catalyst property-descriptors and performance-descriptors would be derived from experimental results with certain criteria. Finally, catalyst properties regarding to the concept of carbonate stability would be correlated with OCM performance in a quantitative fashion. A unified picture for OCM catalysis is expected to be generated across a large variety of known catalysts.

1.7. Structure of the thesis

In this thesis, the influence of catalyst porosity and carbonate stability on OCM catalytic performance is systematically investigated, respectively.

An OCM study of Mn/Na/W/SiC catalyst using porous SiC as a support is presented in chapter 2. The preparation, characterization and catalytic performance testing procedure of catalysts are described in section 2.1. Comparison between uncoated supports and catalysts before and after catalytic testing with respect to structural properties are discussed in section 2.2. Then, the gas atmosphere applied for calcination is obtained as a critical factor on catalyst structure. In section 2.3, catalytic performance of Mn/Na/W/SiC catalysts calcined in different atmosphere is presented and property-performance correlations are then evaluated in section 2.4. Afterwards, a general comparison between SiC and conventional SiO_2 as a support is discussed in section 2.5.

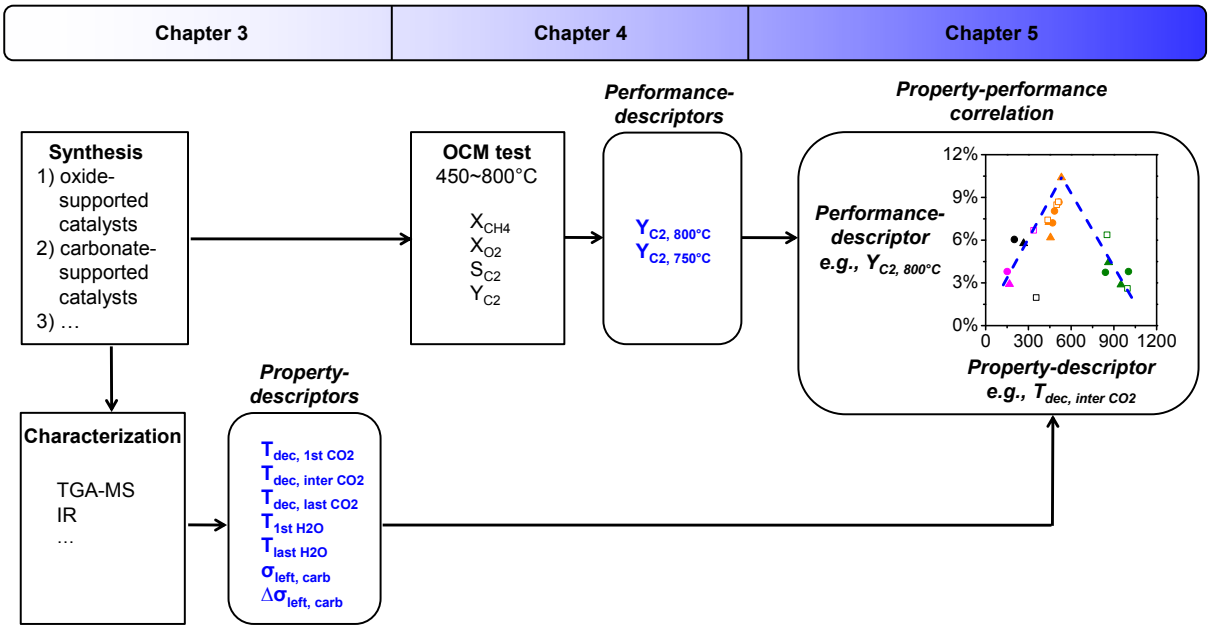

Scheme 1.1: Workflow in this thesis to generate descriptors and establish property-performance correlations. Chapter 3: catalysts synthesis, characterization and derivation of property-descriptors. Chapter 4: OCM catalytic test and derivation of performance descriptors. Chapter 5: property-performance correlations construction and evaluation.

In order to establish a quantitative and universal property-performance correlation, different property-descriptors and performance-descriptors are generated and correlated for

exemplary catalysts in chapter 3, 4 and 5. Oxide-supported catalysts composed of alkali carbonate (Rb_2CO_3 and Cs_2CO_3), alkaline earth carbonate (Mg acetate as precursor) and rare-earth metal oxide (Sm_2O_3, Y_2O_3, Gd_2O_3 and CeO_2), alkaline-earth metal oxide (SrO and BaO) or conventional Al_2O_3 support are presented. With regards to the selected catalysts, carbonate ($Sm_2(CO_3)_3$ and $SrCO_3$)-supported Rb_2CO_3 and Cs_2CO_3 are also introduced as a comparison. In addition, typical OCM well-performing catalysts such as Li/MgO and Mn-Na_2WO_4/SiO_2 are also incorporated.

In chapter 3, the synthesis of catalysts and characterization techniques are described in section 3.1 and 3.2. Analytics of oxide-supported carbonate catalysts as well as pure oxides support before and after catalytic testing are discussed in section 3.3. Specifically, the thermal stability of carbonate species in catalysts is systematically investigated. Different property-descriptors ($T_{dec,\ 1st\ CO2}$, $T_{dec,\ inter\ CO2}$, $T_{dec,\ last\ CO2}$, $T_{1st\ H2O}$, $T_{last\ H2O}$, $\sigma_{left,\ carb}$ and $\Delta\sigma_{left,\ carb}$) based on characterization result are derived to represent corresponding physico-chemical property of catalysts. Characterization data of carbonate-supported carbonate catalysts is presented in section 3.4. Afterwards, Li/MgO and Mn-Na_2WO_4/SiO_2 catalysts are also characterized in section 3.5. The effect of CO_2 on carbonate stability is studied through comparison of thermogravimetric analysis in Ar and CO_2 atmosphere in section 3.6.

In chapter 4, OCM catalytic performance of above catalysts is presented in detail. The catalytic testing procedure is described in section 4.1, where OCM measurement in N_2 feed and CO_2 feed are independently performed. Performance data of oxide-supported carbonate catalysts as well as pure oxide support are presented in section 4.2. Performance-descriptors regarding to C_2 yield at typical OCM temperatures ($Y_{C2,\ 800\ °C}$ and $Y_{C2,\ 750\ °C}$) are generated based on performance data. Catalytic testing results of carbonate-supported carbonate catalysts in N_2 OCM feed are discussed in section 4.3. Afterwards, performance data of selected typical OCM catalysts, Li/MgO and Mn-Na_2WO_4/SiO_2, are presented in section 4.4. OCM performance of $Sm_2(CO_3)_3$ supported catalysts tested in CO_2 OCM feed are compared to the results tested in N_2 OCM feed in order to explore the effect of CO_2 in atmosphere in section 4.5.

In chapter 5, correlations between property-descriptors and performance-descriptors are established and evaluated. In section 5.1, the approach used to establish and evaluate property-performance correlations is briefly introduced. Thereafter, OCM performance in terms of C_2 yield is correlated with $T_{dec,\ 1st\ CO2}$, $T_{dec,\ inter\ CO2}$, $T_{dec,\ last\ CO2}$ in section 5.2. In section 5.3, correlations between C_2 yield and $T_{1st\ H2O}$, $T_{last\ H2O}$ are presented. Correlations between C_2 yield and $\sigma_{left,\ carb}$, $\Delta\sigma_{left,\ carb}$ are shown in section 5.4. A linear regression analysis is performed for all proposed correlations in order to assess the quality of fitting between regression model and experimental data. Based on the linear regression analysis, whether the descriptor could reflect the property controlling OCM reaction or not is discussed in section 5.5. In addition, Li/MgO and Mn-Na_2WO_4/SiO_2 catalysts are also presented in section 5.6 to examine whether the correlations built by oxide-supported carbonate catalysts could be extended to typical OCM catalysts.

In chapter 6, proposed mechanistic and basicity concepts in OCM catalysis are generally discussed. In section 6.1, for the studied oxide-supported carbonate catalysts, the comparison of interaction between carbonate and cations is presented concerns different polarizing power of cations. Subsequently, possible coordination states are suggested and depicted based on experimentally measured IR-related parameter. Afterwards, in section 6.2, the established property-performance correlation is reasonably explained by three different

simplified surface structure models proposed on the basis of distinct carbonate stability in catalysts. The effects of carbonate presence, transfer and decomposition on catalytic performance are summarized and illustrated taken Sm_2O_3 supported Rb_2CO_3 as an example. In section 6.3, the concepts of basicity is calculated under certain assumption and then correlated with catalytic performance as well. The correlations built by basicity concepts are further compared with the correlations established by the concept of carbonate stability.

2. OCM investigation of Mn/Na/W/SiC catalyst using porous silicon carbide as a support

In this chapter, an OCM study of Mn/Na/W/SiC catalyst using porous SiC as a support is presented. The study aims to assess the role of porosity on SiC supported catalysts.

The preparation, characterization and catalytic performance testing procedure of catalysts are described in section 2.1. Analytics of uncoated supports and catalysts before and after catalytic testing are discussed in section 2.2. Specifically, the influence of gas atmosphere during calcination on catalyst structure is investigated. In section 2.3, catalytic performance of Mn/Na/W/SiC catalysts calcined in different atmosphere is discussed. Property-performance correlations are then evaluated in section 2.4. Afterwards, a general comparison between SiC and conventional SiO_2 as a support is discussed in section 2.5. Finally, in section 2.7, the observed effects and relationships are summarized.

2.1. Experimental

2.1.1. Catalysts preparation

Commercial porous SiC granules with different pore sizes were obtained from SICAT and named “SiC 27” and “SiC 56”, where the number indicates the most frequent pore size measured in nm. The granules were grounded and sieved into size fraction from 224 to 500 µm.

Mn/Na/W/SiC catalysts containing 2 wt% Mn and 5 wt% Na_2WO_4 on SiC were synthesized via a new two-step drop-wise impregnation in a self-made apparatus (Scheme 2.1). It is composed of a syringe pump and a rotary evaporator with controlled vacuum. The concept of reactor design is to enhance the dispersion of precursor solution into porous SiC support and suppress the aggregation of precursor on the surface of support. Typically, 1.0 g of SiC support was put into a 100 mL flask and preheated for 15 min in a water bath to 72 °C with rotation at 58 rpm. 91.0 mg $Mn(NO_3)_2{\cdot}4H_2O$ (Aldrich, ≥97.0%) was dissolved in 10 mL milli-Q H_2O. The $Mn(NO_3)_2$ solution was continuously dosed to the SiC in the rotary evaporator (80 mbar) via syringe pump at a rate of 1.7 mL/h. The entire impregnation process took 5 h approximately. The material was then dried in air at 120 °C overnight. After that, the obtained material was impregnated with 10 mL aqueous solution of 56.0 mg $Na_2WO_4{\cdot}2H_2O$ (Aldrich, ≥99.0%) and dried in a similar fashion.

Finally, the as-coated SiC samples were heated up to 250 °C with 10 K min^{-1} in air or nitrogen for 1h to remove water and other species residues. Thereafter, they were further heated to 800 °C with 10 K min^{-1} in air or nitrogen and maintained at the same temperature for 8h.

Uncoated SiC was thermally treated in the same way for comparison.

Moreover, a Mn/Na/W/SiO_2 catalyst was synthesized in a similar way as comparison by using silica gel (Aldrich, Davisil, Grade 634) as support material.

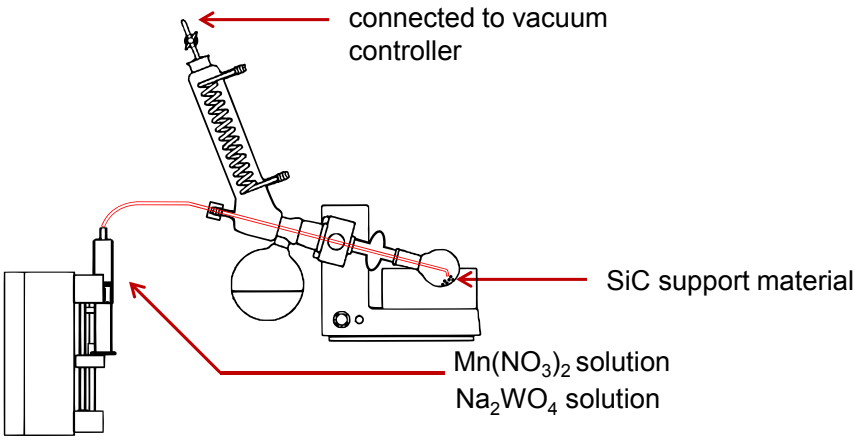

Scheme 2.1: Sketch of the reactor setup for preparation of Mn/Na/W/SiC catalysts

2.1.2. Instruments and characterization methods

Scanning electron microscopy (SEM) and energy dispersive X-ray spectroscopy (EDX)

SEM and EDX analyses were performed using a Jeol 7401 F instrument and an attached Bruker Quantax EDX detector. Samples were crushed and pasted on carbon tape. Morphological images were taken with 10 kV acceleration voltage and 6 mm as working distance. EDX mapping were recorded with 15 kV acceleration and 12 mm as working distance. Different color in EDX mapping represent for Mn, Na, W and Si, respectively.

X-ray diffraction (XRD)

XRD was measured using a Bruker D8 advance powder diffractometer in Bragg-Brentano geometry (CuKα source, λ = 0.15405 nm), variable divergence slit and a position sensitive LynxEye detector. Bragg reflexes were assigned manually using PDFMaintEx library Version 9.0.133. Samples were placed in a shallow cave of polished Si single crystal wafer with high index surface orientation. XRD was recorded in 2θ interval 15° - 80° with a step of 0.02°.

N_2 physisorption

N_2 physisorption was performed on a Quantachrome Autosorb-1. Samples were degassed in a glass tube at 150 °C for 24 h prior to physisorption measurement. Thereafter, physisorption was measured at 77K by recording adsorption (40 points) and desorption (39 points) isotherm in p/p_0 interval 0.025 -0.995. BET method for relative pressure p/p_0 from 0.050 - 0.300 was used to determine specific surface area A_{BET}. The pore size distribution was determined by NLDFT equilibrium model of silica with cylindrical pore from the adsorption and desorption branch of the N_2 isotherm.

X-ray photoelectron spectroscopy (XPS)

XP spectra of were recorded with an Omicron DAR 400 X-ray source with Al Kα excitation. Electrons were detected with an EA 125X Hemispherical Energy Analyzer.

Thermogravimetric analysis (TGA)

Thermogravimetric analysis (TGA) was performed using a Perkin Elmer STA 8000. Typically, 20 mg of the sample was placed in a ceramic crucible without lid at 30 °C. The atmosphere of measurement was synthetic air and nitrogen, respectively (100 ml/min). Initial sample mass was taken after typically ~ 10 min, when vibrations as well as strong mass drift due to equilibration of temperature and atmosphere in the sample chamber had reasonably

subsided. Then, the measurement procedure was started firstly by holding the sample at 30 °C for 1 h, to further achieve constant mass. Thereafter, the sample was heated from 30 °C to 1050 °C with a ramping rate of 10 K/min. Higher measurement temperatures were avoided to prevent damage and attrition to the instrument. The sample was held at 1050 °C for 10 min. Thereafter, the measurement was automatically stopped and the sample was cooled down naturally. The identical measurement procedure was employed for blank measurements with empty crucibles. The mass signals of the blank measurements were utilized to subtract the thermal mass drift as well as abrupt changes in the mass signal upon switching from holding temperature to heating ramp. For evaluation, sample masses were normalized to the mass at 30 °C after holding for 1 h.

Inductively Coupled Plasma - Optical Emission Spectroscopy (ICP-OES)

To determine the loading amount on the support, as-coated samples were dissolved in aqua regia and the concentration of Mn, Na and W was measured at a Varian 715-ES ICP-OES.

2.1.3. OCM catalytic test

Activity and stability of the catalysts were tested in a reactor system developed at the Leibniz Institute for Catalysis. This system consists of 6 continuous-flow fixed-bed reactors quartz tubular (internal diameter = 6 mm) reactors located in the same oven and operating in parallel. 50 mg catalyst (size fraction 224 - 500 µm) was placed on a quartz wool plug covered with roughly 700 mg SiC particles to ensure proper heat transfer. The feed gas was continuously dosed at a composition of CH_4:O_2:N_2= 2:1:4 (methane and synthetic air as oxygen source) with a total gas flow rate of 88.1 mL_{STP} min^{-1}. This flow was equally distributed to the reactors filled with catalysts. They were initially heated in the feed gas to 450°C. Thereafter, the temperature was increased in steps of 25 K from 450 °C to 800 °C. At each temperature the OCM reaction was performed for about one hour. An online gas chromatograph (Agilent 7890) was used for quantifying O_2, N_2, CO, and CO_2 with a thermal conductivity detector (TCD) and CH_4, C_2H_4, C_2H_6 with a flame ionization detector (FID). N_2 was used as internal standard. After competing OCM tests, the reactors were cooled down to room temperature in the feed gas. With the same feed gas composition, the stability of OCM catalyst was tested at reaction temperature of 600 and 700 °C.

The feed conversion was calculated from the inlet and outlet molar ($\dot{n}$) flow, e.g. CH_4 conversion (X_{CH4}) and O_2 conversion (X_{O2}) according to Equation 2.1 and 2.2. The desired reaction products of OCM are C_2H_4 and C_2H_6. Their overall yield (Y_{C2}) is written in Equation 2.3. Selectivity of C_2H_4 and C_2H_6 was calculated by Y_{C2} and X_{CH4} in Equation 2.4. Carbon balance was calculated from carbon input (as CH_4) and output (as CH_4, CO, CO_2, C_2H_4, C_2H_6, C_3H_6 and C_3H_8) according to Equation 2.5.

$$X_{CH_4} = \frac{\dot{n}_{CH_4,inlet} - \dot{n}_{CH_4,outlet}}{\dot{n}_{CH_4,inlet}} \quad (2.1)$$

$$X_{O2} = \frac{\dot{n}_{O2,inlet} - \dot{n}_{O2,outlet}}{\dot{n}_{O2,inlet}} \quad (2.2)$$

$$Y_{C_2} = \frac{2*\dot{n}_{C_2H_4,outlet} + 2*\dot{n}_{C_2H_6,outlet}}{\dot{n}_{CH_4,inlet}} \quad (2.3)$$

$$S_{C_2} = \frac{Y_{C2}}{X_{CH4}} \quad (2.4)$$

$$B_C = \frac{\dot{n}_{CH_4,outlet} + \dot{n}_{CO,outlet} + \dot{n}_{CO_2,outlet} + 2*\dot{n}_{C_2H_4,outlet} + 2*\dot{n}_{C_2H_6,outlet} + 3*\dot{n}_{C_3H_6,outlet} + 3*\dot{n}_{C_3H_8,outlet}}{\dot{n}_{CH_4,inlet}} \quad (2.5)$$

2.2. Catalyst characterization

2.2.1. SiC support materials

SiC support materials were analyzed "as is", after calcination in air at 800 °C, and after calcination in N_2 at 800 °C via SEM, N_2 sorption and XRD. Obtained representative results are shown in Fig. 2.1.

SiC 27 and SiC 56 in the "as is" state are composed of fine particles with apparent interparticle voids. Type IV adsorption-desorption isotherms with H3 hysteresis loop was determined for these both supports (Fig. A2.1). The adsorption and desorption mainly occurs above p/p_0 = 0.8, indicating a significant contribution of large mesopores arising from SiC interparticle voids. Specific surface areas of SiC 27 and SiC 56 amount to 26.1 and 28.4 $m^2 g^{-1}$ respectively (Table 2.1). As seen in Fig. 2.1 b, pore size distributions calculated via NLDFT equilibrium model feature a broad peak centered around 27 nm (SiC 27-as is) or 56 nm (SiC 56-as is). XRD analysis (Fig. 2.1 c) shows well-defined reflection which can be attributed to a 3C-SiC phase (PDF No: 01-074-2307).

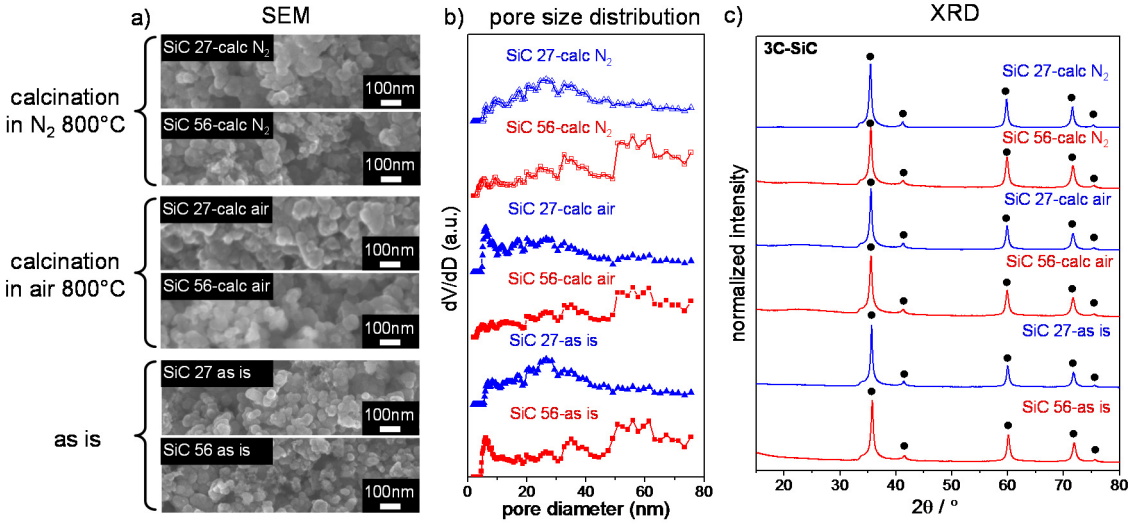

Fig. 2.1: (a) SEM images, (b) N_2 sorption and (c) XRD patterns of uncoated SiC in their “as is” forms and after calcination for 8 h at 800 °C in air or N_2. (a) The fresh samples of SiC 27 and SiC 56 show a fine-grained morphology that is preserved during treatments in air and N_2. (b) The pore size distributions of the “as is” samples show broad features with maxima at about 56 nm (“SiC 56 - as is”) and 27 nm (“SiC 27 - as is”). The maxima are preserved during treatments in air and N_2. (c) The observed XRD signals can be attributed to the (•) 3C-SiC crystal phase. Treatments in air and N_2 do not induce significant changes in crystal phase. All samples were ground and sieved into size fraction 224-500 µm prior to the treatment and analysis.

The influence of heat treatments to the SiC supports at 800 °C in either air (SiC 27-calc air, SiC 56-calc air) or N_2 (SiC 27-calc N_2, SiC 56-calc N_2) was then investigated. Calcination under both conditions scarcely alter their fine-grained morphology significantly. The supports also retain their high surface area of about 30 m^2/g (Table 2.1) and do not change their pore size distribution (Fig. 2.1 b): the maxima around 27 nm (SiC 27) and 56 nm (SiC 56) are still observed. In addition, calcination in air and in N_2 preserves the 3C-SiC crystalline phases as well. Hence, both investigated porous SiC support materials are considered to be stable in N_2 and in air at typical OCM temperatures.

2.2.2. Mn/Na/W/SiC catalysts before OCM

The SiC support SiC 27 and SiC 56 materials were impregnated with Mn and Na_2WO_4 precursor solutions and calcined in air (SiC xx-Mn/Na/W-calc air) and in N_2 flow (SiC xx-Mn/Na/W-calc N_2) at 800 °C in order to obtain active catalysts.

The bulk composition of catalysts was determined by ICP-OES. As shown in Table A2.1, e.g., SiC 27-Mn/Na/W, the amount of Na, W and Mn of the catalysts is 0.63%, 2.52% and 1.81%. The determined Mn, Na and W values are close to intended values within acceptable experimental error.

Table 2.1: Specific surface area and pore diameter of SiC 27, SiC 56 and SiO_2 support, fresh catalyst and after OCM, from N_2 sorption data. SiC 27 and SiC 56 support after calcination in air and N_2 still exhibited similar specific surface area and pore diameter to the "as is" samples without calcination. Coated SiC-Mn/Na/W catalysts exhibit very low specific surface areas after calcination in air, but retain most of surface area when calcined in N_2. After 800 °C in methane-oxygen mixtures (OCM) all catalysts possess a very low surface area independent of the initially applied calcination procedure. [a] Specific surface area was determined using BET method for relative pressure p/p_0 from 0.05 to 0.30. [b] Pore size was calculated using NLDFT equilibrium model.

	supports treated in different atmosphere at 800°C			supported Mn/Na/W catalysts before OCM		supported Mn/Na/W catalysts after OCM	
	as is	calc. air	calc. N_2	calc. air	calc. N_2	calc. air	calc. N_2
BET specific surface area ($m^2\ g^{-1}$) [a]							
SiC 27	26.1	31.2	26.6	1.9	15.0	1.9	1.5
SiC 56	28.4	27.9	31.4	1.2	18.8	1.2	1.6
SiO_2	407.8	341.4	n.a.	7.0	n.a.	6.9	n.a.
pore size maximum value extracted from pore size distribution (nm) [b]							
SiC 27	27.0	27.0	27.0	n.a.	35.0	n.a.	n.a.
SiC 56	56.0	56.0	56.0	n.a.	56.0	n.a.	n.a.
SiO_2	9.3	8.2	n.a.	n.a.	n.a.	n.a.	n.a.

Moreover, EDX mapping analysis of Mn/Na/W/SiC catalysts was performed to detect whether the Mn, Na and W element had been dispersed homogeneously over the whole catalyst structure. As shown in Fig. A2.2, the morphology of materials can be clearly distinguished from EDX mapping of Si, indicating this magnitude exhibits sufficient resolution. The homogeneous distribution of Mn, Na and W element in micrometer scale is observed for Mn/Na/W/SiC catalysts calcined in air and in N_2. It suggests that our new two-step wet impregnation in the self-made apparatus is able to effectively facilitate the diffusion of Mn/Na/W precursor into SiC support.

Fig. 2.2 displays corresponding (a) SEM, (b) N_2 sorption and (c) XRD data of Mn/Na/W/SiC catalysts. For both catalysts, calcination in air induces particle sintering and loss of the fine-grained morphology (Fig. 2.2 a). Physisorption result indicates a complete loss of mesoporosity (Fig. A2.3 a). The maxima in pore size distribution observed for the uncoated SiC supports disappear completely (Fig. 2.2 b). Moreover, the surface area of the air-calcined catalysts is drastically lower (1.9 $m^2\ g^{-1}$ for SiC 27-Mn/Na/W-calc air; 1.2 $m^2\ g^{-1}$ for SiC 27-Mn/Na/W-calc air) than that of the corresponding fresh and air-calcined supports (Table 2.1). For both air-calcined catalysts, XRD analysis indicates that the original 3C-SiC phase converts into a mixture of 3C-SiC, 5H-SiC (PDF No: 00-042-1360) as well as crystalline SiO_2 α-cristobalite (00-039-1425). Moreover, crystalline Na_2WO_4, Mn_2WO_4 and Mn_2O_3 are formed (see magnification of XRD pattern in Fig. A2.3 b), i.e. phases that were

previously reported in literature for Mn/Na/W/SiO_2 catalysts.[99] These metal-containing crystal phases exhibit small number of signals and relatively low intensity. Therefore, calcination of Mn/Na/W/SiC in air induces a complete loss of porosity of SiC support and a structural transformation, whereas uncoated SiC supports retained their porosity and structure under the same calcination conditions (Fig. 2.1).

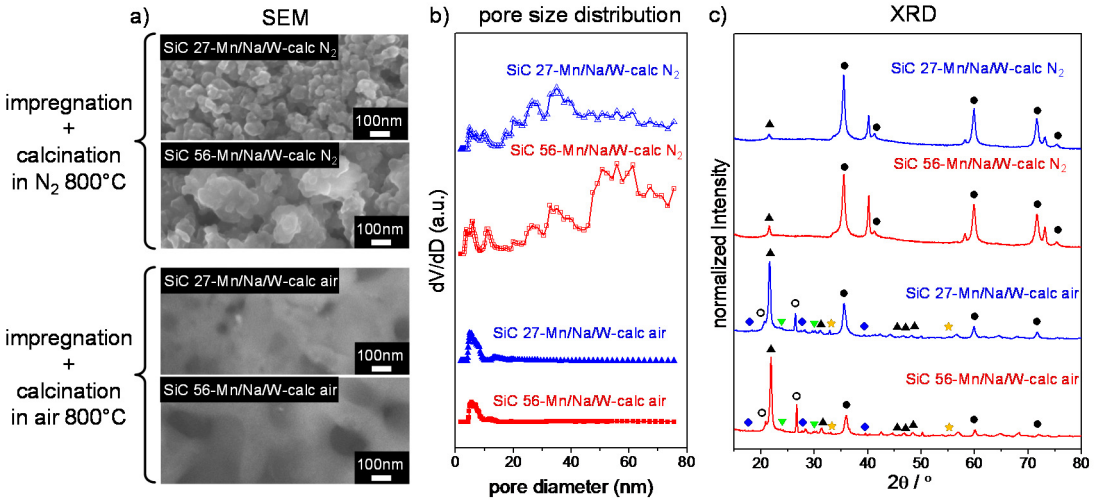

Fig. 2.2: (a) SEM images, (b) N_2 sorption and (c) XRD patterns of the catalysts SiC 27-Mn/Na/W and SiC 56-Mn/Na/W after different treatments. The supports SiC 27 and SiC 56 were sequentially impregnated with $Mn(NO_3)_2$ and then Na_2WO_4 precursor solution using a syringe pump and rotary evaporator, followed by calcined in either air or in N_2 for 8h at 800°C. (a) SEM shows calcination in air induces a complete loss of the supports morphology, whereas calcination in N_2 retains most of the particle structure. (b) The loss of morphology for both air-calcined samples is accompanied by a complete change in pore size distribution and loss of surface area. In contrast, calcination in N_2 retains for both supports main features of the pore-size distribution. (c) Calcination in air transforms both supports into mixtures of (•) 3C-SiC, (○) 5H-SiC and (▲) α-cristobalite. Moreover, additional phases (▼) $MnWO_4$, (◆) Na_2WO_4 and (★) Mn_2O_3 are formed. (see also Fig. A2.3 b). In contrast, calcination in N_2 retains the primary phase of 3C-SiC, with negligible amount of α-cristobalite. (note: the unlabeled peaks cannot be assigned to common Si_xN_y or C_xN_y phases and possibly represent some undefined SiC phases).

Fig. 2.2 also shows analytics of Mn/Na/W/SiC treat in N_2. In comparison to the air-treated Mn/Na/W/SiC catalysts, their N_2-treated counterparts retain their fine grained morphology and the original pore size distribution of SiC support. In addition, BET analysis indicates that about 60% of the initial surface area of the support, i.e. about 15 - 18 m^2/g, are preserved (Table 2.1). Moreover, XRD indicates that the N_2-calcined catalysts also retain the 3C-SiC of the support with negligible amounts of α-cristobalite being formed. Besides, minor amounts of Si_xN_y, C_xN_y or other SiC phases appear to be formed and no metal-containing crystal phase can be apparently observed. Hence, calcination of Mn/Na/W/SiC in N_2 preserves the structure and porosity of SiC much better than calcination in air.

In order to elucidate the origin of the calcination-induced modifications to Mn/Na/W/SiC catalysts, TGA of SiC supports and Mn/Na/W/SiC catalysts was performed in N_2 as well as air atmosphere. Fig. 2.3 plots the TGA data obtained for materials based on SiC 56 as relative mass vs. temperature. The mass of uncoated support SiC 56 remains stable up to 1000 °C and up to 810 °C, when the support was treated in nitrogen and air respectively, indicating the well stability of uncoated SiC support. The slight increase in mass can be attributed to the oxidation of SiC to SiO_2, which typically forms a protective layer on the surface of SiC and prevents further oxidation of SiC.[118] Also the SiC 56-Mn/Na/W does not show a significant increase in mass when heated in N_2. In contrast, it shows a dramatic increase in mass already at 450 °C when heated in air, which progressively increases at higher temperatures. The progressing mass increase implies the oxidation of the support far

beyond a passivating surface layer, i.e. bulk oxidation of about 50% of the SiC into SiO_2. Similarly, the SiC 27-Mn/Na/W also exhibits progressing mass when heated in air (Fig. A2.4). However, SiC 27-Mn/Na/W exhibited a slower weight increase rate and less total oxidized amount than SiC 56-Mn/Na/W. This suggests that SiC 27-Mn/Na/W undergoes less oxidation than SiC 56-Mn/Na/W at same temperature ramping and atmosphere condition. For both cases, the ongoing oxidation can be attributed to the presence of metal species, and in particular sodium, which probably induces a melting of the protective SiO_2 layer.[162, 163] In consequence, no effective passivation layer is formed, thus the oxidation of SiC progresses further into the bulk of the material and destroys the supports original pore structure. However, the bulk oxidation and sintering of the support can be prevented by calcination in N_2, which produces Mn/Na/W/SiC catalysts with high surface area and porosity.

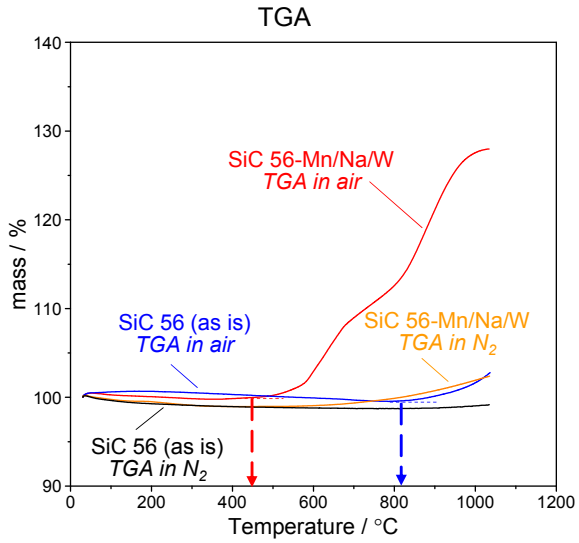

Fig. 2.3: TGA of support SiC 56 and uncalcined catalyst SiC 56-Mn/Na/W in N_2 and in air, respectively. SiC 56-Mn/Na/W was obtained via impregnation of SiC 56 with $Mn(NO_3)_2$ and Na_2WO_4 precursor solution and dying at 120 °C. Only minimal changes in the mass are observed when support and catalyst are calcined in N_2 flow. In contrast, a slight increase in weight increase is observed above 810 °C when the SiC support is calcined in air. When SiC 56-Mn/Na/W is calcined in air, the weight gain starts already at 450 °C and drastically progresses to 128% of the initial mass at 1050 °C. The mass gain can be explained by oxidation of the SiC support to SiO_2, which is strongly promoted by the presence of the Mn/Na/W coating.

XPS were recorded in Mn_{2p}, Na_{1s}, W_{4f}, W_{5d}, O_{1s}, Si_{2p} and C_{1s} region in order to determine the near-surface composition of the catalysts. The spectra of each element are shown in Fig. 2.4. The charging process occurred on the air-calcined sample and its element scans were corrected with -4.4 eV. XP spectrum of N_2-calcined catalyst shows that in Si_{2p} region, two distinct contributions can be assigned to SiC as well as SiO_2. Both are about the same amount, which indicates the formation of a protective SiO_2 layer on the surface of SiC.[118] The contrast air-calcined catalyst shows that in Si_{2p} region, only one signal contribution suggesting that negligible amount of SiC was retained. Similar observation can be made in C_{1s} region of spectra. Also the N_2-calciend catalyst shows additional signals at 282.5 eV and 284.2 eV, which can be assigned to Si-C and graphite carbon. However, these two peaks cannot be observed for the air-calcined catalyst. In addition, XP spectrum of N_2-calcined catalyst depicts characteristic signals for Mn and W while these signals significantly diminish for the air-calcined catalyst. Differently, the intensity of characteristic signal for Na keeps similar for both N_2-calcined and air-calcined catalyst.

Table 2.2: the surface composition (at%) of of Mn, Na, W, O, Si and C determined by XPS for SiC 27-Mn/Na/W calcined in air and in N_2. The N_2-calcined catalyst shows higher Mn, Na and W amount on the surface compared to the bulk composition. However, for the air-calcined catalyst, Mn and W seem to disappear from the surface due to significant structure reconstruction when calcination in air. Besides, the air-calcined catalyst exhibits higher O and lower C surface amount compared to the N_2-calcined catalyst, which confirms the oxidation of SiC support into SiO_2 when calcination in air.

metal components	SiC 27- Mn/Na/W-calc air	SiC 27- Mn/Na/W-calc N_2	intended bulk composition
	at.%	at.%	at.%
Mn (2p)	< 0.2	2.3	0.7
Na (1s)	3.3	2.3	0.7
W (4f)	n.a.	0.5	0.3
O (1s)	62.8	40.5	2.4
Si (2p)	25.4	25.7	48.0
C (1s)	8.3	28.7	48.0

Note that the sample where subject to significant charging during XPS analysis hangs no clear assignment to different oxidation state or specific species which can be made based on binding energy alone. However, the relative amount of surface species of different metals as well as O, Si and C were calculated from the relative size of the peak areas as shown in Table 2.2. The N_2-calcined catalyst shows higher Mn, Na and W amount on the surface compared to the bulk composition. However, for the air-calcined catalyst, Mn and W seem to disappear from the surface due to significant structure reconstruction when calcination in air. The higher Na amount of the air-calcined catalyst reveals that the existence of Na on the surface induces a melting of the protective SiO_2 layer and subsequently destroys the porous structure of SiC support, which is consistent with the explanation for the observation of Mn/Na/W/SiC tested in air. Besides, the air-calcined catalyst exhibits higher O and lower C surface amount compared to the N_2-calcined catalyst, which confirms the oxidation of SiC support into SiO_2 when calcination in air.

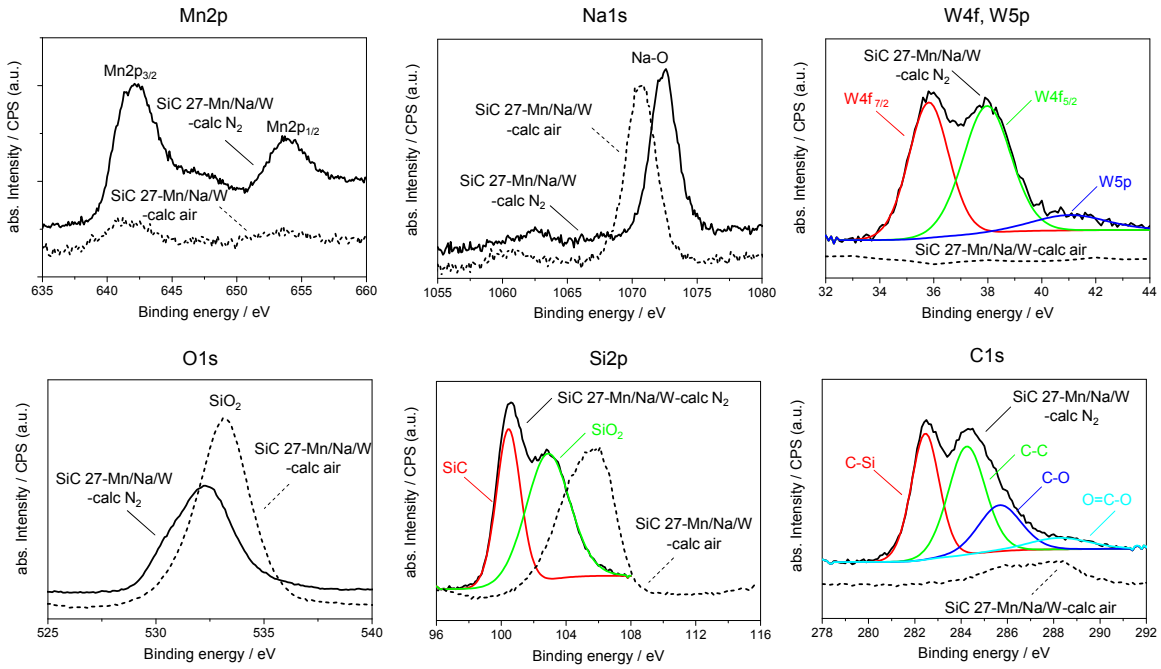

Fig. 2.4: XP spectra of of Mn, Na, W, O, Si and C for SiC 27-Mn/Na/W calcined in air (dash line) and in N_2 (solid line). The charging process occurred on the air-calcined sample and its element scans were corrected with -4.4 eV, but this does not affect the relative amount of surface species which was calculated from the overview scan areas. XP spectrum of N_2-calcined catalyst shows that in Si_{2p} region, two distinct contributions can be assigned to SiC as well as SiO_2. Both are about the same amount. The contrast air-calcined catalyst shows that in Si_{2p} region, only one signal contribution suggesting that only minor amount of SiC was retained. Similar observation can be made in C_{1s} region of spectra. Also the N_2-calciend catalyst shows additional signals at 282.5 eV and 284.2 eV, which can be assigned to Si-C and graphite carbon. However, these two peaks cannot be observed for the air-calcined catalyst. Note that the sample where subject to significant charging during XPS analysis hangs no clear assignment to different oxidation state or specific species which can be made based on binding energy alone.

2.2.3. Mn/Na/W/SiC catalysts after OCM

The different Mn/Na/W/SiC catalysts were tested in OCM up to 800 °C and subsequently analyzed to reveal reaction-induced property changes. Fig. 2.5 displays corresponding data obtained via SEM, N_2 sorption, and XRD. SEM analysis indicates that all catalysts show a sintered morphology after OCM testing (Fig. 2.5 a). Moreover, the catalysts surface area decrease to about 1.2 to 1.9 m^2/g for all catalysts (Table 2.1). Hence, the initial pore structure of Mn/Na/W/SiC that was preserved in N_2 atmosphere at 800 °C significantly degrades in OCM feed gas ($CH_4/O_2/N_2$) at 800 °C. None of the catalysts can retain the supports initial pore size distribution and distinct mesoporosity under OCM conditions (Fig. 2.5 b). Moreover, all used Mn/Na/W/SiC catalysts show well-distinguished XRD reflections that can be assigned to α-cristobalite along with 3C-SiC after OCM (Fig. 2.5 c). Other phases observed on all catalysts after OCM include Na_2WO_4, Mn_2WO_4, Mn_2O_3. Therefore, Na promoted SiC oxidation occurs also under OCM atmosphere, producing for all tested Mn/Na/W/SiC catalysts similar structure, composition and porosity independent of the initially applied calcination atmosphere.

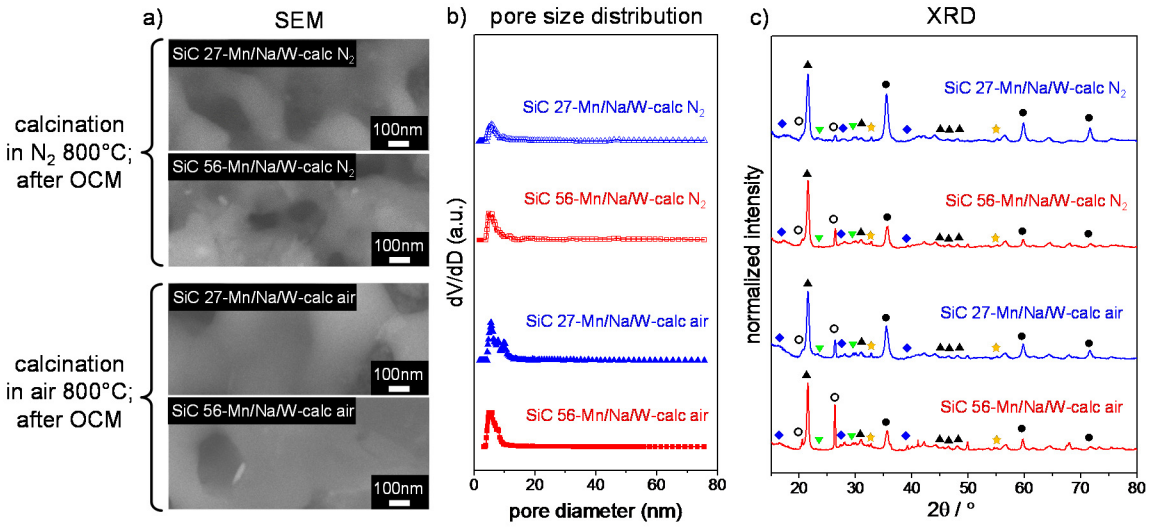

Fig. 2.5: (a) SEM images, (b) pore size distribution and (c) XRD patterns of SiC 27-Mn/Na/W and SiC 56-Mn/Na/W calcined in air or N_2 after OCM testing. (•) 3C-SiC, (○) 5H-SiC, (▲) α-cristobalite, (▼) $MnWO_4$, (◆) Na_2WO_4 and (★) Mn_2O_3. Catalysts were tested in feed gas composed of $CH_4/O_2/N_2$ = 2/1/4 with flow rate 14.7 mL/min from 450 to 800 °C, each 25 °C. All of the catalysts after OCM testing showed sintering structure. Meanwhile, peak around 27 and 56 nm disappeared in pore size distribution plot for both of Mn/Na/W/SiC catalysts calcined in air and N_2. Fresh SiC catalysts calcined in N_2, which retain morphology of fine particles and porous structure, lost its pristine structure after OCM testing. Furthermore, mixed phase composed of 3C-SiC, 5H-SiC and α-cristobalite formed in Mn/Na/W/SiC calcined in N_2, which is similar to the phase composition of Mn/Na/W/SiC calcined in air. Compared to catalyst before OCM, $MnWO_4$ seemed to diminish while Na_2WO_4 and Mn_2O_3 became more pronounced. Generally, all of catalysts after OCM exhibited identical phase composition.

2.3. OCM Catalytic test results

The OCM performance of Mn/Na/W/SiC catalysts with different supports and different calcination procedure was tested by co-feeding CH_4:O_2:N_2 = 2:1:4 continuously to a reactor and increasing temperature in steps of 25 K from 450 °C to 800 °C. The product of OCM reaction at the outlet was detected by GC. The concentration of product was calculated by considering the peak area of components and corresponding calibration factor, as shown in Fig. 2.6. Thereafter, CH_4 conversion, O_2 conversion and C_2 yield were calculated from the feed according to Equation 2.1, 2.2 and 2.3, respectively, as shown in Fig. 2.7. Carbon balance was calculated from carbon input and output according to Equation 2.5, as shown in Table A2.2.

2.3.1. OCM product concentration and carbon balance

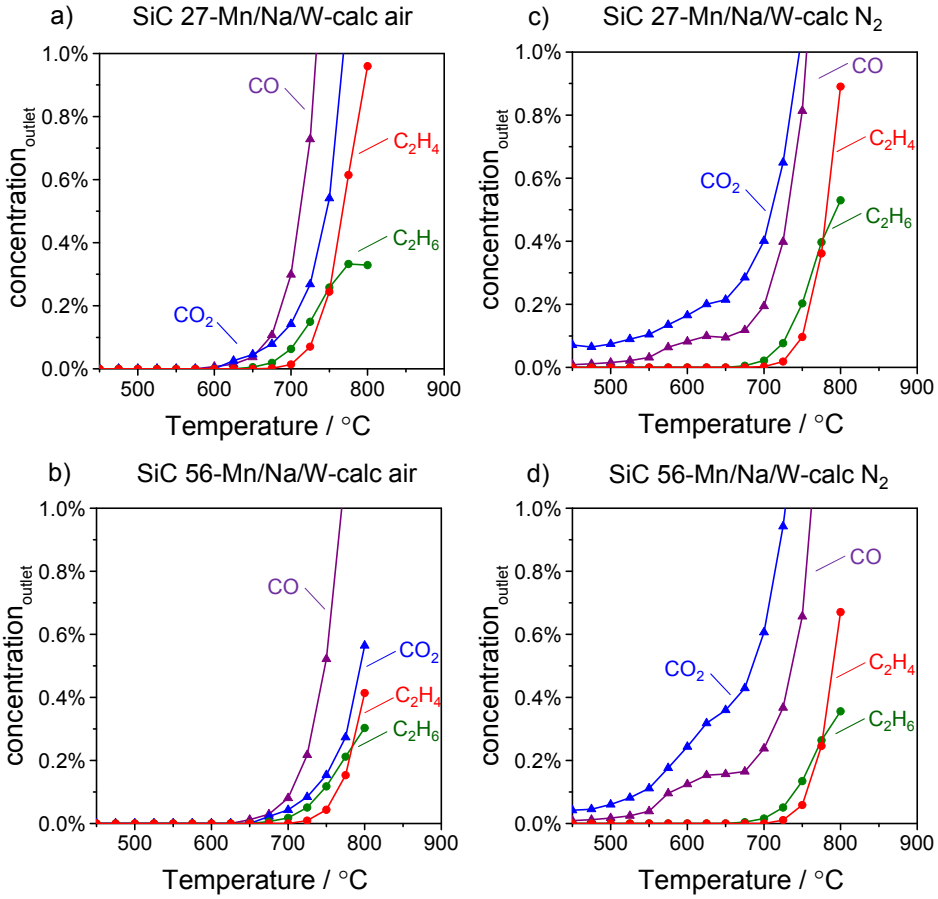

Fig. 2.6: OCM product concentration vs. temperature for SiC 27-Mn/Na/W and SiC 56-Mn/Na/W after calcination in air (a, b) and in N_2,(c, d). The concentration of OCM reaction product at the outlet was determined by GC through calculation considering the component peak area and corresponding calibration factor. All SiC supported catalysts show significant OCM performance. Both SiC-catalysts calcined in N_2 produce CO and CO_2 at about 450 to 600 °C without converting methane (c, d), which is not observed for air calcined catalysts (a, b) and thus attributed to oxidation of the SiC support.

Fig. 2.6 shows for each tested catalyst the concentration of products formed at different temperatures. The catalysts that were calcined in air, i.e. SiC 27-Mn/Na/W-calc air and SiC 56-Mn/Na/W-calc air produce CO and CO_2 starting at about 625 °C. Ethane formation starts at about 650 °C, followed by ethylene formation at temperatures above 675 - 700 °C. Propane and propene form significantly between 750 and 800 °C (Fig. A2.5). They are in a small quantity, which are much less than C_2 product at the same temperature. Therefore, for both catalysts ethane and ethylene are the main product at 800 °C. In general, higher product formation rates were observed for SiC 27-Mn/Na/W-calc air, i.e. that catalyst that retains a higher surface area after OCM (see Table 2.1).

However, the catalysts calcined in N_2, i.e. SiC 27-Mn/Na/W-calc N_2 and SiC 56-Mn/Na/W-calc N_2 show a different behavior during OCM catalysis below 700 °C. Both catalysts form CO and CO_2 already below 500 °C. Formation of ethane starts at around 675 °C, followed by ethylene formation. At 800 °C the product spectra look similar to the air-calcined catalysts (Fig. 2.6 a, b), with ethylene being the main C_2 product. The formation of CO_x well below 600 °C is observed only for the N_2 calcined catalysts. No significant amounts methane are converted at such temperatures (Fig. 2.7 a). Hence, the CO_x is likely to originate from Na promoted bulk oxidation of SiC as observed during catalyst calcination in air (Fig. 2.2 and

Fig. 2.3), and corroborated by the loss of pore structure for both N_2-calcined catalysts during OCM (Fig. 2.5).

SiO_2-Mn/Na/W calcined in air (Fig. A2.6 d) shows similar behavior of product concentration to SiC 27-Mn/Na/W and SiC 56-Mn/Na/W calcined in air. This may be attributed to their common crystal phases (Na_2WO_4, Mn_2WO_4, Mn_2O_3 and α-cristobalite), sintering morphology and similarly lower surface area.

Carbon balance for each catalyst at each temperature step was calculated and shown in Table A2.2. All values of nearly 100% with acceptable experimental error indicate that the analytical results are reliable, although there may be minor amount of CO_x produced from N_2-calcined SiC supported catalysts.

2.3.2. OCM performance in terms of X_{CH4}, X_{O2} and Y_{C2}

The obtained CH_4 conversion are plotted vs. temperature (Fig. 2.7 a). The influence of temperature on CH_4 conversion is similar for all tested SiC-based catalysts. CH_4 conversion starts around 625 °C and keeps increasing with temperature until 800 °C. Despite very similar trends, differences can be observed in the achieved overall activity, with catalysts based on SiC 27 converting more methane than catalysts based on SiC 56.

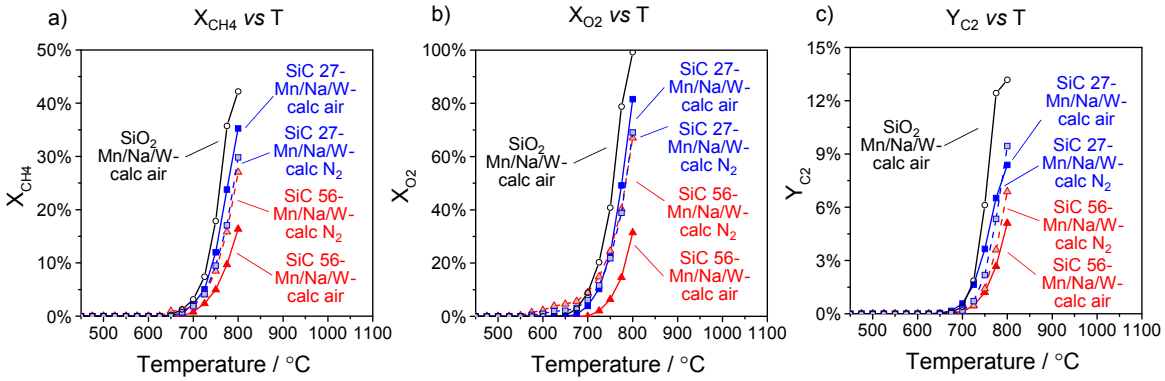

Fig. 2.7: OCM performance in terms of CH_4, O_2 conversion (a, b) and C_2 yield (c) for SiC 27-Mn/Na/W, SiC 56-Mn/Na/W calcined in air and in N_2 plotted vs. temperature. Performance of Mn/Na/W/SiO_2 catalysts prepared in a similar way is shown for comparison. Methane conversion and C_2 yield increase with temperature for all catalysts in a similar way.

O_2 conversion of catalysts is shown in (Fig. 2.7 b). Differently, SiC 27-Mn/Na/W-calc N_2 and SiC 56-Mn/Na/W-calc N_2 already exhibit significant O_2 conversion below 625 °C, when nearly no O_2 conversion appears for SiC supported Mn/Na/W catalysts calcined in air. This is consistent with the difference observed in product concentration (Fig. 2.6 c and d). At this temperature range, O_2 conversion is mainly attributed to oxidation of SiC, producing CO and CO_2 product. When the temperature is above 700 °C, similar influence of temperature on O_2 conversion is observed for all tested SiC-based catalysts, following the trend of CH_4 conversion (Fig. 2.7 a).

Thereafter, Fig. 2.7 c illustrates C_2 yield of tested catalysts. Generally, it roughly corresponds with the temperature-dependent trend of methane conversion, which indicates that similar percentage of converted methane tends to form C_2 product for all tested catalysts although they exhibit different structural properties due to varied treatment in fresh catalysts.

As comparison, OCM performance of SiO_2 supported Mn/Na/W catalysts is also shown in Fig. 2.7. In general, higher CH_4, O_2 conversion and C_2 yield are observed at typical OCM temperature.

2.3.3. Catalyst stability test

In order to examine the catalyst stability, SiC 27-Mn/Na/W calcined in air and in N_2 were chosen as representative to test the catalytic performance at reaction temperature of 600, 700 and 800 °C. At each temperature 5 GC test rounds were performed. The results are shown in Fig. 2.8. Generally, for both catalysts in stability test, products concentration at the outlet including CO, CO_2, C_2H_4 and C_2H_6 stay in line with the previous test results shown in Fig. 2.6 a/c.

Each products of the air-calcined catalyst shows nearly same concentration with longer time at each temperature step, indicating that the air-calcined catalyst exhibits stable catalytic performance. But for the N_2-calcined catalyst, higher CO and CO_2 product concentration was observed than the air-calcined catalyst, which is similar to the comparison between Fig. 2.6 a and Fig. 2.6 c. This is caused by SiC oxidation under OCM feed for the N_2-calcined catalyst as discussed above. Besides, CO and CO_2 concentration typically decrease with longer time at each temperature, which may be attributed to less SiC remaining in the catalyst with SiC oxidation proceeding. Therefore, the N_2-calcined catalyst shows less stable catalytic performance due to the deactivation arising from SiC oxidation under OCM feed.

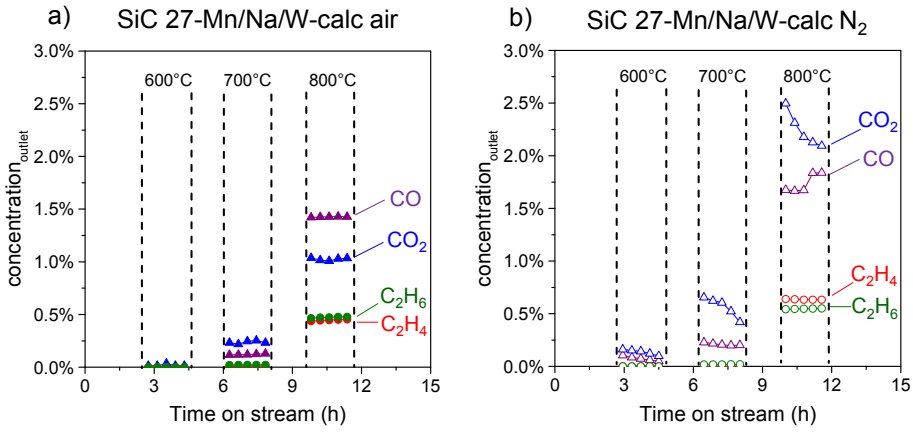

Fig. 2.8: OCM performance in terms of product concentration at the outlet for SiC 27-Mn/Na/W calcined in air (a) and in N_2 (b) during stability test. Each products of the air-calcined catalyst shows nearly same concentration with longer time at each temperature step. But for the N_2-calcined catalyst, it is observed that CO and CO_2 concentration decrease with longer time at each temperature. This may be attributed to less SiC remaining in the catalyst with SiC oxidation proceeding. Therefore, the N_2-calcined catalyst behaves less stable due to the deactivation arising from SiC oxidation under OCM feed.

2.4. Correlation between OCM performance and surface area

In order to quantify the difference between the catalysts, the methane conversion (Fig. 2.7 a) and C_2 yield (Fig. 2.7 c) obtained at 725, 750, 775 and 800 °C (labeled in green, yellow, blue and red color respectively) was plotted vs. the BET surface area of the respective catalysts as measured after OCM catalysis. The left box in Fig. 2.9 includes methane conversion of four SiC supported catalysts with different BET surface area at four different temperature. It is evident that methane conversion scales linear with the amount of surface area preserved during OCM for all SiC-based catalysts. Four dash lines indicate that the linear relationship can be observed at 725, 750, 775 and 800 °C. Moreover, also C_2 yield also scales roughly

linear with the preserved surface area. Hence, OCM catalysis appears to proceed in a very similar fashion over the four Mn/Na/W/SiC catalysts that were prepared with an identical nominal composition, but differed in the initial pore structure of the employed SiC supports as well as the atmosphere applied during calcination at 800 °C. The amount of surface area preserved under OCM conditions therefore appears to be the primary factor that allows high activity and C_2 yields on Mn/Na/W/SiC catalysts. While such a direct correlation between feed conversion and product formation with the provided surface area is expected for surface-catalyzed reactions, it is not straight-forward for reactions that comprise a complex reaction network of coupled surface- and gas-phase reaction as often proposed for OCM. The observed linear dependency thus suggests that at least for the studied catalyst system both, feed consumption as well as C_2 formation rates, are controlled by the corresponding catalytic surface reactions, not subsequent or parallel reaction steps proceeding in the gas phase.

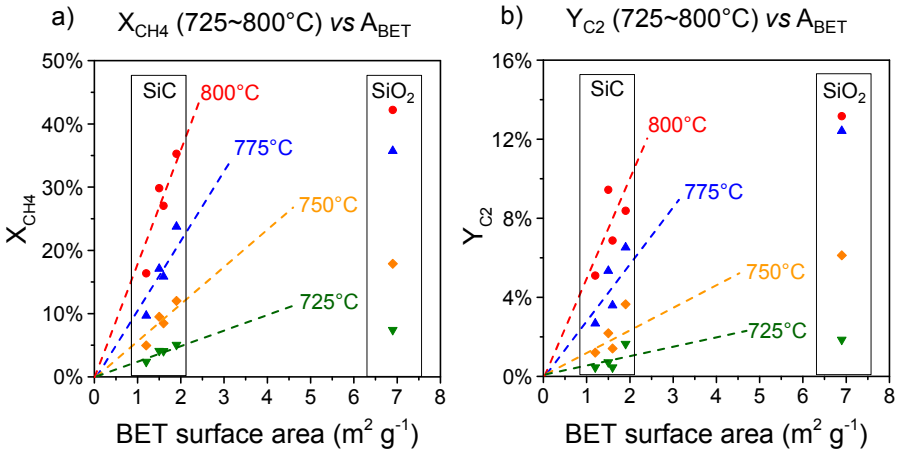

Fig. 2.9: Correlation of methane conversion (a) and C_2 yield (b) at 725, 750, 775 and 800 °C with BET surface area as measured after OCM catalysis. Methane conversion and C_2 yield scale approximately linear with the catalysts surface area, independent of the support and applied catalyst calcination procedure.

2.5. Comparison between SiC and SiO_2 as a support

Catalyst of similar Mn, Na and W composition was prepared for reference on a commercial silica support from Davisil with high-surface area (ca. 400 m^2/g) using the same impregnation procedure and air-calcination at 800 °C. Fig. A2.5 displays corresponding analysis via SEM, N_2 sorption and XRD before and after OCM catalysis.

The fresh Mn/Na/W/SiO_2 catalyst exhibits a sintering morphology, which is similar to the air-calcined Mn/Na/W/SiC but different from the N_2-calcined Mn/Na/W/SiC. Also it shows a severe loss of surface area from more than 400 m^2/g to about 7.0 m^2/g (Table 2.1). An possible explanation is that the presence of Na is suspected of facilitating the structural change of SiO_2,[164] which induces dramatic loss of surface area. XRD pattern exhibits Mn/Na/W/SiO_2 fresh catalyst is composed of α-cristobalite, tridymite, Na_2WO_4 and Mn_2O_3, which is in agreement with the previous report for Mn/Na/W/SiO_2 catalyst system.

After OCM reaction, the used catalyst also shows sintering morphology. Also the surface area of Mn/Na/W/SiO_2 catalyst keeps similar. Besides, crystal phase composition retains same and the XRD signal becomes more pronounced. Therefore, Mn/Na/W/SiO_2 catalyst shows no significant structural changes before and after OCM.

OCM catalytic test was performed for Mn/Na/W/SiO_2 catalyst under same reaction conditions. It shows a similar influence of temperature on product formation (Fig. A2.6 d), CH_4 conversion (Fig. 2.7 a), O_2 conversion (Fig. 2.7 b) and C_2 yield (Fig. 2.7 c) to the air-calcined SiC-supported catalysts. Hence, the partial conversion of SiC into SiO_2 during calcination and OCM catalysis produces catalysts of very similar composition, surface area and catalytic behavior as a synthesis that starts directly from silica. However, when comparing the catalytic performance based on the surface area as measured after OCM, catalysts supported on SiC show a higher methane conversion (left box in Fig. 2.9 a) and C_2 yield (left box in Fig. 2.9 b) per m^2 of surface area than supported on SiO_2 (right box in Fig. 2.9 a and b). This suggests a higher surface coverage with active sites on the SiC based materials, assuming the active site is qualitatively similar in both catalyst systems. Therefore, SiC support for Mn/Na/W catalysts exhibits potential advantage with enhanced catalytic performance, if its surface area could approach a similar level to SiO_2 support under OCM conditions.

2.6. Discussion on oxidation behavior of SiC

SiC is generally taken as a kind of material with high thermal stability and chemical inertness[119] and was reported to behave better than conventional catalyst carrier in heterogeneous catalytic reaction.[127, 128] However, SiC support tends to get greatly oxidized at elevated temperature in O_2-containing atmosphere, resulting in the loss of pristine high surface area and porosity. The reason is discussed in detail as follows.

It is widely acknowledged that the origin of high thermal of SiC comes from a passivation SiO_2 layer on the surface.[118] This SiO_2 layer usually forms during passive oxidation of SiC at lower temperature under sufficient O_2 pressure. After formation of this thin SiO_2 layer, further oxidation is largely suppressed because gaseous O_2 has to be transported through the formed SiO_2 layer to contact with SiC and meanwhile, gaseous products formed by oxidation comes out through the formed SiO_2 layer again by diffusion. Only limited oxidation of SiC could occur due to the slow mass transfer between gas and solid phase as well as within the SiO_2 layer unless the temperature is elevated to a super high level (above 1200 °C).[163] For the SiC supported catalysts in this thesis, the temperature employed in calcination process during catalyst preparation or in OCM reaction is not higher than 800 °C, where SiC support should keep stable theoretically. But the actual observation shows that SiC undergoes severe oxidation at this temperature range. Hence, the temperature is not the dominate factor to modify the oxidation behavior of SiC.

Oxidation of SiC could be accelerated when alkali element is present on SiC. McKEE et al.[162] found that oxidation of SiC readily occurs at 900 °C with exposure to air when doped with Na_2O, Na_2CO_3 or $NaNO_3$ which decomposes at high temperatures to form Na_2O. Na_2O tends to vigorously reacts with SiO_2 to form silicate. In consequence, the pre-formed passivation SiO_2 solid thin layer disappears. Furthermore, the formed silicate species is likely to be a molten state at high temperature, where the mass transfer between gas phase and SiC is greatly enhanced compared to the case through a passivation SiO_2 layer without Na_2O. Similar observation was also reported by Zheng et al.[163]. They investigated the effect of Na on oxidation kinetic of SiC by quantitatively implanting SiC crystals with Na. Based on experimental results at 1100°C in isotope $^{18}O_2/^{16}O_2$ atmosphere, they claimed that the presence of Na (50 ~ 1000 ppm) has significant effect on molecular and ionic oxygen diffusion which accelerates the oxidation of SiC. Therefore, SiC oxidation behavior is proved

to be facilitated by a synergetic effect of certain amount of Na, O_2 and sufficiently high temperature.

In this thesis, the used Mn/Na/W/SiC catalyst contains about 7600 ppm Na, which is far more than the utilized amount in the above paper regarding to SiC oxidation. The O_2 content of gas atmosphere where SiC is exposed to, no matter the synthetic air used for calcination or the OCM feed ($N_2/CH_4/O_2$ ~ 4/2/1) for catalytic reaction, is also quite high. The oxidation of SiC starts to be accelerated from 450 °C (see Fig. 2.3) which is below the onset of OCM reaction. In consequence, the high surface area and porosity from SiC porous structure largely diminishes with the proceeding of SiC oxidation. Hence, the high surface and porosity of Mn/Na/W/SiC catalyst preserved by N_2-atmosphere treatment does not play an important role under the actual reaction conditions. After OCM reaction at 800 °C, all studied Mn/Na/W/SiC catalysts exhibits greatly lower surface area and porosity because the occurrence of severe oxidation of SiC.

2.7. Summary

In this chapter of thesis, different kinds of SiC supported Mn/Na/W/SiC catalysts were investigated regarding to their structural properties and catalytic behaviors. Porous SiC is an efficient support material for the preparation of OCM catalysts with active Mn/Na/W-containing phases. The catalyst pore structure and high surface area could be preserved during calcination in N_2, but not during calcination in air and under conditions of OCM catalysis. In contrast, uncoated SiC supports proved to be stable under similar calcinations conditions. The loss of surface area and pore structure in the presence of the catalytically active elements can be attributed to the presence of sodium. Whereas pure SiC forms a passivating SiO_2 layer under oxidizing conditions, Na promotes a melting of the passivation layer, which results in bulk oxidation of SiC and material sintering. Despite the sintering, Mn/Na/W-SiC catalysts show similar activities and C_2 yields as silica based catalysts. Moreover, CH_4 conversion and C_2 yield scale roughly linear with the specific surface area of used catalysts, suggesting that the number of accessible active site scales with the retained surface area. OCM tests suggest that the performance of Mn/Na/W/SiC catalysts depends critically on the supports stability, i.e. the surface area retained under reaction conditions.

3. Synthesis, characterization and property-descriptors of oxide-supported and carbonate-supported catalysts

In order to explore quantitative property-performance correlations for OCM reaction, appropriate property-descriptors and performance-descriptors should be firstly defined and derived based on experimental results. The goal of this chapter is to generate property-descriptors from characterization data for well-designed exemplary catalysts.

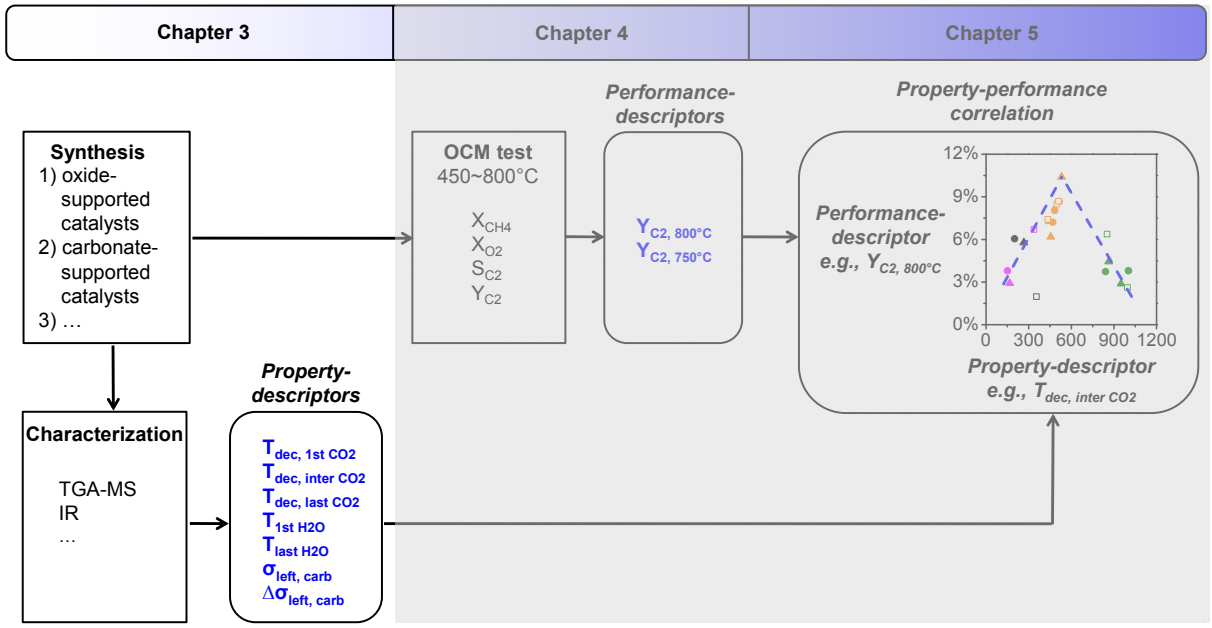

Fig. 3.1 Schematic representation of chapter 3 in this thesis. The goal is to generate property-descriptors from characterization data for exemplary catalysts.

Inspired from statistical analysis by Schmack[139] discussed in section 1.5.2, carbonate formation and stability in catalysts could be essential factors that influence OCM performance. On one hand, concerning the first question proposed in Fig. 1.9 about "Carbonate-supported" and "Inert-supported", different oxide-supported catalyst would be designed in this study. Rare-earth metal oxides and alkaline-earth oxides, Sm_2O_3, Y_2O_3, Gd_2O_3, CeO_2, SrO and BaO, are utilized as oxide support considering that they can keep non-sintering during OCM reaction.[140] More interestingly, these oxides are able to form carbonate with different thermal stability,[144, 165, 166] providing a possibility to investigate the influence of carbonate stability on catalytic performance in a wide variation range. As a comparison, conventional Al_2O_3 support is also utilized because it typically could not form a carbonate. On the other hand, regarding to the second question about "Carbonate thermdyn not stable" and "Carbonate thermdyn stable" in Fig. 1.9, carbonate with different stability would be incorporated in this study. Alkali carbonates, Rb_2CO_3 and Cs_2CO_3, are used since they are able to keep thermodynamically stable at typical OCM temperature.[141] $MgCO_3$, formed by $Mg(OAc)_2$ as precursor, is also utilized since it cannot retain thermodynamically stable at typical OCM temperature.[141]

In order to investigate the third question about the difference between oxide and carbonate as a support for catalysts, carbonate-supported catalysts are designed as well by directly using carbonate as a support instead of oxide for certain catalysts. To be specific, $Sm_2(CO_3)_3$ and $SrCO_3$ are used as support materials rather than Sm_2O_3 and SrO.

Typical OCM well-performing catalysts, Li/MgO and Mn-Na_2WO_4/SiO_2, are also incorporated as a reference.

Afterwards, characterization data is discussed concerning morphology, crystalline phase, chemical species, surface area and decomposition behavior of involved carbonate. Based on these experimental results, several property-descriptors are defined and generated with certain criteria regarding to catalyst properties, e.g., carbonate stability.

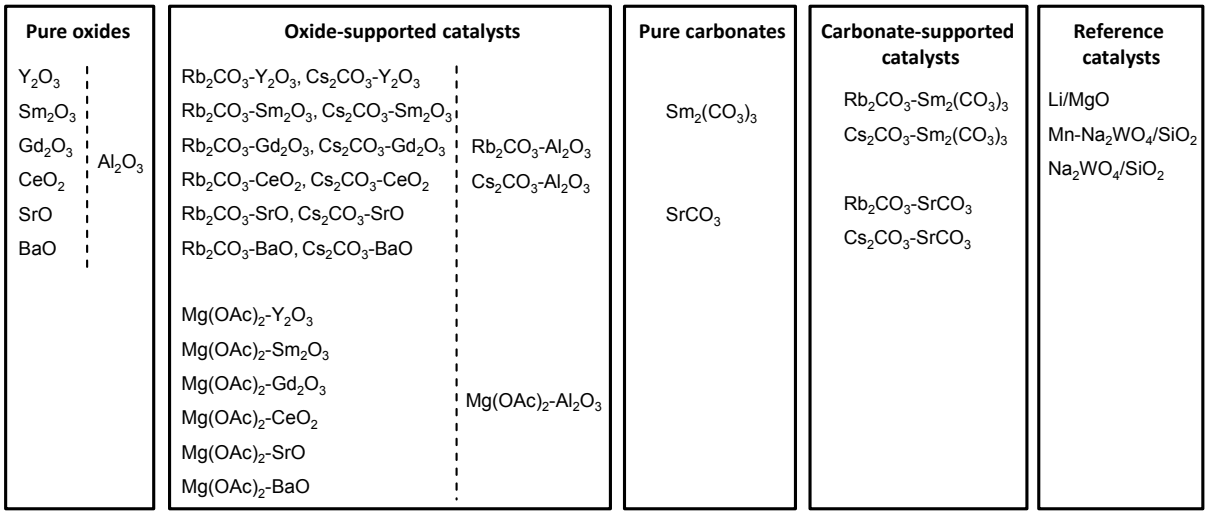

Fig. 3.2 Overview of catalysts prepared in this study with corresponding classifications.

3.1. Synthesis

3.1.1. Synthesis of oxide-supported catalysts

The commercial metal oxides Sm_2O_3, Y_2O_3, Gd_2O_3 and CeO_2 were purchased from ChemPUR Company in the form of pellets with size of millimeter. These pellets were grounded and sieved into granules with size fraction from 224 to 500 µm. SrO and BaO (fine powder, -100 mesh) were obtained from Alfa Asaer. These powders were pressed into tablets, crushed and sieved into size fraction from 224 to 500 µm as well. All obtained metal oxides were treated at 800 °C in air for 2 h before using as the support for impregnation.

A series of catalysts were prepared through drop-wise impregnation of alkali carbonate (Rb_2CO_3 and Cs_2CO_3) or alkaline earth acetate (Mg acetate) aqueous solution onto above metal oxide supports. Since $MgCO_3$ is not sufficiently soluble in water, $Mg(OAc)_2$ is used as an alternative for impregnation process and assumed to become $MgCO_3$ when heating above certain temperature during OCM reaction. The drop-wise impregnation process is similar to the steps shown in section 2.1.1. For all prepared catalysts, the ratio of impregnated metal element to the metal element of metal oxide support keeps a constant number, 10 mol%. Typically, 1.0 g of Y_2O_3 granules were deposited into a 100 mL flask and preheated for 15 min in a water bath to 72 °C with rotation at 50 rpm. 102.3 mg Rb_2CO_3 (Aldrich, 99.8%) was dissolved in 10 mL milli-Q H_2O. The Rb_2CO_3 solution was continuously dosed to the Y_2O_3 in the rotary evaporator (80 mbar) via syringe pump at a rate of 1.7 mL/h. The material was then treated in vacuum oven at 150 °C for 5 h. No further heat treatment was applied. The obtained catalyst was named as "Rb_2CO_3-Y_2O_3" and the naming rule was also used for other oxide-supported catalysts. Al_2O_3 supported Rb_2CO_3, Cs_2CO_3 and

$Mg(OAc)_2$ were obtained from Dr. Roman Schmack (group of Dr.-ing. Ralph Krähnert) at Technische Universität Berlin. The detailed synthesis approach was reported in his thesis.[139] The corresponding characterization and OCM catalytic data are extracted, integrated and discussed later.

As a comparison, as-received Rb_2CO_3, Cs_2CO_3 and $Mg(OAc)_2$ were also treated in vacuum oven at 150 °C for 5 h as the reference sample for decomposition behavior study afterwards.

3.1.2. Synthesis of carbonate-supported catalysts

The commercial carbonate $Sm_2(CO_3)_3$ and $SrCO_3$ were purchased from Alfa Aesar Company in the form of powder. These powders were pressed into tablets, crushed and sieved into size fraction from 224 to 500 µm. The obtained materials were treated in vacuum oven at 150 °C for 5 h to remove water and other residues. Afterwards, the treated materials were used as support for the following impregnation.

Catalysts were prepared through drop-wise impregnation of Rb_2CO_3 and Cs_2CO_3 aqueous solution on above carbonate supports (similar to the preparation process for oxide-supported catalysts). For all prepared catalysts, the molar ratio of impregnated metal element to the metal element of carbonate support is 10 mol%. Typically, 0.5 g of $Sm_2(CO_3)_3$ granules were deposited into a 100 mL flask and preheated for 15 min in a water bath to 72 °C with rotation at 50 rpm. 24.0 mg Rb_2CO_3 was dissolved in 10 mL milli-Q H_2O and the solution was continuously dosed onto $Sm_2(CO_3)_3$ in the rotary evaporator (80 mbar) via syringe pump at a rate of 1.7 mL/h. The material was then dried in vacuum oven at 150 °C for 5 h. No further heat treatment was applied. The obtained catalyst was named as "Rb_2CO_3- $Sm_2(CO_3)_3$" and the naming rule was also used for other carbonate-supported catalysts.

3.1.3. Synthesis of Li/MgO and Mn-Na_2WO_4/SiO_2 catalysts

Two Li/MgO, Mn-Na_2WO_4/SiO_2 and Na_2WO_4/SiO_2 catalyst were also synthesized as a comparison to oxide and carbonate supported catalysts. Li/MgO with 1wt% Li (named as Li/MgO-1) was prepared by a well-known wet impregnation procedure, which has also been used by Lunsford et al.[38, 71] Another Li/MgO with 1 wt% (named as Li/MgO-2) was synthesized by lithium nitrate and magnesium nitrate via a citric acid-assisted approach.[167] 2wt% Mn-5wt% Na_2WO_4/SiO_2 and 5wt% Na_2WO_4/SiO_2 catalyst were synthesized through the similar dropwise impregnation process to the preparation of oxide-supported catalysts, followed by treatment under CO_2 atmosphere at 800 °C for 8 h and cooling down to room temperature in CO_2.

3.2. Instruments and characterization methods

In order to determine catalyst properties regarding to carbonate stability, chemical species and etc., different characterization techniques were utilized, as shown in Table 3.1. In this section, characterization methods and corresponding instruments were briefly presented, from which property-descriptors of catalysts were generated.

Table 3.1 Summary of characterization techniques used to detect respective catalyst property and to generate property-descriptors for catalysts.

Characterization technique	Catalyst property	Property-descriptor	Descriptor definition
TGA-MS	Thermal stability of carbonate and hydroxide	1) $T_{dec,\ 1st\ CO2}$	Mass loss temperature of carbonate decompostion when first CO_2 peak appearing in MS
		2) $T_{dec,\ inter\ CO2}$	Mass loss temperature of carbonate decompostion when CO_2 peak appearing within/closest to the range of 400 ~ 550 °C in MS
		3) $T_{dec,\ last\ CO2}$	Mass loss temperature of carbonate decompostion when last CO_2 peak appearing in MS
		4) $T_{1st\ H2O}$	Mass loss temperature when first H_2O peak appearing in MS
		5) $T_{last\ H2O}$	Mass loss temperature when last H_2O peak appearing in MS
IR	Chemical species (typically carbonate and oxide)	6) $\sigma_{left,\ carb}$	Wavenumber of the left characteristic peak for CO_3^{2-} in IR
		7) $\Delta\sigma_{left,\ carb}$	Wavenumber shift of the left characteristic peak for CO_3^{2-} in IR compared to pure carbonate
SEM	Morphology	-	-
EDX	Elemental distribution	-	-
XRD	Crystalline phase composition	-	-
N_2-physisorption	BET surface area	-	-

3.2.1. Scanning electron microscopy (SEM) and energy dispersive X-ray spectroscopy (EDX)

Morphological images were taken with 10 kV acceleration voltage and 8 mm as working distance. EDX mapping were recorded with 12 kV acceleration and 12 mm as working distance.

3.2.2. X-ray diffraction (XRD)

Samples were placed in a shallow cave of polished Si single crystal wafer with high index surface orientation. XRD was recorded in 2θ interval 15° - 80° with a step of 0.02°.

3.2.3. N_2 physisorption

Samples were degassed in a glass tube at 150 °C for 24 h prior to physisorption measurement. Thereafter, physisorption was measured at 77K by recording adsorption isotherm (31 points) in p/p_0 interval 0.0001 - 0.6. BET method for relative pressure p/p_0 from 0.05 - 0.30 was used to determine specific surface area A_{BET}.

3.2.4. Thermogravimetric analysis coupled with mass spectrometry (TGA-MS)

Thermogravimetric analysis (TGA) was performed using a Perkin Elmer STA 8000 for all fresh catalysts in Ar atmosphere. Typically, 40 mg of the sample was placed in a ceramic crucible without lid at 30 °C. The flow rate of Ar during measurement was 60 ml/min. The measurement procedure was started firstly by holding the sample at 30 °C for 1 h. Thereafter, the sample was heated from 30 °C to 1050 °C with 5 K/min as a ramping rate and held at 1050 °C for 10 min. Thereafter, the measurement was automatically stopped and the sample was cooled down naturally. The blank measurements were utilized to subtract the thermal mass drift as well as abrupt changes in the mass signal upon switching from holding temperature to heating ramp. For evaluation, sample masses were normalized to the mass at 30 °C after holding for 1 h.

Evolved products, CO_2 and H_2O, during heating were monitored by mass spectrometry (PerkinElmer, Clarus SQ8) coupled with TGA. The signals of CO_2 and H_2O species were normalized by ion current of Ar as internal standard.

For carbonate supported catalysts, TGA was also conducted in CO_2 atmosphere with the same ramping procedure and detection technique.

3.2.5. Fourier transform infrared spectroscopy (FTIR)

FTIR spectra in the range between 4000 and 450 cm^{-1} were recorded on a Perkin Elmer Spectrum 100 on samples without pressing in KBr. The background spectrum was measured before each sample run and then automatically subtracted from the corresponding sample spectrum.

3.3. Oxide-supported carbonate catalysts

In this section, characterization data for oxide-supported catalysts with regard to morphology, elemental distribution, crystal phase composition, chemical species and surface area is discussed. Catalyst property-descriptors (shown in Table 5.1) are defined and generated from IR and TGA-MS results by focusing on carbonate species with the feature of CO_2.

3.3.1. Morphology and elemental distribution (SEM and EDX)

Oxide-supported Rb_2CO_3, Cs_2CO_3 and $Mg(OAc)_2$ catalyst are discussed with regard to morphology. Herein, the series of Rb_2CO_3 on oxides (Rb_2CO_3-oxide) is shown as an example. The detailed SEM and EDX results of pure oxides and oxide-supported catalysts are presented in Appendix section A3.3.1.

For Rb_2CO_3-Y_2O_3, -Sm_2O_3, and -Gd_2O_3 fresh catalysts, they are mainly consist of grains with size of 0.5 - 10 µm size and no obvious morphological changes are observed compared to pure oxides. After OCM reaction, the morphology keeps similar and no apparent sintering is observed. Differently, Rb_2CO_3-CeO_2 shows larger granules on the smooth bulk surface. These large granules, however, almost disappears after OCM, probably due to the decomposition of carbonate during reaction. For Rb_2CO_3-SrO and -BaO, apparent grains can be observed with size range of 0.5 - 2 µm, which is different from the pure oxide support. And after OCM, especially for Rb_2CO_3-BaO, quantities of tiny particles are observed with much smaller size, suggesting the occurrence of structural and composition changes during the reaction.

EDX mapping analysis of fresh catalysts was performed to detect whether the Rb element had been dispersed homogeneously over the whole catalyst structure. The morphology can be clearly distinguished from EDX mapping of metal element of support, indicating this magnitude exhibits sufficient resolution. It is observed that the homogeneous distribution of Rb element in micrometer scale for most catalysts.

3.3.2. Crystalline phase (XRD)

In order to detect crystal phase composition, XRD was tested for all oxide-supported catalysts before and after OCM reaction. The detailed XRD patterns of pure oxides and oxide-supported catalysts are presented in Appendix section A3.3.2.

For Rb_2CO_3-Y_2O_3, -Sm_2O_3 and -Gd_2O_3 catalysts, oxides are typically the only crystalline phases detected in fresh and spent catalysts, which is similar to the XRD patterns of pure oxides. Rb_2CO_3 or Rb_2O was not detected by XRD, probably because the carbonate species appears as very tiny crystallites or amorphous forms on the surface of oxide supports which is not detectable by XRD. For Rb_2CO_3-CeO_2, differently, not only CeO_2 but also Rb_2CO_3 phase were somehow detected However, Rb_2CO_3 phase seems to disappear after OCM reaction probably due to carbonate melting and decomposition under OCM temperature. For Rb_2CO_3-SrO and Rb_2CO_3-BaO, the crystal phase composition is more complex. For example, SrO, $Sr(OH)_2$ and $SrCO_3$ phase all appear in the fresh catalysts, while only $SrCO_3$ is present as Sr-containing phase after OCM due to its high thermal stability (also shown later in TGA analysis).

Furthermore, the assigned crystal phase composition for all catalysts before and after OCM reaction is summarized in Table A3.1. Broadly speaking, Sm_2O_3, Y_2O_3, Gd_2O_3 and CeO_2 phase in catalysts keep no change after OCM reaction. SrO and BaO form hydroxide and carbonate in fresh catalysts whereas only carbonate phase retains after OCM. Besides, for Al_2O_3 supported catalysts, aluminate phase appears after OCM reaction. Rb_2CO_3 or Cs_2CO_3 is rarely detected in fresh catalysts, which indicates that they disperse well as fairly small crystallite. After OCM reaction, there is still no certain detection of Rb_2CO_3 or Cs_2CO_3 as well as its decomposition product Rb_2O or Cs_2O.

Honestly, it is plausible to evaluate the existence of carbonate species only by XRD detection when the carbonate exists in forms of tiny crystallite or amorphous phase.

3.3.3. Chemical species (FT-IR)

The above discussion suggests that XRD is not an efficient technique to clearly characterize the possibly existing carbonate in oxide-supported catalysts. In order to definitely examine the existence of carbonate species, FT-IR spectra were recorded for all catalysts before and after OCM. Meanwhile, the influence of oxide support on carbonate structure would be reflected when certain shift of characteristic peaks appears compared to pure carbonate. The results are depicted in Fig. 3.3.

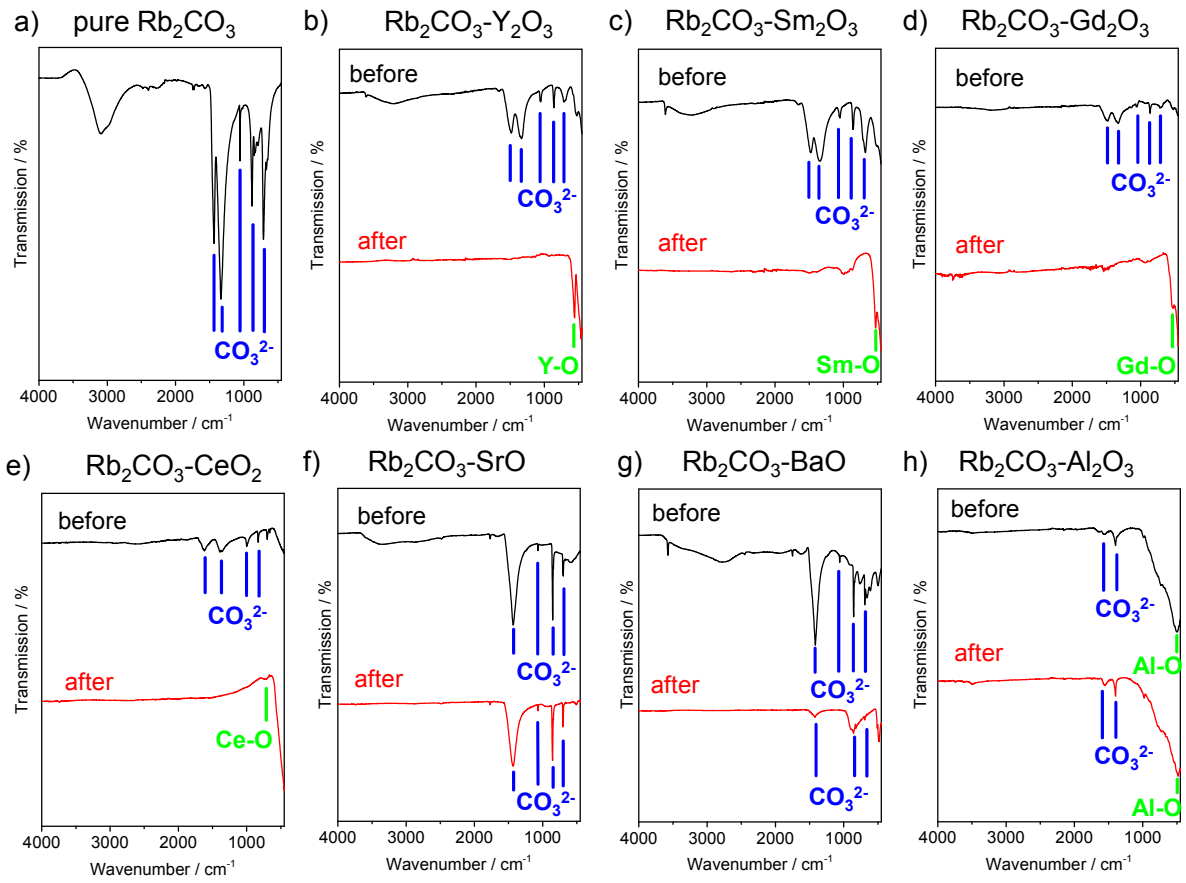

Fig. 3.3: IR spectra of (a) pure Rb_2CO_3 after treatment in vacuum at 150°C and Rb_2CO_3 on (b) Y_2O_3, (c) Sm_2O_3, (d) Gd_2O_3, (e) CeO_2, (f) SrO, (g) BaO and (h) Al_2O_3 support before and after OCM. Pure Rb_2CO_3 exhibited adsorption peaks in the range of 1700 - 650 cm^{-1} attributed to the vibrations of CO_3^{2-} species. All fresh catalysts exhibited the adsorption peaks in the same range. However, for Rb_2CO_3 on Y_2O_3, Sm_2O_3, Gd_2O_3 and CeO_2 catalyst after OCM, characteristic peaks for CO_3^{2-} species significantly reduced while the adsorption band corresponding to oxide groups (525, 513, 526 and 664 cm^{-1} for Y-O, Sm-O, Gd-O and Ce-O, respectively) became more pronounced, suggesting the decomposition of CO_3^{2-} species under OCM conditions. But peaks for CO_3^{2-} species were still observed for Rb_2CO_3 on SrO and BaO after OCM due to the high stability of carbonate.

For example, pure Rb_2CO_3 exhibits adsorption peaks in the range of 1700 - 650 cm^{-1}, which are derived from the vibrations of CO_3^{2-} species. Specifically, the peak at 1435, 1337 and 1056 cm^{-1} corresponds to asymmetric and symmetric stretching mode of CO_3^{2-}, while the peak at 878 and 712 cm^{-1} is assigned to out-of-plane and in-plane bending mode of CO_3^{2-}.[168-171] Similar characteristic adsorption bands are observed for Rb_2CO_3 on different oxides, confirming the presence of carbonate species in all fresh catalysts. Compared to pure Rb_2CO_3, the characteristic peak of Rb_2CO_3 on oxides exhibits varied either blue- or red-shift dependent of the oxides support, which will be discussed in detail in the following. In addition, the adsorption bands in the 3800 - 3000 cm^{-1} region can be attributed to O-H stretching mode of physiosorbed H_2O or from hydroxyl groups of hydroxides (identified from XRD patterns). The weak peak around 670 - 500 cm^{-1} is assigned to oxide group from the support. Hence, FT-IR is an effective approach to prove the presence of carbonate species in fresh catalysts prepared through drop-wise impregnation process.

After OCM reaction, however, obvious changes can be found for the above characteristic peaks in the spectra. Firstly, for Rb_2CO_3-Y_2O_3, -Sm_2O_3, -Gd_2O_3, and -CeO_2 catalysts, CO_3^{2-} species significantly reduces (or disappears) while the adsorption peak corresponding to oxide groups (525, 513, 526 and 664 cm^{-1} for Y-O, Sm-O, Gd-O and Ce-O, respectively) became more pronounced, suggesting the decomposition of CO_3^{2-} species because the

above carbonate species is not thermodynamically stable at typical OCM temperature and tends to decompose to oxides. Differently, for Rb_2CO_3-SrO and Rb_2CO_3-BaO, signals of CO_3^{2-} species are still clearly observed, although the intensity partially decreases. This corresponds to the observation in XRD (Fig. A3.5 e and f). It reveals the presence of CO_3^{2-} species in catalysts after OCM reaction due to the high stability of $SrCO_3$ and $BaCO_3$. Secondly, adsorption bands assigned to O-H disappear after OCM, suggesting that hydroxides also decompose during OCM reaction. The difference before and after OCM with respect to carbonate and hydroxide species is in agreement with the observation of XRD patterns for these samples.

Therefore, carbonate species is confirmed to exist in all oxide-supported fresh catalysts. They tend to either decompose to oxides or keep stable during OCM reaction depending on their thermal stability.

Property-descriptors of $\sigma_{left,\ carb}$ and $\Delta\sigma_{left,\ carb}$ from IR spectra

As discussed above, IR spectra data effectively confirms the existence of carbonate species in catalysts. Importantly, the wavenumbers of characteristic carbonate peak and its relative shift in oxide-supported catalysts compared to pure carbonate provide the possibility to quantitatively describe carbonate structure and the effect of oxide support. Herein, two property-descriptors, $\sigma_{left,\ carb}$ and $\Delta\sigma_{left,\ carb}$, were defined and derived for all catalysts from IR spectra. The descriptor values are shown in a summary table (Table 5.1).

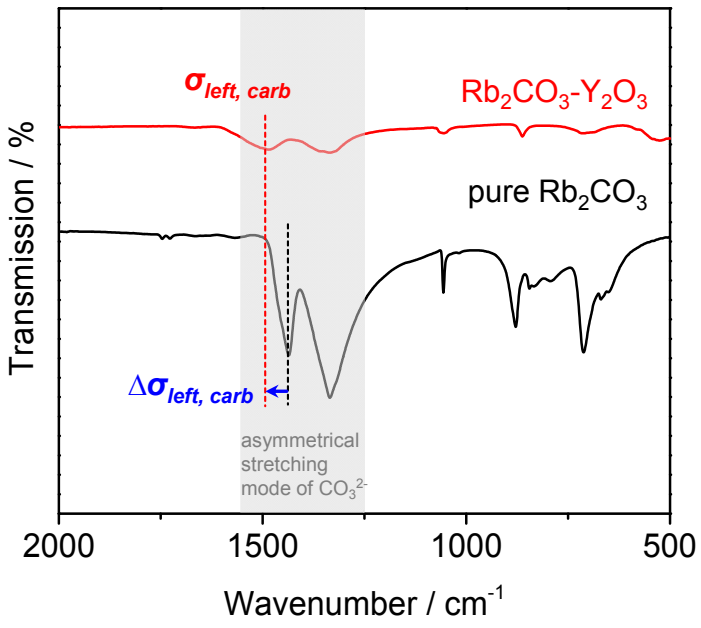

Fig. 3.4 Derivation of property-descriptors ($\sigma_{left,\ carb}$ and $\Delta\sigma_{left,\ carb}$) for Rb_2CO_3-Y_2O_3 as an example based on IR spectra. Descriptor of $\sigma_{left,\ carb}$ represents for wavenumber of the left characteristic peak attributed to asymmetrical stretching mode of CO_3^{2-}. Descriptor of $\Delta\sigma_{left,\ carb}$ means wavenumber shift of the left characteristic peak for CO_3^{2-} compared to the corresponding peak in pure carbonate sample.

Carbonates in catalysts exhibit significant vibrational behaviour in FT-IR spectra shown in Fig. 3.3. The characteristic adsorption band (1700 - 650 cm^{-1}) is derived from the vibrations of CO_3^{2-} species with asymmetric and symmetric stretching, out-of-plane and in-plane bending mode of CO_3^{2-}. There are more characteristic adsorption peak in this range for the acetate species because more kinds of different chemical bond are present in CH_3COO^- group. In

order to simplify and generalize the comparison between different catalysts, the adsorption band for asymmetric stretching of C-O bond (1700 - 1400 cm^{-1}) is chosen as the comparative region because all catalysts exhibit distinct and strong adsorption peak in this range. It is worth mentioning that double peaks appear in this range for most of the measured samples, suggesting the splitting of doubly degenerate asymmetric vibration occurs due to lowering the symmetry of CO_3^{2-} via coordination with cations.[172] Herein, the left one of double peaks, $\sigma_{left,\ carb}$, is defined as one property-descriptor (labelled with red colour in Fig. 3.4).

Compared to pure Rb_2CO_3, oxide-supported Rb_2CO_3 exhibits shift of wavenumber in IR spectra due to the variation of interaction between CO_3^{2-} and cations. For instance, $\sigma_{left,\ carb}$ of Rb_2CO_3-Y_2O_3 is 1485 cm^{-1} while this value is 1435 cm^{-1} for pure Rb_2CO_3. The peak shift is 50 cm^{-1} by considering 1435 cm^{-1} of pure Rb_2CO_3 as a benchmark. Through this approach, peak shift for each catalyst is calculated by employing pure Rb_2CO_3, Cs_2CO_3 and $Mg(OAc)_2$ as the benchmark, respectively. Herein, the peak shift, $\Delta\sigma_{left,\ carb}$, is defined as another property-descriptor (labelled with blue colour in Fig. 3.4) from IR spectra. It indicates the effect of oxide cations on CO_3^{2-} coordinated with Rb^+, Cs^+ or Mg^{2+}.

Property-descriptors, $\sigma_{left,\ carb}$ and $\Delta\sigma_{left,\ carb}$, were compared among all oxide-supported catalysts in order to further explore the influence of the cation from oxide support on carbonate structure. As shown in Fig. 3.5 a, $\sigma_{left,\ carb}$ for Rb_2CO_3-CeO_2, -Y_2O_3, -Sm_2O_3, -Gd_2O_3 and -Al_2O_3 catalysts is higher than the value of pure Rb_2CO_3. This may be attributed to larger polarization effect of Ce, Y, Sm, Gd and Al cations to carbonate anion compared to Rb cation, which significantly changes electronic structure of CO_3^{2-} and increase its polarity. Thus, stretching vibration mode of CO_3^{2-} shifts to a higher frequency. But for Rb_2CO_3-SrO and -BaO, no obvious shift of can be observed probably because Sr and Ba cation possess similar polarization power relative to Rb cation and cause negligible change to electronic structure of CO_3^{2-}. Differently, $\sigma_{left,\ carb}$ for oxide-supported $Mg(OAc)_2$ catalysts seems to be similar to the value of pure $Mg(OAc)_2$, as shown in Fig. 3.5 b. This suggests that oxide cations cause less impact on acetate species than CO_3^{2-} species probably due because of the intrinsic structural complexity of acetate. Fig. 3.5 c depicts the comparison of $\sigma_{left,\ carb}$ for Cs_2CO_3 on oxide catalysts. Qualitatively, the difference in between is similar to the trend obtained from Rb_2CO_3 on oxide catalysts.

Both property-descriptors, $\sigma_{left,\ carb}$ and $\Delta\sigma_{left,\ carb}$, would be employed to correlate with performance-descriptors of corresponding catalyst, which is discussed later in section 5.4.

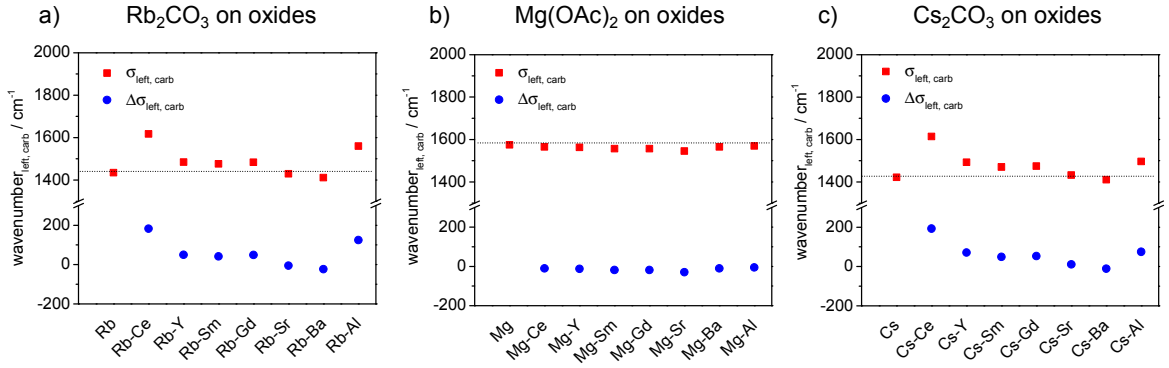

Fig. 3.5: Comparison of property-descriptors, $\sigma_{left,\ carb}$ (red) and $\Delta\sigma_{left,\ carb}$ (blue), for (a) Rb_2CO_3, (b) $Mg(OAc)_2$ and (c) Cs_2CO_3 pure and on oxides. $\sigma_{left,\ carb}$ represents the wavenumber of the left one of double peaks, which is attributed to asymmetric stretching of C-O bond in CO_3^{2-} or CH_3COO^- group. $\Delta\sigma_{left,\ carb}$ is defined as the shift value of characteristic peak for catalyst compared to corresponding pure carbonate or acetate.

3.3.4. Surface area (N_2-physisorption)

N_2 physisorption was measured in order to testify whether oxide-supported catalysts possess sufficient surface area for OCM reaction. BET surface area of fresh and spent catalysts is shown in Table 5.1.

For fresh catalysts, BET specific surface area differs dependent on support kinds. Al_2O_3 supported catalysts show highest surface area than others. After OCM reaction, the surface area exhibits inconsistent trend. In general, the surface area of Rb_2CO_3 on oxides decreases probably due to slight sintering of the materials under reaction conditions. However, the surface area increases for some of Cs_2CO_3 on oxides. A possible explanation is that the impregnated species covers the support surface, leading to low surface area of fresh catalysts. But the species decomposes and forms oxide phases with higher surface areas during catalysis. For $Mg(OAc)_2$ on oxides, the surface area exhibits no consistent variation trend after OCM as well. This may be attributed to decomposition of acetate species and structural reconstruction at certain conditions.

Broadly speaking, there seems no clear and consistent trend for BET surface area of catalysts, which make less sense to correlate with OCM performance. But at least one point is clear. There is no catalyst showing extremely low surface area after OCM reaction, indicating that all metal oxide supports used in this study are thermally stable support that are able to provide sufficient surface area under OCM conditions.

3.3.5. Thermogravimetric analysis coupled with mass spectrometry

Considering that the carbonate species and their stability may be related to OCM performance, its thermal stability was investigated by testing the decomposition behavior through thermogravimetric analysis coupled with mass spectrometry (TGA-MS) for Rb_2CO_3 on oxides, Cs_2CO_3 on oxides, $Mg(OAc)_2$ on oxides fresh catalysts, pure oxide supports as well as pure Rb_2CO_3, Cs_2CO_3 and $Mg(OAc)_2$.

Fig. 3.6 exhibit the TGA-MS result of pure Rb_2CO_3 and Rb_2CO_3 on oxide catalysts. For pure Rb_2CO_3 as shown in Fig. 3.6 a, mass loss below 200 °C with H_2O MS peak is ascribed to desorption of H_2O. The following mass loss above 800 °C with an obvious endothermic peak is attributed to melting and decomposition of Rb_2CO_3[145] when CO_2 product starts to be detected from MS.

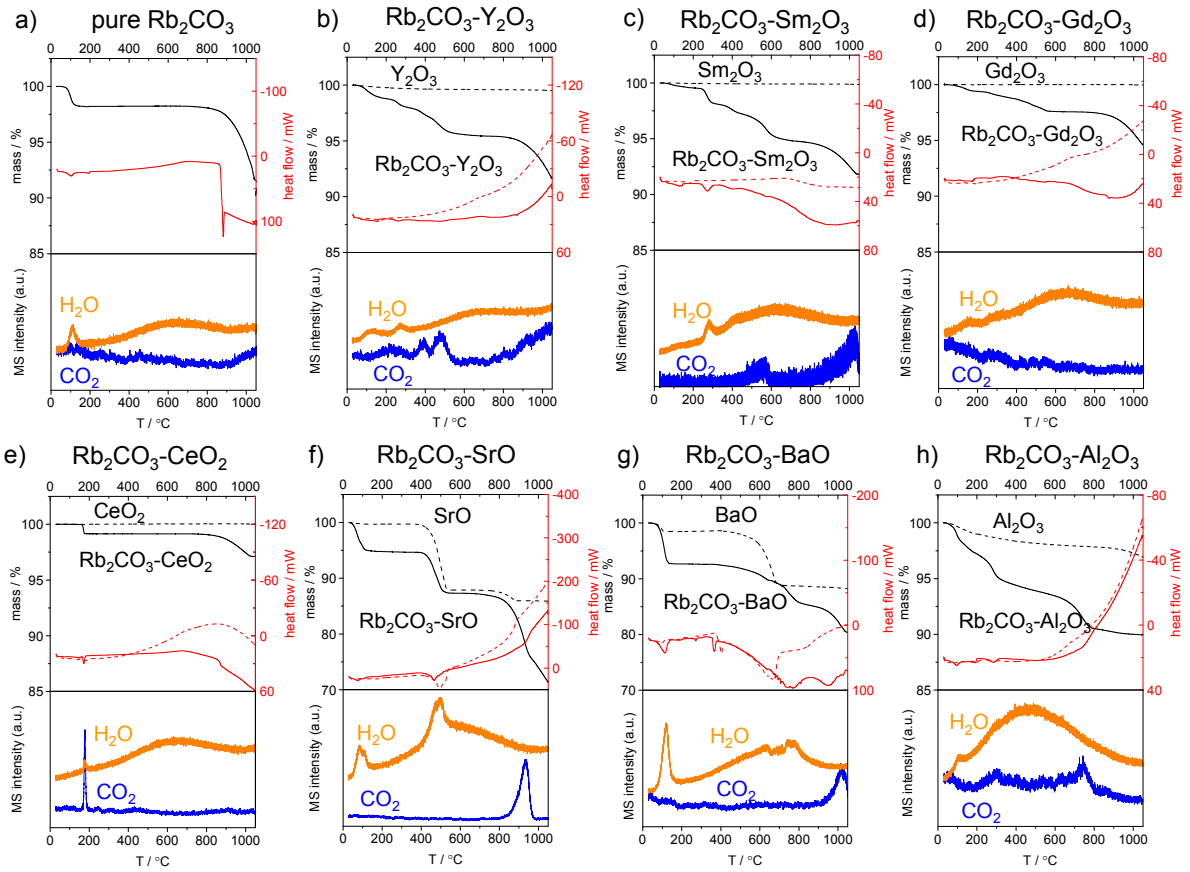

Fig. 3.6: TGA/MS results of (a) pure Rb_2CO_3 and Rb_2CO_3 on (b) Y_2O_3, (c) Sm_2O_3, (d) Gd_2O_3, (e) CeO_2, (f) SrO, (g) BaO and (h) Al_2O_3 support. The mass of pure Y_2O_3 keeps constant roughly during test. However, Rb_2CO_3-Y_2O_3 shows apparently multi-step mass loss and corresponding endothermic heat flows with CO_2 and H_2O evolution, indicating the occurrence of stepwise decomposition dependent on the temperature. Firstly, the mass loss below 200 °C is mainly due to adsorbed H_2O species. Secondly, multi-step mass loss between 200 and 650 °C can be attributed to decomposition of $Y(OH)_x(CO_3)_y{\cdot}zH_2O$ species, which may forms through CO_2 species transfer from Rb_2CO_3 to Y_2O_3. This process is complete when the mass curve plateau appears. Finally, mass loss above 700 °C arises from Rb_2CO_3 decomposition. Differently, Rb_2CO_3-CeO_2 shows an abrupt mass loss and endothermic heat flow below 200 °C with apparent CO_2 and H_2O products. This indicates the decomposition of Ce carbonate (or basic carbonate) with very low thermal stability. Besides, pure SrO exhibits two mass loss steps (400~500 °C and 700~900 °C) derived from the decomposition of $Sr(OH)_2$ and $SrCO_3$, respectively, which may form during the pre-treatment of SrO support before impregnation due to its high reactivity to H_2O and CO_2. Rb_2CO_3-SrO shows similar two step mass loss to pure SrO, but with a changed mass loss rate from 900 °C, suggesting the onset of Rb_2CO_3 decomposition. Similarly, Rb_2CO_3-BaO exhibits decomposition of $Ba(OH)_2$ and $BaCO_3$ at intermediate and high temperature range, respectively. Rb_2CO_3-Al_2O_3 shows mass loss steps before 400 °C and a sluggish mass loss until 650 °C. The mass loss after 650 °C with CO_2 evolution is attributed to Rb_2CO_3 decomposition. Pure Rb_2CO_3 shows decomposition behaviour above 800 °C.

By understanding the pure carbonate decomposition behavior, Rb_2CO_3 on oxide fresh catalysts were tested in the same fashion. The pure oxides support was also measured as a comparison. For example, the mass of pure Y_2O_3 (dash line in Fig. 3.6 b) keeps constant roughly in whole test temperature range. However, Rb_2CO_3-Y_2O_3 (solid line in Fig. 3.6 b) shows multi-step mass loss and endothermic heat flows with CO_2 and H_2O evolution, indicating the occurrence of stepwise decomposition with increase of the temperature. Firstly, the mass loss below 200 °C is mainly due to adsorbed H_2O species. Secondly, the mass exhibits multi-step loss between 200 and 650 °C, which is unlikely attributed to Rb_2CO_3 but other species decomposition. The yttrium carbonate or basic carbonate hydrate, denoted as $Y(OH)_x(CO_3)_y{\cdot}zH_2O$ in general, with metastability readily decomposes in this intermediate temperature range.[144, 165] Therefore in this case, $Y(OH)_x(CO_3)_y{\cdot}zH_2O$ species is believed to undergo multi-step decomposition with CO_2 and H_2O evolution. The formation of

$Y(OH)_x(CO_3)_y \cdot zH_2O$ species in fresh catalysts could be attributed to CO_3^{2-} species transfer from Rb_2CO_3 to Y_2O_3, which was proposed by Dubois[173] when $SrCO_3$ and $BaCO_3$ on Y_2O_3 as the catalyst exhibit improved OCM performance. On the other hand, crystallization H_2O as well as OH species may derive from the hygroscopicity of Rb_2CO_3. The process of $Y(OH)_x(CO_3)_y \cdot zH_2O$ decomposition to Y_2O_3 is complete when the mass curve plateau appears around 700 °C. Finally, mass loss above 700 °C with CO_2 released arises from Rb_2CO_3 decomposition, which is similar to mass loss for pure Rb_2CO_3. Analogously, Rb_2CO_3-Sm_2O_3 and Rb_2CO_3-Gd_2O_3 exhibit stepwise decomposition behavior at 200 ~ 650 °C and above 700 °C, as shown in Fig. 3.6 c and d.

Rb_2CO_3-CeO_2 shows a different decomposition behavior shown in Fig. 3.6 e. The mass shows an abrupt decrease along with a narrow endothermic peak below 200 °C, and apparent CO_2 and H_2O product peak appear simultaneously in MS. It could be assigned to the decomposition of Ce basic carbonate with low thermal stability[174] rather than simply loss of surface-adsorbed CO_2 and H_2O species at this temperature. The plateau between 200 and 650 °C suggests the complete decomposition of the above process and only CeO_2 presence in this intermediate temperature range. Mass loss above 700 °C is attributed to Rb_2CO_3.

As shown in Fig. 3.6 f, Rb_2CO_3-SrO exhibits another kind of decomposition behavior. Pure SrO shows two mass loss steps around 450 °C and 800 °C, which are derived from decomposition of $Sr(OH)_2$ and $SrCO_3$, separately.[168] The appearance of $Sr(OH)_2$ and $SrCO_3$ may arise from high reactivity of SrO with CO_2 and H_2O species during cooling down process after heat treatment in air atmosphere. Rb_2CO_3-SrO shows two mass loss steps around the similar temperature range, but with a changed mass loss rate after roughly 900 °C. To our knowledge, both Rb_2CO_3 and $SrCO_3$ tend to decompose at high temperature. Theoretically, the decomposition of $SrCO_3$ to SrO has a mass loss of 29.8%, which is higher than mass loss of 19.1% for the decomposition of Rb_2CO_3 to Rb_2O. Therefore, it is assumed that the decomposition of $SrCO_3$ and Rb_2CO_3 occurs sequentially. The turning point of mass curve around 900 °C showing slower mass loss suggests the start of Rb_2CO_3 decomposition. The decomposition behavior is similar when BaO is as a support (Fig. 3.6 g). For pure BaO, an endothermic heat flow appears around 400 °C without apparent mass change because of melting of $Ba(OH)_2$ (theoretical T_{melt} = 408 °C).[145] The $Ba(OH)_2$ is readily to decompose after melting and shows mass loss as a result. Rb_2CO_3-BaO shows a melting character of $Ba(OH)_2$ as well, along with a continuous mass loss subsequently until 750 °C due to decomposition of $Ba(OH)_2$. Thereafter, only one mass loss step is observed above 900 °C. Hence, Rb_2CO_3 and $BaCO_3$, both with high stability, are assumed to decompose simultaneously.

Decomposition behavior of conventional Al_2O_3 supported Rb_2CO_3 was also studied as a comparison, shown in Fig. 3.6 h. It exhibits a sluggish mass loss between 200 and 600 °C with CO_2 and H_2O released. This may be attributed to the decomposition of layered double hydroxides (LDH) with low stability,[166, 175] which contains Al^{3+} and Rb^+ inside layer and carbonate at the inter-layer as the main charge-balancing anion. The significant mass loss above 600 °C is due to Rb_2CO_3 decomposition. Differently, Rb_2CO_3 on Al_2O_3 decomposes at much lower temperature than on other metal oxides supports. This reveals that Al_2O_3 support facilitates the decomposition of Rb_2CO_3 to a much large extent than others. Al^{3+} is a strongly polarizing cation with higher charge density than other cations.[141] Polarization weakens the C-O bond of the carbonate polyanion and facilitates its dissociation to the oxide and CO_2.

TGA-MS results for pure Cs_2CO_3 and Cs_2CO_3 on oxide are shown in Fig. A3.6. Similarly, Cs_2CO_3-Y_2O_3, Cs_2CO_3-Sm_2O_3 and Cs_2CO_3-Gd_2O_3 exhibit stepwise mass loss at intermediate temperature range (200 ~ 650 °C) with CO_2 and H_2O evolution. Cs_2CO_3-CeO_2 shows a sharp

mass loss below 200 °C with obvious CO_2 and H_2O product peak appearing simultaneously. For above all samples, mass loss above 700 °C can be observed, which is attributed to Cs_2CO_3 decomposition. Cs_2CO_3-SrO and -BaO both exhibit mass loss with only H_2O released due to decomposition of hydroxide at 400 ~ 700 °C. Mass loss above 700 °C is derived from decomposition of Cs_2CO_3, $SrCO_3$ and $BaCO_3$.

In addition, TGA-MS results of pure $Mg(OAc)_2$and $Mg(OAc)_2$ on oxide are depicted in Fig. A3.7. Mass loss of pure $Mg(OAc)_2$ below 200 °C is due to desorption of adsorbed H_2O. Afterwards, $Mg(OAc)_2$ seems to show mass loss at 315 ~ 360 °C and 360 ~ 500 °C along with one sharp and another one broad CO_2 peak as well as one H_2O peak appearing in MS. This suggests that $Mg(OAc)_2$ may firstly decompose towards $MgCO_3$ as an unstable intermediate and subsequently $MgCO_3$ decomposes to MgO.[176] $Mg(OAc)_2$-Y_2O_3, -Sm_2O_3, -Gd_2O_3 and -CeO_2 (Fig. A3.7 b-e) exhibit one apparent mass loss step from 250 to 350 °C along with a sharp CO_2 peak in MS, which is similar to the decomposition behavior of $Mg(OAc)_2$ at 315 ~ 360 °C. Afterwards, for $Mg(OAc)_2$-Y_2O_3, -Sm_2O_3 and -Gd_2O_3, sluggish mass loss keeps going with broad CO_2 peak signal in MS until the plateau appears in mass curve. $MgCO_3$ may be also involved in the decomposition process of $Mg(OAc)_2$, but no significant plateau could be observed within this process due to its low thermal stability.

$Mg(OAc)_2$-SrO and $Mg(OAc)_2$-BaO exhibit multi-step mass loss behavior, as depicted in Fig. A3.7 f and g. For $Mg(OAc)_2$-SrO, mass loss below 200 °C is derived from desorption of physisorbed H_2O. $Mg(OAc)_2$ decomposition is observed from 200 to 400 °C, showing relatively less significant mass loss than the above four oxides supported samples. Also there is no obvious CO_2 product detected in this temperature range. Thereafter, $Mg(OAc)_2$-SrO shows mass loss from 400 to 500 °C with H_2O as the only product, which is assigned to decomposition of $Sr(OH)_2$. Then a mass loss starting from 700 °C appears with a strong peak of CO_2 detected in MS because of $SrCO_3$ decomposition. $Mg(OAc)_2$-BaO shows similar behavior when the temperature is below 400 °C. After that, a sluggish mass loss between 400 and 900 °C with H_2O evolution is assigned to $Ba(OH)_2$ decomposition. Mass loss after 900 °C with large amount of CO_2 producing is raised by decomposition of $BaCO_3$. Hence, for $Mg(OAc)_2$-SrO and $Mg(OAc)_2$-BaO, almost all carbonate species decomposes at high temperature in the form of $SrCO_3$ and $BaCO_3$ with high thermal stability.

Hence, $MgCO_3$ could be distinguished qualitatively as intermediate of $Mg(OAc)_2$ decomposition towards MgO in certain cases. But the $MgCO_3$ intermediate possesses fairly low thermal stability and tends to easily decompose after it is formed. This is similar to literature on pure $Mg(OAc)_2$ decomposition in absence of oxide support,[177, 178] where $Mg(OAc)_2$ seems to form MgO without distinguishable formation of $MgCO_3$ as a stable intermediate species.

Property-descriptors of $T_{dec,\ 1st\ CO2}$, $T_{dec,\ inter\ CO2}$ and $T_{dec,\ last\ CO2}$ from TGA-MS

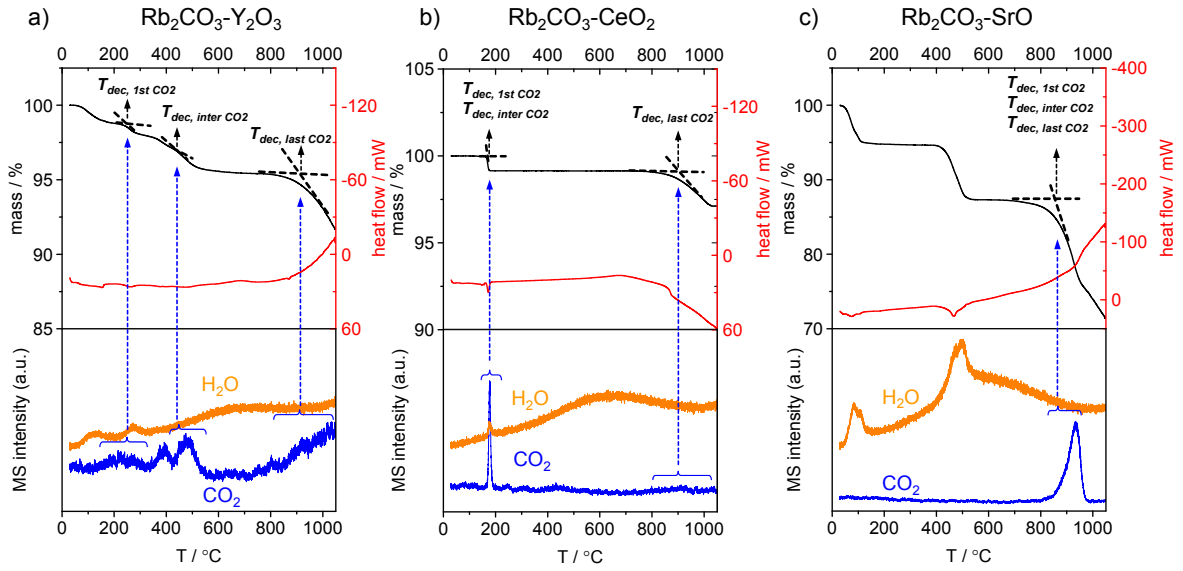

Fig. 3.7: Derivation of property-descriptors, $T_{dec,\ 1st\ CO2}$, $T_{dec,\ inter\ CO2}$ and $T_{dec,\ last\ CO2}$ based on TGA-MS results of (a) Rb_2CO_3-Y_2O_3, (b) Rb_2CO_3-CeO_2 and (c) Rb_2CO_3-SrO. $T_{dec,\ 1st\ CO2}$ or $T_{dec,\ last\ CO2}$ represents for mass loss temperature when the first or last CO_2 peak appears, respectively. $T_{dec,\ inter\ CO2}$ means mass loss temperature when CO_2 peak appears at intermediate temperature range 400 ~ 550 °C. If no CO_2 peak appears at this range, $T_{dec,\ inter\ CO2}$ is defined as mass loss temperature with CO_2 peak which is the closest to 400 ~ 550 °C. $T_{dec,\ 1st\ CO2}$, $T_{dec,\ inter\ CO2}$ and $T_{dec,\ last\ CO2}$ are derived in a universal fashion and labelled in each plot.

As discussed above, there is probably more than one kind of carbonate species present in catalysts and exhibits CO_2 evolution at different temperatures. CO_2 is generally generated as a by-product during OCM reaction. It has possibility to contact with typically oxide catalysts under OCM reaction temperature and atmosphere, which leads to formation/decomposition of carbonate species and may play a role in affecting OCM performance. Therefore, in order to quantitatively describe thermal stability of different carbonate species in catalysts, the decomposition temperatures coupled with the feature of CO_2 in MS is employed as property-descriptors. Herein, three property-descriptors, $T_{dec,\ 1st\ CO2}$, $T_{dec,\ inter\ CO2}$ and $T_{dec,\ last\ CO2}$, were defined and generated for all catalysts from TGA-MS data. The descriptor values are shown in a summary table (Table 5.1).

The decomposition temperature is derived through the intersection of tangents between the initial and inflection point of the mass loss step.[179] Fig. 3.7 depicts the approach to derive property-descriptors, $T_{dec,\ 1st\ CO2}$, $T_{dec,\ inter\ CO2}$ and $T_{dec,\ last\ CO2}$, representing for carbonate species in catalysts with lowest, intermediate and highest thermal stability. For example, $T_{dec,\ 1st\ CO2}$ is derived from mass loss step when the first CO_2 product peak signal appears in MS. It is typically located at low temperature range. $T_{dec,\ last\ CO2}$ is also derived from mass loss step but with the last CO_2 peak in MS typically appearing at high temperature range. Differently, $T_{dec,\ inter\ CO2}$ is preliminarily derived from mass loss step with CO_2 peak appearing in the certain temperature range (400 ~ 550 °C). However, not all samples exhibits mass loss and CO_2 peak in this temperature range. In that case, $T_{dec,\ inter\ CO2}$ is defined as the mass loss temperature with CO_2 peak which is closest to the defined temperature range.

These three property-descriptors are all dependent on carbonate species in catalysts. When there are several species present with distinct thermal stability capable of CO_2 evolution, for example, Rb_2CO_3-Y_2O_3 (Fig. 3.7 a) including possibly $Y_2(CO_3)_3$, $Y_2O_2CO_3$ and Rb_2CO_3, $T_{dec,\ 1st\ CO2}$, $T_{dec,\ inter\ CO2}$ and $T_{dec,\ last\ CO2}$ is different from each other and increases sequentially. Differently, two distinct steps exhibit CO_2 releasing for Rb_2CO_3-CeO_2 (Fig. 3.7 b). Thus, $T_{dec,}$

$T_{dec,\ 1st\ CO2}$ and $T_{dec,\ last\ CO2}$ is derived from the respective step while $T_{dec,\ inter\ CO2}$ is identical to $T_{dec,\ 1st\ CO2}$ based on the above definition. But when the two carbonate possess similar thermal stability, such as Rb_2CO_3 and $SrCO_3$ in Rb_2CO_3-SrO (Fig. 3.7 c), there is only one step with significant CO_2 evolution. In consequence, three property-descriptors, $T_{dec,\ 1st\ CO2}$, $T_{dec,\ inter\ CO2}$ and $T_{dec,\ last\ CO2}$, are all identical with each other for Rb_2CO_3-SrO.

In order to compare carbonate stability among catalysts and explore the possible effect of oxide support on carbonate stability, property-descriptors of $T_{dec,\ 1st\ CO2}$, $T_{dec,\ inter\ CO2}$ and $T_{dec,\ last\ CO2}$ for all catalysts were compared in Fig. 3.8. Based on the above discussion, $T_{dec,\ last\ CO2}$ for Rb_2CO_3 on oxides typically demonstrates the decomposition temperature of alkali carbonate with high stability. As shown in Fig. 3.8 a, Rb_2CO_3 on most of metal oxide supports exhibits similar decomposition temperature compared to pure Rb_2CO_3. However, Rb_2CO_3-Al_2O_3 shows much lower decomposition temperature of Rb_2CO_3 than others. Similar difference is also observed for Cs_2CO_3 on oxides samples. (Fig. 3.8 c) This reveals that Al_2O_3 support facilitates the alkali carbonate decomposition to a much large extent than others. It is derived from the strong polarizing power from Al^{3+} with high charge density, as discussed above. Such behavior is also observed for other Al_2O_3 supported alkali carbonate catalysts in the literature.[139, 180]

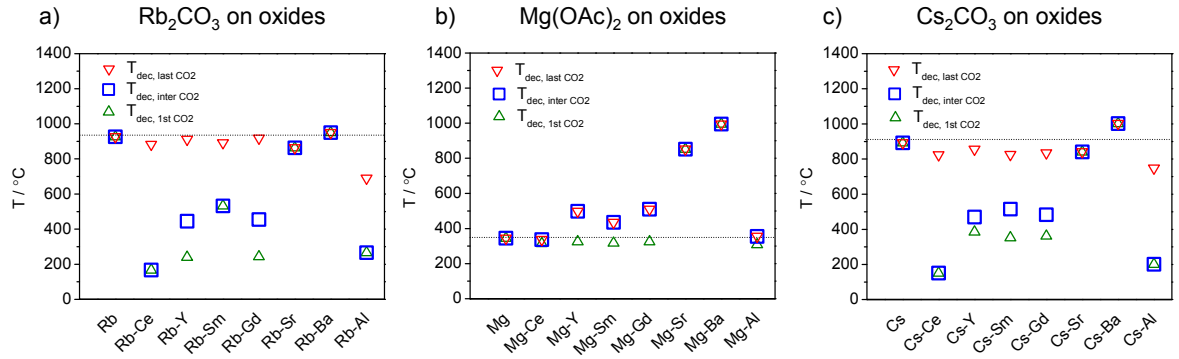

Fig. 3.8: Comparison of property-descriptors, $T_{dec,\ 1st\ CO2}$ (green), $T_{dec,\ inter\ CO2}$ (blue) and $T_{dec,\ last\ CO2}$ (red), for (a) Rb_2CO_3, (b) $Mg(OAc)_2$ and (c) Cs_2CO_3 pure and on oxides. For Rb_2CO_3 on oxides and Cs_2CO_3 on oxides, $T_{dec,\ 1st\ CO2}$ exhibits significant variation. Generally, Rb_2CO_3 and Cs_2CO_3 on CeO_2 and Al_2O_3 show the lowest $T_{dec,\ 1st\ CO2}$, while on Y_2O_3, Sm_2O_3, and Gd_2O_3 exhibit the medium value. Rb_2CO_3 and Cs_2CO_3 on SrO and BaO exhibit highest $T_{dec,\ 1st\ CO2}$. $T_{dec,\ inter\ CO2}$ shows similar variation trend to $T_{dec,\ 1st\ CO2}$. Differently, Rb_2CO_3 and Cs_2CO_3 on Al_2O_3 exhibits much lower $T_{dec,\ last\ CO2}$ than the pure form. However, other metal oxides support exhibits little effect on $T_{dec,\ last\ CO2}$. For $Mg(OAc)_2$ on oxides, all exhibit similar $T_{dec,\ 1st\ CO2}$ except -SrO and -BaO with much higher value. $T_{dec,\ inter\ CO2}$ and $T_{dec,\ last\ CO2}$ both show significant variation dependent on oxide support.

Differently, $T_{dec,\ 1st\ CO2}$ exhibits significant variation dependent on metal oxide support. Generally, Rb_2CO_3 and Cs_2CO_3 on CeO_2 and Al_2O_3 show the lowest $T_{dec,\ 1st\ CO2}$, while on Y_2O_3, Sm_2O_3 and Gd_2O_3 exhibit the medium value. In these catalysts, the first CO_2 product comes from decomposition of the carbonate formed by metal oxides support through CO_3^{2-} species transfer from alkali carbonate. Their decomposition temperature is much lower than the typical temperature in OCM reaction. Rb_2CO_3 and Cs_2CO_3 on SrO and BaO show highest $T_{dec,\ 1st\ CO2}$. Because all involved carbonate, Rb_2CO_3, Cs_2CO_3, $SrCO_3$ and $BaCO_3$, possess high thermal stability and decompose at around or above OCM reaction temperature. Similarly, $T_{dec,\ inter\ CO2}$ exhibits variation dependent of oxide support. The difference between $T_{dec,\ inter\ CO2}$ and $T_{dec,\ inter\ CO2}$ is mainly shown in Rb_2CO_3-Y_2O_3, Rb_2CO_3-Gd_2O_3, Cs_2CO_3-Y_2O_3, Cs_2CO_3-Sm_2O_3 and Cs_2CO_3-Gd_2O_3. These $T_{dec,\ inter\ CO2}$ values are higher than $T_{dec,\ 1st\ CO2}$, which are at intermediate temperature range and much closer to the typical OCM temperatures.

Unlike Rb_2CO_3 and Cs_2CO_3 on oxides, pure $Mg(OAc)_2$ and $Mg(OAc)_2$ on most of oxide supports (Fig. 3.8 b) exhibits similar $T_{dec,\ 1st\ CO2}$, which can be attributed to decomposition of acetate species. However, $T_{dec,\ 1st\ CO2}$ is much higher for $Mg(OAc)_2$-SrO and $Mg(OAc)_2$-BaO because decomposition of $SrCO_3$ and $BaCO_3$ with higher stability is considered to be the only step to release CO_2 in these two samples. On the other hand, $T_{dec,\ inter\ CO2}$ and $T_{dec,\ last\ CO2}$ both exhibit similar trend to $T_{dec,\ 1st\ CO2}$, while $Mg(OAc)_2$-Y_2O_3, $Mg(OAc)_2$-Sm_2O_3 and $Mg(OAc)_2$-Gd_2O_3 possesses distinct values. As discussed above, sluggish mass loss with continuous releasing of CO_2 was observed at 360 ~ 500 °C for these three samples (Fig. A3.7 b-d) and therefore, $T_{dec,\ inter\ CO2}$ and $T_{dec,\ last\ CO2}$ are available correspondingly. This may indicate the formation of $MgCO_3$ as an intermediate species in the decomposition process of $Mg(OAc)_2$ towards MgO, which may be weakly stabilized by the presence of certain oxide support.

In summary, the stability of carbonate species present in catalysts can be described in a quantitative fashion by these three property-descriptors. Through comparison, it reveals that the carbonate stability is strongly influenced by metal oxide support.

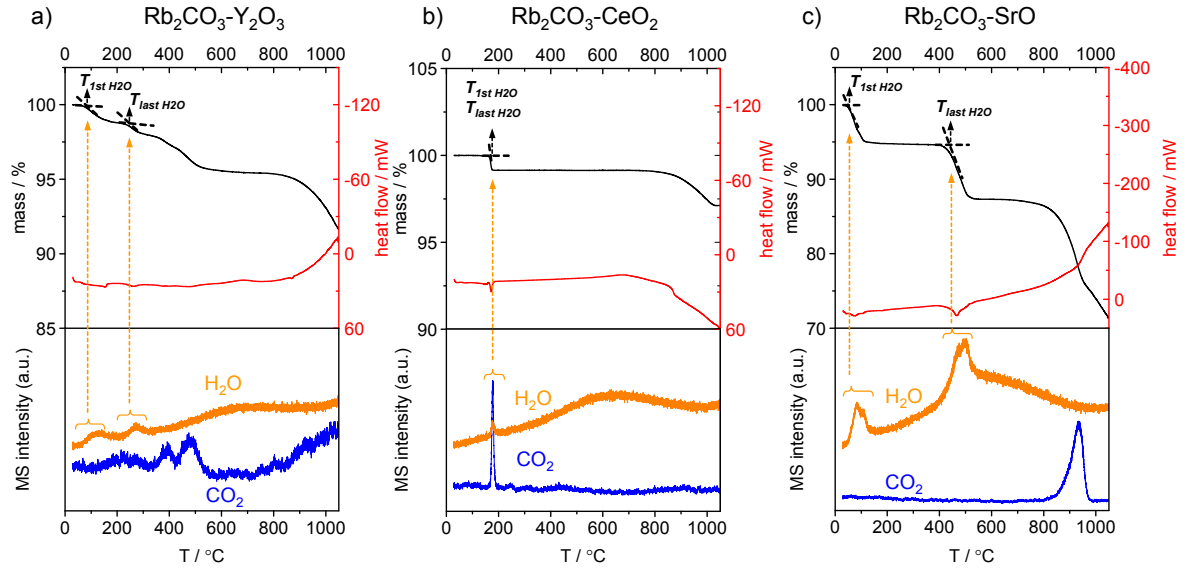

Fig. 3.9: Derivation of property-descriptors, $T_{1st\ H2O}$ and $T_{last\ H2O}$, based on TGA-MS results of (a) Rb_2CO_3-Y_2O_3, (b) Rb_2CO_3-CeO_2 and (c) Rb_2CO_3-SrO. $T_{dec,\ 1st\ CO2}$ or $T_{dec,\ last\ CO2}$ represents for mass loss temperature when the first or last H_2O peak appears, respectively. $T_{1st\ H2O}$ and $T_{last\ H2O}$ are derived in a universal fashion and labeled in each plot.

Property-descriptors of $T_{1st\ H2O}$ and $T_{last\ H2O}$ from TGA-MS

From TGA-MS analysis, H_2O was also observed as one product within the decomposition of various species in oxide-supported catalysts. Typically, H_2O is an inevitable product of OCM reaction along with hydrocarbons. From the point of thermodynamic view, as shown in Equation 1.2 and 1.3 of chapter 1, the formation and removal of H_2O during the reaction play a role in the equilibrium shift of the overall reaction. More importantly, H_2O may have an influence on active species involved in catalysis. In the reaction mechanism proposed by Lunsford,[38, 40, 71] active oxygen species in catalysts abstracts H from CH_4 and forms OH as a result. Subsequently, two adjacent OH tend to form H_2O which escapes from the catalysts and leave one oxygen vacancy responsible for oxygen activation. Another argument is that active site responsible for CH_4 would be blocked by H_2O.[68, 181] A severe competition is proposed between dissociative adsorption of methane at an active site and the corresponding reaction with water, which is temperature-dependent. Therefore, the

temperature regarding to H_2O formation and removal is considerable to be a meaningful descriptor.

Similar to the behavior of CO_2, there is more than one mass loss step releasing H_2O as the product in catalysts based on TGA-MS results. Herein, two property-descriptors, $T_{1st\ H2O}$ and $T_{last\ H2O}$, were defined and generated for all catalysts from TGA-MS data, which represent for species with earliest and latest H_2O evolution. Fig. 3.10 depicts the approach to derive property-descriptors, $T_{1st\ H2O}$ and $T_{last\ H2O}$. The descriptor values are shown in a summary table (Table 5.1).

For Rb_2CO_3-Y_2O_3, first H_2O peak in MS comes from desorption of physisorbed H_2O molecule of samples, which is typically below 100 °C. The last H_2O peak in MS appears at 200 ~ 400 °C, possibly attributed to the decomposition of carbonate hydrate because both H_2O and CO_2 are evolved in this temperature region. Analogous difference between $T_{1st\ H2O}$ and $T_{last\ H2O}$ is also observed for Rb_2CO_3-Sm_2O_3 and Rb_2CO_3-Gd_2O_3, as shown in Fig. 3.6 c and d. Differently, $T_{1st\ H2O}$ and $T_{last\ H2O}$ is identical for Rb_2CO_3-CeO_2, as there is only one significant H_2O peak appearing in MS along with CO_2 simultaneously. Rb_2CO_3-SrO exhibits another behavior regarding to H_2O. An obviously sharp peak appears below 100 °C appears due to the strong hygroscopicity of SrO, which is described by $T_{1st\ H2O}$. Afterwards, the dramatic mass loss around 450 °C with a greatly larger H_2O peak meanwhile without CO_2 signal is definitely derived from decomposition of $Sr(OH)_2$. Rb_2CO_3-BaO shows a continuous mass loss from 400 to 750 °C with H_2O as the only product (Fig. 3.6 g), which is assigned to the decomposition of $Ba(OH)_2$. In these two samples, the decomposition of hydroxide is represented by $T_{last\ H2O}$. Therefore, H_2O-relating property-descriptors of $T_{1st\ H2O}$ and $T_{last\ H2O}$ describe behaviors of various species containing physisorbed H_2O, carbonate hydrate and hydroxide in catalysts, which is much more sophisticated than CO_2-relating property-descriptors of $T_{dec,\ 1st\ CO2}$, $T_{dec,\ inter\ CO2}$ and $T_{dec,\ last\ CO2}$ only focused on carbonate species.

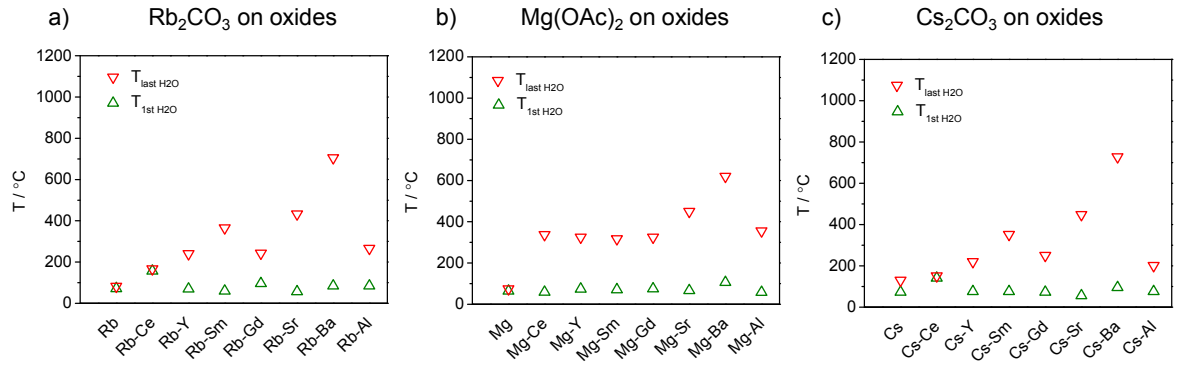

Fig. 3.10: Comparison of property-descriptors, $T_{1st\ H2O}$ (green) and $T_{last\ H2O}$ (red), for (a) Rb_2CO_3, (b) $Mg(OAc)_2$ and (c) Cs_2CO_3 pure and on oxides. In general, $T_{1st\ H2O}$ is below 200°C for all catalysts because $T_{1st\ H2O}$ is typically derived from the desorption of physisorbed water. Differently, $T_{last\ H2O}$ exhibits obvious variation. $T_{last\ H2O}$ of Rb_2CO_3-CeO_2 and Cs_2CO_3 -CeO_2 is identical with $T_{last\ H2O}$ because there is only one mass loss step with H_2O evolution below 200 °C. For Rb_2CO_3, $Mg(OAc)_2$ and Cs_2CO_3 on Y_2O_3, Sm_2O_3 and Gd_2O_3, $T_{last\ H2O}$ is between 200 and 400 °C as the last H_2O may be derived from hydrocarbonate decomposition. But for Rb_2CO_3, $Mg(OAc)_2$ and Cs_2CO_3 on SrO and BaO, last H_2O comes from the decomposition of $Sr(OH)_2$ and $Ba(OH)_2$, which occurs at above 400 °C.

Property-descriptors of $T_{1st\ H2O}$ and $T_{last\ H2O}$ for each catalyst were compared in Fig. 3.10. In general, $T_{1st\ H2O}$ is typically below 100 °C for all catalysts because it is derived from the removal of physisorbed water. Differently, $T_{last\ H2O}$ exhibits obvious variation. For Rb_2CO_3 and Cs_2CO_3 on CeO_2, $T_{1st\ H2O}$ comes from decomposition of Ce carbonate hydrate below 200 °C. For Rb_2CO_3 and Cs_2CO_3 on Y_2O_3, Sm_2O_3 and Gd_2O_3, $T_{1st\ H2O}$ is also derived from carbonate

hydrate but locating at 200 ~ 400 °C due to different stability. $T_{last\ H2O}$ is also in this temperature range 200 ~ 400 °C for $Mg(OAc)_2$ on CeO_2, Y_2O_3, Sm_2O_3 and Gd_2O_3, but could be mainly attributed to decomposition of $Mg(OAc)_2$. Differently, for Rb_2CO_3, Cs_2CO_3 and $Mg(OAc)_2$ and on SrO and BaO, last H_2O comes from the decomposition of $Sr(OH)_2$ and $Ba(OH)_2$, which typically occurs above 450 °C.

Hence, $T_{last\ H2O}$ is more meaningful than $T_{1st\ H2O}$ because it includes the stability information of several species which may be involved in OCM reaction.

3.3.6. Proposed surface structural models for oxide-supported catalysts

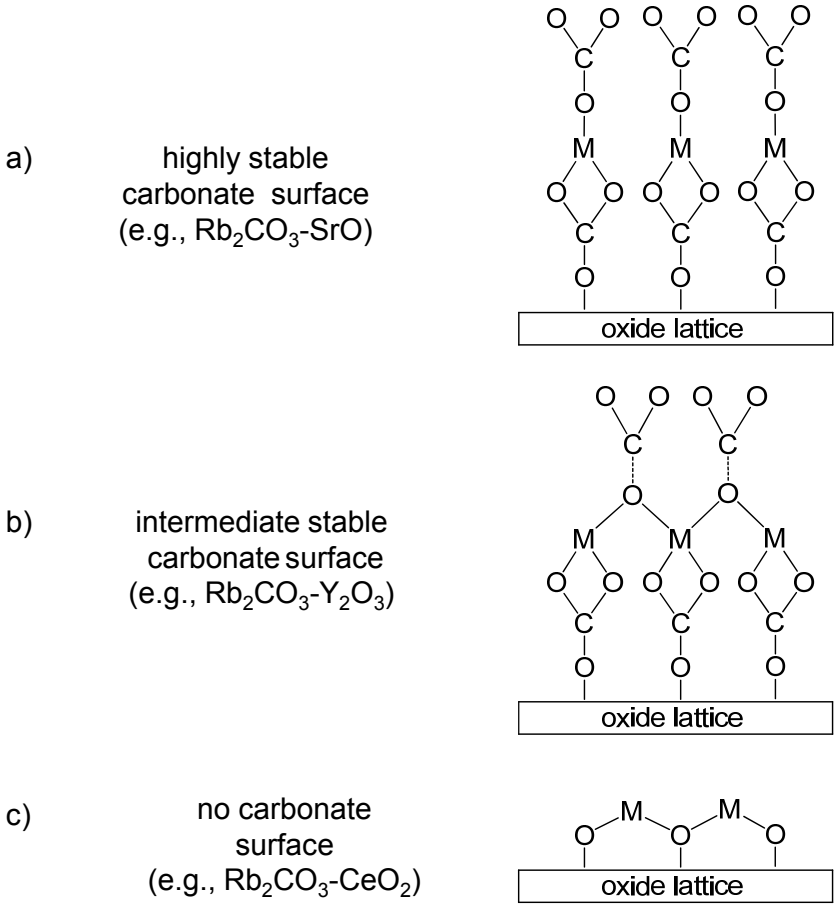

Fig. 3.11: Simplified surface structure illustration of oxide-supported catalysts. a) Highly stable carbonate surface, which rarely decomposes at typical OCM temperatures. b) Intermediate stable carbonate surface, which tends to partially decompose at typical OCM temperatures. Meanwhile, the oxide is almost covered by carbonate species. c) No carbonate surface due to tis low stability, which completely decomposes at typical OCM temperatures.

Based on the characterization data especially TGA-MS results, three different surface structure are proposed for oxide-supported catalysts dependent on the thermal stability of involved carbonate species. Considering the possible complexity of interaction between carbonate and oxide, the simplified structural sketch was shown in Fig. 3.11 in order to present the general surface structure of three types in a visible fashion.

As shown in Fig. 3.11 a, the involved carbonate species possesses high stability, for instance, Rb_2CO_3-SrO catalyst where both Rb_2CO_3 and $SrCO_3$ are usually highly stable, a thin layer of carbonate species is considered to be present as the surface. It tends to retain stable at elevated temperature such as typical OCM reaction temperatures.

When the carbonate species possesses intermediate stability, for example, Rb_2CO_3-Y_2O_3 where Y carbonate are commonly moderately stable, a thin layer of carbonate is regarded to be present as the surface, as shown in Fig. 3.11 b. The oxygen of carbonate may coordinate with several cations and thus results to a relatively weak C-O bond. This carbonate is rather flexible and sensitive to the exposed temperature. At typical OCM temperature, some of these carbonate species tend to decompose via breaking of C-O bond and consequently form active oxygen species, which may be involved in activation of CH_4. Meanwhile, the oxide is still mostly covered by carbonate species.

Fig. 3.11 c depicts the surface structure of oxide-supported catalyst when the involved carbonate has low stability. For instance, for Rb_2CO_3-CeO_2 catalysts, Ce carbonate tends to completely decompose below 200 °C. Hence, no carbonate surface would be present at high temperature such as under OCM reaction condition.

3.4. Carbonate-supported carbonate catalysts

In section 3.3, oxide-supported carbonate catalysts were analyzed. Various carbonate species are proved to exist in catalyst and exhibit complex but interesting decomposition behavior, especially when carbonate species with intermediate stability is incorporated. In order to study the difference between oxide and carbonate as a support for catalysts, herein, carbonate-supported catalysts would be discussed regarding to morphology, crystal phase composition and chemical species. Considering the carbonate formation and decomposition behavior is influenced by the presence of CO_2 in atmosphere, TGA-MS are independently performed in Ar and CO_2 atmosphere in order to explore the effect of CO_2 on the thermal stability of carbonate species in these catalysts. Afterwards, property-descriptors for these carbonate-supported catalyst are generated from IR and TGA-MS data (result shown in Table 5.1).

3.4.1. Morphology

Carbonate-supported Rb_2CO_3 and Cs_2CO_3 are discussed with regard to morphology. The detailed SEM results of pure carbonates and carbonate-supported catalysts are presented in Appendix section A3.4.1.

Pure $Sm_2(CO_3)_3$, Rb_2CO_3 and Cs_2CO_3 on $Sm_2(CO_3)_3$ exhibit similar sheet-like morphology. After OCM, pure $Sm_2(CO_3)_3$ exhibits slight morphological change, while for Rb_2CO_3 and Cs_2CO_3 on $Sm_2(CO_3)_3$, the pristine sheet-like morphology is completely transformed into a network structure consisting of conjunct small particle. This suggests that $Sm_2(CO_3)_3$ may undergo decomposition at OCM reaction temperature and induce the change of the bulk morphology.

Pure $SrCO_3$, Rb_2CO_3 and Cs_2CO_3 on $SrCO_3$ show similar grain-like morphology surrounded by quantities of tiny particles. After OCM, the grains become more pronounced with apparent crystal-like edges. Compared to the significant morphological variance appearing in $Sm_2(CO_3)_3$-supported catalysts, $SrCO_3$-supported catalysts exhibit relatively less changes after reaction, indicating that $SrCO_3$ exhibits higher stability than $Sm_2(CO_3)_3$ during OCM reaction.

3.4.2. Crystalline phase

In order to detect crystal phase composition, XRD was tested for all carbonate-supported catalysts before and after OCM reaction. The detailed XRD patterns of pure carbonates and carbonate-supported catalysts are presented in Appendix section A3.4.2.

For pure $Sm_2(CO_3)_3$, Rb_2CO_3 and Cs_2CO_3 on $Sm_2(CO_3)_3$ fresh catalysts, the main crystal phase is $Sm_2(CO_3)_3$ carbonate phase. But after OCM, only Sm_2O_3 oxide phase can be detected, revealing that $Sm_2(CO_3)_3$ decomposes at OCM reaction temperature and produces Sm_2O_3 as product. No significant Rb_2CO_3 and Cs_2CO_3 crystal phases are detected, possibly because they are present as very tiny crystallites or amorphous forms on the surface of support (as discussed in section 3.3.2).

Pure $SrCO_3$, Rb_2CO_3-$SrCO_3$ and Cs_2CO_3-$SrCO_3$, fresh catalysts show similar consistent crystal phase of $SrCO_3$. After OCM, $SrCO_3$ phase is still intact and becomes more pronounced. It is worth mentioning that no oxide crystal phase could be detected, which is different from the case of $Sm_2(CO_3)_3$ supported catalysts. This reveals that $SrCO_3$ exhibits higher stability than $Sm_2(CO_3)_3$ during OCM reaction.

3.4.3. Chemical species

$Sm_2(CO_3)_3$ supported catalysts

FT-IR was also conducted to determine chemical species. As shown in Fig. 3.12 a, pure $Sm_2(CO_3)_3$ exhibited adsorption peaks in the range of 1700 - 650 cm^{-1}, which are attributed to different vibrational modes of CO_3^{2-} species.[171] These characteristic peaks were also observed in Rb_2CO_3-$Sm_2(CO_3)_3$ and Cs_2CO_3-$Sm_2(CO_3)_3$ fresh catalysts (Fig. 3.12 b and c). In addition, the appeared adsorption bands in the 3800 - 3000 cm^{-1} region can be attributed to O-H stretching mode of crystallization H_2O.

However, the adsorption peaks for CO_3^{2-} species significantly diminished after OCM for all samples. And meanwhile, the peak at 528 cm^{-1} attributed to Sm-O became more pronounced. Besides, adsorption band for -OH disappeared. It is thus confirmed that $Sm_2(CO_3)_3$ hydrate readily decomposes towards oxide under typical OCM temperature during reaction. This is in agreement with the SEM and XRD results. Therefore, all these observations reveal that $Sm_2(CO_3)_3$ possesses intermediate thermal stability.

The characterization data of pure $Sm_2(CO_3)_3$ and $Sm_2(CO_3)_3$-supported catalysts was then compared to the corresponding ones using oxide as support, e.g., pure Sm_2O_3 and Rb_2CO_3-Sm_2O_3 catalyst.

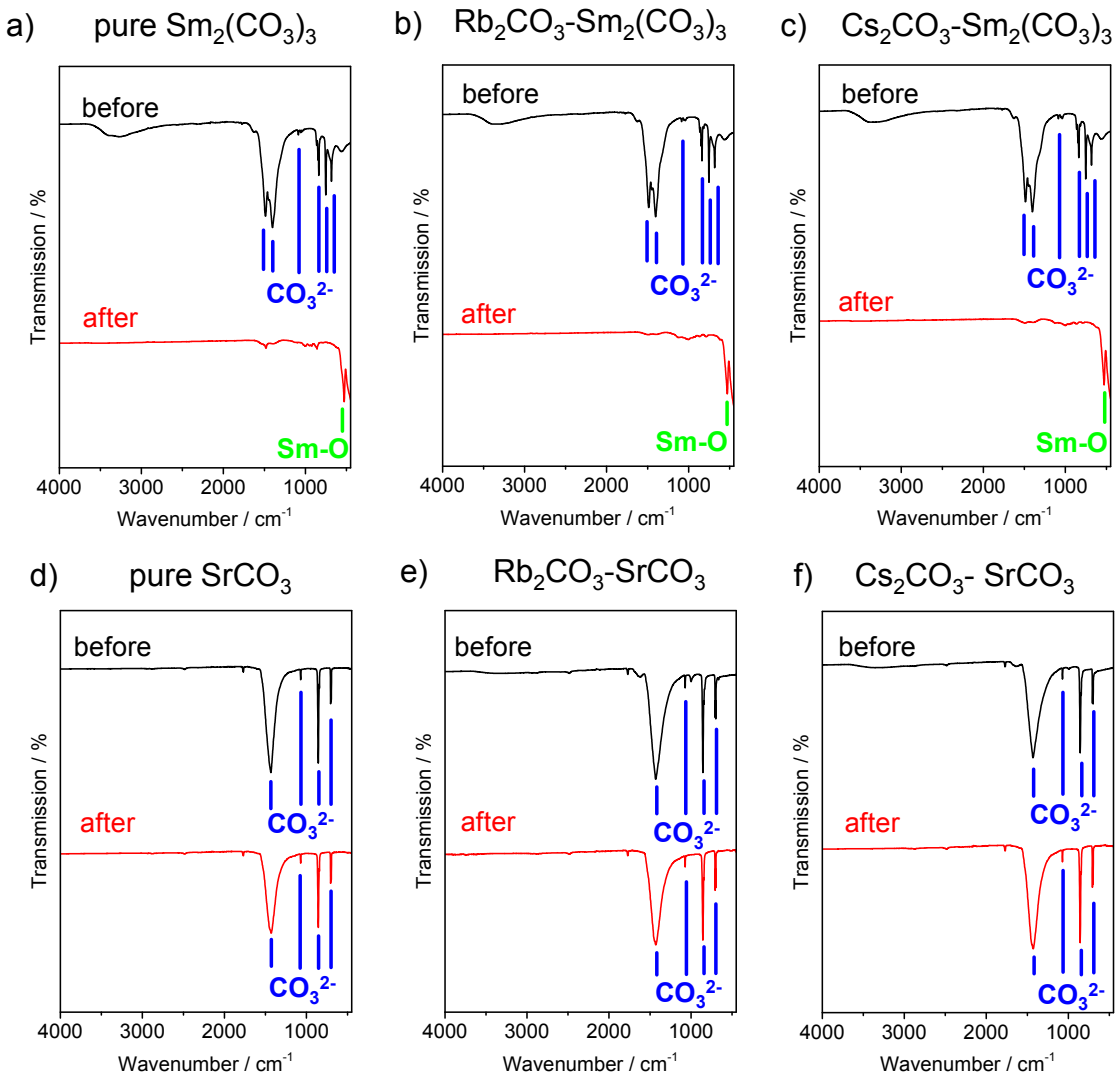

Fig. 3.12: IR spectra of (a) pure $Sm_2(CO_3)_3$, (b) Rb_2CO_3-$Sm_2(CO_3)_3$, (c) Cs_2CO_3-$Sm_2(CO_3)_3$, (d) pure $SrCO_3$, (e) Rb_2CO_3-$SrCO_3$ and (f) Cs_2CO_3-$SrCO_3$ catalysts before and after OCM. Pure $Sm_2(CO_3)_3$ and its supported catalysts before OCM all exhibit characteristic adsorption peak belonging to carbonate species. These peaks significantly diminish after OCM and meanwhile, the signal attributed to Sm-O becomes more pronounced. It proves that carbonate species readily decomposes to oxide during OCM reaction. Pure $SrCO_3$ and its supported catalysts all exhibit characteristic peaks for carbonate species. No significant change of these peaks is observed after OCM, suggesting that carbonate species keeps stable during OCM reaction.

XRD pattern of pure Sm_2O_3 (Fig. A3.4 b) and Rb_2CO_3-Sm_2O_3 (Fig. A3.5 b) are different from pure $Sm_2(CO_3)_3$ and Rb_2CO_3-$Sm_2(CO_3)_3$, which is not surprising because carbonate and oxide are chemically different. However, only Sm_2O_3 phase was observed for both oxide and carbonate supported catalysts after OCM reaction, indicating that $Sm_2(CO_3)_3$ tends to decompose towards oxide and in consequence both catalysts forms identical phase composition after reaction. Furthermore, for Rb_2CO_3-Sm_2O_3, the characteristic peak intensity of CO_3^{2-} species shown in IR spectra (Fig. 3.3 b) is greatly weaker than the corresponding peak in Rb_2CO_3-$Sm_2(CO_3)_3$. It suggests that the amount of carbonate species in fresh Rb_2CO_3-Sm_2O_3 is significantly lower than in fresh Rb_2CO_3-$Sm_2(CO_3)_3$, because the carbonate species is merely from impregnated Rb_2CO_3 in former case but is mainly contributed by the entire $Sm_2(CO_3)_3$ support in the latter case. The IR spectra for both samples after OCM reaction, however, are quantitatively similar because only Sm-O could be apparently distinguished, which reveals that carbonate species present in fresh catalysts decomposes towards oxides during OCM reaction.

In a short summary, obvious difference regarding to SEM, XRD and IR results for $Sm_2(CO_3)_3$ and its supported catalysts is observed before and after OCM. Qualitatively, the carbonate-supported catalysts after OCM reaction are similar to the oxide-supported ones from the view of crystal phase and chemical species. The decomposition of $Sm_2(CO_3)_3$ towards Sm_2O_3 during OCM reaction is confirmed through the above characterization data.

$SrCO_3$ supported catalysts

FT-IR was also tested for pure $SrCO_3$, Rb_2CO_3 and Cs_2CO_3 on $Sm_2(CO_3)_3$ catalysts before and after OCM, as shown in Fig. 3.12 d-f. Before OCM, they all exhibited adsorption band in the range of 1700 - 650 cm^{-1}, which can be derived from the vibrations of CO_3^{2-} species.[168, 182] After OCM reaction, the spectra were qualitatively same as the ones before OCM, where no characteristic adsorption peak for oxides was observed.

The characterization data of pure $SrCO_3$ and $SrCO_3$-supported catalysts was then compared to the corresponding ones using oxide as support, e.g., pure SrO and Rb_2CO_3-SrO catalyst. When SrO was used as a support, hydroxide phase forms due to its high H_2O affinity, which is different from the catalysts using $SrCO_3$ as a support. In addition, carbonate phase forms in SrO-supported fresh catalyst which is similar to the crystal phase of $SrCO_3$-supported catalysts. However, after OCM reaction, only $SrCO_3$ phase was observed for both oxide and carbonate supported catalysts, indicating that $SrCO_3$ rarely decomposes at typical OCM temperature due to its high stability.

Therefore, the characterization results by SEM, XRD and FT-IR consistently proved that $SrCO_3$ support possesses high thermal stability and exhibits rare change at OCM condition. Qualitatively, the carbonate-supported catalysts after OCM reaction are similar to the oxide-supported ones with regards to the crystal phase and chemical species.

3.4.4. Thermogravimetric analysis coupled with mass spectrometry

In order to evaluate the thermal stability of carbonate species present in pure carbonates and carbonate-supported catalysts, TGA-MS test was performed in Ar atmosphere. The results are shown in Fig. 3.13. Generally, multi-step mass loss with more than one CO_2 peak signal in MS was observed for all cases, which is similar to decomposition behavior of oxide-supported catalysts shown in Fig. 3.6.

$Sm_2(CO_3)_3$ supported catalysts

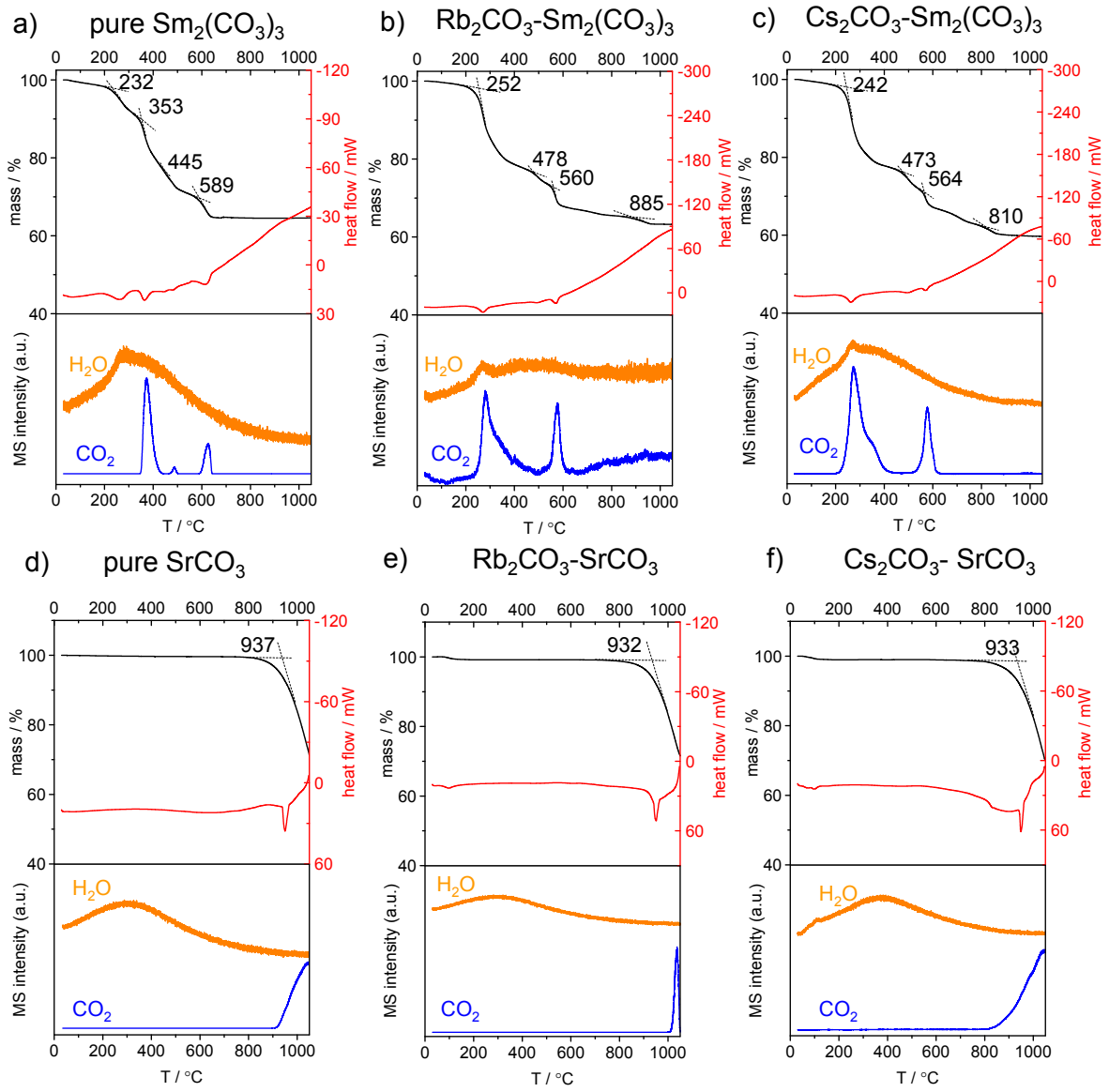

Fig. 3.13: TGA-MS result of (a) pure $Sm_2(CO_3)_3$, (b) Rb_2CO_3-$Sm_2(CO_3)_3$, (c) Cs_2CO_3-$Sm_2(CO_3)_3$, (d) pure $SrCO_3$, (e) Rb_2CO_3-$SrCO_3$ and (f) Cs_2CO_3-$SrCO_3$ tested in Ar atmosphere. Pure $Sm_2(CO_3)_3$ exhibits stepwise mass loss with CO_2 evolution below 650 °C. For Rb_2CO_3-$Sm_2(CO_3)_3$, it shows an obvious mass loss from 200 to 400 °C with an earlier CO_2 evolution onset than pure $Sm_2(CO_3)_3$. The decomposition behavior at 400 ~ 650 °C similar to pure $Sm_2(CO_3)_3$. Differently, an additional mass loss above 800°C is observed for Rb_2CO_3-$Sm_2(CO_3)_3$ due to decomposition of Rb_2CO_3. Cs_2CO_3-$Sm_2(CO_3)_3$ exhibits analogous mass loss behavior to Rb_2CO_3-$Sm_2(CO_3)_3$ but with a relatively lower decomposition temperature of Cs_2CO_3. Pure $SrCO_3$ and its supported catalysts consistently show one significant mass loss step and one CO_2 peak in MS at similar decomposition temperature.

For pure $Sm_2(CO_3)_3$ as shown in Fig. 3.13 a, it exhibited four distinct mass loss steps labelled with onset decomposition temperature T_{dec} ~ 232, 353, 445 and 589 °C, respectively. The first step with T_{dec} ~ 232 °C could be attributed to the loss of crystallization H_2O in $Sm_2(CO_3)_3$ hydrate, because it occurs at relatively lower temperature with H_2O as the only evolution product. $Sm_2(CO_3)_3$ anhydrate is considered to form as a result. Afterwards, the second step with T_{dec} ~ 353 °C exhibited an obvious mass loss with large amounts of CO_2 but no obvious H_2O evolution. This behavior could be derived from the decomposition of $Sm_2(CO_3)_3$ anhydrate towards one kind of oxycarbonate $Sm_2O_x(CO_3)_y$. The subsequent step with T_{dec} ~ 445 °C and less CO_2 evolution could be assigned to decomposition of $Sm_2O_x(CO_3)_y$ towards

intermediate compound $Sm_2O_2CO_3$.[144, 165] The formed $Sm_2O_2CO_3$ subsequently decompose towards Sm_2O_3, which could explain the fourth step with T_{dec} ~ 569 °C and CO_2 evolution.

For Rb_2CO_3-$Sm_2(CO_3)_3$ as shown in Fig. 3.13 b, there were also distinct mass loss steps but with different onset decomposition temperature 252, 478, 560 and 885 °C, respectively. The first step with T_{dec} ~ 252 °C exhibited a dramatic mass loss along with simultaneous appearance of H_2O and CO_2 in MS. Meanwhile, the CO_2 peak was relatively broad, indicating continuous releasing of CO_2 occurs at this temperature region. The first step behavior of Rb_2CO_3-$Sm_2(CO_3)_3$ seems to integrate the first and second step shown in pure $Sm_2(CO_3)_3$ decomposition, which means that there is no unambiguous $Sm_2(CO_3)_3$ anhydrate formed as an intermediate. The following two mass loss steps with T_{dec} ~ 478 °C and T_{dec} ~ 560 °C were assigned to decomposition of $Sm_2O_x(CO_3)_y$ to $Sm_2O_2CO_3$ and subsequently toward Sm_2O_3. Different from pure $Sm_2(CO_3)_3$, the last step of Rb_2CO_3-$Sm_2(CO_3)_3$ at higher temperature range with T_{dec} ~ 885 °C and CO_2 evolution was definitely attributed to decomposition of Rb_2CO_3. One important observation is the sluggish mass loss from 600 to 750 °C with broad CO_2 peak signal in MS. It could not be attributed to the decomposition of $Sm_2(CO_3)_3$ or Rb_2CO_3 individually, but more likely due to the transfer of CO_3^{2-} species from Rb to Sm and its subsequent decomposition. The interesting behavior at this temperature region was also observed for Rb_2CO_3-Sm_2O_3 (Fig. 3.6 c). It is speculated that at certain temperature, CO_3^{2-} species possess sufficient mobility to migrate from highly stable compound to less stable one, which in this case from Rb_2CO_3 to $Sm_2O_2CO_3$. In other words, the presence of Sm tends to destabilize the highly stable Rb_2CO_3.

Similarly, Cs_2CO_3-$Sm_2(CO_3)_3$ exhibited three mass loss steps of below 600 °C due to decomposition of $Sm_2(CO_3)_3$ hydrate towards Sm_2O_3 (Fig. 3.13 c). The last steps with T_{dec} ~ 810 °C was originated from decomposition of Cs_2CO_3. Between 600 and 750 °C, there was also a sluggish mass loss step attributed to CO_3^{2-} species transfer from Cs_2CO_3 to $Sm_2O_2CO_3$ and subsequent decomposition.

$SrCO_3$ supported catalysts

TGA-MS was also measured for pure $SrCO_3$, Rb_2CO_3-$SrCO_3$ and Cs_2CO_3-$SrCO_3$ in order to evaluate the thermal stability of involved carbonate species in catalysts. The results were shown in Fig. 3.13 d-f.

As shown in Fig. 3.13 d, pure $SrCO_3$ exhibits nearly no mass loss below 800 °C. Afterwards, the mass starts to decrease continuously until the TGA test limit. A corresponding endothermic heat flow can be also observed. It reveals that $SrCO_3$ has high stability and only decomposes above 800 °C. Similarly, Rb_2CO_3-$SrCO_3$ (Fig. 3.13 e) and Cs_2CO_3-$SrCO_3$ (Fig. 3.13 f) also show only one significant mass loss above 800 °C with an obvious endothermic heat flow. The derived decomposition temperature is nearly identical to pure $SrCO_3$. No sluggish mass loss at intermediate temperature could be observed, indicating that no CO_3^{2-} species transfer occurs. Hence, Sr behaves different from Sm as a support cation, which is not able to destabilize Rb_2CO_3 and Cs_2CO_3.

3.5. Li/MgO and Mn-Na_2WO_4/SiO_2 catalysts

As a comparison to oxide-supported and carbonate-supported catalysts, typical OCM catalysts, Li/MgO and Mn-Na_2WO_4/SiO_2, were also prepared and characterized with regard to crystalline phase and chemical species. TGA-MS was performed in Ar atmosphere in order to explore the decomposition behavior of possible species in these catalysts.

Thereafter, property-descriptors for these reference catalyst are generated from IR and TGA-MS data (results shown in Table 5.1).

3.5.1. Crystalline phase

As shown in Fig. A3.12 a and b, for both Li/MgO fresh catalysts, MgO and Li_2CO_3 crystal phase were observed in XRD patterns. After OCM reaction, however, Li_2CO_3 phase can be no longer observed and MgO phase still retains in XRD pattern. Hence, it reveals that carbonate species present in fresh Li/MgO catalysts could not be preserved during OCM reaction.

As show in Fig. A3.12 c, for Mn-Na_2WO_4/SiO_2 catalyst, crystalline SiO_2 α-cristobalite, Mn_2O_3 and Na_2WO_4 were detected in XRD, which is similar to the previous report for Mn-Na_2WO_4/SiO_2 catalyst system.[61] For Na_2WO_4/SiO_2 catalyst (Fig. A3.12 d), not surprisingly, α-cristobalite and Na_2WO_4 were detected in XRD. No clear signals attributed to crystalline carbonate can be observed for both catalysts.

3.5.2. Chemical species

FT-IR was measured for Li/MgO and Mn-Na_2WO_4/SiO_2 catalyst in order to determine present chemical species. The results are depicted in Fig. 3.14.

Both Li/MgO fresh catalysts exhibit characteristic adsorption peak at around 1432, 1089 and 859 cm^{-1} assigned to the vibration of CO_3^{2-} species, which corresponds with IR spectra of pure Li_2CO_3 and $MgCO_3$ shown in Fig. A3.13 a. However, characteristic peaks for CO_3^{2-} species are greatly reduced or even disappear in IR spectra after OCM reaction. Hence, it reveals that carbonate species present in fresh Li/MgO catalysts could not be preserved during OCM reaction.

Mn-Na_2WO_4/SiO_2 and Na_2WO_4/SiO_2 catalysts both exhibit strong adsorption peak at 1070, 793, 621 and 468 cm^{-1} attributed to α-cristobalite species.[183, 184] The difference in between is that with the presence of Mn, two more adsorption peaks at 957 and 713 cm^{-1} seem to appear in fresh catalyst. Nevertheless, they are reduced after OCM reaction. Ji el al.[184] and Chua et al.[183] also reported the similar observation, where a change of interaction between active components was claimed to be the explanation without determining a definite species. With the assumption of carbonate species existing in catalysts, IR test for pure Na_2CO_3 and $MnCO_3$ were measured and shown in Fig. A3.13 b. After comparison, peak at 713 cm^{-1} of Mn-Na_2WO_4/SiO_2 is close to 725 cm^{-1}, which is one characteristic peaks for $MnCO_3$. Although a shift is not negligible, $MnCO_3$ or a compound containing Mn^{2+} and CO_3^{2-} may be present in fresh Mn-Na_2WO_4/SiO_2 catalyst.

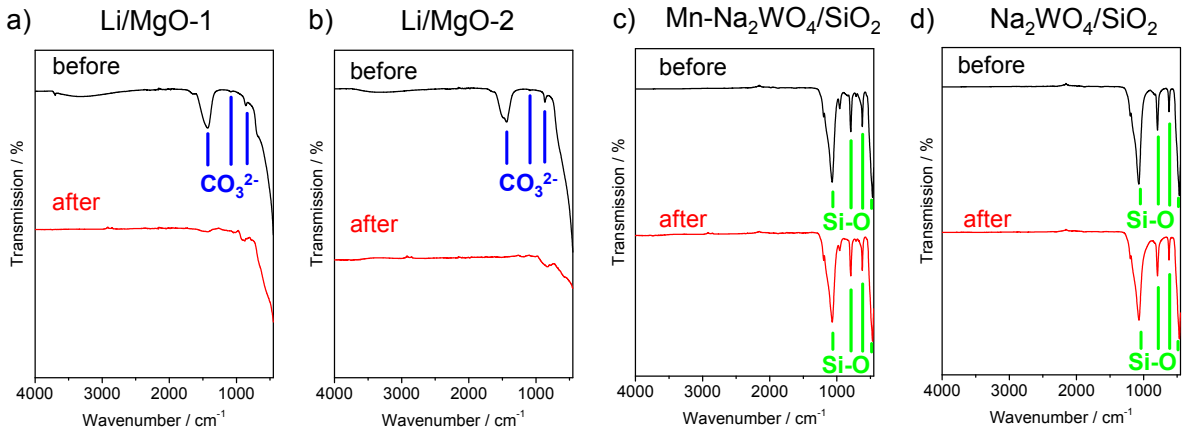

Fig. 3.14: IR spectra of (a) Li/MgO-1, (b) Li/MgO-2, (c) Mn-Na_2WO_4/SiO_2 and (d) Na_2WO_4/SiO_2 before and after OCM. For both Li/MgO catalysts, characteristic peak for CO_3^{2-} species significantly reduces after OCM reaction. Mn-Na_2WO_4/SiO_2 and Na_2WO_4/SiO_2 exhibits obvious adsorption peak attributed to crystalline SiO_2. A weak peak appearing in fresh Mn-Na_2WO_4/SiO_2 catalyst with reduction after reaction may be assigned to Mn-containing carbonate species.

3.5.3. Thermogravimetric analysis

For typical Li/MgO and Mn-Na_2WO_4/SiO_2 catalyst system as a reference, it is worthwhile to investigate their decomposition behavior regarding to the present carbonate species. Thus, TGA-MS was also conducted for prepared Li/MgO, Mn-Na_2WO_4/SiO_2 and Na_2WO_4/SiO_2 fresh catalysts, as shown in Fig. 3.15.

Both Li/MgO and Mn-Na_2WO_4/SiO_2 catalyst exhibit multi-step mass loss in TGA with several CO_2 peaks appearing in MS, which is similar to the observation for oxide-supported catalysts. For Li/MgO-1, three distinct mass loss steps with CO_2 evolution were observed at temperature range of 200 ~ 400 °C, 400 ~ 550 °C and above 600 °C. The latter two steps with intermediate and last CO_2 could be assigned to decomposition of $MgCO_3$ and Li_2CO_3 because the pure form theoretically decomposes at 469 °C and 720 °C, respectively.[141, 185] The first step with first CO_2 may be derived from an undefined species with rather low stability. Li/MgO-2 exhibits similar multi-step mass loss behavior with three apparent CO_2 peaks appearing in MS.

For Mn-Na_2WO_4/SiO_2, the mass loss steps in TGA curve are not as distinguishable as Li/MgO, but MS signal showed at least three distinct CO_2 peaks, which suggest the occurrence of multi-step mass loss. Interestingly, three mass loss steps also take place in varied temperature range, 200 ~ 400 °C, 400 ~ 550 °C and above 600 °C. The first and last step could be derived from decomposition of $MnCO_3$ and Na_2CO_3 based on its corresponding decomposition temperature (300 and 840 °C) in theory.[141, 186] The step in the middle may be caused by an intermediate species $[Na^+ \cdots CO_2^{3-} \cdots Mn^{2+}]$ formed by Mn, Na cation and CO_3^{2-} anion, which is difficult to figure out the unambiguous form. Differently, for Na_2WO_4/SiO_2, only a broad CO_2 peak was observed over a wide temperature range in MS. This indicates that the presence of Mn may be responsible for the formation of the intermediate carbonate species in this catalyst system.

Hence, it can be concluded that there are more than one kind of carbonate-containing species present in typical Li/MgO and Mn-Na_2WO_4/SiO_2 catalysts, which possess distinct thermal stability. Importantly, these catalysts exhibit carbonate decomposition behavior around or above 750 °C, indicating that certain kind of carbonate species in catalysts could

be present at typical OCM temperatures. But no stable carbonate species in Na_2WO_4/SiO_2 catalyst could exist at similar temperatures.

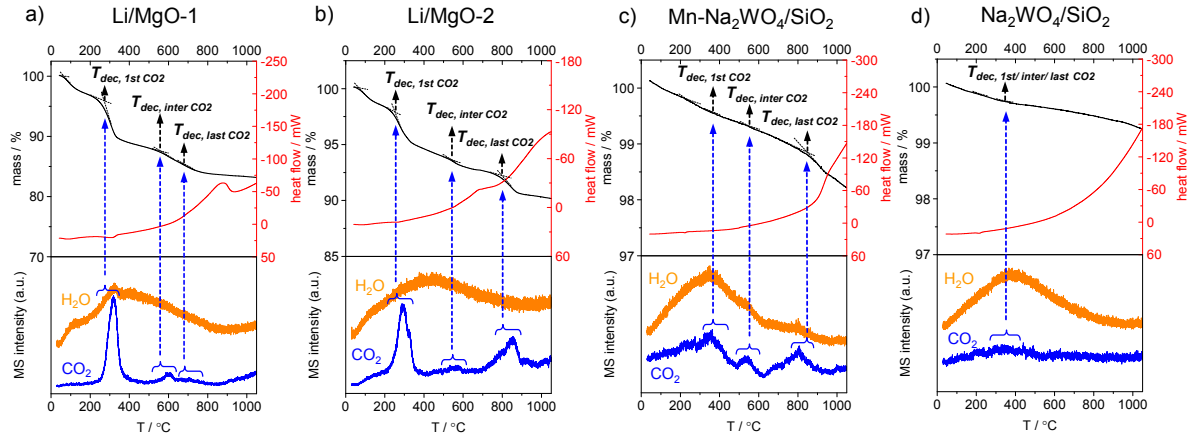

Fig. 3.15: TGA-MS results and $T_{dec,\ 1st\ CO2}$, $T_{dec,\ inter\ CO2}$, $T_{dec,\ last\ CO2}$ of (a) Li/MgO-1, (b) Li/MgO-2, (c) Mn-Na_2WO_4/SiO_2 and (d) Na_2WO_4/SiO_2. Both Li/MgO catalysts exhibit multi-step mass loss behavior with CO_2 evolution at low, intermediate and high temperature range. Mn-Na_2WO_4/SiO_2 catalyst shows at least three steps of mass loss with distinguishable CO_2 signal in MS. Differently, Na_2WO_4/SiO_2 catalyst only exhibits a sluggish mass loss with a broad CO_2 peak in MS. $T_{dec,\ 1st\ CO2}$, $T_{dec,\ inter\ CO2}$, $T_{dec,\ last\ CO2}$ were derived for all samples according to the defined criterion.

3.6. Influence of CO_2 on carbonate stability

In actual OCM reaction, CO_2 is typically present in the gas phase due to unselective oxidation of both reactant and product. Basically, CO_2 in the gas phase can participate in the chemical equilibrium of decomposition/formation of certain species such as carbonates, which may further has an impact on OCM catalytic reaction as reported in literatures[40, 156, 157, 159]. In order to determine carbonate stability under an atmosphere close to actual OCM condition, TGA-MS test was also performed in CO_2 atmosphere. Typically, the decomposition of carbonates in CO_2 atmosphere is expected to shift towards higher temperatures. The decomposition temperatures measured in Ar and CO_2 atmosphere are thus estimations of upper and lower limit, respectively. Decomposition of carbonates under actual OCM reaction conditions is assumed to occur in the region defined by measured limits, as CO_2 concentration under OCM reaction is between 0 and 100%, which depends on actual feed composition (diluent, CH_4 / O_2 ratio) and the catalyst performance.

In order to clearly figure out the influence of CO_2 on carbonate stability, TGA-MS results tested in CO_2 vs Ar atmosphere for pure $Sm_2(CO_3)_3$, Rb_2CO_3 and Cs_2CO_3 on $Sm_2(CO_3)_3$ catalysts were compared in Fig. 3.16.

As shown in Fig. 3.16 a, multi-step mass loss was observed for pure $Sm_2(CO_3)_3$ tested in CO_2. The decomposition steps below 500 °C are similar to the result tested in Ar. However, an obvious plateau was observed from 550 to 700 °C, indicating the formation of stable $Sm_2O_2CO_3$ intermediate species. The last mass loss step, assigned to decomposition of $Sm_2O_2CO_3$ towards Sm_2O_3, exhibits a significant shift of decomposition temperature from 589 °C in Ar to 756 °C in CO_2 atmosphere. Meanwhile, it shows a stronger endothermic heat flow with a corresponding shift as well. This suggests that CO_2 in gas atmosphere has the most significant influence on the last step of decomposition for pure $Sm_2(CO_3)_3$ sample.

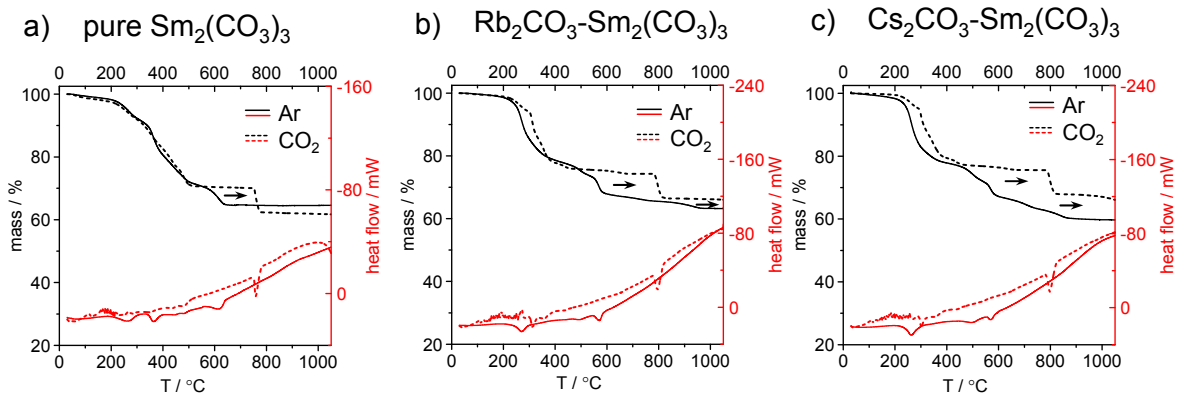

Fig. 3.16: TGA result of (a) pure $Sm_2(CO_3)_3$, (b) Rb_2CO_3-$Sm_2(CO_3)_3$ and (c) Cs_2CO_3-$Sm_2(CO_3)_3$ tested in CO_2 vs in Ar atmosphere. All samples were treated in vacuum oven at 150 °C for 5 h before TGA test. All samples exhibits significant shift of carbonate decomposition temperature to higher temperatures when tested in CO_2 atmosphere.

TGA result of Rb_2CO_3-$Sm_2(CO_3)_3$ was shown in Fig. 3.16 b. Differently, the mass curve exhibits more significant shift regarding to almost all mass loss steps compared to the result tested in Ar. The shift for the mass loss behavior between 200 and 400 °C is about 56 °C, which is assigned to decomposition of $Sm_2(CO_3)_3$ hydrate to $Sm_2O_x(CO_3)_y$. The plateau around 500 °C illustrates the formation of stable $Sm_2O_x(CO_3)_y$ intermediate due to the presence of CO_2 in gas atmosphere. The shift of $Sm_2O_x(CO_3)_y$ decomposition to $Sm_2O_2CO_3$ is 132 °C. Similarly, $Sm_2O_2CO_3$ forms as a stable intermediate species subsequently because another plateau around 750 °C can be observed. The shift of $Sm_2O_2CO_3$ decomposition to Sm_2O_3 is even larger, 228 °C. Afterwards, no apparent sluggish mass loss can be observed until the last ambiguous mass loss step above 950 °C, which could be attributed to the decomposition of Rb_2CO_3 with a shift of 95 °C. Hence, compared to pure $Sm_2(CO_3)_3$, the influence of CO_2 on the decomposition of carbonate species in Rb_2CO_3-$Sm_2(CO_3)_3$ seems to be much more complicated. The possible decomposition steps exhibits various temperature shifts.

Cs_2CO_3-$Sm_2(CO_3)_3$ also exhibits different temperature shift for each decomposition step, as depicted in Fig. 3.16 c. Note that the decomposition process above 950 °C is probably not complete at the final test temperature 1050 °C. But it was not possible to obtain data above 1050 °C due to the limitation of TGA instrument. Therefore, the final relative mass tested in CO_2 is significantly different from the value tested in Ar. The decomposition of Cs_2CO_3 shows a shift increase of 163 °C.

In order to explain different decomposition behaviors of carbonate in Ar and CO_2 atmosphere, the carbonate decomposition/formation reaction is shown in equation 4.1.

$$M_2CO_3 \rightleftharpoons M_2O + CO_2 \qquad (4.1)$$

It can be considered that in Ar atmosphere, evolved CO_2 product upon carbonate decomposition is transported away from the system by the Ar stream. Rb_2CO_3 and Cs_2CO_3 tend to be destabilized by Sm through carbonate transfer effect. As a result, for Rb_2CO_3-$Sm_2(CO_3)_3$ and Cs_2CO_3-$Sm_2(CO_3)_3$, the decomposition temperature of Rb_2CO_3 and Cs_2CO_3 both shifted to lower temperature.

On the contrary, in CO_2 atmosphere the backward reaction of equation 4.1 towards a carbonate could occur efficiently. In other words, CO_2 atmosphere is able to stabilize carbonates and suppress its decomposition. In consequence, the decomposition temperature of carbonate is generally shifted towards higher temperature. Herein, the shift of

decomposition temperature of Cs_2CO_3 is larger than Rb_2CO_3 ($\Delta T_{dec,\ CO2}$ = 163 °C for Cs, 95 °C for Rb). One possible explanation is that the destabilization effect of Sm is less critical under CO_2 atmosphere and the carbonate decomposition behavior is mainly influenced by the reaction equilibrium itself. Typically, carbonate decomposition/formation equilibrium is strongly dependent on the charge density of the cation[141] and the backward reaction is more favored for cations with lower charge density. As Cs^+ has lower charge density than Rb^+, the degree of stabilization effect by CO_2 atmosphere for Cs_2CO_3 is thus larger than Rb_2CO_3.

However, the decomposition of $Sm_2(CO_3)_3$ cannot be simply described by equation 4.1, as there are multiple steps during decomposition process towards oxide, in which several stable or unstable intermediate may form. Equilibria among initial carbonate, intermediate species and final oxide could interact with each other. This may explain why the decomposition temperature shifted to different extent for each step in CO_2 atmosphere. This shift seems to consistently increase with the proceeding of decomposition for $Sm_2(CO_3)_3$, Rb_2CO_3-$Sm_2(CO_3)_3$ and Cs_2CO_3-$Sm_2(CO_3)_3$, i.e., the decomposition of $Sm_2O_2CO_3$ to Sm_2O_3 exhibits largest temperature shift. It is in agreement with the report by Moscardini et al.[165, 187] using as starting compound. They found that the increase of decomposition temperature in CO_2 compared with the result in air atmosphere was mainly for $Sm_2O_2CO_3$ intermediate. One possible reason is shown as follows.

$$Sm_2(CO_3)_3 \rightleftharpoons Sm_2O_2CO_3 + 2\ CO_2 \qquad (4.2)$$

$$Sm_2O_2CO_3 \rightleftharpoons Sm_2O_3 + CO_2 \qquad (4.3)$$

It is assumed that decomposition of $Sm_2(CO_3)_3$ can be simplified into two steps via $Sm_2O_2CO_3$ intermediate. In CO_2 atmosphere, decomposition/formation equilibrium (4.2) and (4.3) are both influenced by CO_2 in gas phase. But backward reaction in (4.3) is more favored than in (4.2) because it requires less amount of CO_2 to participate in. Therefore, equilibrium (4.3) tends to be affected to a higher degree and as a result, $Sm_2O_2CO_3$ exhibits a larger decomposition temperature shift value in CO_2 atmosphere compared to other species during decomposition steps.

As a short summary, when CO_2 is present in atmosphere, carbonate species in carbonate-supported catalysts could be present at high temperature, e.g., typical OCM temperatures. Because CO_2 in atmosphere is able to stabilize carbonate species in catalysts and leads to the shift of thermal stability towards higher temperatures.

3.7. Summary

In this chapter of thesis, oxide-supported, carbonate-supported as well as selected typical OCM catalysts were synthesized and characterized regarding to morphology, elemental distribution, crystal phase composition, chemical species, surface area and carbonate stability. Property-descriptors, $T_{dec,\ 1st\ CO2}$, $T_{dec,\ inter\ CO2}$, $T_{dec,\ last\ CO2}$, $T_{1st\ H2O}$, $T_{last\ H2O}$, $\sigma_{left,\ carb}$ and $\Delta\sigma_{left,\ carb}$, were defined and generated on the basis of IR and TGA-MS characterization results in order to quantitatively describe catalyst properties typically carbonate stability. Both oxide-supported and carbonate-supported catalysts feature the multi-step mass loss with several peaks for CO_2 and H_2O product in MS. which is attributed to more than one kind of carbonate species with different thermal stability in catalyst. The oxide support could facilitate carbonate transfer from highly stable form to carbonate species with lower stability, which is easier to decompose at sufficiently high temperatures. Three distinct surface structural models of oxide-supported catalysts are proposed including carbonate species with high, intermediate and low stability. Carbonate species is present in Li/MgO and Mn-Na_2WO_4/SiO_2

reference catalysts, which possesses distinct thermal stability similar to oxide-supported catalysts. Importantly, these catalysts contain certain kind of carbonate species that is also present at typical OCM temperatures. For certain carbonate-supported catalysts, TGA-MS result tested in CO_2 compared to in Ar atmosphere exhibits consistent shift of carbonate decomposition behaviors towards higher temperatures, revealing the stabilization effect of CO_2 in atmosphere on carbonate stability. When CO_2 is present in atmosphere, carbonate species in carbonate-supported catalysts could be present at typical OCM temperatures.

Property-descriptors, $T_{dec,\ 1st\ CO2}$, $T_{dec,\ inter\ CO2}$, $T_{dec,\ last\ CO2}$, $T_{1st\ H2O}$, $T_{last\ H2O}$, $\sigma_{left,\ carb}$ and $\Delta\sigma_{left,\ carb}$, would be correlated with performance-descriptors later and the correlations would be discussed in chapter 5.

4. OCM performance and performance-descriptors of oxide-supported and carbonate-supported catalysts

Synthesis and characterization of oxide-supported and carbonate-supported catalysts were discussed in chapter 3. Property-descriptors for all catalysts were generated. In this chapter, their OCM catalytic performance is tested and compared in detail. The goal of this chapter is to generate performance-descriptors for all catalysts from catalytic test results.

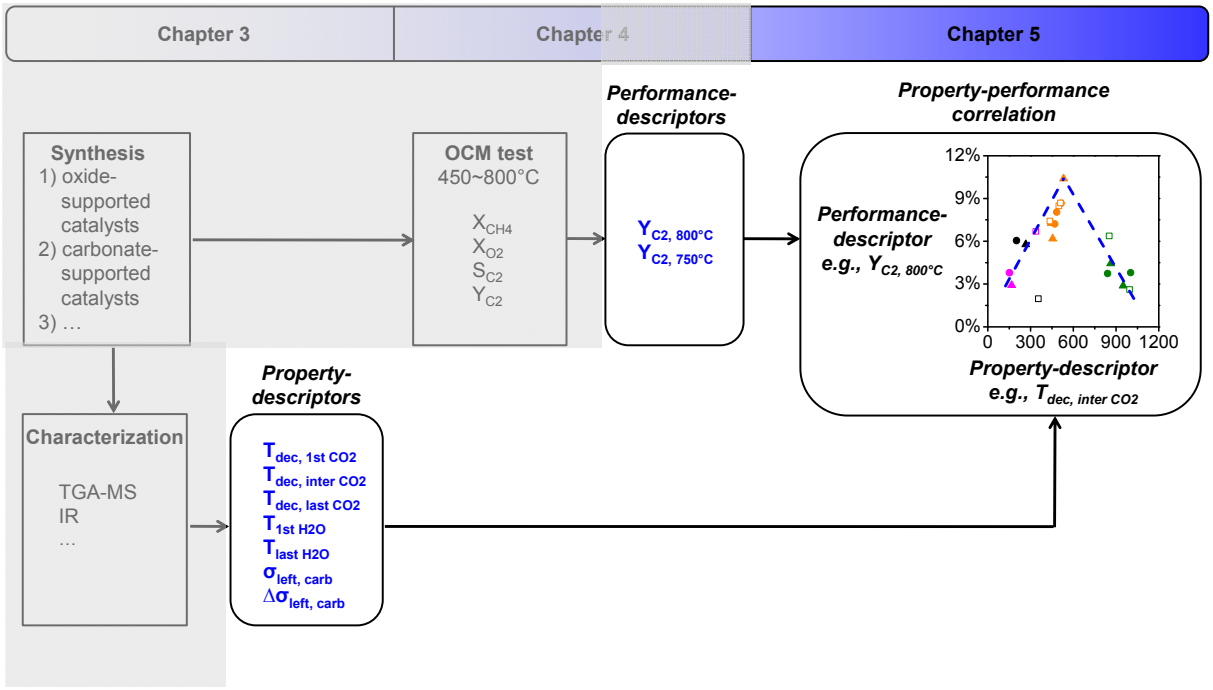

Fig. 4.1 Schematic representation of chapter 4 in this thesis. The goal is to generate performance-descriptors from catalytic performance data for exemplary catalysts.

4.1. Catalytic testing procedure

Activity of the catalysts was tested in a fixed-bed reactor system developed at the Leibniz Institute for Catalysis (LIKAT) in Rostock. The overview of test procedure is shown in Fig. 4.2. The setup possesses 6 quartz tube reactors with 4 mm inner diameter plus 1 by-pass channel. A glass wool plug is employed to hold the fixed bed and guarantee it at equal height for each reactor. 50 mg catalyst (size fraction 224 - 500 µm) was placed on a quartz wool plug covered with roughly 700 mg SiC particles to ensure the temperature of the feed being identical to heating temperature.

Pure oxides and oxide-supported catalysts were tested in N_2 OCM feed. The feed gas was continuously dosed at a composition of CH_4:O_2:N_2 ~ 26:15:59 mol% (methane and synthetic air as oxygen source) with a total gas flow rate of 102.2 mL_{STP} min^{-1}. They were initially heated in the feed gas to 450 °C with a ramping rate of 5 K/min. Thereafter, the temperature was increased in steps of 25 K from 450 °C to 800 °C. Two gas chromatograph (GC) test rounds were performed at each temperature. The time length for each catalyst exposed to each temperature including holding and GC test process was ~ 3 h per testing procedure. Specifically, at 800 °C three GC test rounds were performed. After the final GC test cycle, the reactors were cooled down (5 K/min ramp) to 25 °C in OCM feed. An online-GC was used for monitoring and quantifying O_2, N_2, CO, and CO_2 with a thermal conductivity detector (TCD) and CH_4, C_2H_4, C_2H_6 with a flame ionization detector (FID). N_2 was used as internal standard.

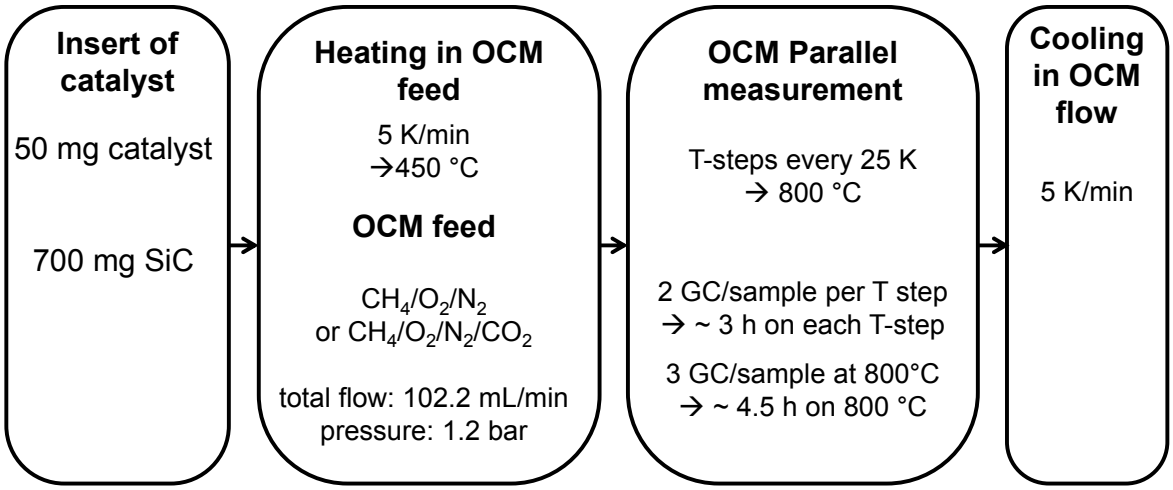

OCM feed	CH_4	O_2	N_2	CO_2
N_2 OCM feed	26 mol%	15 mol%	59 mol%	-
CO_2 OCM feed	26 mol%	15 mol%	3 mol%	56 mol%

Fig. 4.2 OCM test procedure and OCM feed composition used in this study.

In addition, OCM performance of Al_2O_3-supported catalysts were tested by utilizing identical amount of catalysts, feed composition, flow rate per channel and reaction temperature range (details shown in [139]). Their performance would be compared to other oxide-supported catalysts in order to answer the question proposed in section 1.5.2 about performance difference between “Inert-supported” and “Carbonate-supported” group.

Pure carbonates and carbonate-supported catalysts were independently tested in N_2 or CO_2 OCM feed by the same test procedure. N_2 was used as diluent in the “N_2 OCM feed”. In the “CO_2 OCM feed”, N_2 was almost totally replaced by CO_2. A low concentration of N_2 was necessary to be a reference for conversion and yield calculation. The composition of N_2 and CO_2 OCM feed are given on the bottom line in Fig. 4.2.

The CH_4 conversion, O_4 conversion, C_2 selectivity and yield were calculated on the basis of feed using peak areas of a FID (CH_4, C_2H_6, C_2H_4) and a TCD (O_2, N_2), as shown in Equation 2.1, 2.2, 2.3 and 2.4 in section 2.1.3.

4.2. Oxide-supported carbonate catalysts

4.2.1. Pure oxide support

OCM performance of pure oxides support was firstly plotted in Fig. 4.3 to illustrate the effect of pure support independently. Gd_2O_3, Sm_2O_3 and Y_2O_3 exhibit similar temperature-dependent CH_4 and O_2 conversion trend to Al_2O_3. They are significantly active (X_{CH4}: 25% ~ 35%) at typical OCM temperature. But Al_2O_3 exhibits lower C_2 yield, although it reaches as high O_2 and CH_4 conversion as Gd_2O_3, Sm_2O_3 and Y_2O_3. This reveals that Al_2O_3 support is active but not selective because it facilitates the combustion reaction, which is in agreement with the previous report.[188, 189]

CeO_2 shows lowest CH_4 activation ability among all oxides. Similar observation was previously reported for pure CeO_2 [74] and CeO_2 pre-coated SiO_2-Al_2O_3 support[131]. The lower basicity is considered to be the reason for worse activity.

SrO and BaO, as highly basic metal oxides, show low O_2 and CH_4 conversion at typical OCM temperature. For pure SrO and BaO in this study, they exist in form of hydroxides before OCM reaction (Fig. A3.4 e and f). But after reaction, carbonates appear as the main crystal phase. Hence it is possible that with increase of reaction temperature, hydroxide tends to form carbonate via interaction with CO_2. The formed carbonate species with high stability may covers active surface as a catalyst poison and consequently deteriorates OCM performance. It was discussed that the OCM activity of $SrCO_3$ or $BaCO_3$ is enhanced through lowering its thermal stability and creating more oxygen species by addition of certain cations.[190] Therefore, strong basicity may be a prerequisite for good catalyst performance, but the accompanying carbonate formation with high stability is viewed as detrimental to catalytic performance.

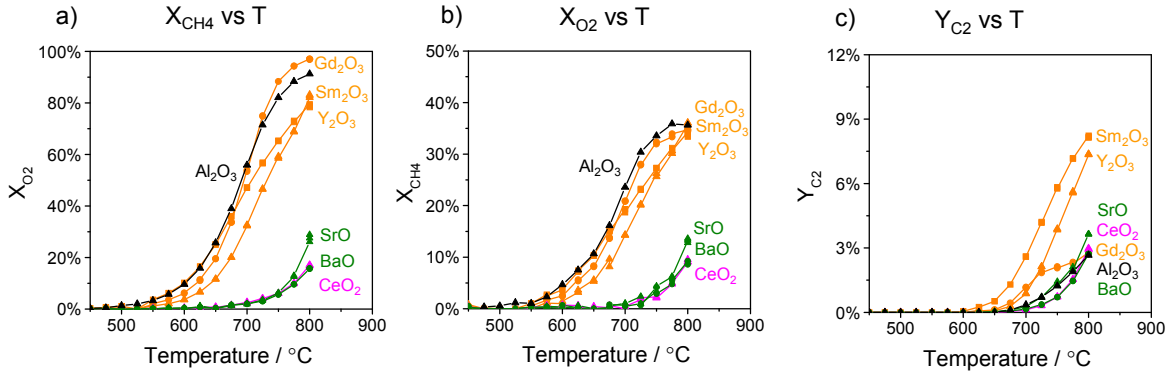

Fig. 4.3: OCM performance in terms of (a) CH_4 conversion, (b) O_2 conversion and (c) C_2 yield for pure oxides. Gd_2O_3, Sm_2O_3, Y_2O_3 as well as Al_2O_3 exhibits higher X_{CH4} and X_{O2} than SrO, BaO and CeO_2. The trend of Y_{C2} mainly follows the trend of X_{CH4} over whole temperature range. Al_2O_3 exhibits fairly lower Y_{C2} than Gd_2O_3, Sm_2O_3 and Y_2O_3, suggesting that Al_2O_3 is not a selective support for OCM reaction.

4.2.2. Oxide-supported carbonate catalysts

Fig. 4.4 depicts OCM performance of oxide-supported catalysts in terms of CH_4 conversion and C_2 yield. The catalysts are labeled with corresponding abbreviation and colors. For instance, Rb_2CO_3 on oxides catalysts group are divided with pink color for Rb-Ce, green color for Rb-Sr and Rb-Ba, orange color for Rb-Sm, Rb-Y and Rb-Gd, and black color for Rb-Al. As shown in Fig. 4.4 a, qualitatively, Rb_2CO_3 on oxides catalysts show similar temperature-dependent trend of CH_4 conversion except Rb-Al. Rb-Al exhibits significant CH_4 conversion at fairly lower temperature (550 °C), whereas other catalysts start to convert CH_4 from 625 °C. The difference of other catalysts becomes more apparent when temperature is above 700 °C. Rb-Sm, Rb-Y and Rb-Gd show higher CH_4 conversion than Rb-Ce, Rb-Sr and Rb-Ba at typical OCM temperatures. O_2 conversion (Fig. A4.1 a) of the catalysts roughly follows the trend of CH_4 conversion. Rb-Al shows fast O_2 conversion until 700 °C when complete O_2 conversion reaches. In addition, similar temperature-dependent CH_4 and O_2 conversion trend were observed for Cs_2CO_3 on oxide catalysts, as shown in Fig. 4.4 c and Fig. A4.1 c.

Fig. 4.4 d and f show C_2 yield of Rb_2CO_3 and Cs_2CO_3 on oxides catalysts. C_2 yield mainly follows the trend of CH_4 conversion except Rb-Al and Cs-Al. Although the latter two catalysts reach fairly higher CH_4 conversion at typical OCM temperatures, they shows medium C_2 yield, revealing that large amount of CH_4 is not selectively converted to C_2 product. This indicates that Al_2O_3 behaves not as selective as other metal oxides as a support, which corresponds with the observation for pure oxide support.

In general, oxide supports strongly influence CH_4 conversion and C_2 yield of oxide-supported catalysts. The variation of performance provides a possibility to explore quantitative correlations between performance and catalyst properties.

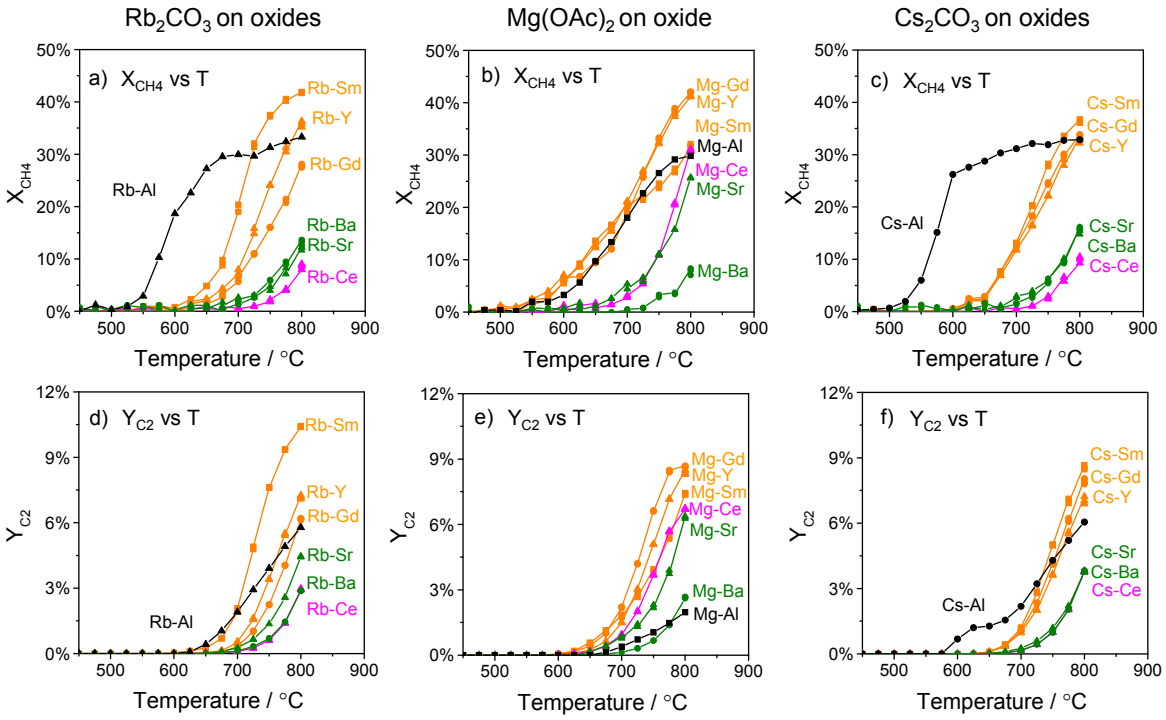

Fig. 4.4: OCM performance in terms of (a, b, c) CH_4 conversion and (d, e, f) C_2 yield for Rb_2CO_3, $Mg(OAc)_2$ and Cs_2CO_3 on oxides vs temperature. Qualitatively, Rb_2CO_3 on oxides catalysts show similar T-dependent trend of CH_4 conversion except Rb-Al. For Rb-Al, CH_4 conversion becomes significant at lower temperature (550 °C) than others and shows fast increase until 700 °C when full O_2 conversion is reached. Besides, C_2 yield of catalysts mainly follows the trend of CH_4 conversion except Rb-Al. Rb-Al does not show fast increase of C_2 yield when CH_4 conversion increases rapidly at the same temperature. This reveals that Rb-Al is not as selective as other metal oxides supported catalysts. Differently, Mg-Al exhibit similar onset of CH_4 conversion compared to other catalysts. And it shows the lowest C_2 yield at 800 °C. Significantly higher CH_4 conversion of Mg-Ce and Mg-Sr are observed at 800 °C, which is comparable to Mg-Gd, Mg-Y and Mg-Sm. Most of catalysts exhibit fairly higher C_2 yield (6%~9%). Cs_2CO_3 on oxide catalysts exhibit similar trend of CH_4 conversion and C_2 yield to Rb_2CO_3 on oxide.

Fig. 4.4 b and e depict CH_4 conversion and C_2 yield of $Mg(OAc)_2$ on oxides catalysts. Different behaviors from Rb_2CO_3 and Cs_2CO_3 on oxides catalysts are observed. Firstly, Mg-Al does not exhibit earlier onset of CH_4 conversion than other catalysts. And it shows the lowest C_2 yield at 800 °C. Secondly, significantly higher CH_4 conversion of Mg-Ce and Mg-Sr are observed at 800 °C, which is comparable to Mg-Gd, Mg-Y and Mg-Sm. Thirdly, most of catalysts (Mg-Gd, Mg-Y, Mg-Sm, Mg-Ce, Mg-Sr) exhibit fairly higher C_2 yield (6% ~ 9%). All these distinct behaviors of catalysts may be related to property of $MgCO_3$ formed as unstable intermediate and decomposed easily, which generates active species playing a dominant role on OCM performance possibly independent of oxides support.

In order to examine the catalytic stability, three GC test rounds were performed for all catalysts at the highest reaction temperature (800 °C). As shown in Fig. 4.4 and Fig. A4.1, all catalysts show stable CH_4, O_2 conversion and C_2 yield at 800 °C without significant decrease. Therefore, it indicates that Rb_2CO_3, Cs_2CO_3 and $Mg(OAc)_2$ on oxides catalysts show well catalytic stability and no obvious deactivation occurs at typical OCM temperature.

Performance-descriptors of $Y_{C2,\ 800\ °C}$ and $Y_{C2,\ 750\ °C}$ from performance data

Herein, C_2 yield, as a compensation of CH_4 conversion and C_2 selectivity, is employed as the performance-descriptor of catalysts. For the extraction of C_2 yield, two temperatures of 800 °C and 750 °C are selected, which are widely accepted as the commonly applied temperatures for OCM tests. Performance-descriptors of $Y_{C2,\ 800\ °C}$ and $Y_{C2,\ 750\ °C}$ of each catalyst are presented in Table 5.1.

4.3. Carbonate-supported carbonate catalysts

In this section, catalytic testing results of $Sm_2(CO_3)_3$ and $SrCO_3$ supported catalysts are presented. Afterwards, performance-descriptors, $Y_{C2,\ 800\ °C}$ and $Y_{C2,\ 750\ °C}$, for each catalyst are generated and presented in Table 5.1.

4.3.1. $Sm_2(CO_3)_3$ supported catalysts

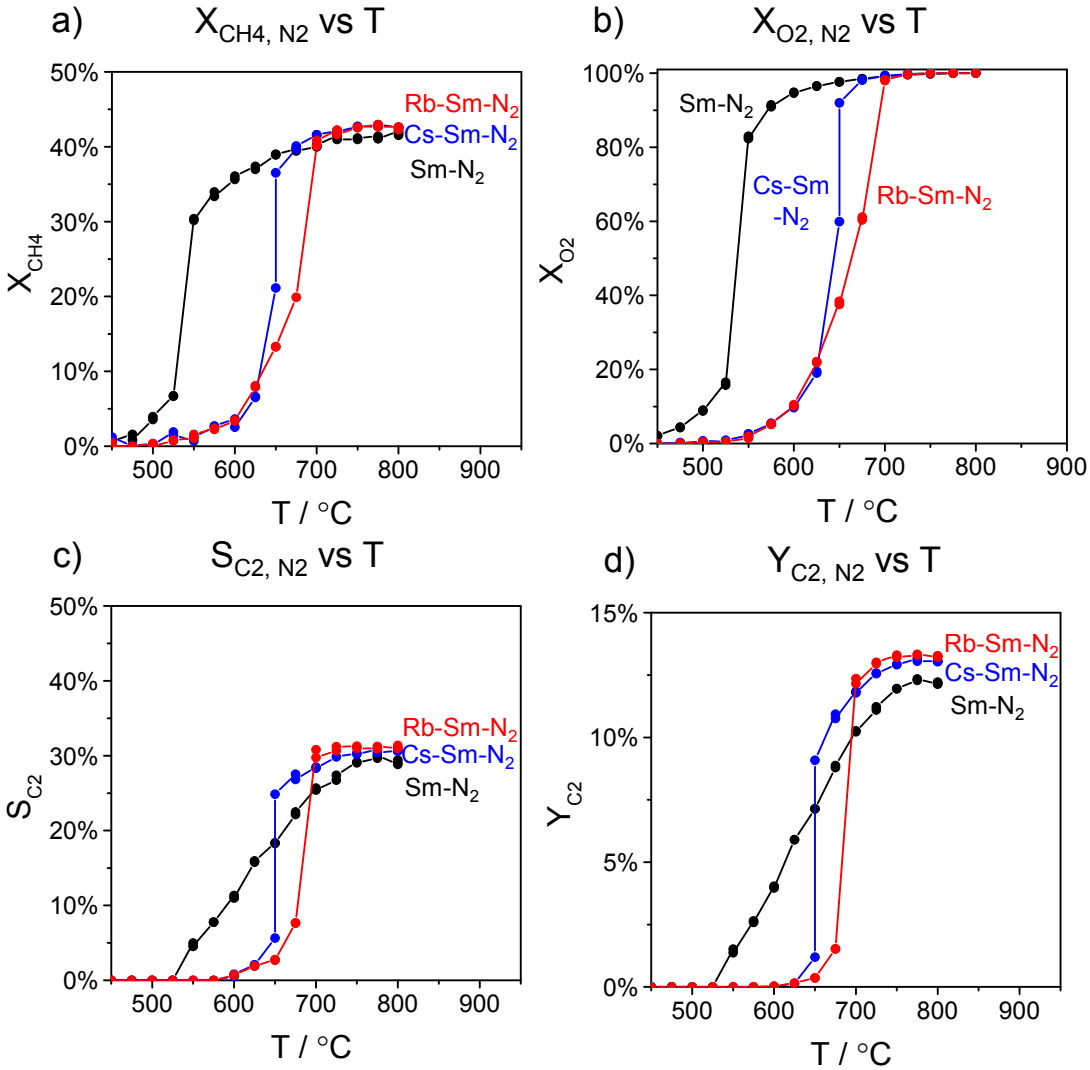

Fig. 4.5: (a) CH_4 conversion, (b) O_2 conversion, (c) C_2 selectivity and (d) C_2 yield of pure $Sm_2(CO_3)_3$, Rb_2CO_3 and Cs_2CO_3 on $Sm_2(CO_3)_3$ catalysts measured in N_2-containing feed. $Sm_2(CO_3)_3$ shows an abrupt CH_4 and O_2 conversion increase from 525 to 550 °C, while Rb_2CO_3 and Cs_2CO_3 on $Sm_2(CO_3)_3$ exhibit similar fast increase at higher temperature (600 °C). C_2 selectivity of $Sm_2(CO_3)_3$ increases steadily and its C_2 yield mainly follows the trend of C_2 selectivity. Rb_2CO_3 and Cs_2CO_3 on $Sm_2(CO_3)_3$ exhibit fast increase of C_2 selectivity when CH_4 conversion increases dramatically. Their C_2 yields follow both trend of CH_4 conversion and C_2 selectivity.

Fig. 4.5 a and b depict X_{CH4} and X_{O2} comparison between pure $Sm_2(CO_3)_3$ and $Sm_2(CO_3)_3$ supported carbonate.

Pure $Sm_2(CO_3)_3$ exhibits a slow X_{CH4} and X_{O2} increase below 525 °C. Considering TGA result shown in Fig. 3.13 a, the observed activity for CH_4 may be derived from $Sm_2O_2CO_3$ intermediate with a small amount of active O species. Surprisingly, it shows an abrupt X_{CH4} and X_{O2} increase from 525 to 550 °C. Around this temperature range, a mass loss step is shown in TGA result (Fig. 3.13 a) that is attributed to decomposition of $Sm_2O_2CO_3$ toward Sm_2O_3. Hence, this decomposition process could be beneficial to enhancing conversion, possibly through active O species released from $Sm_2O_2CO_3$ decomposition. Above 550 °C, X_{CH4} increases continuously but with slower rate until it reaches maximum 41 % at 800 °C because full completion of O_2 is reached.

X_{CH4} and X_{O2} for Rb_2CO_3-$Sm_2(CO_3)_3$ exhibit a shift to higher temperature compared to pure $Sm_2(CO_3)_3$. Decomposition of $Sm_2O_2CO_3$ to Sm_2O_3 around 550 °C is also considered to occur based on TGA result of in Fig. 3.13 b. However, active O species formed by this decomposition process does not give rise to significant enhancement of CH_4 activation. The reason may be that the formed O species tends to be covered by other carbonate species such as Rb_2CO_3 which keeps stable at this temperature. Along with the increase of temperature, X_{CH4} and X_{O2} start to increase dramatically from 600 to 700 °C. Around this temperature range, a sluggish mass loss is shown in TGA result (Fig. 3.13 b) that is caused by CO_3^{2-} transfer effect as discussed in section 3.4.4. CO_3^{2-} species of Rb_2CO_3 tends to migrate from Rb to Sm and decompose at fairly lower temperature. This process would release active O species as well. Therefore, the formed O species achieves to greatly promote CH_4 activation and induces abrupt increase of CH_4 conversion at this temperature region. Finally, Rb_2CO_3-$Sm_2(CO_3)_3$ exhibits a slightly higher X_{CH4} (43% at 800 °C) than pure $Sm_2(CO_3)_3$.

X_{CH4} and X_{O2} for Cs_2CO_3-$Sm_2(CO_3)_3$ exhibit a similar behavior to Rb_2CO_3-$Sm_2(CO_3)_3$. They start to increase abruptly from 600 °C as well. But compared to Rb_2CO_3-$Sm_2(CO_3)_3$, this abrupt increase occurs within a narrower temperature region, 600 ~ 650 °C, corresponding to sluggish mass loss temperature range in TGA (Fig. 3.13 c). This difference may be caused by faster proceeding of CO_3^{2-} species transfer and decomposition process. At highest temperature 800 °C, a similar X_{CH4} for Cs_2CO_3-$Sm_2(CO_3)_3$ is reached compared to Rb_2CO_3-$Sm_2(CO_3)_3$.

Comparison of S_{C2} is shown in Fig. 4.5 c. For pure $Sm_2(CO_3)_3$, there is no obvious C_2 product observed below 525 °C. Afterwards, S_{C2} exhibits a steady increase with the increase of reaction temperature. No abrupt increase is observed over whole temperature region. It suggests that O species formed by decomposition of $Sm_2O_2CO_3$ to Sm_2O_3 behaves very active but only moderately selective. Differently, for Rb_2CO_3 and Cs_2CO_3 on $Sm_2(CO_3)_3$, S_{C2} exhibits an abrupt increase similar to the trend of X_{CH4} at the corresponding temperature region. This may suggests that O species derived from CO_3^{2-} transfer and decomposition could be both highly active and selective, which is different from individual decomposition of single carbonate species.

The comparison of Y_{C2} is shown in Fig. 4.5 d. For pure $Sm_2(CO_3)_3$, Y_{C2} mainly follows the trend of S_{C2}. For Rb_2CO_3 and Cs_2CO_3 on $Sm_2(CO_3)_3$, Y_{C2} follows both trends of X_{CH4} and S_{C2}. At typical OCM temperatures of 750 ~ 800 °C, they exhibit higher Y_{C2} than pure $Sm_2(CO_3)_3$.

4.3.2. $SrCO_3$ supported catalysts

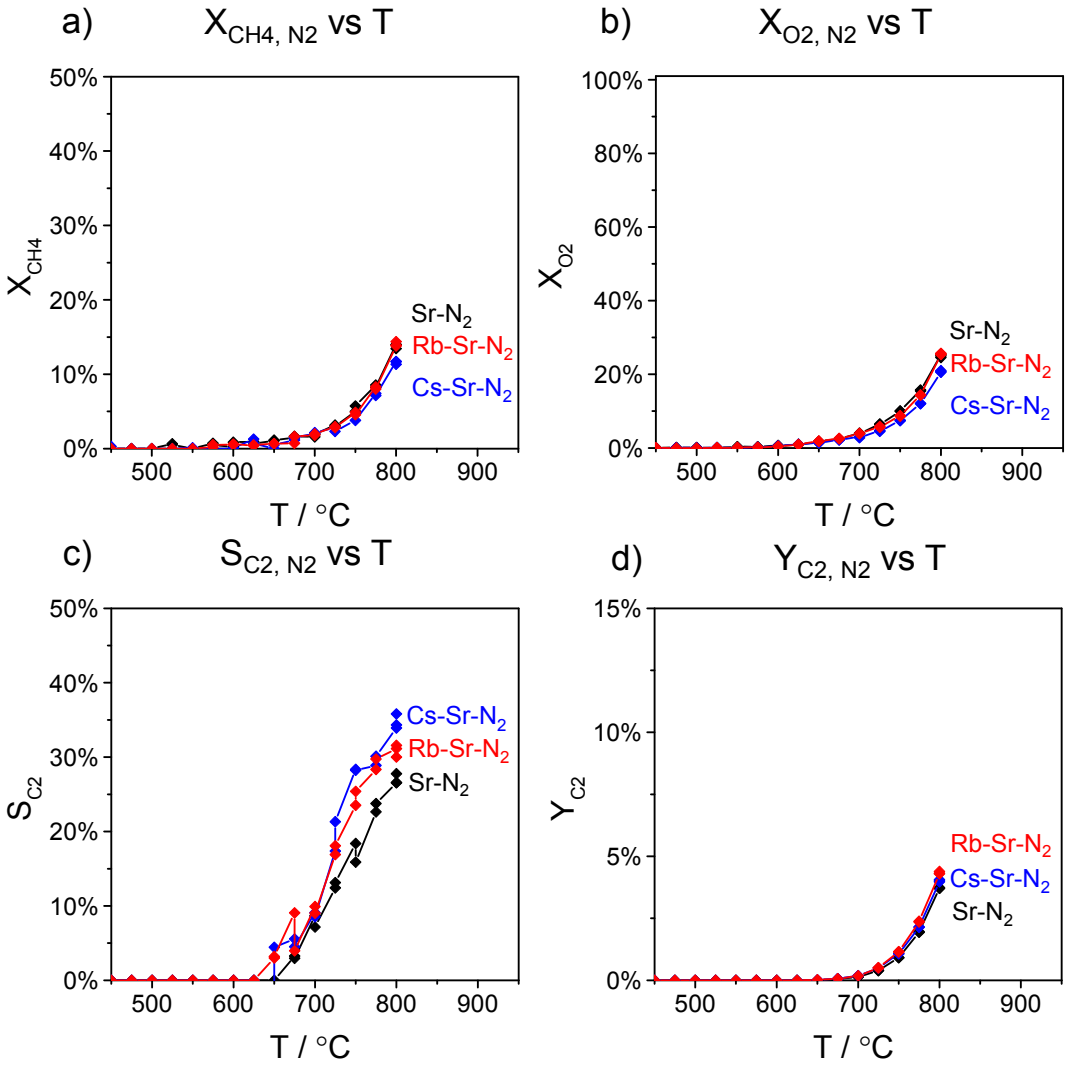

Fig. 4.6: (a) CH_4 conversion, (b) O_2 conversion, (c) C_2 selectivity and (d) C_2 yield of pure $SrCO_3$, Rb_2CO_3 and Cs_2CO_3 on $SrCO_3$ catalysts measured in N_2-containing feed. In general, all samples exhibit low conversion and C_2 yield.

In addition to $Sm_2(CO_3)_3$, $SrCO_3$ with high thermal stability is also employed as the support material. $SrCO_3$ supported catalysts were measured with identical OCM test program in N_2 OCM feed and their catalytic performance is depicted in Fig. 4.6.

Pure $SrCO_3$, Rb_2CO_3 and Cs_2CO_3 on $SrCO_3$ exhibit qualitatively similar temperature-dependent trend of X_{CH4} and X_{O2}. Considering the absolute X_{CH4} and X_{O2} value for these samples are quite low, the effect of blank activity should be considered. As shown in Fig. A4.2, peak area of each species measured by GC for black reactor without any catalysts exhibits no variation during the whole test. No C_2H_6, C_2H_4, CO or CO_2 product is detected by GC. Therefore, any significant increase of OCM performance above zero appearing in catalysts testing is believed to be induced by the addition of catalysts into reactors.

All samples show a steady increase of X_{CH4} and X_{O2} over whole test temperature range (Fig. 4.6 a and b). No abrupt increase can be observed at intermediate temperature region like the behavior of $Sm_2(CO_3)_3$ supported catalysts (Fig. 4.5). At highest temperature 800 °C, they exhibit relatively inferior OCM performance, X_{CH4} < 15% and X_{O2} < 30%, compared to

$Sm_2(CO_3)_3$ supported catalysts at the same temperature. One possible reason is that all existing carbonate species in pure $SrCO_3$, Rb_2CO_3 and Cs_2CO_3 on $SrCO_3$ possess high thermal stability and only extremely less decomposition is able to occur under OCM condition even at 800 °C. As a result, rather low amount of active O species could be formed from carbonate decomposition which is responsible for CH_4 activation.

Although pure $SrCO_3$, Rb_2CO_3 and Cs_2CO_3 on $SrCO_3$ exhibit relatively low conversion CH_4 of and O_2, Fig. 4.6 c depicts that their C_2 selectivity is at medium level, which is comparable to $Sm_2(CO_3)_3$ supported catalysts at corresponding temperature. This suggests that although only rare amount of stable carbonate species tends to decompose at OCM temperature, the formed O species would be rather selective and beneficial for the formation of C_2 product.

However, C_2 yields for all samples are rather low, as shown in Fig. 4.6 d. Because in these cases, C_2 yield is mainly contributed by CH_4 conversion rather than C_2 selectivity. At highest reaction temperature of 800 °C, they exhibit similar Y_{C2} value around 4%.

4.4. Li/MgO and Mn-Na_2WO_4/SiO_2 catalysts

In addition to oxide-supported and carbonate-supported catalysts, typical OCM catalysts, Li/MgO and Mn-Na_2WO_4/SiO_2 were also tested in order to compare with oxide-supported and carbonate-supported catalysts. Afterwards, performance-descriptors, $Y_{C2,\ 800\ °C}$ and $Y_{C2,\ 750\ °C}$, for these reference catalysts are generated and presented in Table 5.1.

Fig. 4.7 depicts temperature dependent OCM performance of two Li/MgO, Mn-Na_2WO_4/SiO_2 and Na_2WO_4/SiO_2 catalysts tested in N_2 OCM feed.

As shown in Fig. 4.7 a and b, both Li/MgO catalysts exhibit earlier onset of CH_4 and O_2 conversion at around 500 °C although no C_2 products are observed at this temperature. The formation of C_2 products starts from 600 °C (Fig. 4.7 c and d) and they exhibit a fast increase until 700 °C when the maximum of CH_4 and O_2 conversion are achieved. At highest reaction temperature 800 °C, they both show fairly high C_2 yield (15.6% for Li/MgO-1 and 11.1% for Li/MgO-2) but with an obvious decrease (about 1%) when holding at this temperature for longer operation time. This observation corresponds with previous report concerning the investigation of deactivation mechanism for Li/MgO catalysts system.[78, 79, 191]

Differently, for Mn-Na_2WO_4/SiO_2 and Na_2WO_4/SiO_2 catalysts, the conversion of CH_4 and O_2 start from around 675 °C (Fig. 4.7 a and b) while C_2 products start to form at 700 °C (Fig. 4.7 c). CH_4 conversion of Mn-Na_2WO_4/SiO_2 is always higher than Na_2WO_4/SiO_2. Their C_2 selectivities become different at typical OCM temperatures when Na_2WO_4/SiO_2 without Mn exhibits a limited selectivity towards C_2 products. At highest reaction temperature 800 °C, Mn-Na_2WO_4/SiO_2 exhibits much higher C_2 yield (16.6%) than Na_2WO_4/SiO_2 (2.9%). Both catalysts show stable catalytic performance at 800 °C without significant deactivation. It is in agreement with the common feature for Mn-Na_2WO_4/SiO_2 catalyst system, which typical exhibits superior stability at high temperature for long operation time.[32, 55, 56]

Therefore, typical OCM catalysts, Li/MgO and Mn-Na_2WO_4/SiO_2 prepared in this study shows remarkable CH_4 conversion, C_2 selectivity and yield. This could be related to the presence of carbonate species at OCM temperatures, as discussed in section 3.5.3. However, Na_2WO_4/SiO_2 inferior catalytic performance at OCM temperatures, probably due to no existence of carbonate species in catalyst at this high temperature.

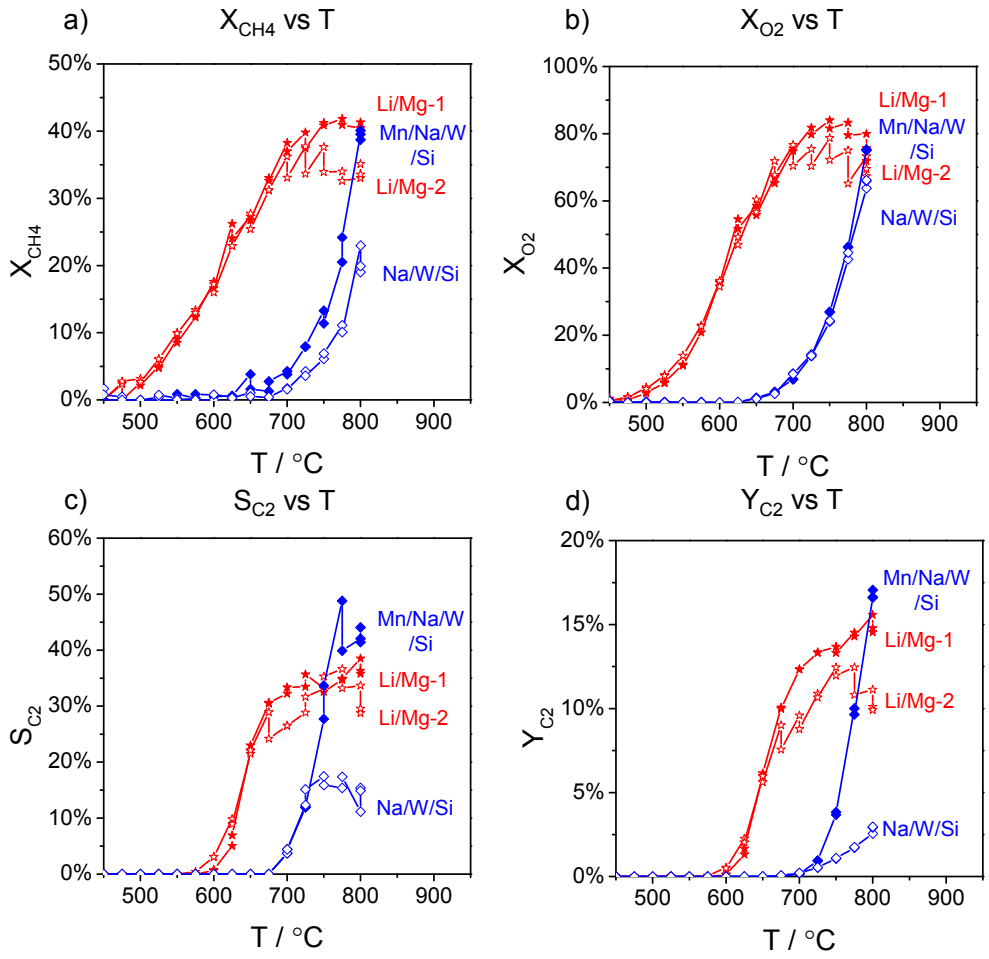

Fig. 4.7: OCM performance in terms of (a) CH_4 conversion, (b) O_2 conversion, (c) C_2 selectivity and (d) C_2 yield for Li/MgO-1, Li/MgO-2, Mn-Na_2WO_4/SiO_2, Na_2WO_4/SiO_2 catalyst.

4.5. Influence of CO_2 in OCM feed on catalytic performance

As discussed in section 3.6, when CO_2 is present in atmosphere, carbonate species exhibits increased thermal stability and could be present at typical OCM temperatures. It is worthwhile to investigate whether the enhanced carbonate stability in catalysts results to variation of catalytic performance. Therefore, pure $Sm_2(CO_3)_3$, Rb_2CO_3 and Cs_2CO_3 on $Sm_2(CO_3)_3$ were also tested in CO_2 containing OCM feed as a comparison. The OCM performance tested in N_2 OCM feed is jointly compared with performance tested in CO_2 OCM feed, as shown in Fig. 4.8.

Qualitatively, when tested in CO_2 OCM feed, pure $Sm_2(CO_3)_3$, Rb_2CO_3 and Cs_2CO_3 on $Sm_2(CO_3)_3$ exhibit consistent shift of X_{CH4} to higher temperature (Fig. 4.8 a). For example, the abrupt increase of CH_4 conversion for $Sm_2(CO_3)_3$ tested in CO_2 feed starts from 575 °C, which is higher than the corresponding value (550 °C) for the same sample tested in N_2 feed. For Rb_2CO_3-$Sm_2(CO_3)_3$ tested in CO_2 feed, the fast increase of X_{CH4} occurs from 725 °C, which is much higher than the corresponding value (600 °C) tested in N_2 feed. Similar shift is also observed for Cs_2CO_3-$Sm_2(CO_3)_3$ from testing in N_2 feed to testing in CO_2 feed. As discussed in section 4.3.1, the abrupt increase of reaction activity could be associated with CO_3^{2-} transfer effect, where CO_3^{2-} species of Rb_2CO_3/Cs_2CO_3 tends to migrate from Rb/Cs to Sm and decompose at lower temperature. As a result, more active O species would be released from this process and are responsible for CH_4 conversion enhancement. But when

the OCM test is conducted in CO_2 feed, all involved carbonate species including Rb, Cs and Sm become more stable, which corresponds with the shift of decomposition steps towards higher temperatures above 750 °C in TGA results tested in CO_2 vs in Ar atmosphere shown in Fig. 3.16. Hence, CO_3^{2-} transfer tends to be delayed and shift to higher temperature as well. The degree of this performance shift could be dependent on the stability of carbonate species existing in catalysts.

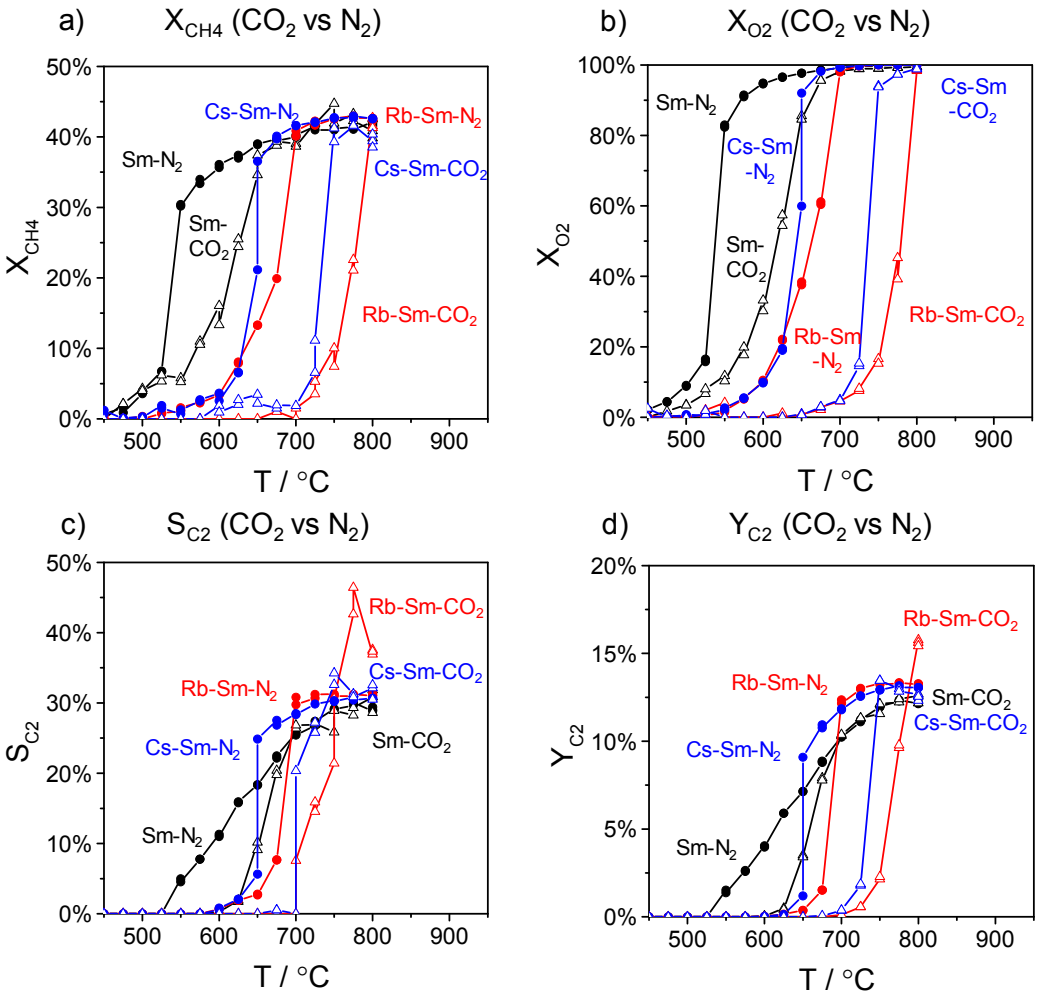

Fig. 4.8: Comparison of (a) CH_4 conversion, (b) O_2 conversion, (c) C_2 selectivity and (d) C_2 yield tested in CO_2 vs in N_2 OCM feed for pure $Sm_2(CO_3)_3$, Rb_2CO_3 and Cs_2CO_3 on $Sm_2(CO_3)_3$ catalysts. All samples exhibit a significant shift of OCM performance when tested in CO_2 OCM feed compared to the one tested in N_2 OCM feed. For Rb_2CO_3-$Sm_2(CO_3)_3$, C_2 yield at 800 °C is improved in CO_2 feed, while $Sm_2(CO_3)_3$ and Cs_2CO_3-$Sm_2(CO_3)_3$ tested in CO_2 feed exhibit no obvious change of C_2 yield at typical OCM temperatures compared to the results in N_2 feed.

As shown in Fig. 4.8 b, $Sm_2(CO_3)_3$, Rb_2CO_3-$Sm_2(CO_3)_3$ and Cs_2CO_3-$Sm_2(CO_3)_3$ catalysts also exhibit consistent shift of O_2 conversion to higher temperature when tested in CO_2 feed, which is similar to the observation for X_{CH4}. They all show nearly full conversion of O_2 at the highest reaction temperature 800 °C.

Fig. 4.8 c depicts the comparison of S_{C2} for catalysts tested in CO_2 feed and N_2 feed. Herein, it is hard to compare C_2 selectivity because these catalysts exhibit inconsistent CH_4 conversion level. Only at 800 °C when nearly same CH_4 conversion is reached for several catalysts, the comparison of C_2 selectivity would be somehow meaningful. Rb_2CO_3-$Sm_2(CO_3)_3$ tested in CO_2 feed exhibits higher C_2 selectivity than the one tested in N_2 feed.

The comparison of C_2 yield is shown in Fig. 4.8 d, representing a combined effect of conversion and selectivity. Not surprisingly, all catalysts exhibit consistent shift of Y_{C2} to higher temperature when tested in CO_2 feed. For Rb_2CO_3-$Sm_2(CO_3)_3$, C_2 yield at 800 °C increases from 13.2% tested in N_2 feed to 15.8% tested in CO_2 feed. This enhancement could be mainly contributed by the improved C_2 selectivity. For $Sm_2(CO_3)_3$ and Cs_2CO_3-$Sm_2(CO_3)_3$, no obvious improvement of C_2 yield is observed at typical OCM temperatures.

In a short summary, pure $Sm_2(CO_3)_3$ and $Sm_2(CO_3)_3$ supported catalysts exhibit a significant shift of OCM performance in terms of CH_4, O_2 conversion and C_2 yield when tested in CO_2 OCM feed compared to N_2 OCM feed. The main effect of CO_2 atmosphere on catalytic performance may be improving C_2 selectivity at typical OCM temperatures. To what extent this beneficial influence on OCM performance is dependent of the stability of carbonate species in catalysts.

4.6. Summary

In this chapter of thesis, OCM catalytic performance of oxide-supported, carbonate-supported as well as selected typical OCM catalysts were tested and compared. Performance-descriptors, $Y_{C2,\ 800\ °C}$ and $Y_{C2,\ 750\ °C}$, were defined and generated from OCM performance data in order to quantitatively describe catalyst performance at typical OCM temperatures. Oxide supports strongly influence CH_4 conversion and C_2 yield of oxide-supported catalysts. Pure carbonate and carbonate-supported catalysts exhibit abrupt increase of performance at intermediate temperature range, where carbonate transfer and decomposition may occur and active oxygen species could be released that is responsible for CH_4 activation. Typical OCM catalysts, Li/MgO and Mn-Na_2WO_4/SiO_2, exhibit remarkable performance possibly related to the presence of carbonate species at OCM temperatures.

When tested in CO_2 OCM feed, pure carbonate and carbonate-supported catalysts exhibit a significant shift of OCM performance to higher temperatures. The main reason may be the delayed decomposition of carbonate species in catalyst which could retain stable at OCM temperatures under CO_2 atmosphere.

Performance-descriptors, $Y_{C2,\ 800\ °C}$ and $Y_{C2,\ 750\ °C}$, would be correlated with property-descriptors derived in chapter 3 and the correlations would be discussed in chapter 5.

5. Correlations between catalyst properties and OCM performance

On one hand, oxide-supported, carbonate-supported catalysts as well as selected typical OCM catalysts were characterized in chapter 3. Property-descriptors are generated from IR or TGA-MS results shown in section 3.3.3 and 3.3.5, in order to demonstrate the certain physico-chemical catalyst properties. On the other hand, OCM performance in terms of CH_4 and O_2 conversion as well as C_2 yield are shown for all catalysts in chapter 4. Performance-descriptors are generated from OCM performance data in order to quantitatively describe catalyst performance at typical OCM temperatures shown in section 4.2.2.

In order to deeply explore the influence of catalyst properties on catalytic performance, it is worthwhile to connect performance-descriptors with property-descriptors in a quantitative fashion and then evaluate the proposed property-performance correlations, in order to testify whether or not the descriptors can reflect a certain kind of physico-chemical catalyst properties which is crucial to OCM reaction.

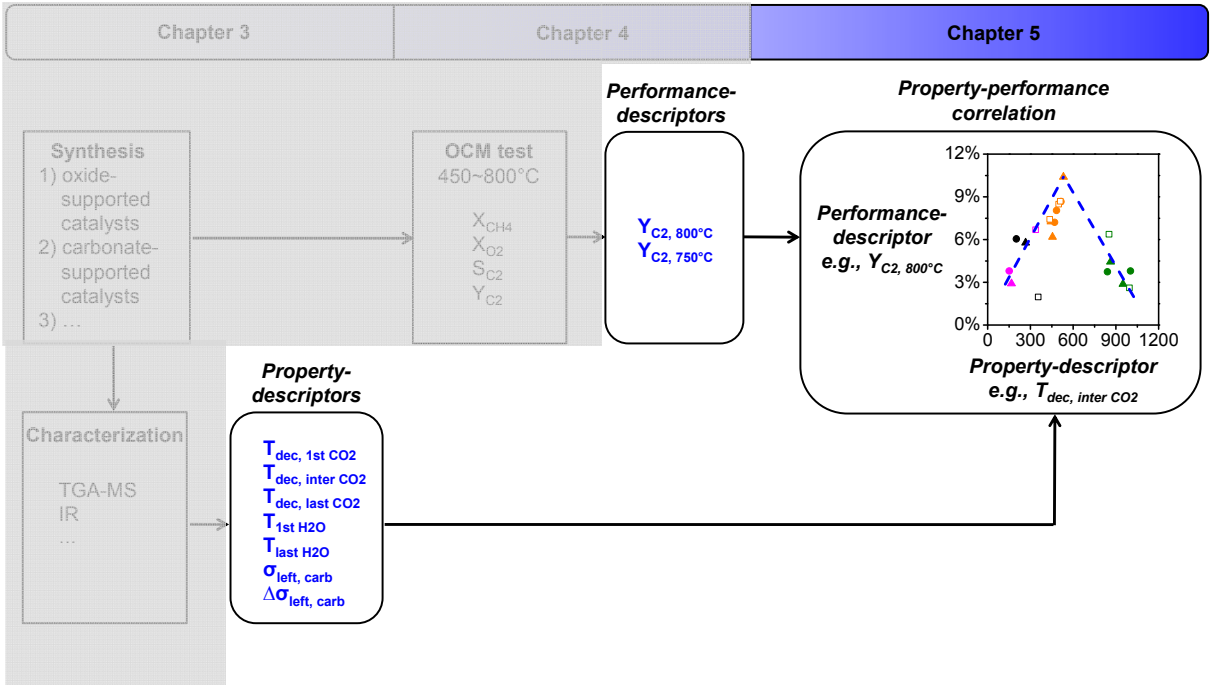

Fig. 5.1 Schematic representation of chapter 5 in this thesis. The goal is to establish and evaluate property-performance correlations.

5.1. Method to establish and evaluate correlations

In this section, the method to establish property-performance correlations by experimental data and subsequent evaluation are presented.

Potential property-descriptors, $T_{dec,\ 1st\ CO2}$, $T_{dec,\ inter\ CO2}$, $T_{dec,\ last\ CO2}$, $T_{1st\ H2O}$, $T_{last\ H2O}$, $\sigma_{left,\ carb}$ and $\Delta\sigma_{left,\ carb}$, are generated from TGA-MS and IR results, while performance-descriptors, $Y_{C2,\ 800\ °C}$ and $Y_{C2,\ 750\ °C}$, are derived from OCM performance data. All of these descriptors are summarized in Table 5.1. Subsequently, property-performance correlations are established in a quantitative fashion by using property-descriptor as x-axis value and performance-descriptors as y-axis value.

In order to evaluate the quality of these property-performance correlations, a preliminary analysis of linear regression is conducted for each proposed correlation. This analysis indicates the quality of fitting between regression line and experimental data. If the quality of

fitting is sufficiently high, it can be concluded that the proposed property-performance correlation is convincible. In other words, the descriptor is capable of reflecting a certain kind of physico-chemical catalyst properties which is crucial to OCM reaction. Residual sum of squares (RSS) is employed as a criterion in comparison of the fitting regression in a universal fashion. The mathematic definition of RSS is the sum of the square of the vertical deviations from each data point to the fitting regression line, as shown in Equation 5.1.

$$RSS = \sum_{i=1}^{n}[y_i - (a + bx_i)]^2 \qquad (5.1)$$

where *a* and *b* is the intercept and slope value of the linear regression fitting, respectively. This RSS parameter is useful to decide whether the fitted regression line is a good fit or not for the dataset. Generally speaking, the smaller the RSS, the better of regression line fits with the data. Two postulations are incorporated into the linear regression fitting. One is the regression line is forced to pass through the data point with highest y-axis value (Rb-Sm). The other is linear regression fitting is separately conducted in two regions, assumed that all data points with lower x-axis value than Rb-Sm are assigned to the left region while the points with higher x-axis value than Rb-Sm to the right region. Afterwards, each regression fitting analysis provides values of RSS, RSS_{left} and RSS_{right}, and the sum of both RSS values are shown in each property-performance correlation plot as the criterion value to compare in between quantitatively.

By comparing RSS values in between, the quality of each linear correlation is revealed and therefore, whether or not the defined property-descriptor is proper to represent a certain catalyst property responsible for OCM performance would be presented. In addition, the concept of defined descriptors is also extended to Li/MgO and Mn-Na_2WO_4/SiO_2 catalysts, in order to check if the established correlations are valid for typical OCM catalysts or not.

Table 5.1 Summary information of all studied catalysts, including BET surface area before and after OCM, property-descriptors ($T_{dec,\ 1st\ CO2}$, $T_{dec,\ inter\ CO2}$, $T_{dec,\ last\ CO2}$, $T_{dec,\ 1st\ H2O}$, $T_{dec,\ last\ H2O}$, $\sigma_{left,\ carb}$, $\Delta\sigma_{left,\ carb}$) values and performance-descriptors ($Y_{C2,\ 800\ °C}$ and $Y_{C2,\ 750\ °C}$) values. [a] 1 wt% Li to MgO. [b] 2 wt% Mn and 5 wt% Na_2WO_4 to SiO_2.[c] TGA-MS was measured in Ar atmosphere and OCM performance was tested in N_2 OCM feed. [d] TGA-MS was measured in CO_2 atmosphere and OCM performance was tested in CO_2 OCM feed.

Composition	Precursor + Support	$metal_{impre}$ /$metal_{supp}$	A_{BET} ($m^2\ g^{-1}$)		Potential property-descriptors							Performance-descriptors	
					TGA-MS					FT-IR		OCM	
			before OCM	after OCM	$T_{dec,1st\ CO2}$ (°C)	$T_{dec,inter\ CO2}$ (°C)	$T_{dec,last\ CO2}$ (°C)	$T_{1st\ H2O}$ (°C)	$T_{last\ H2O}$ (°C)	$\sigma_{left,\ carb}$ (cm^{-1})	$\Delta\sigma_{left,\ carb}$ (cm^{-1})	$Y_{C2,\ 800°C}$ (%)	$Y_{C2,\ 750°C}$ (%)
Oxide-supported catalysts													
Rb	pure Rb_2CO_3	n.a.	n.a.	n.a.	926	926	926	82	82	1435	n.a.	n.a.	n.a.
Rb-Y	Rb_2CO_3+Y_2O_3	10 mol%	23.9	21.4	240	445	912	70	240	1485	50	7.3	3.4
Rb-Sm	Rb_2CO_3+Sm_2O_3	10 mol%	49.8	12	532	532	892	60	365	1477	42	10.4	7.6
Rb-Gd	Rb_2CO_3+Gd_2O_3	10 mol%	31.2	5.6	243	455	918	96	243	1484	49	6.2	2.3
Rb-Ce	Rb_2CO_3+CeO_2	10 mol%	21.9	13.2	167	167	883	167	167	1618	183	2.9	0.6
Rb-Sr	Rb_2CO_3+SrO	10 mol%	31.5	24.2	863	863	863	57	433	1430	-5	4.4	1.4
Rb-Ba	Rb_2CO_3+BaO	10 mol%	2.1	23.6	950	950	950	85	705	1412	-23	2.9	0.7
Rb-Al	Rb_2CO_3+Al_2O_3	10 mol%	52.1	57	266	266	690	85	266	1560	125	5.8	3.9
Mg	pure $Mg(OAc)_2$	n.a.	n.a.	n.a.	345	345	345	74	74	1575	n.a.	n.a.	n.a.
Mg-Y	$Mg(OAc)_2$+Y_2O_3	10 mol%	30.4	22.9	325	498	498	74	325	1563	-12	8.5	5.1
Mg-Sm	$Mg(OAc)_2$+Sm_2O_3	10 mol%	28.4	44.3	317	435	435	71	317	1557	-18	7.4	3.9
Mg-Gd	$Mg(OAc)_2$+Gd_2O_3	10 mol%	17.1	17.7	325	510	510	75	325	1557	-18	8.7	6.6
Mg-Ce	$Mg(OAc)_2$+CeO_2	10 mol%	14	16.6	315	337	337	59	337	1565	-10	6.7	3.7
Mg-Sr	$Mg(OAc)_2$+SrO	10 mol%	35.7	19.8	852	852	852	67	450	1546	-29	6.4	2.3
Mg-Ba	$Mg(OAc)_2$+BaO	10 mol%	16.7	41	995	995	995	106	620	1565	-10	2.6	0.7
Mg-Al	$Mg(OAc)_2$+Al_2O_3	8 mol%	82.2	67.3	308	355	355	58	355	1570	-5	2	1.0
Cs	pure Cs_2CO_3	n.a.	n.a.	n.a.	892	892	892	73	130	1422	n.a.	n.a.	n.a.
Cs-Y	Cs_2CO_3+Y_2O_3	10 mol%	16.7	38.8	385	470	856	76	220	1493	71	7.2	3.7
Cs-Sm	Cs_2CO_3+Sm_2O_3	10 mol%	38.2	14.9	352	515	826	76	352	1471	49	8.7	5.0
Cs-Gd	Cs_2CO_3+Gd_2O_3	10 mol%	22.3	16.9	362	483	835	73	250	1475	53	8	4.2
Cs-Ce	Cs_2CO_3+CeO_2	10 mol%	0.5	17.4	151	151	824	151	151	1615	193	3.8	1.0
Cs-Sr	Cs_2CO_3+SrO	10 mol%	28.2	61.5	841	841	841	56	448	1433	11	3.7	1.2
Cs-Ba	Cs_2CO_3+BaO	10 mol%	32.2	51.7	1002	1002	1002	95	728	1411	-11	3.8	1.0
Cs-Al	Cs_2CO_3+$A_{l2}O_3$	7 mol%	58.2	64.1	201	201	750	76	201	1497	75	6.1	4.3
Carbonate-supported catalysts[c]													
Sm	pure $Sm_2(CO_3)_3$	n.a.	8.2	17.8	348	589	589	77	230	1488	n.a.	12.1	12.0
Rb-Sm	Rb_2CO_3+$Sm_2(CO_3)_3$	10 mol%	16.8	33.7	252	560	885	70	252	1488	0	13.2	13.3
Cs-Sm	Cs_2CO_3+$Sm_2(CO_3)_3$	10 mol%	13.1	21.7	244	564	817	71	243	1487	-1	13.1	13.0
Sr	pure $SrCO_3$	n.a.	35.1	28.5	937	937	937	n.a.	n.a.	1433	n.a.	3.7	0.9
Rb-Sr	Rb_2CO_3+$SrCO_3$	10 mol%	15.3	27.3	932	932	932	110	110	1431	-2	4.3	1.1
Cs-Sr	Cs_2CO_3+$SrCO_3$	10 mol%	13.5	47.7	933	933	933	106	106	1432	-1	4.0	1.1
Reference catalysts													
Li/MgO-1	Li_2CO_3+MgO	1 wt%[a]	91.5	23.6	270	555	690	64	270	1432	-54	15.6	13.7
Li/MgO-2	$LiNO_3$, $Mg(NO_3)_2$	1 wt%[a]	37.5	27.9	251	538	796	64	251	1487	1	11.1	12.5
Mn-Na_2WO_4/SiO_2	$Mn(NO_3)_2$, Na_2WO_4+SiO_2	2 wt%Mn 5 wt%Na_2WO_4[b]	16.8	14.9	356	542	855	230	855	1628	204	16.6	3.7
Na_2WO_4/SiO_2	$Mn(NO_3)_2$+SiO_2	2 wt%Mn[b]	46.5	3.5	354	354	354	220	220	1623	199	2.6	1.1
Carbonate-supported catalysts tested in CO_2[d]													
Sm	pure $Sm_2(CO_3)_3$	n.a.	8.2	18.0	332	756	756	60	221	1488	n.a.	12.6	11.6
Rb-Sm	Rb_2CO_3+$Sm_2(CO_3)_3$	10 mol%	16.8	30.5	308	788	1020	68	233	1488	0	15.8	2.2
Cs-Sm	Cs_2CO_3+$Sm_2(CO_3)_3$	10 mol%	13.1	20.5	300	792	980	70	230	1487	-1	12.7	13.5

5.2. Correlation between performance and carbonate stability

CO_2 is commonly generated as a by-product along with OCM reaction. In the literature, the effect of CO_2 on catalytic process is controversial. CO_2 is often regarded as a catalyst poison, as it adsorbs on strongly basic sites of catalyst responsible for CH_4 activation.[40] A decreased CH_4 conversion is observed for different catalysts containing basic oxides.[157, 159] However, a beneficial effect of CO_2 on C_2 selectivity has also been reported in literature.[156, 159] Although the role of CO_2 is ambiguous, one point is clear. When catalysts containing metal oxides are exposed to OCM reaction temperature and atmosphere, the by-product CO_2 has possibility to

contact with metal oxides, which leads to formation of carbonate species and subsequently plays a role in its decomposition in the catalysts. Property-descriptors from TGA-MS results, $T_{dec,\ 1st\ CO2}$, $T_{dec,\ inter\ CO2}$, $T_{dec,\ last\ CO2}$, are introduced and generated as shown in Fig. 3.7, which are decomposition temperature of carbonate based on the first, intermediate and last CO_2 product evolution. The underlying concept of $T_{dec,\ 1st\ CO2}$, $T_{dec,\ inter\ CO2}$, $T_{dec,\ last\ CO2}$ is to reflect different thermal stability of carbonate in a quantitative way by the consideration of CO_2 product, which makes it feasible to seek for the correlation between carbonate thermal stability and OCM performance.

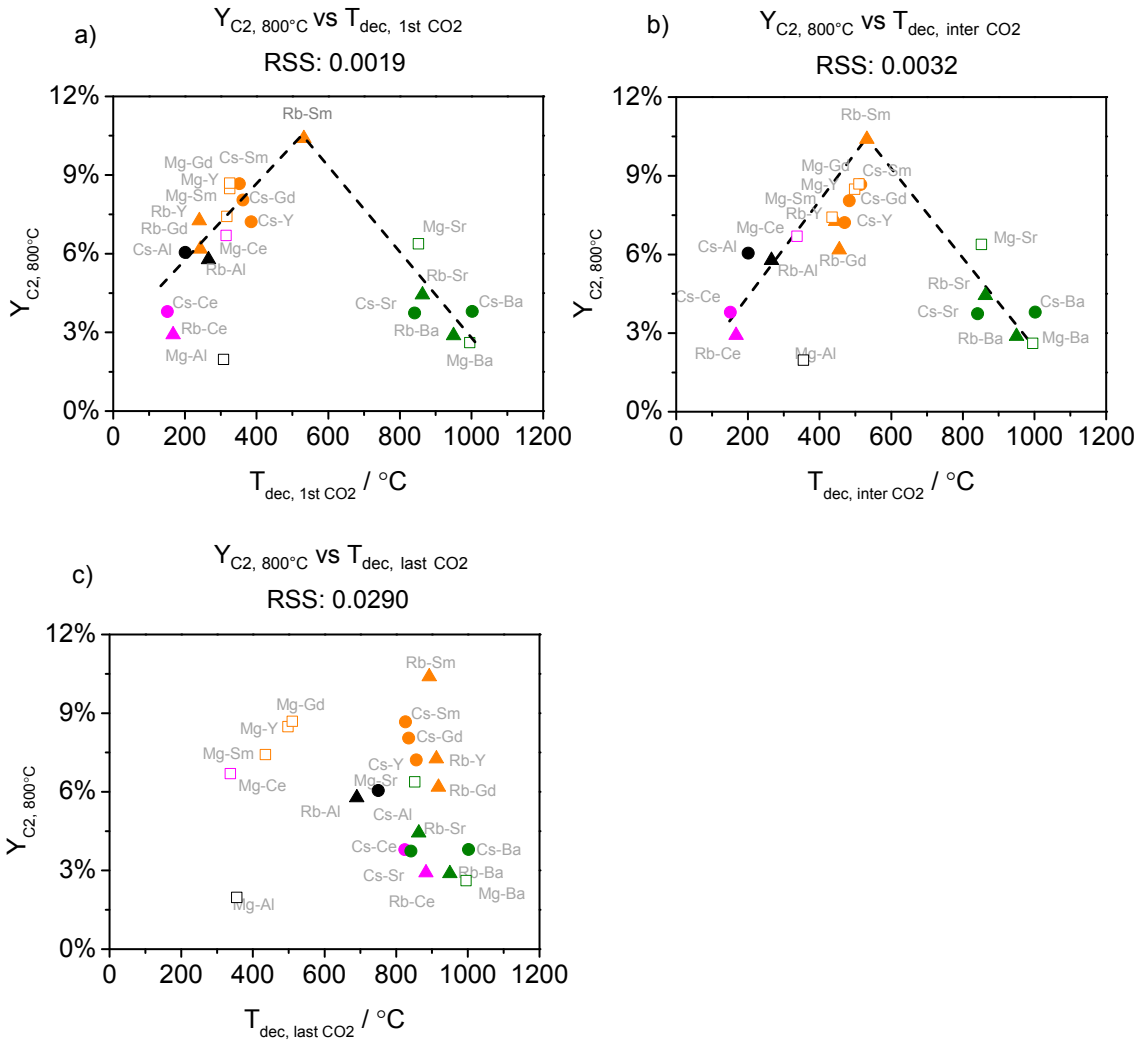

Fig. 5.2: Correlation between C_2 yield at 800 °C and (a) $T_{dec,\ 1st\ CO2}$, (b) $T_{dec,\ inter\ CO2}$ or (c) $T_{dec,\ last\ CO2}$ of Rb_2CO_3 (triangle), Cs_2CO_3 (dot) and $Mg(OAc)_2$ (square) on Y_2O_3, Sm_2O_3 and Gd_2O_3 (orange), CeO_2 (pink), SrO and BaO (green), Al_2O_3 (black). A volcano-like correlation between C_2 yield and $T_{dec,\ 1st\ CO2}$ can be observed. The correlation between C_2 yield and $T_{dec,\ inter\ CO2}$ also shows volcano-like trend but is more convincible because more points shifts to the intermediate temperature range and the entire trend is established on a series of more dispersive data. Differently, there is no simple correlation between C_2 yield and $T_{dec,\ last\ CO2}$ in general.

Fig. 5.2 a depicts that correlation between C_2 yield at 800 °C and $T_{dec,\ 1st\ CO2}$. Interestingly, C_2 yield increases and then decreases with the increase of $T_{dec,\ 1st\ CO2}$. The trend is also observed when C_2 yield at 750 °C is employed to correlate with $T_{dec,\ 1st\ CO2}$, as shown in Fig. A5.1 a. To our knowledge, it is the first time to report the “volcano-like” correlation between OCM catalytic performance and catalyst properties in a quantitative fashion. One weakness of the obtained correlation is that there are too many data points locating at x-axis range 200 to 400 °C, which may degrade the reliability of the established trend. Nevertheless, the

"volcano-like" correlation between C_2 yield at 800 °C and $T_{dec,\ inter\ CO2}$ (Fig. 5.2 b) is considered to be more convincible because more points shifts to the intermediate temperature range and the entire trend is established on a series of more dispersive data. The trend is also observed when C_2 yield at 750 °C is employed to correlate with $T_{dec,\ inter\ CO2}$, as shown in Fig. A5.1 b.

RSS values obtained from linear regression analysis are relatively small for proposed property-performance correlations using $T_{dec,\ 1st\ CO2}$ and $T_{dec,\ inter\ CO2}$ as property-descriptor, revealing a good quality of fitting between regression line and experimental data. Hence, it can be concluded that these established property-performance correlations are convincible.

For Rb_2CO_3 and Cs_2CO_3 on oxides catalysts, oxides support is able to form carbonate through CO_3^{2-} species transfer from alkali carbonate. This behavior can be also considered as an ability of oxide cations to take CO_3^{2-} species from stable alkali carbonate and subsequently decompose at relatively low temperature. For example, Ce cation captures carbonate species and forms carbonate which decomposes at very low temperature, while C_2 yield of Rb_2CO_3-CeO_2 and Cs_2CO_3-CeO_2 are relatively lower. Y, Sm and Gd cations tend to form carbonate with intermediate stability and the corresponding catalysts on these support exhibit higher C_2 yield. Sr and Ba cations are likely to form highly stable carbonate, and C_2 yield of the respective supported catalysts is also relatively lower. But for $Mg(OAc)_2$-oxides catalysts, Ce, Y, Sm and Gd cations are not preferred to capture carbonate species with subsequent decomposition because $MgCO_3$ itself is easier to decomposes due to its lower stability. In contrast, Sr and Ba cations are still apt to capture carbonate species and form highly stable forms, which may be related to their high basicity. In addition, $Mg(OAc)_2$-Al_2O_3 seems to be an outlier. MgAl layered double hydroxides (LDHs) may form in this case, with some carbonate as main charge-balancing anions and interlayer species.[192, 193] This substance is beyond our discussion based on typical carbonate species. Therefore, the performance of $Mg(OAc)_2$-Al_2O_3 could not well fit with the trajectory established on basis of carbonate.

Fig. 5.2 c shows the correlation between C_2 yield at 800 °C and $T_{dec,\ last\ CO2}$. Differently, there is no simple correlation observed in general. Rb_2CO_3 on different oxides, for example, exhibit similar $T_{dec,\ last\ CO2}$ but distinct C_2 yield. Rb_2CO_3-Al_2O_3 with fairly lower $T_{dec,\ last\ CO2}$ shows medium C_2 yield. This also occurs for Cs_2CO_3 on oxide catalysts. It is even more randomly distributed for $Mg(OAc)_2$-oxides catalysts. When the OCM performance in terms of C_2 yield at 750 °C is considered, there is still no simple correlation observed as shown in Fig. A5.1 c. Meanwhile, RSS values are relatively large for assumed property-performance correlations using $T_{dec,\ last\ CO2}$ as property-descriptor, suggesting a bad quality of fitting between regression line and experimental data.

As discussed before, diversified kinds of carbonate species are potential to exist in catalysts. From the observed correlation, it is conclude that carbonate species with intermediate stability would be the dominating factor to have an impact on OCM performance rather than the least and most stable carbonate species in catalysts.

5.3. Correlation between performance and H_2O-relating property

Carbonate stability in terms of $T_{dec,\ 1st\ CO2}$, $T_{dec,\ inter\ CO2}$ and $T_{dec,\ last\ CO2}$ were employed as property-descriptors to connect with OCM catalytic performance. $T_{dec,\ inter\ CO2}$ behaves as a successful one to illustrate a general correlation between catalyst property and performance. In this section, H_2O-relating property-descriptors on the basis of TGA-MS are incorporated

into the correlation and assessed to examine whether they are appropriate descriptors as well.

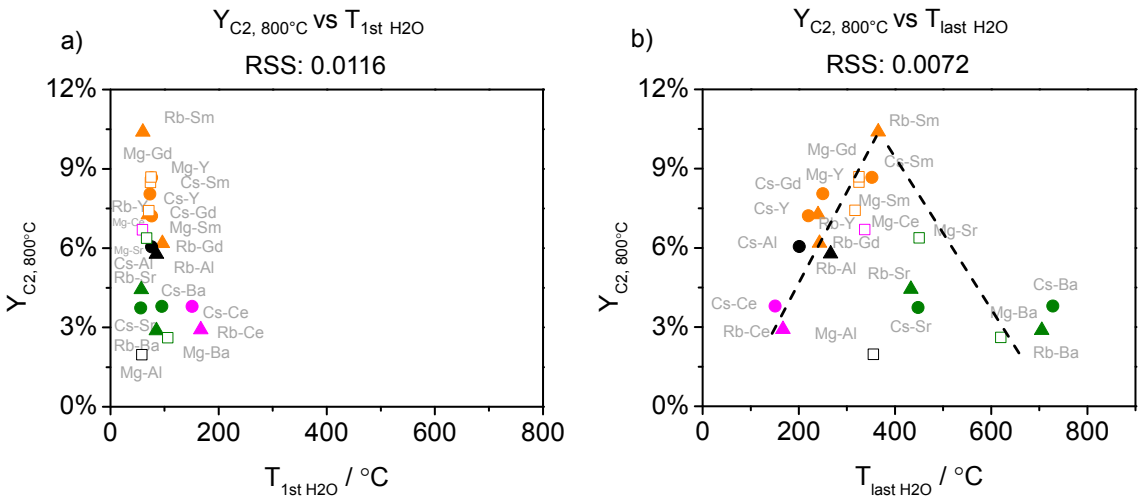

Fig. 5.3: C_2 yield at 800 °C vs. (a) $T_{1st\ H2O}$ or (b) $T_{last\ H2O}$ of Rb_2CO_3 (triangle), Cs_2CO_3 (dot) and $Mg(OAc)_2$ (square) on Y_2O_3, Sm_2O_3 and Gd_2O_3 (orange), CeO_2 (pink), SrO and BaO (green) and Al_2O_3 (black). No simple correlation is observed between C_2 yield and $T_{1st\ H2O}$ in general. A volcano-like correlation could be observed between C_2 yield and $T_{last\ H2O}$.

H_2O-relating descriptors from TGA-MS results, $T_{1st\ H2O}$ and $T_{last\ H2O}$, are introduced and generated as shown in Fig. 3.9. Afterwards, C_2 yield at 800 °C is correlated with $T_{1st\ H2O}$ and $T_{last\ H2O}$, respectively. Note that the temperature range showing in x-axis is amplified and not as large as the range in Fig. 5.2. This modification guarantees that all data points could be well distributed in the presented plot.

As shown in Fig. 5.3 a, there is no simple correlation observed between C_2 yield at 800 °C and $T_{1st\ H2O}$ in general. When C_2 yield at 750 °C is employed, there is still no simple correlation observed (Fig. A5.2 a). Meanwhile, RSS values are relatively large for assumed property-performance correlations using $T_{1st\ H2O}$ as property-descriptor, indicating a bad quality of fitting between regression line and experimental data.

Fig. 5.3 b shows the correlation between C_2 yield at 800 °C and $T_{last\ H2O}$. C_2 yield of catalysts seems to firstly increase and afterwards decrease with $T_{last\ H2O}$. This correlation is similar to the observed trend between C_2 yield and $T_{dec,\ 1st\ CO2}$ (Fig. 5.2 a). RSS value obtained from linear regression analysis is relatively small for proposed property-performance correlations using $T_{last\ H2O}$ as property-descriptor. It reflects a good quality of fitting between regression line and experimental data.

In fact, both $T_{last\ H2O}$ and $T_{dec,\ 1st\ CO2}$ exhibits variation dependent on the oxide support. Especially for some rare earth oxide supported carbonate, these two parameters are quite similar or even identical when they are employed to describe the decomposition behavior of the same carbonate. Take Rb_2CO_3-Y_2O_3 as an example, (Fig. 3.7 a and Fig. 3.9 a), mass loss step from 200 to 300 °C is observed where the last H_2O and first CO_2 evolves simultaneously from the sample, which is in agreement with the previous report of yttrium carbonate hydrate thermolysis.[194] $T_{last\ H2O}$ and $T_{dec,\ 1st\ CO2}$ for Rb_2CO_3-Y_2O_3 derived from TGA-MS results are thus identical. Hence, it is not surprising that the observed correlation between C_2 yield at 800 °C and $T_{last\ H2O}$ exhibits similarity to the correlation when $T_{dec,\ 1st\ CO2}$ is employed.

The observed correlation between OCM performance and the H_2O-relating descriptor may be also explained from both positive and negative contribution of H_2O. Considering that H abstraction of CH_4 occurs on active oxygen species and hydroxyl group forms as a result, H_2O tends to form with two adjacent hydroxyl group and escape from the catalysts surface when a certain temperature reaches. As a result, this process leaves an oxygen vacancy involved in oxygen activation and active oxygen species regeneration.[38, 40] Hence, the ability of H_2O removal could in a way describe the capability of active oxygen species regeneration. This may explain why SrO and BaO supported catalysts with high $T_{last\ H2O}$ exhibited low C_2 yield. Because $Sr(OH)_2$ and $Ba(OH)_2$ are too stable and H_2O could not be easily removed from their decomposition process. On the other hand, H_2O and the corresponding hydroxyl or hydroxide are also claimed to be beneficial to OCM reaction in some papers. Zahrani et al.[195] reported a long-term increase of CH_4 conversion when the Li/MgO catalyst was treated with liquid H_2O under reactions. They proposed that H_2O reacts with the relatively inactive Li_2CO_3 to form Li^+OH^- at a local low temperature region and subsequently the formed Li^+OH^- decomposes stepwise with the participation of O_2 and generate active site Li^+O^-. Similarly, Dooley et al.[174] found enhancement of both activity and selectivity with the increase of H_2O content in H_2O-containing feed. They attributed such behavior to an active phase or surface based on a hydroxide or adsorbed H_2O.

5.4. Correlation between performance and IR bond position

One of the carbonate properties, thermal stability, was evaluated with TGA-MS for all catalysts and various decomposition temperatures were derived based on CO_2 or H_2O as the descriptor rule. In addition, carbonate in catalysts also exhibit significant vibrational behaviour in FT-IR spectra shown in Fig. 3.3. Property-descriptors, $\sigma_{left,\ carb}$ and $\Delta\sigma_{left,\ carb}$, from IR results are introduced and generated as shown in Fig. 3.4. In general, they represent vibrational characters of carbonate species in catalysts and the effect of oxide cation on impregnated carbonate species.

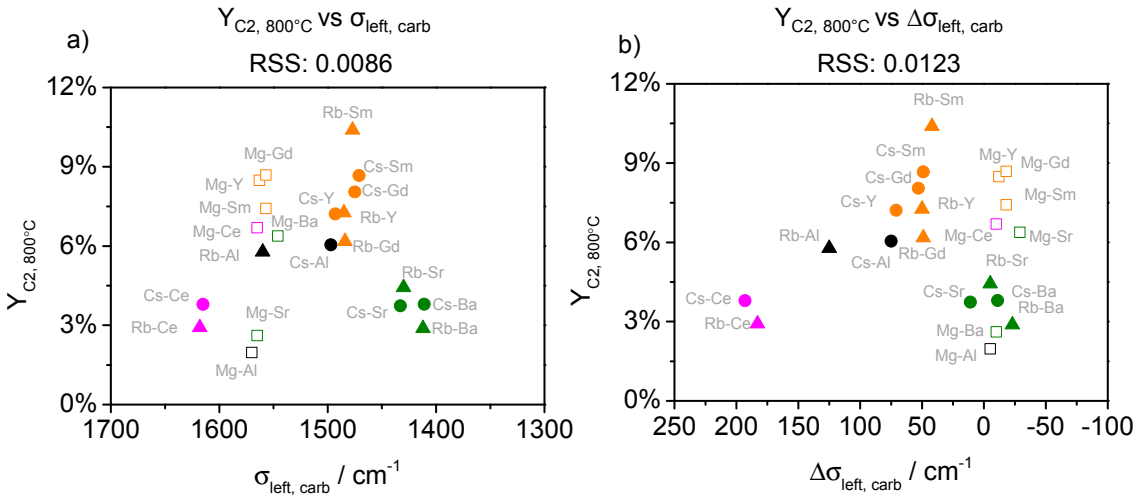

Fig. 5.4: C_2 yield at 800 °C vs. (a) $\sigma_{left,\ carb}$ or (b) $\Delta\sigma_{left,\ carb}$ of Rb_2CO_3 (triangle), Cs_2CO_3 (dot) and $Mg(OAc)_2$ (square) on Y_2O_3, Sm_2O_3 and Gd_2O_3 (orange), CeO_2 (pink), SrO and BaO (green) and Al_2O_3 (black). In general, no significant correlations can be observed between C_2 yield and the descriptor of $\sigma_{left,\ carb}$ or $\Delta\sigma_{left,\ carb}$.

C_2 yield at 800 °C is firstly correlated with $\sigma_{left,\ carb}$, as shown in Fig. 5.4 a. In general, no significant correlation is observed. When the OCM performance in terms of C_2 yield at 750 °C is considered, there is still no simple correlation observed as shown in Fig. A5.3 a. One

possible reason for the poor correlation could be that $\sigma_{left,\ carb}$ stands for the characteristics of CO_3^{2-} species present in the fresh catalysts. The CO_3^{2-} species, especially the ones with low and intermediate stability, tends to decomposes during OCM reaction and is unable to return back to the initial state. Therefore, it is difficult to establish a strong correlation on the basis of a parameter for the initial CO_3^{2-} species but with irreversible changes in the practical reaction conditions.

As shown in Fig. 5.4 b, C_2 yield at 800 °C is then correlated with $\Delta\sigma_{left,\ carb}$. Similarly to the above case with $\sigma_{left,\ carb}$ descriptor, no simple correlation could be found. One reason could be that is $\Delta\sigma_{left,\ carb}$ based on IR measurement of fresh catalysts, which is insufficient to well evaluate the actual reaction as discussed above. Another possible reason may be the effect of oxide support on carbonate species could not be simply expressed by $\Delta\sigma_{left,\ carb}$. The peak shift is also manipulated by the coordination state between CO_3^{2-} and the cation, exhibiting mono-, bi- or poly-dentate forms, which is much more complicated than our postulated situation. The details concerning this point will be discussed in section 6.1.

5.5. Discussion on descriptors

The complex OCM reaction network contains a large body of probable elementary chemical reactions, which makes the comprehensive OCM mechanism still not totally understood yet. No agreement on reaction mechanism also impedes to elucidate the nature of active species in a catalyst. In consequence, it is a great challenge to design an optimal OCM catalyst for further improvement of catalytic performance without solid knowledge of fundamental reaction mechanism and active species. One promising key to cope with this challenging task is to seek for appropriate descriptors that are able to bridge the physico-chemical properties of catalysts with their behavior in actual reaction.

The descriptor of simple elemental composition is not sufficient to explain the complex catalytic OCM reaction.[69] In this thesis, property-descriptors about physico-chemical properties of catalysts are introduced and consistently derived from characterization results (FT-IR and TGA-MS), which are typically more powerful and chemically meaningful than only elemental composition as the descriptor. The experimentally derived descriptors could reflect the realistic properties of catalysts and connect with catalytic performance in a more convincible fashion.

The results of linear regression assessment reveal that the smaller the distance between descriptors and the actual reaction condition is, the more realistic correlation between catalyst properties and OCM performance descriptors can reflect (see Fig. A5.4). Descriptors derived from IR to TGA-MS (H_2O-relating) and finally TGA-MS (CO_2-relating) stepwise approach to the practical reaction condition such as ramping temperature and gas atmosphere. $T_{last\ H2O}$, $T_{dec,\ 1st\ CO2}$ and $T_{dec,\ inter\ CO2}$ perform well among all property-descriptors. The reason is that they already reflect some kind of complex chemical reactivity related to OCM reaction. Convincible volcano-like property-performance correlations can be established by using these descriptors. Furthermore, the CO_2-relating descriptor of $T_{dec,\ inter\ CO2}$ is the best-performing one. Therefore, it can be concluded that carbonate species with intermediate stability in catalysts would be a key factor to influence OCM catalytic performance.

5.6. Carbonate concept extended to typical Li/MgO and Mn-Na_2WO_4/SiO_2 catalysts

Li/MgO and Mn-Na_2WO_4/SiO_2 are two kinds of most frequently studied model catalysts for OCM reaction, which exhibit remarkable conversion and selectivity.[5, 69] For Li/MgO catalyst, the presence of monovalent Li^+ is able to replace divalent Mg^{2+} in the crystal structure, creating Li substitutional defects with a localized electronic hole (so-called [Li^+O^-] center) in consequence, which was proposed to be responsible for CH_4 activation.[38, 71] Differently, for Mn-Na_2WO_4/SiO_2 catalyst, it is much more controversial regarding to the role of each component in reaction. Distorted WO_4 tetrahedron species is proposed by Wu et al.[57] to be responsible for CH_4 activation. Jiang et al.[58] claimed an oxygen spill-over mechanism including a complete redox cycle where activation of CH_4 takes place on W^{6+} sites and the activation of gas phase O_2 on Mn^{3+} sites. Na-O-Mn species was also proposed by Wang et al.[155] to be involved in CH_4 activation. Besides, the transition of SiO_2 from amorphous to crystalline phase was claimed by Palermo et al.[59] to have a positive influence on dispersing and stabilizing active species. Due to the intrinsic complexity in OCM process, the reaction mechanism as well as active species could be diversified for different kinds of catalysts. However, this thesis tried to propose a universal descriptor concerning carbonate stability in catalyst in order to correlate with catalytic performance and further elucidate reaction mechanism.

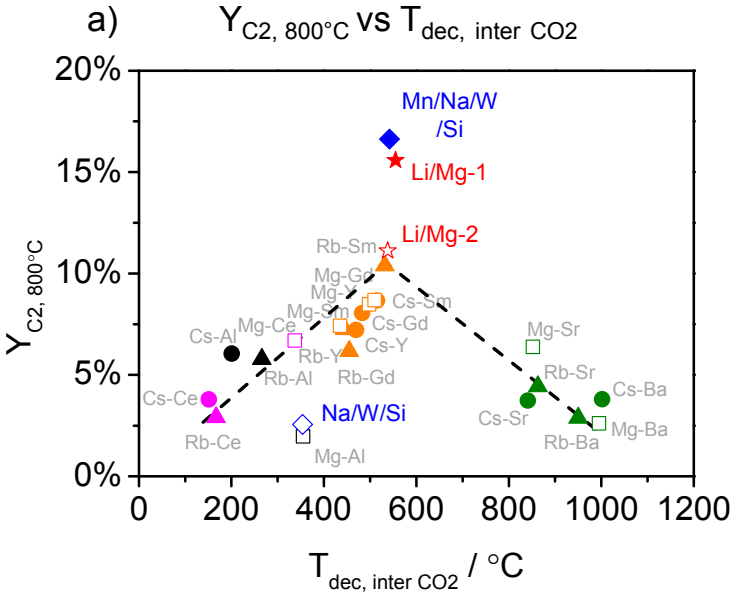

Fig. 5.5: The location of Li/MgO-1 (red solid star), Li/MgO-2 (red hollow star), Mn-Na_2WO_4/SiO_2 (blue solid diamond) and Na_2WO_4/SiO_2 (blue hollow diamond) catalyst in volcano-like correlation between C_2 yield at 800 °C and $T_{dec,\ inter\ CO2}$. In general, these selected typical OCM catalysts are close to the top region of volcano trend established by oxide-supported catalysts. The concept of intermediate carbonate stability could be extended to typical OCM catalysts.

In section 3.5.3, TGA-MS results of both Li/MgO catalysts exhibit unambiguous mass loss the defined intermediate temperature range 400 ~ 550 °C with CO_2 evolution. At this temperature range, Mn-Na_2WO_4/SiO_2 catalyst also shows mass loss with CO_2 releasing. But for Na_2WO_4/SiO_2 catalyst, only an unobvious mass loss with CO_2 evolution at lower temperature (< 400 °C) is found. All these observations could be associated with the decomposition behavior of certain carbonate, where property-descriptor of $T_{dec,\ inter\ CO2}$ is generated for these catalysts. Afterwards, catalytic performance of these typical OCM

catalysts were tested under same reaction conditions as oxide-supported catalysts. Their distinct performance data were already discussed in section 4.4. Herein, C_2 yield at 800 °C is correlated with the derived $T_{dec,\ inter\ CO2}$ for corresponding catalyst in order to examine whether the typical OCM catalysts fit with the established volcano-like correlation concerning carbonate stability.

In general, two carbonate species ($MgCO_3$ and Li_2CO_3) would be present in typical Li/MgO catalyst with distinct thermal stability. Individual $MgCO_3$ tends to decompose at intermediate temperature (469 °C) while independent Li_2CO_3 decomposition would occur at high temperature (720 °C). At typical OCM temperature and atmosphere, CO_3^{2-} species transfer from Li to Mg would occur and an intermediate compound $[\mathrm{Li}^+ \cdots \mathrm{CO}_2^{3-} \cdots \mathrm{Mg}^{2+}]$ may form in catalyst, which is beneficial to improve its reaction activity. Meanwhile, the presence of Li_2CO_3 on catalyst surface at high temperature would contribute to enhancing C_2 selectivity via suppressing unselective oxidation.

For Mn-Na_2WO_4/SiO_2 catalyst treated under CO_2 atmosphere in this study, $MnCO_3$ species can be somehow determined to be present in fresh catalyst by the corresponding IR spectrum (Fig. 3.14 c). In addition to $MnCO_3$, it is assumed that Na_2CO_3 species also exist in fresh catalyst after CO_2 treatment. Individual $MnCO_3$ and Na_2CO_3 decompose at low (300 °C) and high temperature (840 °C), respectively. At typical OCM temperature and atmosphere, CO_3^{2-} species may transfer from Na to Mn via an intermediate compound $[\mathrm{Na}^+ \cdots \mathrm{CO}_2^{3-} \cdots \mathrm{Mn}^{2+}]$ and its subsequent decomposition could be favorable to enhance catalytic performance. But for Na_2WO_4/SiO_2 catalyst, no intermediate compound can form without the participation of Mn. As a result, Na_2CO_3 is the only carbonate species present in catalyst and keeps rather stable at typical OCM temperature. No carbonate transfer would occur in this case and thus, the catalytic performance of is fairly worse.

In addition, it is observed that exact values of C_2 yield for Li/MgO and Mn-Na_2WO_4/SiO_2 catalyst are relatively higher than the top value of C_2 yield from volcano trend based on the concept of carbonate stability. The extra performance indicates that except carbonate stability, there may be additional catalyst properties that would be beneficial to OCM reaction. Taken Mn-Na_2WO_4/SiO_2 catalyst as an example, surface distorted tetrahedral WO_4 species[57], redox cycle by W^{6+}/W^{4+} and Mn^{3+}/Mn^{2+} sites[58], formation of crystalline SiO_2 phase[59] and a mixed molten phase containing WO_4 species[60, 61] have ever been proposed to be important to influence OCM performance. Therefore, it is concluded that for typically OCM catalysts, carbonate stability would be a main contributor to influence OCM reaction, while other properties could in a way promote catalytic performance to some extent.

5.7. Summary

In this chapter of thesis, property-descriptors and performance-descriptors of studied catalysts were correlated. The proposed property-performance correlations were evaluated by linear regression analysis. It is the first time to report quantitative and convincible volcano-like correlations between C_2 yield and property-descriptors generated from experimental results. Among these, $T_{dec,\ inter\ CO2}$ performs as the best descriptor reflecting certain chemical reactivity related to OCM reaction. This reveals that carbonate species with intermediate stability would be the dominating factor to have an impact on OCM performance. In addition, typical Li/MgO and Mn-Na_2WO_4/SiO_2 catalysts also somehow fit with the volcano-like correlation between C_2 yield and carbonate stability, suggesting that the effect of carbonate could be extended to typical OCM catalysts and considered as a universal concept for OCM reaction.

6. Mechanistic and basicity concepts in OCM catalysis

In this chapter, potential mechanism and alternative basicity concept regarding to property-performance correlations are generally discussed. First, the interaction between carbonate and cations is presented concerns different polarizing power of cations and subsequently possible coordination states are suggested based on literature report and experimentally measured IR-related parameter (section 6.1). Afterwards, three proposed simplified surface structure models are connected with their distinct performance behavior in order to explain the volcano-like correlation between OCM performance and carbonate stability (section 6.2). The effects of carbonate presence, transfer and decomposition on catalytic performance are summarized and illustrated taken Sm_2O_3 supported Rb_2CO_3 as an example. In section 6.3, alternative concept of basicity and its correlation with performance is discussed.

6.1. Possible interaction between carbonate and cations

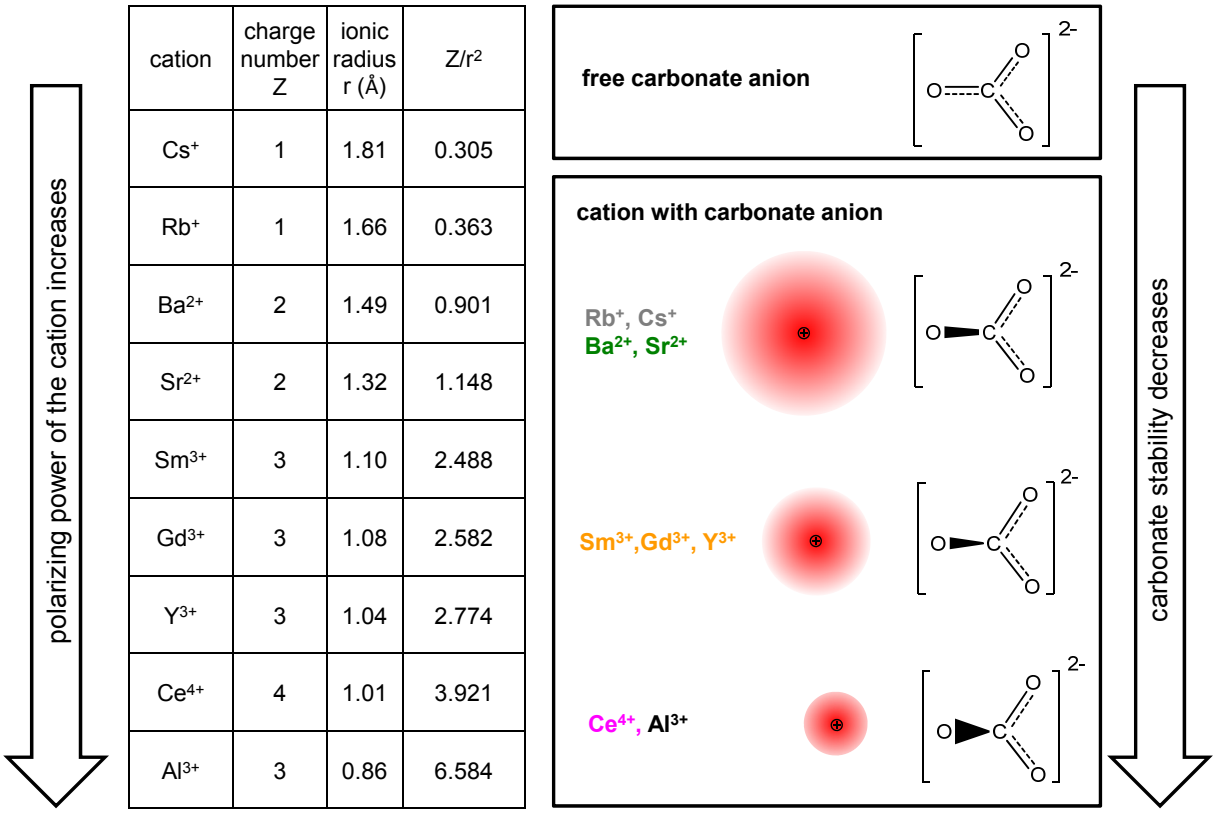

cation	charge number Z	ionic radius r (Å)	Z/r^2
Cs^+	1	1.81	0.305
Rb^+	1	1.66	0.363
Ba^{2+}	2	1.49	0.901
Sr^{2+}	2	1.32	1.148
Sm^{3+}	3	1.10	2.488
Gd^{3+}	3	1.08	2.582
Y^{3+}	3	1.04	2.774
Ce^{4+}	4	1.01	3.921
Al^{3+}	3	0.86	6.584

Fig. 6.1: Ionic radius and polarizing powder of cations appearing in this thesis as well as the simplified sketch about interaction between different cations and CO_3^{2-} anion. The values were abstracted from from [196] and [143]. In general, the polarization of CO_3^{2-} anion becomes stronger when the cation has higher polarizing powder, which facilitates the break of C-O bond and induces the decomposition of carbonate species. In consequence, the carbonate stability decreases with the increase of polarizing power of cations.

Carbonate stability is related to polarizing power of the cation. As shown Fig. 6.1, the carbonate used in these experimental contains Cs^+ or Rb^+ cation with the lowest polarizing power. The attractive force between the cation and carbonate anion is relatively weaker and as a result, pure Cs_2CO_3 or Rb_2CO_3 exhibits high stability. However, carbonate species shows various stability when Cs_2CO_3 or Rb_2CO_3 was impregnated onto different oxide support. The reason could be the variation of interaction between the cation and carbonate anion, as both Cs^+ or Rb^+ cation and the cation of oxide support may have an influence on

the carbonate. The cations of all investigated oxides possess higher polarizing power than Cs^+ or Rb^+ and in consequence, the combination of Cs^+ or Rb^+ and oxide cation would typically enhance the attractive force, facilitate the deformation of carbonate species and decrease the carbonate stability. For example, Sr^{2+} and Ba^{2+} with relatively lower polarizing power could only exhibit limited decreasing effect of carbonate stability, which explains the reason why the carbonate in Rb_2CO_3-SrO and Rb_2CO_3-BaO shows high stability similar to pure Rb_2CO_3. However, for Rb_2CO_3 on oxides with the cation possessing relatively higher polarizing power, especially Al^{3+}, the decomposition temperature is remarkably decreased, revealing the significant destabilizing effect of Al^{3+} on the carbonate species in Rb_2CO_3-Al_2O_3. For Sm^{3+}, Gd^{3+} and Y^{3+} with medium polarizing power, their influence on carbonate anion is larger than Sr^{2+} and Ba^{2+} but less than Ce^{4+} and Al^{3+}. This probably accounts for the intermediate stability of carbonate species in Rb_2CO_3-Sm_2O_3, Rb_2CO_3-Gd_2O_3 and Rb_2CO_3-Y_2O_3. Hence, the stability of carbonate is considered to be determined by the interaction strength between carbonate anion and combined cations.

Besides the polarizing effect of cations, it is also worthwhile to further explore how the carbonate anion and respective cation is chemically bonded. Generally, there are several type of coordination interaction possibly existing between them, which are monodentate, bidentate, bridged and polydentate.[172] One possible way to estimate the coordination state is employing splitting value of characteristic peak in IR spectra as a quantitative criterion.[142, 172] The experimental result in Fig. 3.3 already depicted that pure carbonate and oxides supported carbonate typically show remarkable splitting of asymmetric stretching vibration ($\Delta\nu_{as}$) of C=O bond in CO_3^{2-}. The reason is that the oscillators of three similar C=O in carbonate anion are interactive so that the original vibration energy states result in split energy states due to the coupling of vibrations. The splitting phenomenon is known to occur when the symmetry of CO_3^{2-} is reduced by versatile coordination with cations. The use of $\Delta\nu_{as}$ splitting to distinguish the coordination state were proposed by several groups based on IR detection of carbonate ions in metal complexes with known simple structures. A review from Busca et al.[172] summarized the relationship between $\Delta\nu_{as}$ and type of coordination. Generally, $\Delta\nu_{as}$ < 100 cm^{-1} corresponds with monodentate coordination type; 100 < $\Delta\nu_{as}$ < 300 cm^{-1} stands for polydentate coordination type; 300 < $\Delta\nu_{as}$ < 400 cm^{-1} is related to bidentate coordination type; $\Delta\nu_{as}$ higher than 400 cm^{-1} is derived from bridged type of coordination. Although the IR data was measured for carbonate anions (probably coexisting with other groups such as NH_3) in metal complexes which are different from carbonate species in this thesis, this classification on the basis of a quantitative criterion provides an available approach to conduct a reasonable speculation on the coordination structure between cation and carbonate anion.

Fig. A6.1 depicts the proposed structure for different types of coordination between cations and CO_3^{2-} anion. In monodentate coordination, only one cation is bonded to one oxygen of CO_3^{2-}, which lowers the symmetry of CO_3^{2-} to a less extent. But in bidentate coordination, one cation is bonded to two oxygens of CO_3^{2-} simultaneously. In this structure, the symmetry of CO_3^{2-} is reduced to a greater extent, showing a larger $\Delta\nu_{as}$ value. The symmetry of CO_3^{2-} is even lower in the structure of bridged coordination type where two cations are bonded to two different oxygen of CO_3^{2-}. Unbonded oxygen is present in above three coordination structures. Differently, all three oxygens are bonded to cations in the case of polydentate coordination. The corresponding $\Delta\nu_{as}$ value is between monodentate and bidentate/bridged type, indicating that polydentate coordination could lower the symmetry of CO_3^{2-} to an intermediate extent.

The value of Δv_{as} for Rb_2CO_3 and Cs_2CO_3 on oxide catalysts as well as pure carbonate was calculated and summarized in Table A6.1 based on FT-IR measurement. For pure Rb_2CO_3 and Cs_2CO_3, Δv_{as} is typically less than 100 cm^{-1}, suggesting the presence of monodentate coordination type between single Rb^+ or Cs^+ and CO_3^{2-}. For Rb_2CO_3 and Cs_2CO_3 on BaO and SrO, no significant splitting (Δv_{as} = 0) but a relatively broader peak (1445 cm^{-1}) was observed, which is in agreement with the previous report.[168, 197] Ba^{2+} or Sr^{2+} could be the preferred cation coordinated with CO_3^{2-} rather than Rb^+ or Cs^+. One possible explanation for no peak splitting is that the coordination interplay between Ba^{2+} or Sr^{2+} and CO_3^{2-} is too weak to reduce the symmetry of CO_3^{2-} and induce the splitting of energy states. Differently, for Rb_2CO_3 and Cs_2CO_3 on Sm_2O_3, Gd_2O_3 and Y_2O_3, CeO_2 and Al_2O_3, Δv_{as} is always between 100 and 300 cm^{-1}, suggesting the existence of polydentate coordination. There are a few of possible structures which are shown in Fig. A6.1. One CO_3^{2-} anion could be connected with two, three or even four cations via various bond types. “M” represents for both Rb^+/Cs^+ and Sm^{3+}/Gd^{3+}/Y^{3+}/Ce^{4+}/Al^{3+}. For instance, both Rb^+ and Sm^{3+} are proposed to be involved in the coordination with CO_3^{2-} for Rb_2CO_3-Sm_2O_3, where an intermediate species $[\mathrm{Rb}^+ \cdots \mathrm{CO}_2^{3-} \cdots \mathrm{Sm}^{3+}]$ forms as a result.

To our knowledge, no direct and clear relationship between coordination type and carbonate species stability was reported which could be available as a reference. But one can at least speculate the different stability between monodentate carbonate and polydentate carbonate species by polarizing effect of cations. For example, monodentate coordination $[\mathrm{Rb}^+ \cdots \mathrm{CO}_2^{3-}]$ may be present in pure Rb_2CO_3, where CO_3^{2-} tends to be polarized from one side. However, $[\mathrm{Rb}^+ \cdots \mathrm{CO}_2^{3-} \cdots \mathrm{Sm}^{3+}]$ possibly exists in Rb_2CO_3-Sm_2O_3, where CO_3^{2-} tends to be polarized from at least two sides. The chemical bond between C and O is easier to be broken in Rb_2CO_3-Sm_2O_3 compared to pure Rb_2CO_3, because the polarization of CO_3^{2-} is greatly enhanced with more cations involving in the coordination structure. This argument is in agreement with TGA-MS result, where Rb_2CO_3-Sm_2O_3 exhibits lower decomposition temperature of carbonate than pure Rb_2CO_3.

In general, the stability of carbonate species decreases when there is cation with high polarizing power involving in the compound. From the view of structure, polydentate coordination between CO_3^{2-} and at least two cations is considered to enhance the polarization of CO_3^{2-} than monodentate coordination type, which facilitates the decomposition of carbonate species via breaking of C-O bond. Both effects well explains why the stability of carbonate on rare earth oxides and Al_2O_3 becomes lower compared to the pure carbonate.

6.2. Explanation of volcano-like property-performance correlation

In section 3.3.6, three different surface structure models for oxide-supported carbonate catalysts were proposed dependent on the thermal stability of involved carbonated species on the basis of characterization data, especially TGA-MS results. Herein, the simplified reaction scheme regarding to each surface structural model is proposed in Fig. 6.2 to explain the volcano-like correlation between OCM performance and carbonate stability in a visible fashion on the whole.

The left part of Fig. 6.2 depicts the surface structure for oxide-supported catalyst when the involved carbonate has low stability. Hence, no carbonate species would be present at OCM temperature, which leads to a surface composed of oxide exposed to OCM feed. In this situation, total oxidation reaction is much more favored compare to selective oxidation reaction. As a result, CO_x is the primary product rather than C_2 products. The low level of C_2

selectivity thus mainly contributes to low OCM performance for these catalysts, which could explain the left region of volcano plot of correlation between C_2 yield and carbonate stability.

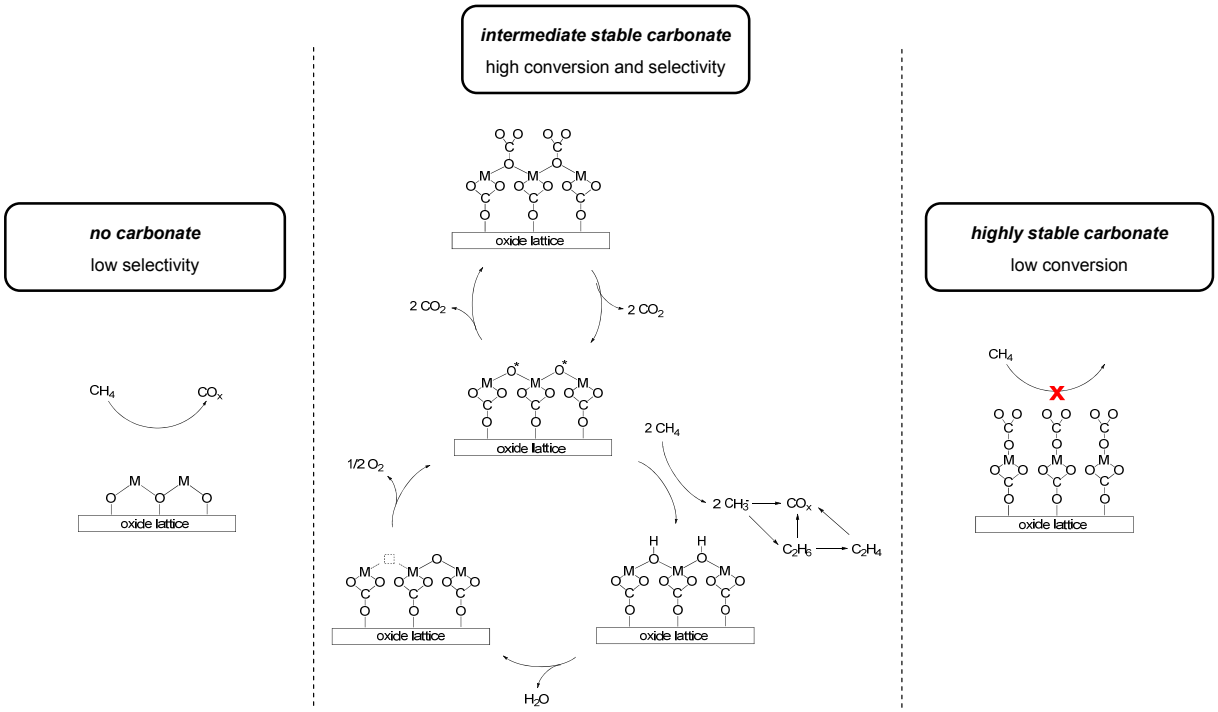

Fig. 6.2: Possible reaction pathways in three proposed surface structural models for oxide-supported carbonate with high, intermediate and low stability. No carbonate surface is favorable for total oxidation and leads to low C_2 selectivity. Upon partial decomposition of carbonate, intermediate stable carbonate surface could generate isolated sites and oxygen species surrounded by remaining carbonate, which would improve both conversion and selectivity. Highly stable carbonate surface could not generate active oxygen species to activate CH_4 and results to low conversion.

As shown in the middle part of Fig. 6.2, when the carbonate species possesses intermediate stability, a thin layer of carbonate is regarded to be present as the surface. This carbonate is rather flexible and sensitive to the exposed temperature under reaction conditions. At typical OCM temperature, some of these carbonate species tend to decompose via breaking of C-O bond and consequently form certain oxygen species involved in activation of CH_4. Meanwhile, the surface is still mostly composed of the layer of carbonate and thus total oxidation reaction induced by possible oxygen species could be suppressed. As a result, reaction intermediate species (such as methyl radicals) could have more opportunities towards formation of C_2 product and the formed C_2 product could be less further oxidized into CO_x. Therefore, two positive aspects including increased CH_4 conversion and enhanced C_2 selectivity lead to high C_2 yield for these catalysts, which explains the top region of volcano plot of correlation between C_2 yield and carbonate stability.

In order to further elucidate how the carbonate with intermediate stability contributes to OCM reaction, a possible reaction pathway is proposed including the concept of “site isolation”. At typical OCM temperature, carbonate species tends to partially decompose and in consequence, CO_2 is produced and escapes from the surface. Meanwhile, isolated sites are considered to form that are surrounded by the remaining carbonate. Oxygen species could then appear on the sites responsible for selective CH_4 activation because the amount of oxygen immediately available is stoichiometric sufficient for selective oxidation, but insufficient for total oxidation.[153] As a competitive reaction to CH_4 activation, these formed isolated sites may also capture CO_2 from the gas phase and form carbonate species again because CO_2 is inevitably present as a by-product during the reaction. The intermediate

stability of carbonate enables the fast revolution of formation and decomposition of carbonate, which is beneficial to keep a relatively high amount of isolated sites and oxygen species. The oxygen species could abstract H from CH_4 molecule and form OH as a result. When the reaction temperature is sufficiently high, two adjacent OH species may interact with each other and forms a H_2O molecule, which could be removed from the catalyst surface when a favorable temperature is reached. As a result, an oxygen vacancy is formed and responsible for O_2 activation. On the other hand, two $CH_3\cdot$ produced by H abstraction from CH_4 could couple in the gas-phase and form C_2H_6 product. Subsequently, C_2H_4 could form via dehydrogenation reaction of C_2H_6. All radical intermediate species and C_2 products have possibility to be further oxidized towards CO_x product. The presence of intermediate stable carbonate could effectively suppress the occurrence of these unselective reactions on catalyst surface.

The right part of Fig. 6.2 depicts the surface structure when the involved carbonate species possesses high stability. A thin layer of stable carbonate species is considered to be present as the surface. Even at OCM temperature, these carbonate species are able to keep rather intact. As a result, no oxygen species could be produced via breaking of C-O bond (i.e., carbonate decomposition), which is responsible for CH_4 activation. Therefore, the low level of CH_4 conversion mainly contributes to low OCM performance for these catalysts, which may explain the right region of volcano plot of correlation between C_2 yield and carbonate stability.

The effect of carbonate presence, transfer and decomposition on OCM performance

In chapter 3, 4 and 5, the effect of carbonate presence, transfer and decomposition on OCM performance was preliminarily discussed. Herein, a schematic presentation regarding to these processes is shown in Fig. 6.3 taken Sm_2O_3 supported Rb_2CO_3 as an example.

Pure Rb_2CO_3 is a highly stable carbonate and its decomposition temperature is ~ 921 °C from our experimental test. Stable carbonate is beneficial to C_2 selectivity proposed by Tong et al.[147]. They suggested that carbonate could partially cover the oxide surface and decrease the reaction rate of methyl radical with surface, therefore providing more opportunity for the radicals to couple towards C_2 product. Herein, the stable Rb_2CO_3 covers part of the oxide support and is able to suppress the unselective oxidation reaction. Hence, the selectivity of C_2 product could retain at a considerable level.

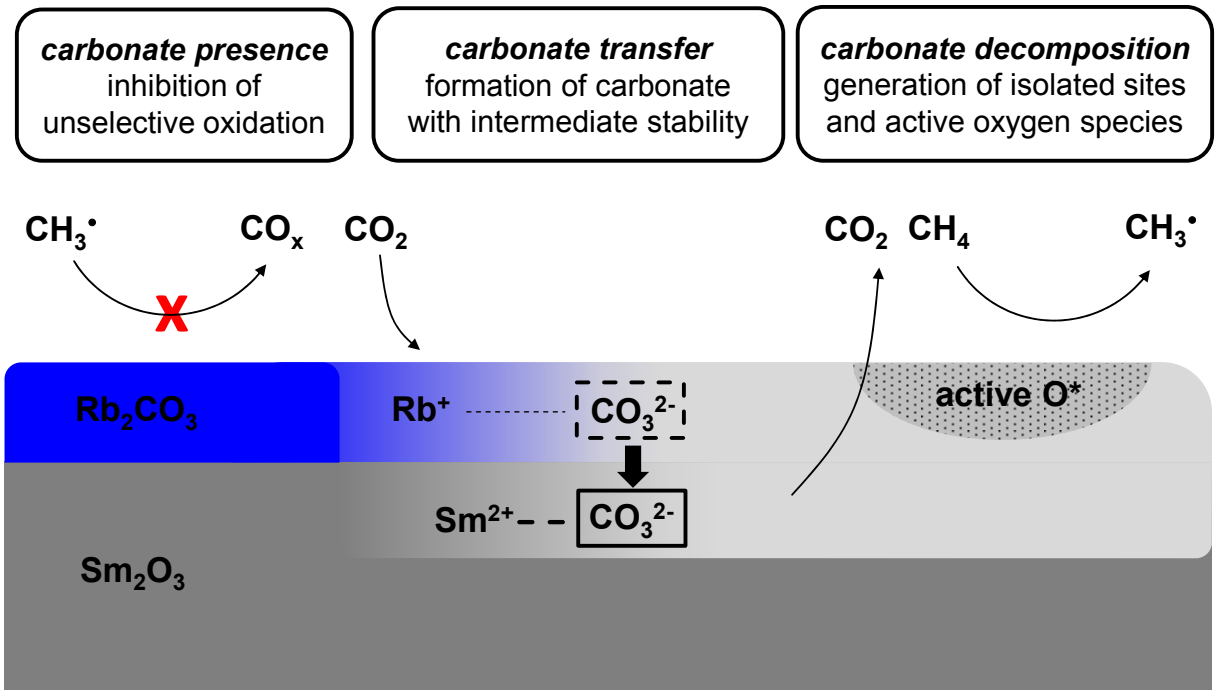

Fig. 6.3: Schematic representation of the effect of carbonate presence, transfer and decomposition on OCM performance. The presence of carbonate could suppress the unselective oxidation reaction. The carbonate species is transferred from Rb^+ to Sm^{2+} and forming a carbonate compound with intermediate stability. The formed carbonate tends to decompose under OCM temperature and release isolated site and active oxygen species responsible for selective CH_4 activation.

When Rb_2CO_3 is combined with Sm_2O_3, different behavior tends to occur due to synergetic effect of two cations. As discussed in section 6.1, Sm^{2+} has higher polarizing power than Rb^+ and thus shows stronger interaction with CO_3^{2-} anion. Hence, it has higher tendency to capture CO_3^{2-} species from Rb^+. Especially under the actual reaction condition, the transfer process is much more favored at the elevated reaction temperature. Although Rb_2CO_3 has fairly high melting point, T_m ~ 837 °C,[145] its structure mobility starts to be pronounced under much lower temperature, which is expressed by Tammann temperature.[140] It describes the temperature at which the mobility and reactivity of atoms or molecules in a solid become appreciable, such as sintering. The Tammann temperature is often calculated via multiplication of a compound's melting point with a pre-factor that diversified from 0.37[198] to 0.75 in previous literature[199, 200]. One can assume the factor as 0.5 based on the empirical rule[199] that it is approximately half the melting point in kelvin. The Tammann temperature of Rb_2CO_3 is ~ 555 K (282 °C). This suggests that above 282 °C, part of Rb_2CO_3 proceeds structural change and as a result, it may form a molten phase consisting of Rb^+, Sm^{2+} cation and CO_3^{2-} anion, denoted as $[Rb^+ \cdots CO_2^{3-} \cdots Sm^{3+}]$. Mass transfer would be greatly enhanced in this molten compound. Therefore, it is not difficult for CO_3^{2-} species to transfer from Rb^+ to Sm^{2+}. After the transfer process, CO_3^{2-} species undergoes decomposition in the form of $Sm_2(CO_3)_3$, $Sm_2O_2CO_3$ or $[Rb^+ \cdots CO_2^{3-} \cdots Sm^{3+}]$ towards oxide. The formed oxide is able to uptake CO_2 from the gas-phase under reaction condition and form CO_3^{2-} species again. Due to the presence of carbonate transfer and decomposition in the possibly formed molten phase, the CO_2 adsorption and carbonate formation would be not detrimental to catalyst performance.

As a result of carbonate decomposition process, isolated sites surround by carbonate species would form on the surface. And active oxygen species would form on these isolated sites, which may be molecular oxygen species such as peroxide O_2^{2-} [43-49] or atomic oxygen species O^- [38, 40, 42]. No matter what exactly the oxygen species is, it would be beneficial to

CH_4 activation and leads to the increased OCM activity. This is in agreement with the report from Dubois et al.[173], where the addition of Y_2O_3 to $SrCO_3$ and $BaCO_3$ could significantly improve reaction activity. They proposed a possible carbonate transfer from the component forming the more stable carbonate to the component forming the less stable carbonate. As a result of carbonate decomposition, more vacancies required for oxygen activation, more crystal disorder and possibly higher surface area were also suggested.

Overall, Sm_2O_3 supported Rb_2CO_3 exhibited higher catalytic performance at typical OCM temperatures. It is attributed to synergetic effect of enhanced C_2 selectivity by the presence of carbonate and improved OCM activity upon carbonate transfer and decomposition.

6.3. Alternative basicity concepts and OCM performance

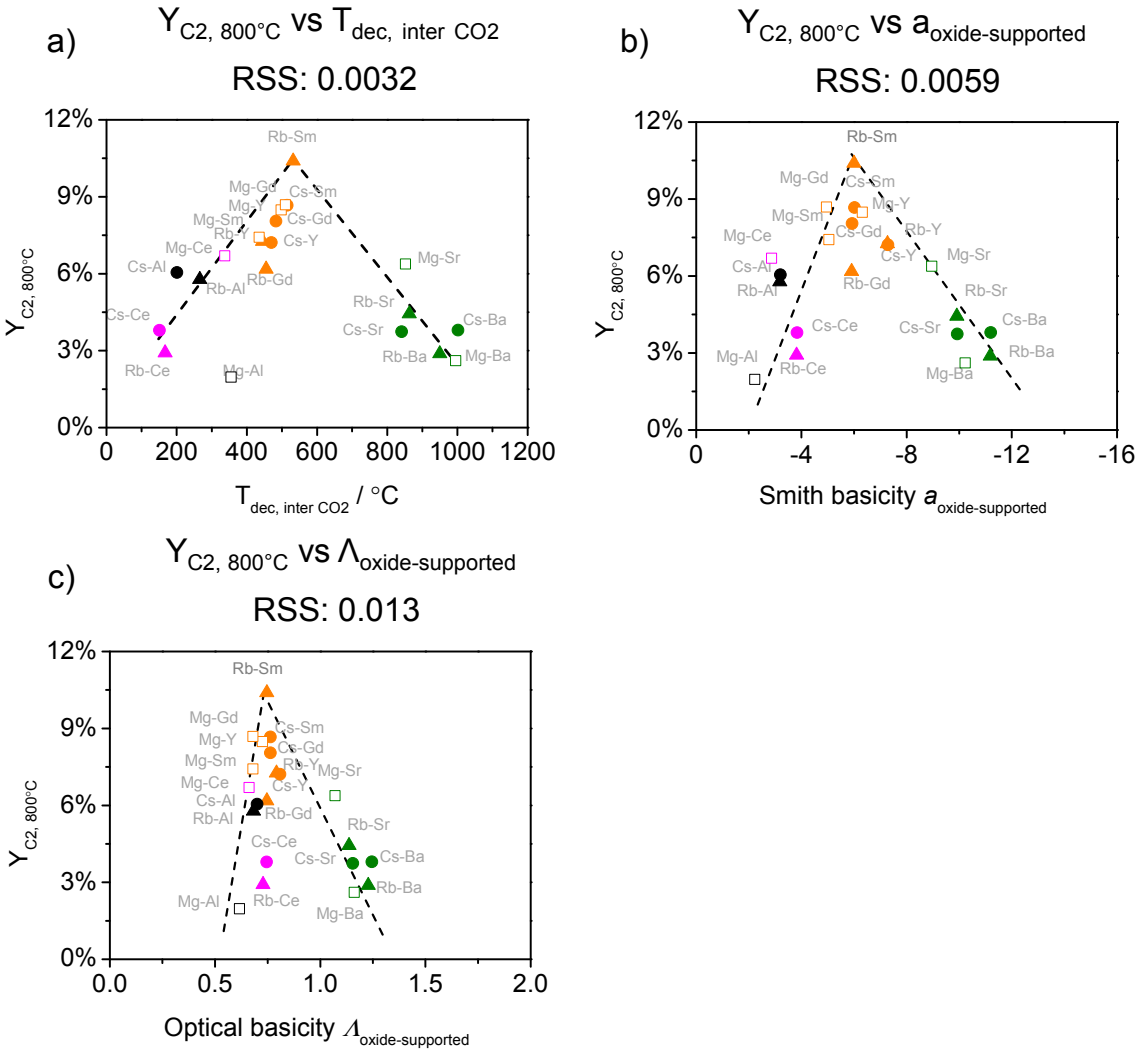

Fig. 6.4 C_2 yield at 800 °C vs. (a) $T_{dec,\ inter\ CO2}$ and (b, c) calculated Smith basicity and optical basicity of oxide-supported carbonate catalysts in this study. C_2 yield value is abstracted from performance data measured in N_2 OCM feed. $T_{dec,\ inter\ CO2}$ is derived from TGA-MS result tested in Ar atmosphere. Smith basicity and optical basicity for each catalyst is assumed to be the weighted average of values from the oxide support and corresponding oxide from alkali or alkaline earth element. Data point labels indicate the cation combination of the respective catalyst. The dash lines indicate the volcano-like trend.

In this thesis, a quantitative correlation was established between OCM performance and thermal stability of carbonate in catalysts. To my knowledge, it is the first time to report a clear and universal quantitative property-performance correlation for a variety of catalysts over OCM reaction. The concept of carbonate stability is different from the basicity property proposed by previous researchers,[72, 74, 77, 131, 136] which may influence CH_4 conversion and/or C_2 product selectivity. Furthermore, there is no clear quantitative correlation ever reported in literature between OCM performance and strength of catalyst basicity, as discussed in section 1.5.1.

In order to further clarify the difference of concepts between basicity and carbonate stability, correlations built by basicity descriptors are compared to the correlations established by the best carbonate descriptor $T_{dec,\ inter\ CO2}$.

Catalyst basicity can be expressed in different ways, herein, Smith basicity[133] and optical basicity[135] are utilized as a theoretical evaluation of basicity strength in a quantitative fashion because these two scales exhibit significant numerical variation among a variety of elements. In this thesis, the molar ratio between carbonate cation and oxide cation is consistently 10 mol% for each catalyst. The calculation of basicity for the whole catalyst should take both carbonate and oxide support into consideration through a weighted average approach. For example, Smith basicity of Rb_2CO_3-Sm_2O_3 is assumed to be calculated by Equation 6.1.

$$a(Rb_2CO_3 - Sm_2O_3) = [a(Rb_2O) * 10\ \% + a(Sm_2O_3) * 100\ \%]/110\ \% \quad (6.1)$$

Optical basicity of is assumed to be calculated in the same approach shown in Equation 6.2.

$$\Lambda(Rb_2CO_3 - Sm_2O_3) = [\Lambda(Rb_2O) * 10\ \% + \Lambda(Sm_2O_3) * 100\ \%]/110\ \% \quad (6.2)$$

The correlation between OCM performance and $T_{dec,\ inter\ CO2}$ has already been discussed for oxide-supported catalysts (see sections 5.2). They are compared to the case when Smith basicity and optical basicity are employed. As shown in Fig. 6.4 b and c, volcano-like correlations are also observed between C_2 yield and Smith basicity and optical basicity of catalysts. However, RSS values from linear regression analysis reveals that their quality of fitting between regression line and experimental data is worse than the case between C_2 yield and carbonate stability. It suggest that these basicity descriptors work not as good as carbonate descriptor $T_{dec,\ inter\ CO2}$. The reason would be that basicity is only a scale of one catalyst property that is not necessarily involved in actual OCM reaction. However, the concept of carbonate and CO_2 closely contribute to OCM reaction and are part of the proposed reaction mechanism (see Fig. 6.2). The site isolation within the carbonate is one possible important path to generate special selective oxygen species and to suppress total oxidation on the oxide (see Fig. 6.3).

In summary, it is the first time to report a universal quantitative property-performance correlation by using the concept of carbonate stability. This concept is different from the catalyst basicity. When utilized to describe property-performance correlations, basicity concept could not behave as good as carbonate concept that reflects the essential property involved in OCM.

7. Conclusion and outlook

Conclusion

The oxidative coupling of methane is a “dream reaction” in heterogeneous catalysis to achieve direct conversion for natural gas towards value-added and easily transportable C_2 products with high economic relevance. Although a huge body of catalysts with various composition have been studied, no universal and quantitative correlation between catalyst properties and OCM performance is presented so far.

Porous SiC supported Mn/Na/W/SiC catalysts were synthesized and investigated regarding to their structural properties and catalytic behaviors. OCM tests suggest that the performance of Mn/Na/W/SiC catalysts depends critically on the supports stability, for example, the surface area retained under reaction conditions.

In order to deeply explore the catalyst property that is essential to OCM reaction, this thesis presented an efficient approach to generate descriptors, testify descriptors, correlate property-descriptors with performance-descriptors and evaluate the proposed property-performance correlations. Oxide-supported, carbonate-supported as well as typical Li/MgO and Mn-Na_2WO_4/SiO_2 catalysts were synthesized and characterized regarding to morphology, elemental distribution, crystal phase composition, chemical species, surface area and carbonate stability. Property-descriptors, $T_{dec,\ 1st\ CO2}$, $T_{dec,\ inter\ CO2}$, $T_{dec,\ last\ CO2}$, $T_{1st\ H2O}$, $T_{last\ H2O}$, $\sigma_{left,\ carb}$ and $\Delta\sigma_{left,\ carb}$, were defined and generated on the basis of IR and TGA-MS characterization results. Proven by TGA-MS, more than one kind of carbonate species with different thermal stability are present in both oxide-supported, carbonate-supported and typical OCM catalysts. The oxide support could facilitate carbonate transfer from highly stable form to carbonate species with lower stability, which is easier to decompose at sufficiently high temperatures.

OCM catalytic performance of all catalysts were tested in N_2 OCM feed. Performance-descriptors, $Y_{C2,\ 800\ °C}$ and $Y_{C2,\ 750\ °C}$, were defined and generated from OCM performance data. Oxide supports strongly influence CH_4 conversion and C_2 yield of oxide-supported catalysts. Carbonate-supported catalysts exhibit abrupt increase of performance at intermediate temperature range. Typical OCM catalysts exhibit remarkable performance possibly related to the presence of carbonate species at OCM temperatures. The presence of CO_2 in OCM feed results to a significant shift of OCM performance to higher temperatures, which is attributed to the stabilization effect of CO_2 on carbonate species.

Afterwards, property-descriptors and performance-descriptors of studied catalysts were correlated and the proposed property-performance correlations were evaluated by linear regression analysis. It is the first time to report a quantitative and convincible volcano-like correlation between C_2 yield and property-descriptor of carbonate stability ($T_{dec,\ inter\ CO2}$). It reveals that carbonate species with intermediate stability would be beneficial to influencing OCM performance. The isolated sites surrounded by carbonate are one possible critical path to generate special selective oxygen species and to suppress total oxidation on the oxide. In addition, this volcano-like property-performance correlation could be somehow extended to typical OCM catalysts. The concept of carbonate stability behaves better than basicity concepts, because it reflects certain chemical reactivity related to OCM reaction and is involved in the proposed mechanism.

The property-performance correlations illustrated in this work contribute to the understanding of OCM reaction by focusing on importance of carbonate formation and stability to reach a generally valid concept. The obtained insights are of certain significance in guiding further improvement of quantitative approaches on property-performance evaluation in heterogeneous catalysis research. Moreover, the results can be used for further improvement of catalytic performance through rational design of catalysts by incorporation the concept of carbonate.

Outlook for SiC supported OCM catalysts

SiC is generally considered as a good heterogeneous catalyst support with high stability at elevated temperatures. We expected that porous SiC could behave as a stable support for OCM catalyst. However, dramatic loss of surface area and porosity was found at air-calcined condition or under OCM reaction due to accelerated oxidation of SiC promoted by the presence of alkali element Na. It results in the weakness that the influence of porosity on OCM performance by using Mn/Na/W/SiC catalyst could be only studied in a very limited range. In order to extend this range, a few of solutions could be considered for the future experimental design.

One possible way is to increase the surface area of starting SiC materials. In this thesis, two kinds of commercial porous SiC materials were employed, with BET surface area < 30 m^2/g. After calcination in air or OCM reaction, BET surface area of catalysts came to < 2 m^2/g. If a SiC material with larger surface area is used as a support material, it is possible that the prepared Mn/Na/W/SiC catalyst would retain higher surface area afterwards assuming similar oxidation kinetics occurs during treatment or under reaction conditions. Several previous papers have reported on synthesis of mesoporous SiC materials with high surface area. Shi et al.[126] prepared an ordered mesoporous SiC material via a one-step nanocasting process using commercial polycarbosilane as a precursor and mesoporous silica as hard templates. This SiC has high BET surface areas (up to 720 m^2/g) and narrow pore-size distributions (2.0 ~ 3.7 nm), even upon calcination at temperatures as high as 1400 °C. In a later paper from the same group,[122] they reported a low temperature synthetic process for direct converting SiO_2/C composite to the corresponding SiC without losing their nanostructure via magnesiothermic reduction. The obtained SiC with high BET surface area ~ 410 m^2/g and hierarchical pore size (~ 230 nm and ~ 4.7 nm). Therefore, different approaches are available to achieve the synthesis of SiC material with high surface area and adjustable pore size. Afterwards, if SiC with various surface area and pore size are employed as support for Mn/Na/W/SiC catalysts, it would provide a much wider range for model catalyst system to investigate the influence of catalyst porosity on OCM performance.

Another possibility is to suppress the oxidation of SiC in the premise of sacrificing catalytic performance as less as possible. The presence of Na, O_2 in gas atmosphere and a sufficiently high temperature are three main factors to induce the accelerated SiC oxidation which leads to loss of porosity. Firstly, the removal or substitution of Na would not be a proper option based on the report from Palermo et al.[201] Secondly, avoid using O_2 for the catalytic reaction is not feasible because by introducing O_2, the thermodynamic restrictions for coupling of methane can be overcome and the process becomes thermodynamically feasible.[27] Finally, the only option could be decrease reaction temperature to a certain extent. A recent report by Wang et al.[100] pointed out the required temperature for Mn-Na_2WO_4/SiO_2 system could be lowered to 650 °C via certain modification of catalyst without significant reduce of performance. If this concept is incorporated in to Mn/Na/W/SiC catalyst, the remarkable catalytic performance is expected to achieve at a relatively low temperature,

where only limited oxidation of SiC occurs and the preservation of most surface area and porosity from SiC support becomes possible.

Outlook for oxide-supported carbonate catalysts

The property-performance correlation is investigated on oxide-supported model catalysts by introducing the concept of carbonate stability in this thesis. A volcano-like correlation is established between OCM performance and carbonate stability. Carbonate with intermediate stability is considered to be critical for a good OCM catalyst. Based on these, several directions can be designed to continue the research topic in this thesis.

First possible approach is to further improve the observed volcano-like correlation by testing more designed catalysts. One weakness of volcano plot in this thesis is that most data points locate in the left side but fewer points are on the right side. Especially in the region with x-axis from 600 to 800 °C, there is even no catalyst data point available. In order to improve the quality of linear regression and make the correlation more convincible, catalysts with appropriate composition should be designed and used to fill in this gap. CaO could be one option to be employed as a support for carbonate. The thermal stability of carbonate derived from CaO is expect to locate between the studied ones formed by rare earth and alkaline earth oxide support. New data from CaO supported catalysts could be integrated into the volcano plot and thus, all data points would be more distributed over whole temperature range.

Second possibility is to investigate the effect of carbonate amount in catalysts on OCM performance. In this thesis, the molar ratio of impregnated cation to support cation is 10 % and consistent for all oxide-supported catalysts. It is highly worthwhile to further optimize the impregnation amount of carbonate onto oxide support, especially for well-performing one in this thesis, e.g. Rb_2CO_3-Sm_2O_3. Partially decomposition of carbonate could generate isolated sites and selective oxygen species responsible for activating CH_4 and suppressing total oxidation. Therefore, there would be an optimal carbonate amount that the catalytic performance achieves the best which is synergistically contributed by two beneficial aspects of carbonate. This requires continuous optimization of experimental recipe for the catalysts.

Last but not the least, the carbonate transfer is proposed to be critical to catalytic process and a complex molten phase may form at certain temperature during OCM reaction. The exact form and composition of this molten phase as well as its formed oxygen species must be experimentally verified to further elucidate the mechanistic role of carbonates. This could be conducted by in-situ spectroscopic techniques, although these are not easy to achieve considering the constraints of reactor design, required high temperatures and possibly vacuum conditions. A reactor allowing rapid quenching of the catalyst followed by ex-situ characterization could also give new possibilities. But one should keep in mind that ex-situ observations do not necessarily resemble the catalyst's state under reaction conditions.[68] A theoretical approach would also be another option to address this question. Although great computational effort is required, molecular dynamic simulations with description of the electronic structure on DFT level is suggested to capture the fluctuations of the electronic structure at the high temperatures employed during reaction. Such simulations may provide meaningful information on the formation of related carbonate or oxygen species as well as on the activation of CH_4.

Bibliography

[1] J.H. Lunsford, Catalytic conversion of methane to more useful chemicals and fuels: A challenge for the 21st Century, *Catalysis Today*, 2000, 63, 165-174.

[2] V. Kuuskraa, S. Stevens, T.V. Leeuwen and K. Moodhe, World shale gas resources: An initial assessment of 14 regions outside the United States, U.S. Energy Information Administration, Washington, DC, 2011, pp. 7.

[3] D. Saha, H.A. Grappe, A. Chakraborty and G. Orkoulas, Postextraction separation, on-board storage, and catalytic conversion of methane in natural gas: A review, *Chemical Reviews*, 2016, 116, 11436-11499.

[4] A. Holmen, Direct conversion of methane to fuels and chemicals, *Catalysis Today*, 2009, 142, 2-8.

[5] E.V. Kondratenko, Fundamentals of the oxidative conversion of methane to higher hydrocarbons and oxygenates, *DGMK Conference*, Berlin, 2008, pp. 45-58.

[6] P. Schwach, X. Pan and X. Bao, Direct conversion of methane to value-added chemicals over heterogeneous catalysts: Challenges and prospects, *Chemical Reviews*, 2017, 117, 8497-8520.

[7] E. McFarland, Unconventional chemistry for unconventional natural gas, *Science*, 2012, 338, 340-342.

[8] O. Deutschmann, H. Knözinger, K. Kochloefl and T. Turek, Heterogeneous catalysis and solid catalysts, *Ullmann's Encyclopedia of Industrial Chemistry*, Wiley-VCH Verlag GmbH & Co. KGaA, 2000, pp. 6-7.

[9] K. Weissermel and H.-J. Arpe, Basic Products of Industrial Syntheses, *Industrial Organic Chemistry*, WILEY-VCH Verlag GmbH & Co. KGaA, 2008, pp. 15-57.

[10] J.R. Rostrup-Nielsen, Production of synthesis gas, *Catalysis Today*, 1993, 18, 305-324.

[11] P.F. van den Oosterkamp and R.W. van den Brink, Synthesis gas generation-industrial, *Encyclopedia of Catalysis*, John Wiley & Sons, Inc., 2002, pp. 2.

[12] J.J.C. Geerlings, J.H. Wilson, G.J. Kramer, H.P.C.E. Kuipers, A. Hoek and H.M. Huisman, Fischer-Tropsch technology - from active site to commercial process, *Applied Catalysis A: General*, 1999, 186, 27-40.

[13] H. Schulz, Short history and present trends of Fischer-Tropsch synthesis, *Applied Catalysis A: General*, 1999, 186, 3-12.

[14] G.E. Keller and M.M. Bhasin, Synthesis of ethylene via oxidative coupling of methane, *Journal of Catalysis*, 1982, 73, 9-19.

[15] M.J. Gradassi and N. Wayne Green, Economics of natural gas conversion processes, *Fuel Processing Technology*, 1995, 42, 65-83.

[16] Siluria Technologies, Demonstration Plant, http://siluria.com/Technology/Demonstration_Plant, 2015.

[17] E.C. Scher, F.R. Zurcher, J.M. Cizeron, W.P. Schammel, A. Tkachenko, J. Gamoras, D. Karshtedt and G. Nyce, Production of ethylene with nanowire catalysts, U.S. Patent 9718054, 2011.

[18] E.C. Scher, F.R. Zurcher, J.M. Cizeron, W.P. Schammel, A. Tkachenko, J. Gamoras, D. KARSHTEDT and G. NYCE, Nanowire catalysts, U.S. Patent 20120041246, 2012.

[19] F.R. Zurcher, E.C. Scher, J.M. Cizeron, W.P. Schammel, A. TKACHENCKO, J. Gamoras, D. Karshtedt, G. Nyce, A. RUMPLECKER and J. Mccormick, Nanowire catalysts and methods for their use and preparation, U.S. Patent 8962517, 2013.

[20] E.V. Kondratenko and U. Rodemerck, Recent progress in oxidative coupling of methane to value-added products, in: P. Granger, V.I. Parvulescu, S. Kaliaguine, W.

Prellier (Eds.) *Perovskites and Related Mixed Oxides*, Wiley-VCH Verlag GmbH & Co. KGaA, Weinheim, 2016, pp. 517.

[21] R. Horn and R. Schlögl, Methane activation by heterogeneous catalysis, *Catalysis Letters*, 2015, 145, 23-39.

[22] Y.S. Su, J.Y. Ying and W.H. Green Jr, Upper bound on the yield for oxidative coupling of methane, *Journal of Catalysis*, 2003, 218, 321-333.

[23] S. Arndt, T. Otremba, U. Simon, M. Yildiz, H. Schubert and R. Schomäcker, Mn-Na_2WO_4/SiO_2 as Catalyst for the oxidative coupling of methane. What is really known?, *Applied Catalysis A: General*, 2012, 425-426, 53-61.

[24] M.E. Dry, The Fischer-Tropsch process: 1950-2000, *Catalysis Today*, 2002, 71, 227-241.

[25] M.E. Günay and R. Yildirim, Knowledge Extraction from Catalysis of the Past: A Case of Selective CO Oxidation over Noble Metal Catalysts between 2000 and 2012, *ChemCatChem*, 2013, 5, 1395-1406.

[26] P.A. Kilty and W.M.H. Sachtler, The mechanism of the selective oxidation of ethylene to ethylene oxide, *Catalysis Reviews*, 1974, 10, 1-16.

[27] J.S. Lee and S.T. Oyama, Oxidative coupling of methane to higher hydrocarbons, *Catalysis Reviews*, 1988, 30, 249-280.

[28] V. Fleischer, R. Steuer, S. Parishan and R. Schomäcker, Investigation of the surface reaction network of the oxidative coupling of methane over $Na_2WO_4/Mn/SiO_2$ catalyst by temperature programmed and dynamic experiments, *Journal of Catalysis*, 2016, 341, 91-103.

[29] B. Beck, V. Fleischer, S. Arndt, M.G. Hevia, A. Urakawa, P. Hugo and R. Schomäcker, Oxidative coupling of methane - A complex surface/gas phase mechanism with strong impact on the reaction engineering, *Catalysis Today*, 2014, 228, 212-218.

[30] M.R. Lee, M.-J. Park, W. Jeon, J.-W. Choi, Y.-W. Suh and D.J. Suh, A kinetic model for the oxidative coupling of methane Over $Na_2WO_4/Mn/SiO_2$, *Fuel Processing Technology*, 2012, 96, 175-182.

[31] J. Sun, J.W. Thybaut and G.B. Marin, Microkinetics of methane oxidative coupling, *Catalysis Today*, 2008, 137, 90-102.

[32] S. Pak, P. Qiu and J.H. Lunsford, Elementary reactions in the oxidative coupling of methane over $Mn/Na_2WO_4/SiO_2$ and $Mn/Na_2WO_4/MgO$ Catalysts, *Journal of Catalysis*, 1998, 179, 222-230.

[33] N.R. Farooji, A. Vatani and S. Mokhtari, Kinetic Simulation of oxidative coupling of methane over perovskite catalyst by genetic algorithm: Mechanistic aspects, *Journal of Natural Gas Chemistry*, 2010, 19, 385-392.

[34] R. Ghose, H.T. Hwang and A. Varma, Oxidative coupling of methane using catalysts synthesized by solution combustion method: Catalyst optimization and kinetic studies, *Applied Catalysis A: General*, 2014, 472, 39-46.

[35] J.W.M.H. Geerts, Q. Chen, J.M.N. van Kasteren and K. van der Wiele, Thermodynamics and kinetic modeling of the homogeneous gas phase reactions of the oxidative coupling of methane, *Catalysis Today*, 1990, 6, 519-526.

[36] H. Schwarz, M. Geske, C. Franklin Goldsmith, R. Schlögl and R. Horn, Fuel-rich methane oxidation in a high-pressure flow reactor studied by optical-fiber laser-induced fluorescence, multi-species sampling profile measurements and detailed kinetic simulations, *Combustion and Flame*, 2014, 161, 1688-1700.

[37] H. Zanthoff and M. Baerns, Oxidative coupling of methane in the gas phase. Kinetic simulation and experimental verification, *Industrial & Engineering Chemistry Research*, 1990, 29, 2-10.

[38] D.J. Driscoll, W. Martir, J.X. Wang and J.H. Lunsford, Formation of gas-phase methyl radicals over magnesium oxide, *Journal of the American Chemical Society*, 1985, 107, 58-63.

[39] P.F. Nelson, C.A. Lukey and N.W. Cant, Measurements of kinetic isotope effects and hydrogen/deuterium distributions over methane oxidative coupling catalysts, *Journal of Catalysis*, 1989, 120, 216-230.

[40] J.H. Lunsford, The catalytic oxidative coupling of methane, *Angewandte Chemie International Edition in English*, 1995, 34, 970-980.

[41] H.S. Zhang, J.X. Wang, D.J. Driscoll and J.H. Lunsford, Activation and oxidative dimerization of methane over lithium-promoted zinc oxide, *Journal of Catalysis*, 1988, 112, 366-374.

[42] C. H. Lin, J.X. Wang and J.H. Lunsford, Oxidative dimerization of methane over sodium-promoted calcium oxide, *Journal of Catalysis*, 1988, 111, 302-316.

[43] C. Moneuse, M. Cassir, G. Martin and J. Devynck, Oxidative dimerization of methane in molten Na_2CO_3-K_2CO_3 eutectic at 800°C, *Applied Catalysis A: General*, 1992, 85, 147-155.

[44] K. Otsuka, Y. Murakami, Y. Wada, A.A. Said and A. Morikawa, Oxidative couplings of methane, ethane, and propane with sodium peroxide at low temperatures, *Journal of Catalysis*, 1990, 121, 122-130.

[45] D. Dissanayake, J.H. Lunsford and M.P. Rosynek, Oxidative coupling of methane over oxide-supported barium catalysts, *Journal of Catalysis*, 1993, 143, 286-298.

[46] K.C.C. Kharas and J.H. Lunsford, Catalytic partial oxidation of methane over barium metaplumbate $BaPbO_3$: possible involvement of peroxide ion, *Journal of the American Chemical Society*, 1989, 111, 2336-2337.

[47] J.H. Lunsford, X. Yang, K. Haller, J. Laane, G. Mestl and H. Knoezinger, In situ Raman spectroscopy of peroxide ions on barium/magnesium oxide catalysts, *The Journal of Physical Chemistry*, 1993, 97, 13810-13813.

[48] K.D. Campbell, H. Zhang and J.H. Lunsford, Methane activation by the lanthanide oxides, *The Journal of Physical Chemistry*, 1988, 92, 750-753.

[49] H. Yamashita, Y. Machida and A. Tomita, Oxidative coupling of methane with peroxide ions over barium-lanthanum-oxygen mixed oxide, *Applied Catalysis A: General*, 1991, 79, 203-214.

[50] J.X. Wang and J.H. Lunsford, Evidence for the thermal generation of superoxide ions on lanthanum oxide (La_2O_3), *The Journal of Physical Chemistry*, 1986, 90, 3890-3891.

[51] W. Xia, J.H. Li, W.Z. Weng and H.L. Wan, Can superoxide species be formed at small La–O clusters in the presence of oxygen? A DFT study, *Chemical Physics Letters*, 2006, 423, 427-433.

[52] W. Xia, D. Zhang, W. Weng and H. Wan, Pathways between superoxide and peroxide species on small La-O clusters, *Chinese Journal of Catalysis*, 2013, 34, 2130-2137.

[53] W. Ding, Y. Chen and X. Fu, Oxidative coupling of methane over Ce^{4+}-doped Ba_3WO_6 catalysts: investigation on oxygen species responsible for catalytic performance, *Catalysis Letters*, 1994, 23, 69-78.

[54] Y.H. Hou, W.C. Han, W.S. Xia and H.L. Wan, Structure sensitivity of $La_2O_2CO_3$ catalysts in the oxidative coupling of methane, *ACS Catalysis*, 2015, 5, 1663-1674.

[55] Z.C. Jiang, C.J. Yu, X.P. Fang, S.B. Li, J.H. He and X.H. Luo, Oxidative coupling of methane on W-Mn catalysts, *Journal of Molecular Catalysis (China)*, 1992, 427-433.

[56] S.B. Li, Oxidative coupling of methane over W-Mn/SiO_2 Catalyst, *Chinese Journal of Chemistry*, 2001, 19, 16-21.

[57] J. Wu and S. Li, The role of distorted WO_4 in the oxidative coupling of methane on supported tungsten oxide catalysts, *The Journal of Physical Chemistry*, 1995, 99, 4566-4568.

[58] Z.C. Jiang, H. Gong and S.B. Li, Methane activation over Mn_2O_3-Na_2WO_4/SiO_2 catalyst and oxygen spillover, in: C. Li, Q. Xin (Eds.) *Studies in Surface Science and Catalysis*, Elsevier1997, pp. 481-490.

[59] A. Palermo, J.P. Holgado Vazquez, A.F. Lee, M.S. Tikhov and R.M. Lambert, Critical influence of the amorphous silica-to-cristobalite phase transition on the performance of Mn/Na_2WO_4/SiO_2 catalysts for the oxidative coupling of methane, *Journal of Catalysis*, 1998, 177, 259-266.

[60] S. Sadjadi, S. Jaso, H.R. Godini, S. Arndt, M. Wollgarten, R. Blume, O. Gorke, R. Schomacker, G. Wozny and U. Simon, Feasibility study of the Mn-Na_2WO_4/SiO_2 catalytic system for the oxidative coupling of methane in a fluidized-bed reactor, *Catalysis Science & Technology*, 2015, 5, 942-952.

[61] U. Simon, O. Görke, A. Berthold, S. Arndt, R. Schomäcker and H. Schubert, Fluidized bed processing of sodium tungsten manganese catalysts for the oxidative coupling of methane, *Chemical Engineering Journal*, 2011, 168, 1352-1359.

[62] M. Yildiz, Y. Aksu, U. Simon, T. Otremba, K. Kailasam, C. Göbel, F. Girgsdies, O. Görke, F. Rosowski, A. Thomas, R. Schomäcker and S. Arndt, Silica material variation for the Mn_xO_y-Na_2WO_4/SiO_2, *Applied Catalysis A: General*, 2016, 525, 168-179.

[63] Z.L. Zhang and M. Baerns, Oxidative coupling of methane over CaO-CeO_2 catalysts: Effect of oxygen-ion conductivity on C_2 selectivity, *Journal of Catalysis*, 1992, 135, 317-320.

[64] Z.L. Zhang, X.E. Verykios and M. Baerns, Effect of electronic properties of catalysts for the oxidative coupling of methane on their selectivity and activity, *Catalysis Reviews*, 1994, 36, 507-556.

[65] E.V. Kondratenko, N.G. Maksimov, G.E. Selyutin and A.G. Anshits, Oxidative coupling of methane over oxides of alkali earth metals using N_2O as oxidant, *Catalysis Today*, 1995, 24, 273-275.

[66] M.C. Wu, C.M. Truong, K. Coulter and D.W. Goodman, Investigations of active sites for methane activation in the oxidative coupling reaction over pure and Li-promoted MgO catalysts, *Journal of Catalysis*, 1993, 140, 344-352.

[67] M.C. Wu, C.M. Truong and D.W. Goodman, Electron-energy-loss-spectroscopy studies of thermally generated defects in pure and lithium-doped MgO(100) films on Mo(100), *Physical Review B*, 1992, 46, 12688-12694.

[68] R. Schlögl, Heterogeneous catalysis, *Angewandte Chemie International Edition*, 2015, 54, 3465-3520.

[69] G. Spoto, E.N. Gribov, G. Ricchiardi, A. Damin, D. Scarano, S. Bordiga, C. Lamberti and A. Zecchina, Carbon monoxide MgO from dispersed solids to single crystals: a review and new advances, *Progress in Surface Science*, 2004, 76, 71-146.

[69] U. Zavyalova, M. Holena, R. Schlögl and M. Baerns, Statistical analysis of past catalytic data on oxidative methane coupling for new insights into the composition of high-performance catalysts, *ChemCatChem*, 2011, 3, 1935-1947.

[70] N. Nilius and H.-J. Freund, Activating nonreducible oxides via doping, *Accounts of Chemical Research*, 2015, 48, 1532-1539.

[71] T. Ito, J. Wang, C.H. Lin and J.H. Lunsford, Oxidative dimerization of methane over a lithium-promoted magnesium oxide catalyst, *Journal of the American Chemical Society*, 1985, 107, 5062-5068.

[72] V.R. Choudhary, V.H. Rane and M.Y. Pandit, Comparison of alkali metal promoted MgO catalysts for their surface acidity/basicity and catalytic activity/selectivity in the oxidative coupling of methane, *Journal of Chemical Technology & Biotechnology*, 1997, 68, 177-186.

[73] S.J. Korf, J.A. Roos, L.J. Veltman, J.G. van Ommen and J.R.H. Ross, Effect of additives on lithium doped magnesium oxide catalysts used in the oxidative coupling of methane, *Applied Catalysis*, 1989, 56, 119-135.

[74] A.M. Maitra, I. Campbell and R.J. Tyler, Influence of basicity on the catalytic activity for oxidative coupling of methane, *Applied Catalysis A: General*, 1992, 85, 27-46.

[75] Y. Osada, S. Koike, T. Fukushima, S. Ogasawara, T. Shikada and T. Ikariya, Oxidative coupling of methane over Y_2O_3-CaO catalysts, *Applied Catalysis*, 1990, 59, 59-74.

[76] V.H. Rane, S.T. Chaudhari and V.R. Choudhary, Influence of alkali metal doping on surface properties and catalytic activity/selectivity of CaO catalysts in oxidative coupling of methane, *Journal of Natural Gas Chemistry*, 2008, 17, 313-320.

[77] J.A.S.P. Carreiro and M. Baerns, Oxidative coupling of methane, *Journal of Catalysis*, 1989, 117, 396-403.

[78] S. Arndt, G. Laugel, S. Levchenko, R. Horn, M. Baerns, M. Scheffler, R. Schlögl and R. Schomäcker, A critical assessment of Li/MgO-based catalysts for the oxidative coupling of methane, *Catalysis Reviews*, 2011, 53, 424-514.

[79] C. Mirodatos, V. Perrichon, M.C. Durupty and P. Moral, Deactivation of alkali promoted magnesia in oxidative coupling of methane, in: B. Delmon, G.F. Froment (Eds.) *Studies in Surface Science and Catalysis*, Elsevier1987, pp. 183-195.

[80] S.J. Korf, J.A. Roos, N.A. de Bruijn, J.G. van Ommen and J.R.H. Ross, Oxidative coupling of methane over lithium doped magnesium oxide catalysts, *Catalysis Today*, 1988, 2, 535-545.

[81] S.J. Korf, J.A. Roos, N.A. De Bruijn, J.G. Van Ommen and J.R.H. Ross, Lithium chemistry of lithium doped magnesium oxide catalysts used in the oxidative coupling of methane, *Applied Catalysis*, 1990, 58, 131-146.

[82] S.J. Korf, J.A. Roos, N.A. de Bruijn, J.G. van Ommen and J.R.H. Ross, Influence of CO_2 on the oxidative coupling of methane over a lithium promoted magnesium oxide catalyst, *Journal of the Chemical Society, Chemical Communications*, 1987, 1433-1434.

[83] V.R. Choudhary, V.H. Rane and R.V. Gadre, Influence of precursors used in preparation of MgO on its surface properties and catalytic activity in oxidative coupling of methane, *Journal of Catalysis*, 1994, 145, 300-311.

[84] S. Ardizzone, C.L. Bianchi, M. Fadoni and B. Vercelli, Magnesium salts and oxide: an XPS overview, *Applied Surface Science*, 1997, 119, 253-259.

[85] I.M. Mellor, A. Burrows, S. Coluccia, J.S.J. Hargreaves, R.W. Joyner, C.J. Kiely, G. Martra, M. Stockenhuber and W.M. Tang, Probing possible structure sensitivity in the exchange of isotopic oxygen with the surface of MgO, *Journal of Catalysis*, 2005, 234, 14-23.

[86] W. Hinsen and M. Baerns, Oxidative coupling of methane to C_2-hydrocarbons in the presence of different catalysts, *Chemiker-Zeitung*, 1983, 107, 223-226.

[87] C.A. Jones, J.J. Leonard and J.A. Sofranko, Fuels for the future: remote gas conversion, *Energy & Fuels*, 1987, 1, 12-16.

[88] I.T.A. Emesh and Y. Amenomiya, Oxidative coupling of methane over the oxides of Group IIIA, IVA, and VA metals, *The Journal of Physical Chemistry*, 1986, 90, 4785-4789.

[89] Y. Tong and J.H. Lunsford, Mechanistic and kinetic studies of the reactions of gas-phase methyl radicals with metal oxides, *Journal of the American Chemical Society*, 1991, 113, 4741-4746.

[90] G.-y. Adachi and N. Imanaka, The binary rare earth oxides, *Chemical Reviews*, 1998, 98, 1479-1514.

[91] S. Horoz, S. Simsek, S. Palaz and A.M. Mamedov, Electronic and optical properties of rare earth oxides: *Ab initio* calculation, *World Journal of Condensed Matter Physics*, 2015, 5, 78-85.

[92] K. Otsuka, K. Jinno and A. Morikawa, Active and selective catalysts for the synthesis of C_2H_4 and C_2H_6 via oxidative coupling of methane, *Journal of Catalysis*, 1986, 100, 353-359.

[93] Y. Tong, M.P. Rosynek and J.H. Lunsford, Secondary reactions of methyl radicals with lanthanide oxides: their role in the selective oxidation of methane, *The Journal of Physical Chemistry*, 1989, 93, 2896-2898.

[94] D. Noon, A. Seubsai and S. Senkan, Oxidative coupling of methane by nanofiber catalysts, *ChemCatChem*, 2013, 5, 146-149.

[95] P. Huang, Y. Zhao, J. Zhang, Y. Zhu and Y. Sun, Exploiting shape effects of La_2O_3 nanocatalysts for oxidative coupling of methane reaction, *Nanoscale*, 2013, 5, 10844-10848.

[96] H. Liu, X. Wang, D. Yang, R. Gao, Z. Wang and J. Yang, Scale up and stability test for oxidative coupling of methane over Na_2WO_4-Mn/SiO_2 catalyst in a 200 ml fixed-bed reactor, *Journal of Natural Gas Chemistry*, 2008, 17, 59-63.

[97] J. Wang, L. Chou, B. Zhang, H. Song, J. Zhao, J. Yang and S. Li, Comparative study on oxidation of methane to ethane and ethylene over Na_2WO_4-Mn/SiO_2 catalysts prepared by different methods, *Journal of Molecular Catalysis A: Chemical*, 2006, 245, 272-277.

[98] S.F. Ji, T.C. Xiao, S.B. Li, C.Z. Xu, R.l. Hou, K.S. Coleman and M.L.H. Green, The relationship between the structure and the performance of Na-W-Mn/SiO_2 catalysts for the oxidative coupling of methane, *Applied Catalysis A: General*, 2002, 225, 271-284.

[99] M. Yildiz, Y. Aksu, U. Simon, K. Kailasam, O. Goerke, F. Rosowski, R. Schomacker, A. Thomas and S. Arndt, Enhanced catalytic performance of Mn_xO_y-Na_2WO_4/SiO_2 for the oxidative coupling of methane using an ordered mesoporous silica support, *Chemical Communications*, 2014, 50, 14440-14442.

[100] P. Wang, G. Zhao, Y. Wang and Y. Lu, $MnTiO_3$-driven low-temperature oxidative coupling of methane over TiO_2-doped Mn_2O_3-$Na_2WO_4SiO_2$ catalyst, *Science Advances*, 2017, 3.

[101] R. Burch, G.D. Squire and S.C. Tsang, Role of chlorine in improving selectivity in the oxidative coupling of methane to ethylene, *Applied Catalysis*, 1989, 46, 69-87.

[102] D.J. Wang, M.P. Rosynek and J.H. Lunsford, The effect of chloride ions on a Li^+-MgO catalyst for the oxidative dehydrogenation of ethane, *Journal of Catalysis*, 1995, 151, 155-167.

[103] K. Paredis, L.K. Ono, S. Mostafa, L. Li, Z. Zhang, J.C. Yang, L. Barrio, A.I. Frenkel and B.R. Cuenya, Structure, chemical composition, and reactivity correlations during the in situ oxidation of 2-Propanol, *Journal of the American Chemical Society*, 2011, 133, 6728-6735.

[104] B. Roldan Cuenya, M. Alcántara Ortigoza, L.K. Ono, F. Behafarid, S. Mostafa, J.R. Croy, K. Paredis, G. Shafai, T.S. Rahman, L. Li, Z. Zhang and J.C. Yang, Thermodynamic properties of Pt nanoparticles: Size, shape, support, and adsorbate effects, *Physical Review B*, 2011, 84, 245438.

[105] K.S.W. Sing, D.H. Everett, R.A.W. Haul, L. Moscou, R.A. Pierotti, J. Rouquerol and T. Siemieniewska, Reporting physisorption data for gas/solid systems, *Handbook of Heterogeneous Catalysis*, Wiley-VCH Verlag GmbH & Co. KGaA2008.
[106] A. Taguchi and F. Schüth, Ordered mesoporous materials in catalysis, *Microporous and Mesoporous Materials*, 2005, 77, 1-45.
[107] M.E. Davis, C. Saldarriaga, C. Montes, J. Garces and C. Crowdert, A molecular sieve with eighteen-membered rings, *Nature*, 1988, 331, 698.
[108] A.H. Janssen, A.J. Koster and K.P. de Jong, Three-dimensional transmission electron microscopic observations of mesopores in dealuminated zeolite Y, *Angewandte Chemie*, 2001, 113, 1136-1138.
[109] C.T. Kresge, M.E. Leonowicz, W.J. Roth, J.C. Vartuli and J.S. Beck, Ordered mesoporous molecular sieves synthesized by a liquid-crystal template mechanism, *Nature*, 1992, 359, 710.
[110] U. Ciesla and F. Schüth, Ordered mesoporous materials, *Microporous and Mesoporous Materials*, 1999, 27, 131-149.
[111] A. Corma, From microporous to mesoporous molecular sieve materials and their use in catalysis, *Chemical Reviews*, 1997, 97, 2373-2420.
[112] F. Schüth, Non-siliceous mesostructured and mesoporous materials, *Chemistry of Materials*, 2001, 13, 3184-3195.
[113] B. Chiche, E. Sauvage, F. Di Renzo, I.I. Ivanova and F. Fajula, Butene oligomerization over mesoporous MTS-type aluminosilicates, *Journal of Molecular Catalysis A: Chemical*, 1998, 134, 145-157.
[114] A. Wingen, N. Anastasievič, A. Hollnagel, D. Werner and F. Schüth, Fe-MCM-41 as a catalyst for sulfur dioxide oxidation in highly concentrated gases, *Journal of Catalysis*, 2000, 193, 248-254.
[115] D. Zhao, J. Feng, Q. Huo, N. Melosh, G.H. Fredrickson, B.F. Chmelka and G.D. Stucky, Triblock copolymer syntheses of mesoporous silica with periodic 50 to 300 angstrom pores, *Science*, 1998, 279, 548-552.
[116] X.S. Zhao, F. Audsley and G.Q. Lu, Irreversible change of pore structure of MCM-41 upon hydration at room temperature, *The Journal of Physical Chemistry B*, 1998, 102, 4143-4146.
[117] M. Yildiz, U. Simon, T. Otremba, Y. Aksu, K. Kailasam, A. Thomas, R. Schomäcker and S. Arndt, Support material variation for the Mn_xO_y-Na_2WO_4/SiO_2 catalyst, *Catalysis Today*, 2014, 228, 5-14.
[118] J. Roy, S. Chandra, S. Das and S. Maitr, Oxidation behaviour of silicon carbide - a review, *Reviews On Advanced Materials Science*, 2014, 38, 29-39.
[119] M.J. Ledoux and C. Pham-Huu, Silicon carbide: A novel catalyst support for heterogeneous catalysis, *CATTECH*, 2001, 5, 226-246.
[120] G.-Q. Jin and X.-Y. Guo, Synthesis and characterization of mesoporous silicon carbide, *Microporous and Mesoporous Materials*, 2003, 60, 207-212.
[121] J. Parmentier, J. Patarin, J. Dentzer and C. Vix-Guterl, Formation of SiC via carbothermal reduction of a carbon-containing mesoporous MCM-48 silica phase: A new route to produce high surface area SiC, *Ceramics International*, 2002, 28, 1-7.
[122] Y. Shi, F. Zhang, Y.-S. Hu, X. Sun, Y. Zhang, H.I. Lee, L. Chen and G.D. Stucky, Low-temperature pseudomorphic transformation of ordered hierarchical macro-mesoporous SiO_2/C nanocomposite to SiC via magnesiothermic reduction, *Journal of the American Chemical Society*, 2010, 132, 5552-5553.

[123] B. Zhao, H. Zhang, H. Tao, Z. Tan, Z. Jiao and M. Wu, Low temperature synthesis of mesoporous silicon carbide via magnesiothermic reduction, *Materials Letters*, 2011, 65, 1552-1555.
[124] P. Krawiec, C. Weidenthaler and S. Kaskel, SiC/MCM-48 and SiC/SBA-15 Nanocomposite Materials, *Chemistry of Materials*, 2004, 16, 2869-2880.
[125] P. Krawiec, C. Schrage, E. Kockrick and S. Kaskel, Tubular and rodlike ordered mesoporous silicon (oxy)carbide ceramics and their structural transformations, *Chemistry of Materials*, 2008, 20, 5421-5433.
[126] Y.F. Shi, Y. Meng, D.H. Chen, S.J. Cheng, P. Chen, H.F. Yang, Y. Wan and D.Y. Zhao, Highly ordered mesoporous silicon carbide ceramics with large surface areas and high stability, *Advanced Functional Materials*, 2006, 16, 561-567.
[127] C. Hoffmann, P. Plate, A. Steinbruck and S. Kaskel, Nanoporous silicon carbide as nickel support for the carbon dioxide reforming of methane, *Catalysis Science & Technology*, 2015, 5, 4174-4183.
[128] P. Leroi, B. Madani, C. Pham-Huu, M.-J. Ledoux, S. Savin-Poncet and J.L. Bousquet, Ni/SiC: A stable and active catalyst for catalytic partial oxidation of methane, *Catalysis Today*, 2004, 91-92, 53-58.
[129] H. Liu, D. Yang, R. Gao, L. Chen, S. Zhang and X. Wang, A novel Na_2WO_4-Mn/SiC monolithic foam catalyst with improved thermal properties for the oxidative coupling of methane, *Catalysis Communications*, 2008, 9, 1302-1306.
[130] T. Serres, C. Aquino, C. Mirodatos and Y. Schuurman, Influence of the composition/texture of Mn-Na-W catalysts on the oxidative coupling of methane, *Applied Catalysis A: General*, 2015, 504, 509-518.
[131] V.R. Choudhary, S.A.R. Mulla and B.S. Uphade, Oxidative coupling of methane over alkaline earth oxides deposited on commercial support precoated with rare earth oxides, *Fuel*, 1999, 78, 427-437.
[132] V.D. Sokolovskii, S.M. Aliev, O.V. Buyevskaya and A.A. Davydov, Type of hydrocarbon activation and nature of active sites of base catalysts in methane oxidative dehydrodimerization, *Catalysis Today*, 1989, 4, 293-300.
[133] D.W. Smith, An acidity scale for binary oxides, *Journal of Chemical Education*, 1987, 64, 480.
[134] J.A. Duffy, A review of optical basicity and its applications to oxidic systems, *Geochimica et Cosmochimica Acta*, 1993, 57, 3961-3970.
[135] A. Lebouteiller and P. Courtine, Improvement of a bulk optical basicity table for oxidic systems, *Journal of Solid State Chemistry*, 1998, 137, 94-103.
[136] V.R. Choudhary, S.A.R. Mulla and V.H. Rane, Surface basicity and acidity of alkaline earth-promoted La_2O_3 catalysts and their performance in oxidative coupling of methane, *Journal of Chemical Technology & Biotechnology*, 1998, 72, 125-130.
[137] G.V. Glass, Primary, secondary, and meta-analysis of research, *Educational Researcher*, 1976, 5, 3-8.
[138] E.V. Kondratenko, M. Schluter, M. Baerns, D. Linke and M. Holena, Developing catalytic materials for the oxidative coupling of methane through statistical analysis of literature data, *Catalysis Science & Technology*, 2015, 5, 1668-1677.
[139] R. Schmack, Property-performance relationships of catalysts in the oxidative coupling of methane: a combined statistical and experimental approach, Doctoral thesis, Technische Universitaet Berlin, 2016.
[140] G. Tammann and A. Sworykin, Zur Bestimmung der Temperatur des Zusammenbackens, *Zeitschrift für anorganische und allgemeine Chemie*, 1928, 176, 46-48.

[141] K.H. Stern, The effect of cations on the thermal decomposition of salts with oxyanions: A semi-empirical correlation, *Journal of Chemical Education*, 1969, 46, 645.
[142] M. Kantschewa, E.V. Albano, G. Etrtl and H. Kno¨zinger, Infrared and x-ray photoelectron spectroscopy study of K_2CO_3/γ-Al_2O_3, *Applied Catalysis*, 1983, 8, 71-84.
[143] Y. Zhang, Electronegativities of elements in valence states and their applications. 1. Electronegativities of elements in valence states, *Inorganic Chemistry*, 1982, 21, 3886-3889.
[144] R.G. Charles, Rare-earth carbonates prepared by homogeneous precipitation, *Journal of Inorganic and Nuclear Chemistry*, 1965, 27, 1489-1493.
[145] D.R. Lide, Physical constants of inorganic compounds, *CRC Handbook of Chemistry and Physics, 88th Edition*, CRC Press 2007, pp. 4-50.
[146] K.-i. Aika, T. Moriyama, N. Takasaki and E. Iwamatsu, Oxidative dimerization of methane over $BaCO_3$, $SrCO_3$ and these catalysts promoted with alkali, *Journal of the Chemical Society, Chemical Communications*, 1986, 1210-1211.
[147] Y. Tong, M.P. Rosynek and J.H. Lunsford, The role of sodium carbonate and oxides supported on lanthanide oxides in the oxidative dimerization of methane, *Journal of Catalysis*, 1990, 126, 291-298.
[148] A.M. Gaffney, C.A. Jones, J.J. Leonard and J.A. Sofranko, Oxidative coupling of methane over sodium promoted praseodymium oxide, *Journal of Catalysis*, 1988, 114, 422-432.
[149] A.J. Appleby and S. Nicholson, The reduction of oxygen in molten lithium carbonate, *Journal of Electroanalytical Chemistry and Interfacial Electrochemistry*, 1974, 53, 105-119.
[150] A.J. Appleby and S.B. Nicholson, Reduction of oxygen in lithium-potassium carbonate melt, *Journal of Electroanalytical Chemistry and Interfacial Electrochemistry*, 1980, 112, 71-76.
[151] L.J. Chen, X. Cheng, C.J. Lin and C.M. Huang, In-situ Raman spectroscopic studies on the oxide species in molten Li/K_2CO_3, *Electrochimica Acta*, 2002, 47, 1475-1480.
[152] G. Moutiers, M. Cassir and J. Devynck, Electrochemical characterization of the O_2^-/O_2^{2-} system in molten Na_2CO_3+K_2CO_3 eutectic at 750 °C, *Journal of Electroanalytical Chemistry and Interfacial Electrochemistry*, 1991, 315, 103-112.
[153] J.L. Callahan and R.K. Grasselli, A selectivity factor in vapor-phase hydrocarbon oxidation catalysis, *AIChE Journal*, 1963, 9, 755-760.
[154] J.N. Michaels, D.L. Stern and R.K. Grasselli, Oxydehydrogenation of propane over Mg-V-Sb-oxide catalysts. II. Reaction kinetics and mechanism, *Catalysis Letters*, 1996, 42, 139-148.
[155] D.J. Wang, M.P. Rosynek and J.H. Lunsford, Oxidative coupling of methane over oxide-supported sodium-manganese catalysts, *Journal of Catalysis*, 1995, 155, 390-402.
[156] D. Wang, M. Xu, C. Shi and J.H. Lunsford, Effect of carbon dioxide on the selectivities obtained during the partial oxidation of methane and ethane over Li^+/MgO catalysts, *Catalysis Letters*, 1993, 18, 323-328.
[157] M. Xu, C. Shi, X. Yang, M.P. Rosynek and J.H. Lunsford, Effect of carbon dioxide on the activation energy for methyl radical generation over lithium/magnesia catalysts, *The Journal of Physical Chemistry*, 1992, 96, 6395-6398.
[158] J. Shi, L. Yao and C. Hu, Effect of CO_2 on the structural variation of Na_2WO_4/Mn/SiO_2 catalyst for oxidative coupling of methane to ethylene, *Journal of Energy Chemistry*, 2015, 24, 394-400.

[159] Y. Xu, L. Yu, C. Cai, J. Huang and X. Guo, A study of the oxidative coupling of methane over SrO-La_2O_3/CaO catalysts by using CO_2 as a probe, *Catalysis Letters*, 1995, 35, 215-231.
[160] K.P. Peil, J.G. Goodwin, Marcelin, Jr. and G. Marcelin, Influence of product CO_2 on the overall reaction network in the oxidative coupling of methane, in: A. Holmen, K.J. Jens, S. Kolboe (Eds.) *Studies in Surface Science and Catalysis*, Elsevier1991, pp. 73-79.
[161] B. Litawa, P. Michorczyk and J. Ogonowski, Influence of CO_2 on the catalytic performance of La_2O_3/CeO_2 and CaO/CeO_2 catalysts in the oxidative coupling of methane, *Polish Journal of Chemical Technology*, 2013, 22.
[162] D.W. McKee and D. Chatterji, Corrosion of silicon carbide in gases and alkaline melts, *Journal of the American Ceramic Society*, 1976, 59, 441-444.
[163] Z. Zheng, R.E. Tressler and K.E. Spear, The effect of sodium contamination on the oxidation of single crystal silicon carbide, *Corrosion Science*, 1992, 33, 545-556.
[164] C. Mazzara, J. Jupille, A.M. Flank and P. Lagarde, Stereochemical order around sodium in amorphous silica, *The Journal of Physical Chemistry B*, 2000, 104, 3438-3445.
[165] L.M. D'Assunção, I. Giolito and M. Ionashiro, Thermal decomposition of the hydrated basic carbonates of lanthanides and yttrium, *Thermochimica Acta*, 1989, 137, 319-330.
[166] M.J. Hernandez, M.A. Ulibarri, J. Cornejo, M.J. Peña and C.J. Serna, Thermal stability of aluminium hydroxycarbonates with monovalent cations, *Thermochimica Acta*, 1985, 94, 257-266.
[167] B. Eckhardt, Synthesis of micelle-templated metal oxides as catalysts for the oxidative coupling of methane, Doctoral Thesis, Technische Universitaet Berlin, 2014.
[168] M.A. Alavi and A. Morsali, Syntheses and characterization of $Sr(OH)_2$ and $SrCO_3$ nanostructures by ultrasonic method, *Ultrasonics Sonochemistry*, 2010, 17, 132-138.
[169] B. Eckhardt, E. Ortel, D. Bernsmeier, J. Polte, P. Strasser, U. Vainio, F. Emmerling and R. Kraehnert, Micelle-templated oxides and carbonates of zinc, cobalt, and aluminum and a generalized strategy for their synthesis, *Chemistry of Materials*, 2013, 25, 2749-2758.
[170] T. Mokkelbost, I. Kaus, T. Grande and M.-A. Einarsrud, Combustion synthesis and characterization of nanocrystalline CeO_2-based powders, *Chemistry of Materials*, 2004, 16, 5489-5494.
[171] M. Rahimi-Nasrabadi, S.M. Pourmortazavi, M. Aghazadeh, M.R. Ganjali, M. Sadeghpour Karimi and P. Novrouzi, Samarium carbonate and samarium oxide; synthesis, characterization and evaluation of the photo-catalytic behavior, *Journal of Materials Science: Materials in Electronics*, 2017, 28, 5574-5583.
[172] G. Busca and V. Lorenzelli, Infrared spectroscopic identification of species arising from reactive adsorption of carbon oxides on metal oxide surfaces, *Materials Chemistry*, 1982, 7, 89-126.
[173] D. Jean-Luc and C.C. J., Synergy between stable carbonates and yttria in selective catalytic oxidation of methane, *Chemistry Letters*, 1991, 20, 1089-1092.
[174] K.M. Dooley and J.R.H. Ross, Potassium/calcium/nickel oxide catalysts for oxidative coupling of methane, *Applied Catalysis A: General*, 1992, 90, 159-174.
[175] H.F.W. Taylor, Crystal-structures of some double hydroxideminerals, *Mineralogical Magazine*, 1973, 39, 377-389.
[176] B. Eckhardt, E. Ortel, J. Polte, D. Bernsmeier, O. Görke, P. Strasser and R. Kraehnert, Micelle-templated mesoporous films of magnesium carbonate and magnesium Oxide, *Advanced Materials*, 2012, 24, 3115-3119.

[177] S.W. Bian, J. Baltrusaitis, P. Galhotra and V.H. Grassian, A template-free, thermal decomposition method to synthesize mesoporous MgO with a nanocrystalline framework and its application in carbon dioxide adsorption, *Journal of Materials Chemistry*, 2010, 20, 8705-8710.

[178] H.G. McAdie and J.M. Jervis, The pyrolysis of metal acetates, *Thermochimica Acta*, 1970, 1, 19-28.

[179] A.A. Askadskii, Temperature of onset of intense thermal degradation of polymers, *Computational Materials Science of Polymers,* 2003, pp. 408.

[180] W.H.J. Stork and G.T. Pott, Studies of compound formation on alkali/.gamma.-aluminum oxide catalyst systems using chromium, iron, and manganese luminescence, *The Journal of Physical Chemistry*, 1974, 78, 2496-2506.

[181] R. Włodarczyk, M. Sierka, K. Kwapień, J. Sauer, E. Carrasco, A. Aumer, J.F. Gomes, M. Sterrer and H.-J. Freund, Structures of the ordered water monolayer on MgO(001), *The Journal of Physical Chemistry C*, 2011, 115, 6764-6774.

[182] X. Lu, Z. Liu, Y. Zhu and L. Jiang, Sonochemical synthesis and photocatalytic property of zinc oxide nanoparticles doped with magnesium(II), *Materials Research Bulletin*, 2011, 46, 1638-1641.

[183] Y.T. Chua, A.R. Mohamed and S. Bhatia, Oxidative coupling of methane for the production of ethylene over sodium-tungsten-manganese-supported-silica catalyst (Na-W-Mn/SiO_2), *Applied Catalysis A: General*, 2008, 343, 142-148.

[184] S. Ji, T. Xiao, S. Li, L. Chou, B. Zhang, C. Xu, R. Hou, A.P.E. York and M.L.H. Green, Surface WO_4 tetrahedron: the essence of the oxidative coupling of methane over M-W-Mn/SiO_2 catalysts, *Journal of Catalysis*, 2003, 220, 47-56.

[185] J.-W. Kim and H.-G. Lee, Thermal and carbothermic decomposition of Na_2CO_3 and Li_2CO_3, *Metallurgical and Materials Transactions B*, 2001, 32, 17-24.

[186] W.M. Shaheen and M.M. Selim, Thermal decompositions of pure and mixed manganese carbonate and ammonium molybdate tetrahydrate, *Journal of Thermal Analysis and Calorimetry*, 2000, 59, 961-970.

[187] L.M. D'Assunção, M. Ionashiro, D.E. Rasera and I. Giolito, Thermal decomposition of the hydrated basic carbonates of lanthanides and yttrium in CO_2 atmosphere, *Thermochimica Acta*, 1993, 219, 225-233.

[188] S.H. Kim, S.M. Cho and K.J. Yoon, Oxidative coupling of methane over Na^+-ZrO_2-Cl^-/Al_2O_3 catalysts, *Korean Journal of Chemical Engineering*, 1997, 14, 69-73.

[189] J. Rynkowski, A. Kaźmierczak, A. Praźmowska-Wilanowska and T. Paryjczak, Influence of calcination and lithium promotion on the surface properties of oxide supports, *Reaction Kinetics and Catalysis Letters*, 1996, 58, 169-175.

[190] A.M. Maitra, Solid-state basicity as a guide to formulation of improved catalysts for oxidative coupling of methane, *Applied Catalysis A: General*, 1994, 114, 65-81.

[191] S. Arndt, U. Simon, S. Heitz, A. Berthold, B. Beck, O. Görke, J.-D. Epping, T. Otremba, Y. Aksu, E. Irran, G. Laugel, M. Driess, H. Schubert and R. Schomäcker, Li-doped MgO from different preparative routes for the oxidative coupling of methane, *Topics in Catalysis*, 2011, 54, 1266-1285.

[192] A. Vaccari, Preparation and catalytic properties of cationic and anionic clays, *Catalysis Today*, 1998, 41, 53-71.

[193] J.S. Valente, G. Rodriguez-Gattorno, M. Valle-Orta and E. Torres-Garcia, Thermal decomposition kinetics of MgAl layered double hydroxides, *Materials Chemistry and Physics*, 2012, 133, 621-629.

[194] P.P. Fedorov and N.V. Il'in, Yttrium carbonate thermolysis, *Russian Journal of Inorganic Chemistry*, 2012, 57, 237-241.

[195] S.M.S. Al-Zahrani and L.L. Lobban, Effects of steam and liquid water treatment on the oxidative coupling of methane over a Li/MgO Catalyst, *Industrial & Engineering Chemistry Research*, 1995, 34, 1060-1073.

[196] R.D. Shannon, Revised effective ionic-radii and systematic studies of interatomic distances in halides and chalcogenides, *Acta Crystallographica Section A*, 1976, 32, 751-767.

[197] H.R. Momenian, S. Gholamrezaei, M. Salavati-Niasari, B. Pedram, F. Mozaffar and D. Ghanbari, Sonochemical synthesis and photocatalytic properties of metal hydroxide and carbonate (M:Mg, Ca, Sr or Ba) Nanoparticles, *Journal of Cluster Science*, 2013, 24, 1031-1042.

[198] A. Davidson and M. Che, Temperature-induced diffusion of probe vanadium(IV) ions into the matrix of titanium dioxide as investigated by ESR techniques, *The Journal of Physical Chemistry*, 1992, 96, 9909-9915.

[199] D.J.M. Bevan, J.P. Shelton and J.S. Anderson, 351. Properties of some simple oxides and spinels at high temperatures, *Journal of the Chemical Society (Resumed)*, 1948, 1729-1741.

[200] R. Merkle and J. Maier, On the Tammann-Rule, *Zeitschrift für anorganische und allgemeine Chemie*, 2005, 631, 1163-1166.

[201] A. Palermo, J.P. Holgado Vazquez and R.M. Lambert, New efficient catalysts for the oxidative coupling of methane, *Catalysis Letters*, 2000, 68, 191-196.

[202] S.C. Su and A.T. Bell, Raman studies of peroxide formation, decomposition, and reduction on Ba/MgO, *Catalysis Letters*, 1996, 36, 15-19.

[203] S. Aldridge, The chemistry of the Group 13 metals in the +3 oxidation state: Simple inorganic compounds, *The Group 13 metals aluminium, gallium, indium and thallium: Chemical patterns and peculiarities*, John Wiley & Sons, Ltd, 2011, pp. 75-147.

[204] K. Foger, M. Hoang and T.W. Turney, Formation and thermal decomposition of rare-earth carbonates, *Journal of Materials Science*, 1992, 27, 77-82.

[205] D. Vijayalakshmi, N.V. Chandra Shekar, S. Ramya, P.C. Sahu and G. Meenakshi, Investigation of diphasic region in the Pr_2O_3+Sm_2O_3 mixed oxide system at various temperatures, *Journal of Alloys and Compounds*, 2010, 505, 733-738.

Acknowledgement

I would like to thank many people who have supported me for my doctoral research in the last four years. I am very grateful for their help and support.

First of all, I would like to extend my sincere gratitude to my supervisor, Dr.-Ing. Ralph Krähnert. His instructive guidance and useful advices have always been of great benefit to me. I would also like to thank him for the numerous discussions and feedback, as well as the opportunities for scientific communication with cooperation partners and participation in conferences.

Second, I would like to express my heartfelt gratitude to my co-advisor, PD Dr. Evgenii Kondratenko in Leibniz-Institut für Katalyse, for his tremendous help and advices with regard to catalytic performance testing.

Special thanks to the reviewers of this thesis, Prof. Dr. Thomas Risse and Prof. Dr. Reinhard Schomäcker. I also thank Prof. Arne Thomas for his willingness to take charge of the defense of my thesis.

I am also deeply indebted to the Cluster of Excellence UniCat for their scientific support as well as the scholarship of graduate school BIG-NSE. I would like to express my special thanks to Dr.-Ing. Jean-Philippe Lonjaret for organizing beneficial initial phase, numerous scientific lectures and social events, as well as his warming help to me in the past years. I would like to thank all BIG-NSE students for their professional scientific discussions as well as their diversified cultural insights.

I would like to thank my colleagues in the Working Group of Krähnert: Kornelia Weh, Benjamin Paul, Dr. Roman Schmack, Dr. Denis Bernsmeier, Dr. Björn Eckhardt, Dr. Michael Bernicke, Katrin Schulz, René Sachse and Quan Li. I thank these wonderful colleagues for their continuous assistance, personal friendship and an open-minded atmosphere in the group.

I would also like to thank Prof. Peter Strasser and the colleagues of his working group for their support and the friendly interaction, in particular Dr. Arno Bergmann, Dr. Nathaniel Leonard, Manuel Gliech, Fang Luo, Camillo Spöri, Wen Ju, Xingli Wang and Yanyan Sun.

Many thanks to the cooperation partners for the fruitful collaboration: Dr. Sergey Sokolov, Matthias Albrecht, Tatiana Otroshchenko, Shanlei Han and Zeynep Aydin in Leibniz-Institut für Katalyse, Chengyue Guan in UniCat BASF JointLab, Stefan Rümmler in Martin-Luther-Universität Halle-Wittenberg.

I would also like to thank the team of analytical test center in Institut für Chemie, Astrid Müller-Klauke and Dr. Frank Beuster for the ICP-OES and FT- IR analysis, as well as numerous scientists from other cooperation.

My special thanks to my beloved parents, my wife, and all my friends who supported me during my doctoral research.

Appendix

A1. Introduction

A1.5 Concept for a unified explanation of OCM across all active catalysts

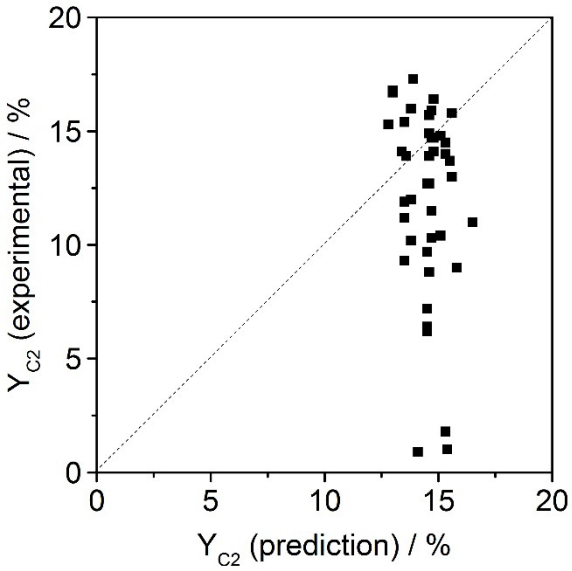

Fig. A1.1: Correlation between predicted and experimentally measured C_2 yield for catalysts presented in Kondratenko's paper.[138] The data of predicted and experimental C_2 yield were abstracted from Table 1 shown in the paper.

Table A1.1: Smith basicity scale values of selected oxides, adapted from [133]. More basic oxide has more negative a value.

	oxide	a	oxide	a	
water	H_2O	0	TiO_2	0.7	**transition metals**
alkali metal	Li_2O	-9.2	ZrO_2	0.1	
	Na_2O	-12.5	V_2O_5	3.0	
	K_2O	-14.6	CrO_3	6.6	
	Rb_2O	-15.0	MoO_3	5.2	
	Cs_2O	-15.2	MnO	-4.8	
alkaline earth metal	BeO	-2.2	Mn_2O_7	9.6	
	MgO	-4.5	Tc_2O_7	9.6	
	CaO	-7.5	Re_2O_7	9.0	
	SrO	-9.4	FeO	-3.4	
	BaO	-10.8	Fe_2O_3	-1.7	
	RaO	-11.5	CoO	-3.8	
rare earth metal	Y_2O_3	-6.5	NiO	-2.4	
	La_2O_3	-6.1	Cu_2O	-1.0	
	Ce_2O_3	-5.8	CuO	-2.5	
	CeO_2	-2.7	Ag_2O	-5.0	
	Nd_2O_3	-5.7	ZnO	-3.2	
	Sm_2O_3	-5.1	CdO	-4.4	
	Gd_2O_3	-5.0	HgO	-3.5	
	Pr_2O_3	-5.8	WO_3	4.7	
	Eu_2O_3	-5.1	Al_2O_3	-2.0	**others**
	Tb_2O_3	-4.3	PbO	-4.5	
	Dy_2O_3	-4.7	Bi_2O_3	-3.7	
	Ho_2O_3	-4.5	Ga_2O_3	-1.6	
	Er_2O_3	-4.3	B_2O_3	1.5	
	Tm_2O_3	-4.2	CO_2	5.5	
	Yb_2O_3	-4.5	SO_3	10.5	
	Lu_2O_3	-3.3	P_4O_{10}	7.5	
	ThO_2	-3.8	SiO_2	0.9	

Table A1.2: Polarizing power values of selected cations, adapted from [143].

	cation	Z/r^2	cation	Z/r^2	
alkali metal	Li^+	1.235	Ti^{4+}	7.207	**transition metal**
	Na^+	0.743	Zr^{4+}	5.408	
	K^+	0.433	V^{5+}	13.007	
	Rb^+	0.363	Cr^{3+}	5.263	
	Cs^+	0.305	Mo^{6+}	11.259	
alkaline earth metal	Be^{2+}	5.746	Mn^{2+}	3.287	
	Mg^{2+}	2.704	Fe^{2+}	3.463	
	Ca^{2+}	1.539	Co^{2+}	3.652	
	Sr^{2+}	1.148	Ni^{2+}	3.858	
	Ba^{2+}	0.901	Cu^{2+}	3.858	
rare earth metal	Y^{3+}	2.774	Ag^+	0.601	
	La^{3+}	2.184	Zn^{2+}	3.652	
	Ce^{4+}	3.921	Cd^{2+}	2.041	
	Nd^{3+}	2.379	Al^{3+}	6.584	**others**
	Sm^{3+}	2.488	Pb^{2+}	1.389	
	Gd^{3+}	2.582	Bi^{3+}	3.255	
	Pr^{3+}	2.349	Ga^{3+}	5.194	
	Eu^{3+}	2.539			
	Tb^{3+}	2.655			
	Dy^{3+}	2.711			
	Ho^{3+}	2.768			
	Er^{3+}	2.828			
	Tm^{3+}	2.884			
	Yb^{3+}	2.953			
	Lu^{3+}	2.994			

Table A1.3: Element-property table in the order of atomic number. Melting point of chemically most stable oxide (T_{melt}) and decomposition temperature of carbonate (T_{dec}) for each element are documented by value extraction from literatures.

Element	Atomic number	Melting point of chemically most stable oxide (T_{melt}) / K	Reference of T_{melt}	ability to form a carbonate	Decomp.T of carbonate (T_{dec}) / °C	Reference of T_{dec}
Li	3	1834	Chase, M. W. J. (1998). NIST-JANAF Thermochemical Tables. 4(9).	yes	720	Kim, J.-W. et al. (2001). Metallurgical and Materials Transactions B, 32: 17.
Be	4	2803	Semenov, A.P. (2008), Journal of Friction and Wear, Vol. 28, No. 5, pp.392-404	yes	25	Holleman, A. and Wiberg, N. (2007). vol 102., Berlin
B	5	723	Chase, M. W. J. (1998). NIST-JANAF Thermochemical Tables, 4(9).	no		
C	6			no		
N	7			no		
O	8			no		
F	9			no		
Na	11	1405	Chase, M. W. J. (1998). NIST-JANAF Thermochemical Tables. 4(9).	yes	840	Duval, C. et al. (1963). Inorganic Thermogravimetric analysis, New York.

Mg	12	3105	Chase, M. W. J. (1998). NIST-JANAF Thermochemical Tables, 4(9).	yes	469	Stern, K. H. and Weise, E. L. (1969). Technical report, DTIC Document.
Al	13	2327	Chase, M. W. J. (1998). NIST-JANAF Thermochemical Tables, 4(9).	no		
Si	14	1996	Chase, M. W. J. (1998). NIST-JANAF Thermochemical Tables, 4(9).	no		
P	15	631	Chase, M. W. J. (1998). NIST-JANAF Thermochemical Tables, 4(9).	no		
S	16			no		
Cl	17			no		
K	19	782	Holleman, A. and Wiberg, N. (2007). vol 102., Berlin	yes	875	Duval, C. et al. (1963). Inorganic Thermogravimetric analysis, New York.
Ca	20	3200	Chase, M. W. J. (1998). NIST-JANAF Thermochemical Tables, 4(9).	yes	661	L'vov, B. V. (2002).. Thermochimica Acta, 386(1):1-16.
Sc	21	2676	Holleman, A. and Wiberg, N. (2007). vol 102., Berlin	yes	440	Head, E. L. (1971). Journal of Inorganic and Nuclear Chemistry, 33(4):1201-1203.
Ti	22	2403	Chase, M. W. J. (1998). NIST-JANAF Thermochemical Tables, 4(9).	no		
V	23	943	Chase, M. W. J. (1998). NIST-JANAF Thermochemical Tables, 4(9).	no		
Cr	24	2603	Chase, M. W. J. (1998). NIST-JANAF Thermochemical Tables, 4(9).	yes	200	Bhatti, A. S. et al. (1984),Thermochimica acta, 77(1):395-406.
Mn	25	2123	Holleman, A. and Wiberg, N. (2007). vol 102., Berlin	yes	300	Shaheen, W. M. et al. (2000). Journal of Thermal Analysis and Calorimetry, 59(3):961-970.
Fe	26	1870	Chase, M. W. J. (1998). NIST-JANAF Thermochemical Tables, 4(9).	yes	220	Gotor, F. J. et al., (2000). Chemistry of Minerals, 27(7):495-503.
Co	27	2103	Chase, M. W. J. (1998). NIST-JANAF Thermochemical Tables, 4(9).	yes	360	Avramov, L. et al. (1971). Zeitsch. anorg. und allg. Chemie, 383(1):96-103
Ni	28	2257	Holleman, A. and Wiberg, N. (2007). vol 102., Berlin	yes	280	Mansour, S. A. A. (1993). Thermochim- ica acta, 228:155-171.
Cu	29	1517	Chase, M. W. J. (1998). NIST-JANAF Thermochemical Tables, 4(9).	yes	260	Shaheen, W. M. et al. (2009). J. of Alloys and Compounds, 476(1):366-372.
Zn	30	2248	Holleman, A. and Wiberg, N. (2007). vol 102., Berlin	yes	220	Kanari, N et al. (2004),Thermochimica Acta, 410(1):93-100.
Ga	31	1998	Holleman, A. and Wiberg, N. (2007). vol 102., Berlin	yes	140	Watanabe, T. et al. (2010). Journal of the American Ceramic Society93(11):3908-3915.
Ge	32	1359	Holleman, A. and Wiberg, N. (2007). vol 102., Berlin	no		
As	33	586	Holleman, A. and Wiberg, N. (2007). vol 102., Berlin	no		
Se	34	613	Holleman, A. and Wiberg, N. (2007). vol 102., Berlin	no		

Br	35			no		
Rb	37	705	Holleman, A. and Wiberg, N. (2007). vol 102., Berlin	yes	800	Erdey, L. el at. (1965). Talanta, 12: 883.
Sr	38	2938	Chase, M. W. J. (1998). NIST-JANAF Thermochemical Tables, 4(9).	yes	850	Stern, K. H. and Weise, E. L. (1969). Technical report, DTIC Document.
Y	39	2959	Rao, C. N. R. et al (1974), NBS Reference Data System Paper, 49.	yes	560	d'Assuncao, L. M., et al. (1989). Thermochimica Acta, 137(2):319-330.
Zr	40	2950	Chase, M. W. J. (1998). NIST-JANAF Thermochemical Tables, 4(9).	yes	25	Gestis database Accessed: (January 20, 2016).
Nb	41	1785	Chase, M. W. J. (1998). NIST-JANAF Thermochemical Tables, 4(9).	no		
Mo	42	1074	Chase, M. W. J. (1998). NIST-JANAF Thermochemical Tables, 4(9).	no		
Ru	44	1680	Rao, C. N. R. et al (1974)., NBS Reference Data System Paper, 49.	no		
Rh	45	1323	Holleman, A. and Wiberg, N. (2007). vol 102., Berlin	no		
Pd	46	1070	Rao, C. N. R. et al (1974). NBS Reference Data System Paper, 49.	no		
Ag	47	500	Rao, C. N. R. et al (1974), NBS Reference Data System Paper, 49.	yes	190	Yoshikawa, M., et al. (2014). The Journal of Physical Chemistry C, 118(15):8059-8070.
Cd	48	1773	O. Madelung, et al., (1999), Landolt-Börnstein - Group III Condensed Matter 41B	yes	340	Reich, L. et al.,. (1989). Thermochimica Acta, 138(1):147-160.
In	49	2183	Anthony John Downs (1993). Springer.	no		
Sn	50	1903	Holleman, A. and Wiberg, N. (2007). vol 102., Berlin	no		
Sb	51	928	Holleman, A. and Wiberg, N. (2007). vol 102., Berlin	no		
Te	52	1006	Holleman, A. and Wiberg, N. (2007). vol 102., Berlin	no		
I	53			no		
Cs	55	873	Holleman, A. and Wiberg, N. (2007). vol 102., Berlin	yes	700	Erdey, L. el at. (1965). Talanta, 12: 257.
Ba	56	2386	Chase, M. W. J. (1998). NIST-JANAF Thermochemical Tables, 4(9).	yes	1067	Arvanitidis, I. et al., (1996) Metallurgical and Materials Transactions B, 27(3):409-416.
La	57	2578	Coutures, J. et al., (1989). Pure and Applied Chemistry, 61(8):1461-1482.	yes	670	Charles, R. G. (1965). Journal of Inorganic and Nuclear Chemistry, 27(7):1489-1493.
Ce	58	2998	Semenov, A.P. (2008), Journal of Friction and Wear, Vol. 28, No. 5, pp.392-404	yes	420	Charles, R. G. (1965), Journal of Inorganic and Nuclear Chemistry, 27(7):1489-1493.
Pr	59	2573	Coutures et al. (1989), Pure and Applied Chemistry, 61(8):1461-1482.	yes	530	Charles, R. G. (1965), Journal of Inorganic and Nuclear Chemistry, 27(7):1489-1493.

Nd	60	2593	Coutures et al. (1989), Pure and Applied Chemistry, 61(8):1461-1482.	yes	610	Charles, R. G. (1965), Journal of Inorganic and Nuclear Chemistry, 27(7):1489-1493.
Pm	61	2593	Coutures et al. (1989), Pure and Applied Chemistry, 61(8):1461-1482.	yes		
Sm	62	2608	Coutures et al. (1989), Pure and Applied Chemistry, 61(8):1461-1482.	yes	560	Charles, R. G. (1965), Journal of Inorganic and Nuclear Chemistry, 27(7):1489-1493.
Eu	63	2623	Coutures et al. (1989), Pure and Applied Chemistry, 61(8):1461-1482.	yes	560	Charles, R. G. (1965), Journal of Inorganic and Nuclear Chemistry, 27(7):1489-1493.
Gd	64	2693	Coutures et al. (1989), Pure and Applied Chemistry, 61(8):1461-1482.	yes	600	Charles, R. G. (1965), Journal of Inorganic and Nuclear Chemistry, 27(7):1489-1493.
Tb	65	2683	Coutures et al. (1989), Pure and Applied Chemistry, 61(8):1461-1482.	yes	490	Charles, R. G. (1965), Journal of Inorganic and Nuclear Chemistry, 27(7):1489-1493.
Dy	66	2681	Coutures et al. (1989), Pure and Applied Chemistry, 61(8):1461-1482.	yes	530	Charles, R. G. (1965), Journal of Inorganic and Nuclear Chemistry, 27(7):1489-1493.
Ho	67	2688	Coutures et al. (1989), Pure and Applied Chemistry, 61(8):1461-1482.	yes	570	Charles, R. G. (1965), Journal of Inorganic and Nuclear Chemistry, 27(7):1489-1493.
Er	68	2691	Coutures et al. (1989), Pure and Applied Chemistry, 61(8):1461-1482.	yes	600	Charles, R. G. (1965), Journal of Inorganic and Nuclear Chemistry, 27(7):1489-1493.
Tm	69	2698	Coutures et al. (1989), Pure and Applied Chemistry, 61(8):1461-1482.	yes	600	Charles, R. G. (1965), Journal of Inorganic and Nuclear Chemistry, 27(7):1489-1493.
Yb	70	2708	Coutures et al. (1989), Pure and Applied Chemistry, 61(8):1461-1482.	yes	600	Charles, R. G. (1965), Journal of Inorganic and Nuclear Chemistry, 27(7):1489-1493.
Lu	71	2763	Coutures et al. (1989), Pure and Applied Chemistry, 61(8):1461-1482.	yes	620	Charles, R. G. (1965), Journal of Inorganic and Nuclear Chemistry, 27(7):1489-1493.
Hf	72	3070	Rao, C. N. R. et al (1974), NBS Reference Data System Paper, 49.	no		
Ta	73	2058	Chase, M. W. J. (1998). NIST-JANAF Thermochemical Tables, 4(9).	no		
W	74	1745	Chase, M. W. J. (1998). NIST-JANAF Thermochemical Tables, 4(9).	no		
Re	75	1320	Rao, C. N. R. et al (1974), NBS Reference Data System Paper, 49.	no		
Os	76	310	Rao, C. N. R. et al (1974), NBS Reference Data System Paper, 49.	no		
Ir	77		Rao, C. N. R. et al (1974), NBS Reference Data System Paper, 49.	no		
Pt	78	890	Rao, C. N. R. et al (1974), NBS Reference Data System Paper, 49.	no		
Au	79	433	Holleman, A. and Wiberg, N. (2007). vol 102., Berlin	no		
Hg	80	749	Chase, M. W. J. (1998). NIST-JANAF Thermochemical Tables, 4(9).	no		

Tl	81	1029	Holleman, A. and Wiberg, N. (2007). vol 102., Berlin	yes	615	Duval (1963), Inorganic Thermogravimetric Analysis, 2. and rev. ed., Elsevier, Amsterdam
Pb	82	1170	Holleman, A. and Wiberg, N. (2007). vol 102., Berlin	yes	412	Stern, K. H. and Weise, E. L. (1969). Technical report, DTIC Document.
Bi	83	1098	Holleman, A. and Wiberg, N. (2007). vol 102., Berlin	yes	380	Henmi, H. et al., (1987). Thermochimica Acta, 114(2):393–396.
Po	84					
At	85					
Fr	87					
Ra	88					
Ac	89					
Th	90	3323	Semenov, A.P. (2008), Journal of Friction and Wear, Vol. 28, No. 5, pp.392-404	yes	300	
Pa	91					
U	92					

A2. OCM investigation of Mn/Na/W/SiC catalyst using porous silicon carbide as a support

A2.2 Catalyst characterization

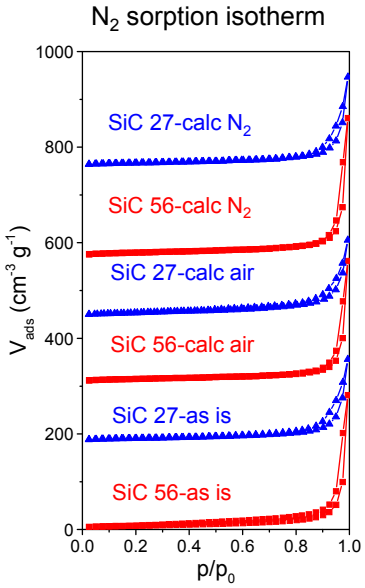

Fig. A2.1: N_2 physisorption isotherms of uncoated SiC 27 and SiC 56 support as is, calcined in air and calcined in N_2 at 800°C for 8h, respectively (appropriate offset). SiC 27 and SiC 56 showed type IV isotherm with H3 hysteresis loop indicating the existence of porous structure. After calcination in air or N_2 at 800 °C, the isotherms still keep similar correspondingly.

Table A2.1: The intended and determined loading of Mn, Na and W by ICP-OES. For SiC supported catalysts, the determined loading amount of Na and W are similar to the intended value. But determined Mn amount is apparently lower than the intended value, which may be attributed to the incomplete dissolution of Mn species in concentrated acid during sample pre-treatment for ICP-OES. For SiO_2 supported catalysts, the determined Mn, Na and W values are close to the intended amount. [a] As-coated samples were used for ICP-OES. Weight ratio of Mn, Na and W are compared to the support. SiC support can be oxidized into SiO_2 after calcination in air, inducing mass increase of the global catalyst. But in as-coated samples, SiC support shows no change, which can be used for a reasonable comparison.

metal components	intended loading (wt%)	determined loading (wt%)		
		SiC 27-Mn/Na/W[a]	SiC 56-Mn/Na/W[a]	SiO_2-Mn/Na/W[a]
Mn	2.00	1.81	1.85	1.98
Na	0.78	0.63	0.73	0.92
W	3.13	2.52	2.62	3.59

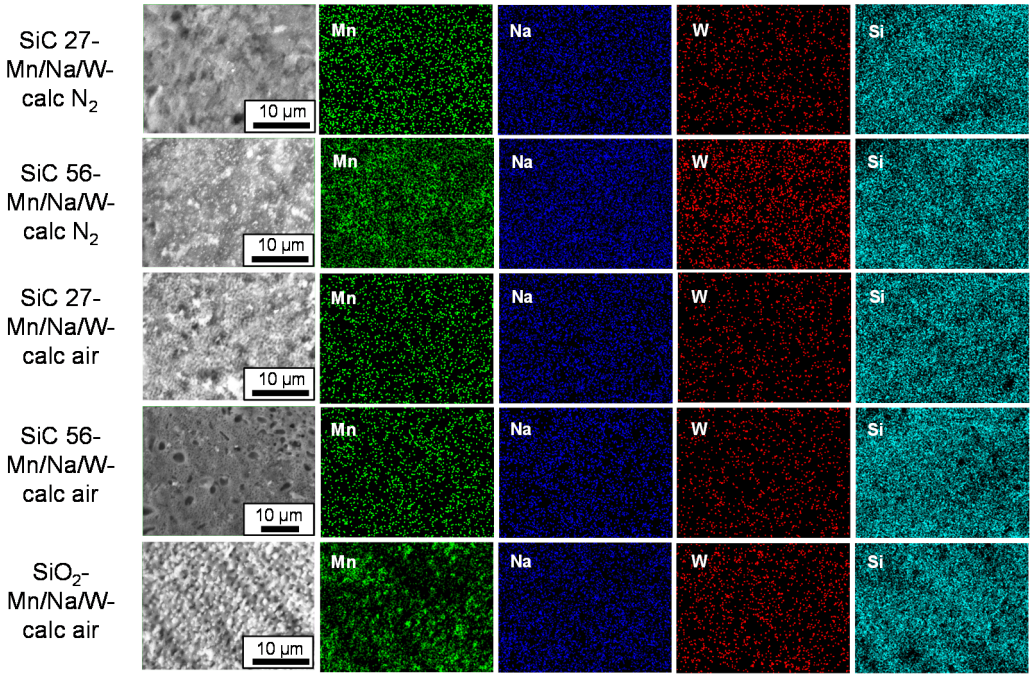

Fig. A2.2: EDX mapping of Mn K-edge (green), Na K-edge (blue), W L-edge (red) and Si K-edge (cyan) for SiC 27-Mn/Na/W and SiC 56-Mn/Na/W calcined in N_2 and in air and SiO_2-Mn/Na/W calcined in air. The homogeneous distribution of Mn, Na and W element in micrometer scale is observed for catalysts calcined in air and in N_2. The morphology can be clearly distinguished from EDX mapping of Si, indicating this magnitude exhibits sufficient resolution.

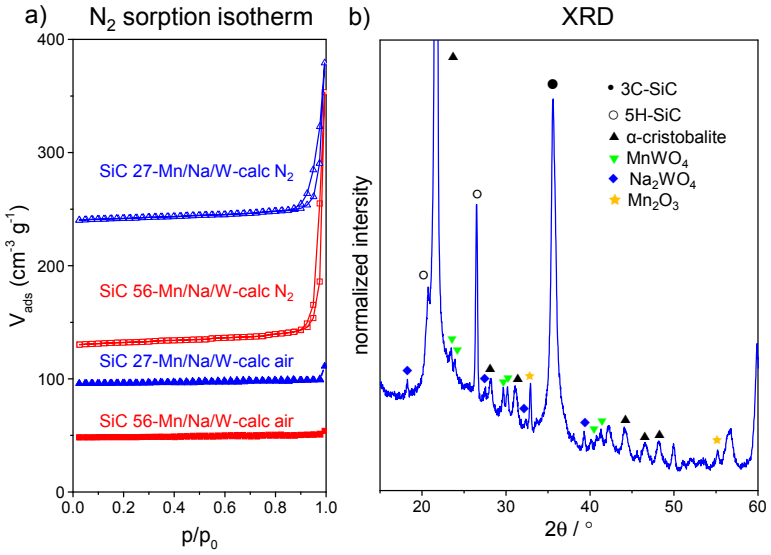

Fig. A2.3: N_2 physisorption isotherms (a) of SiC 27-Mn/Na/W and SiC 56-Mn/Na/W calcined in air and N_2 (appropriate offset). XRD pattern magnification (b) of SiC 27-Mn/Na/W calcined in air at 800 °C. The isotherms of Mn/Na/W/SiC calcined in air did not show hysteresis loop due to the loss of porosity. After calcination in air, 3C-SiC changed to a mixture composed of 3C-SiC, 5H-SiC and α-cristobalite. In addition, Na_2WO_4, Mn_2WO_4, Mn_2O_3 were formed, which usually appeared in Mn/Na/W/SiO_2 catalyst system. However, the isotherms of Mn/Na/W/SiC calcined in N_2 still show hysteresis loop suggesting the existence of porosity.

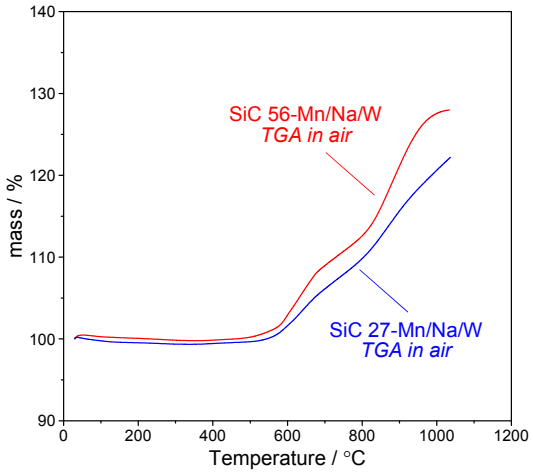

Fig. A2.4: Thermogravimetric analysis record for SiC 27-Mn/Na/W (blue) and SiC 56-Mn/Na/W (red) tested in air. Both of them showed similar onset temperature at about 450 °C. However, SiC 27 exhibited a slower weight increase rate compared to SiC 56. Furthermore, the total oxidized amount of SiC is less than SiC 56. This suggests that SiC 27 undergoes less oxidation than SiC 56 at same temperature ramping and atmosphere condition.

A2.3 OCM Catalytic test results

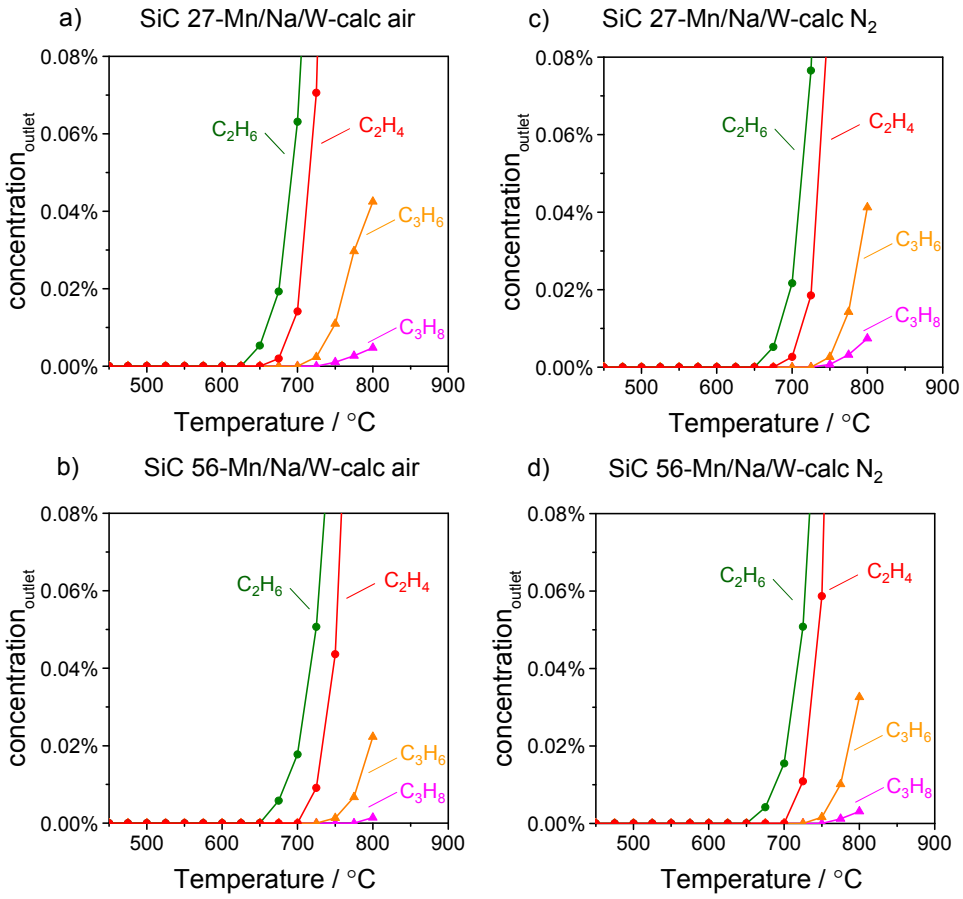

Fig. A2.5: C_2 and C_3 product concentration vs. temperature for SiC 27-Mn/Na/W and SiC 56-Mn/Na/W after calcination in air (a, b) and in N_2,(c, d). Propane and propene form significantly between 750 and 800 °C. They are in a small quantity, which are much less than C_2 product at the same temperature. Therefore, for both catalysts ethane and ethylene are the main product at 800 °C.

Table A2.2: Carbon balance for each catalyst at different temperature. All values are close to 100% within ± 2% for all conditions where SiC is not obviously oxidized.

Temperature (°C)	Carbon balance (%)				
	SiC 27-Mn/Na/W-calc air	SiC 56-Mn/Na/W-calc air	SiC 27-Mn/Na/W-calc N_2	SiC 56-Mn/Na/W-calc N_2	SiO_2-Mn/Na/W-calc air
450	100.4	100.0	100.7	100.4	100.5
475	100.5	100.9	101.5	101.0	100.6
500	100.5	100.7	101.3	100.3	101.3
525	100.8	100.2	100.6	100.8	100.1
550	101.1	101.2	100.6	101.2	100.1
575	100.1	100.4	101.3	101.6	100.8
600	100.4	100.6	101.3	101.2	100.2
625	100.6	100.7	101.5	102.0	100.4
650	100.3	100.5	101.5	101.0	100.4
675	100.2	100.7	100.9	101.1	100.1
700	100.0	99.8	100.6	101.2	100.3
725	100.3	99.2	100.5	101.3	100.6
750	99.5	98.8	99.6	100.6	99.8
775	98.9	98.2	100.1	100.0	98.7
800	100.1	99.4	100.5	100.5	99.6

A2.5 Comparison between SiC and SiO_2 as a support

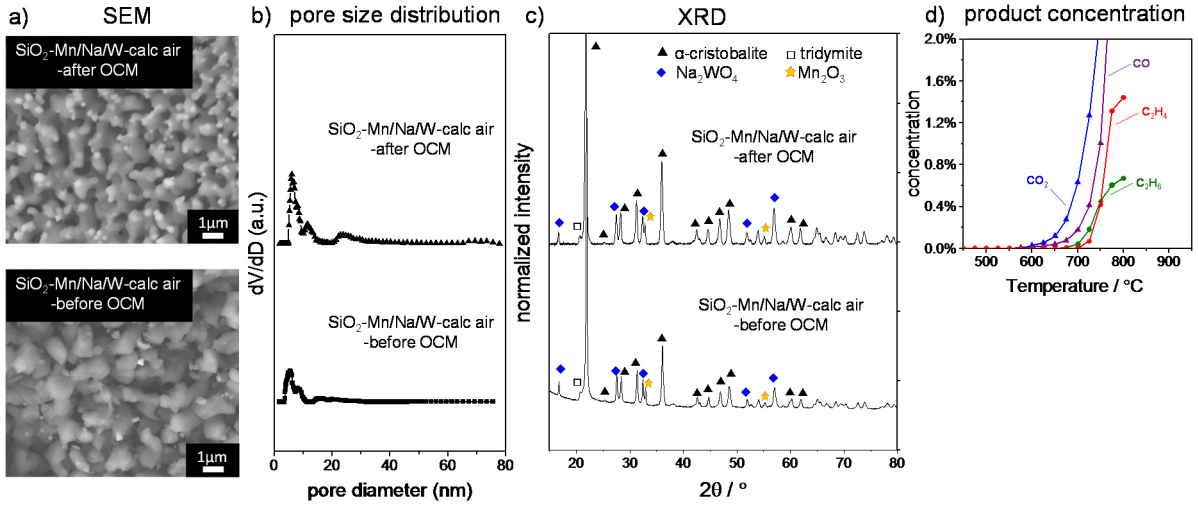

Fig. A2.6: SEM images (a), pore size distribution (b) and XRD patterns (c) of Mn/Na/W/SiO_2 calcined in air before and after OCM testing. Product concentration vs. temperature (d) for SiO_2-Mn/Na/W calcined in air. Fresh catalyst exhibited a sintering structure and further sintering occurred after OCM. Similar to the SiC-based materials, the catalyst is composed of α-cristobalite, tridymite, Na_2WO_4 and Mn_2O_3. Also it shows a similar influence of temperature on product formation.

A3. Synthesis, characterization and property-descriptors of oxide-supported and carbonate-supported catalysts

A3.3 Oxide-supported carbonate catalysts

A3.3.1 Morphology and elemental distribution (SEM and EDX mapping)

Pure oxide supports

Metal oxide granules were calcined at 800 °C in air before using as support in order to maintain stable at typical OCM temperature later.

Fig. A3.1 shows the morphology of pure metal oxide after treatment at 800°C. Y_2O_3 and Gd_2O_3 exhibit grain-like morphology with particle in size range 0.5 - 2.0 µm. Sm_2O_3 and CeO_2 show bulk morphology with rough surface. Differently, SrO, BaO and Al_2O_3 show a bulk morphology, which seem to consist of a large amount of fine particles inside.

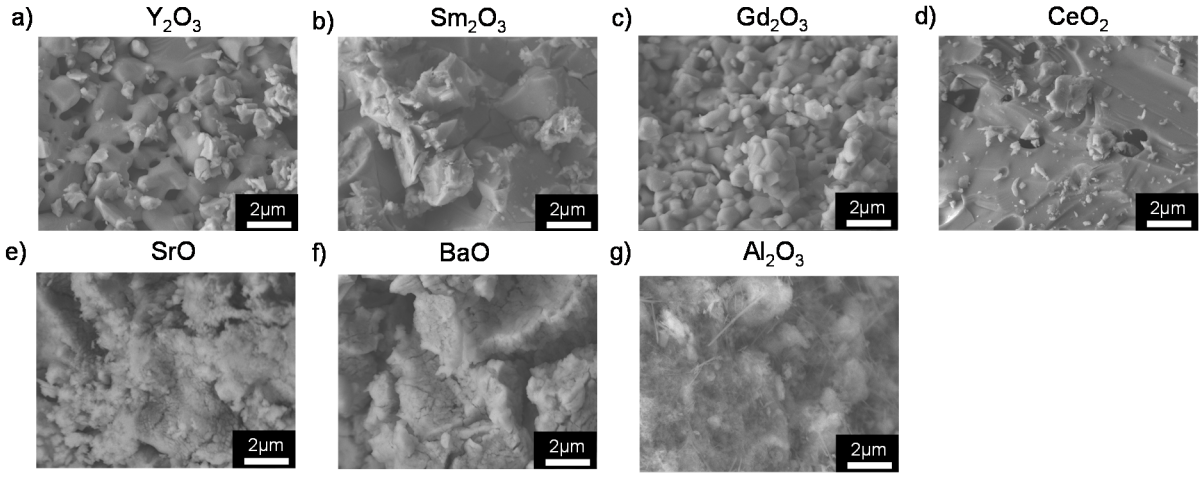

Fig. A3.1: SEM images of pure (a) Y_2O_3, (b) Sm_2O_3, (c) Gd_2O_3, (d) CeO_2, (e) SrO, (f) BaO and (g) Al_2O_3 after calcination at 800 °C in air. In general, they exhibited different morphology such as grain-like and bulk morphology.

Oxide-supported carbonate catalysts

Oxide-supported Rb_2CO_3, Cs_2CO_3 and $Mg(OAc)_2$ catalysts were discussed with regard to morphology. Herein, the series of Rb_2CO_3 on oxides (Rb_2CO_3-oxide) is presented as an example. The morphology of fresh and used Rb_2CO_3 on oxides catalysts are shown in Fig. A3.2.

For Rb_2CO_3-Y_2O_3, -Sm_2O_3, and -Gd_2O_3 fresh catalysts, they are mainly consist of grains with size of 0.5 - 10 µm size and no obvious morphological changes are observed compared to pure metal oxides. And after OCM reaction, the morphology keeps similar and no apparent sintering is observed. Differently, Rb_2CO_3-CeO_2 shows larger granules on the smooth bulk surface. This may be resulted from limited dispersion of carbonate solution into metal oxide support during impregnation, and subsequently the carbonate tends to crystallize on surface readily. These large granules, however, almost disappears after OCM, probably due to the decomposition of carbonate during reaction. For Rb_2CO_3-SrO and -BaO, apparent grains can be observed with size range of 0.5 - 2 µm, which is significantly different from the pure support. SrO and BaO may react with some species during carbonate precursor impregnation process, which is in agreement with the observation from XRD results in the following. And after OCM, especially for Rb_2CO_3-BaO, quantities of tiny particles are

observed with much smaller size, suggesting the occurrence of structural and composition changes during the reaction.

EDX mapping analysis of fresh catalysts was performed to detect whether the Rb element had been dispersed homogeneously over the whole catalyst structure. As shown in Fig. A3.3, the morphology can be clearly distinguished from EDX mapping of metal element of support, indicating this magnitude exhibits sufficient resolution. It is observed that the homogeneous distribution of Rb element in micrometer scale for most catalysts.

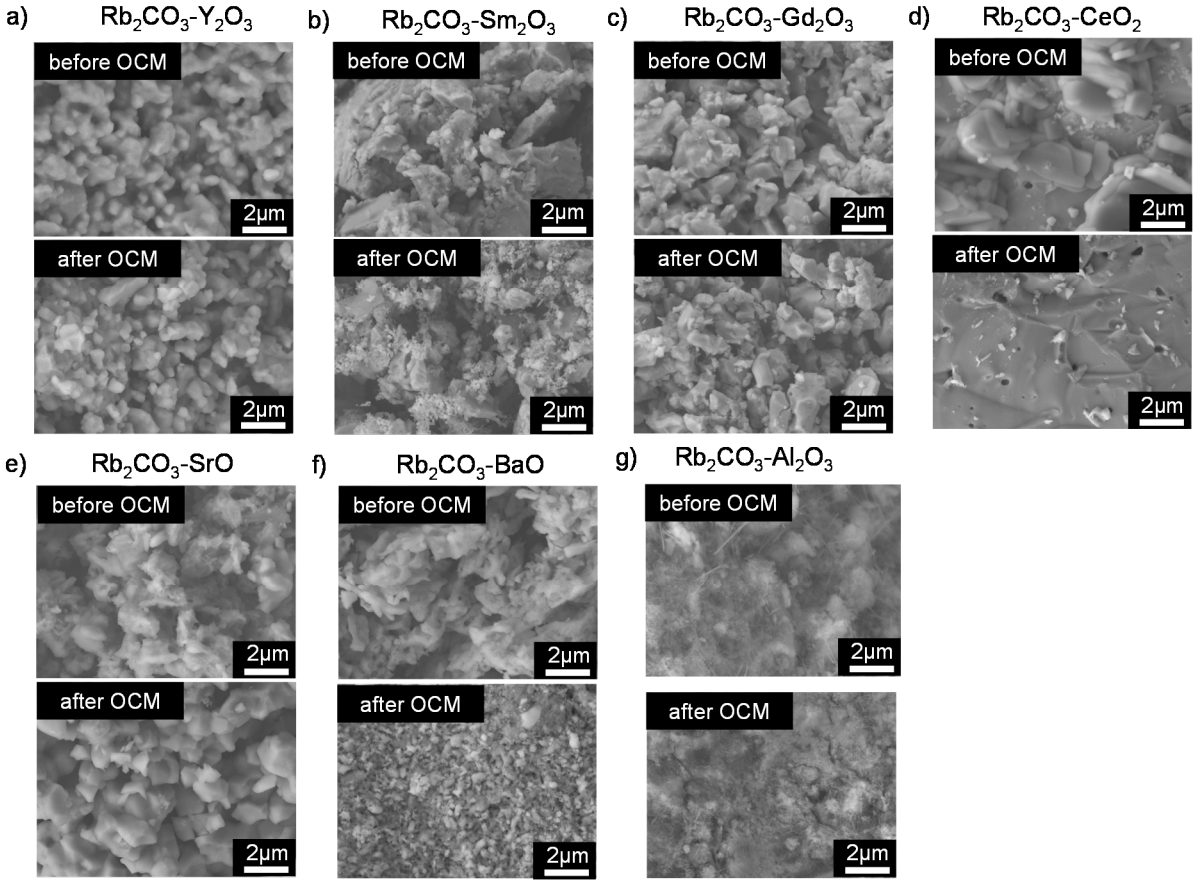

Fig. A3.2: SEM images of Rb_2CO_3 on (a) Y_2O_3, (b) Sm_2O_3, (c) Gd_2O_3, (d) CeO_2, (e) SrO, (f) BaO and (g) Al_2O_3 before and after OCM. Rb_2CO_3 on Y_2O_3, Sm_2O_3, Gd_2O_3, SrO, BaO and Al_2O_3 mainly consist of granules with 0.5~10 μm size. Rb_2CO_3 on CeO_2 shows larger granule size with smooth surface. These larger granules disappear after OCM. Rb_2CO_3 on BaO exhibits morphology with quantities of particles with smaller size than the ones in fresh catalysts.

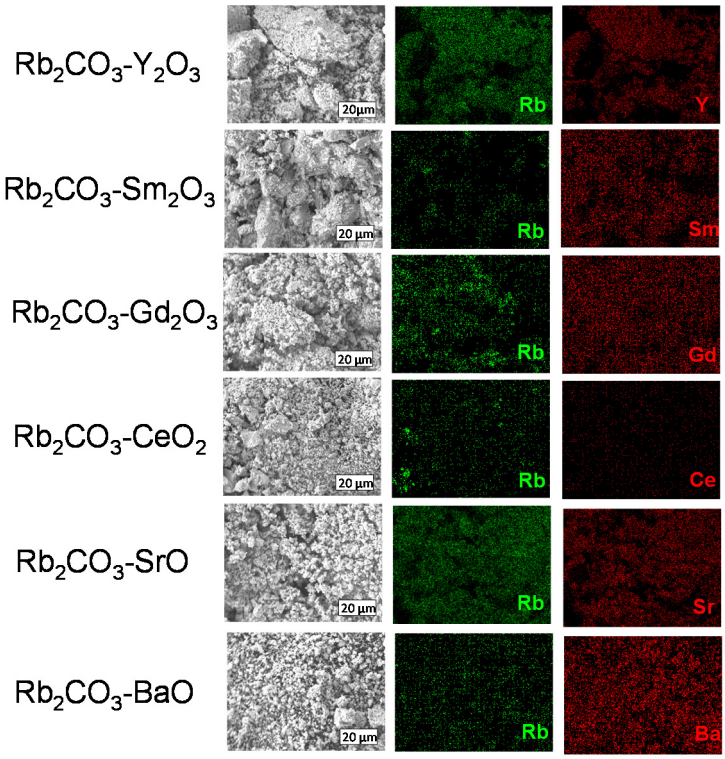

Fig. A3.3: EDX mapping of Rb, Y, Sm, Gd, Ce, Sr and Ba (L-edge) for fresh catalysts Rb_2CO_3 on Y_2O_3, Sm_2O_3, Gd_2O_3, CeO_2, SrO and BaO. The homogeneous distribution of Rb element in micrometer scale is observed in most of catalysts. The morphology can be clearly distinguished from EDX mapping of metal element of support, indicating this magnitude exhibits sufficient resolution.

A3.3.2 Crystalline phase (XRD)

Pure oxide supports

XRD was tested for all oxides before and after OCM to detect the crystal phase composition, as shown in Fig. A3.4. For Y_2O_3, Sm_2O_3, Gd_2O_3, CeO_2 and Al_2O_3 before OCM, metal oxides is the only crystal phase observed, which is Y_2O_3 (PDF No. 00-041-1105), Sm_2O_3 (PDF No. 01-084-1878), Gd_2O_3 (PDF No. 00-042-1465), CeO_2 (PDF No. 01-081-0792), γ-Al_2O_3 (PDF No. 00-050-0741) and δ-Al_2O_3 (PDF No. 00-046-1215), respectively. However, hydroxides, $Sr(OH)_2 \cdot H_2O$/$SrO \cdot 2H_2O$ (PDF No. 00-028-1222) and $Ba(OH)_2$ (PDF No. 00-026-0154) instead of oxide phase for SrO and BaO before OCM are obviously detected, possibly due to the high reactivity of alkaline earth metal oxide with H_2O species during the pretreatment. After OCM, carbonate phases, $SrCO_3$ (PDF No. 01-084-1778) and $BaCO_3$ (PDF No. 00-005-0378) are present in both samples. These carbonate species may forms by the adsorption of by-product CO_2 during OCM reaction. Furthermore, Ba peroxide appears with a certain form perhaps derived from the decomposition of $BaCO_3$ under typical OCM temperature. Hence, SrO and BaO is practically hydroxide in this study when used as support for the following impregnation.

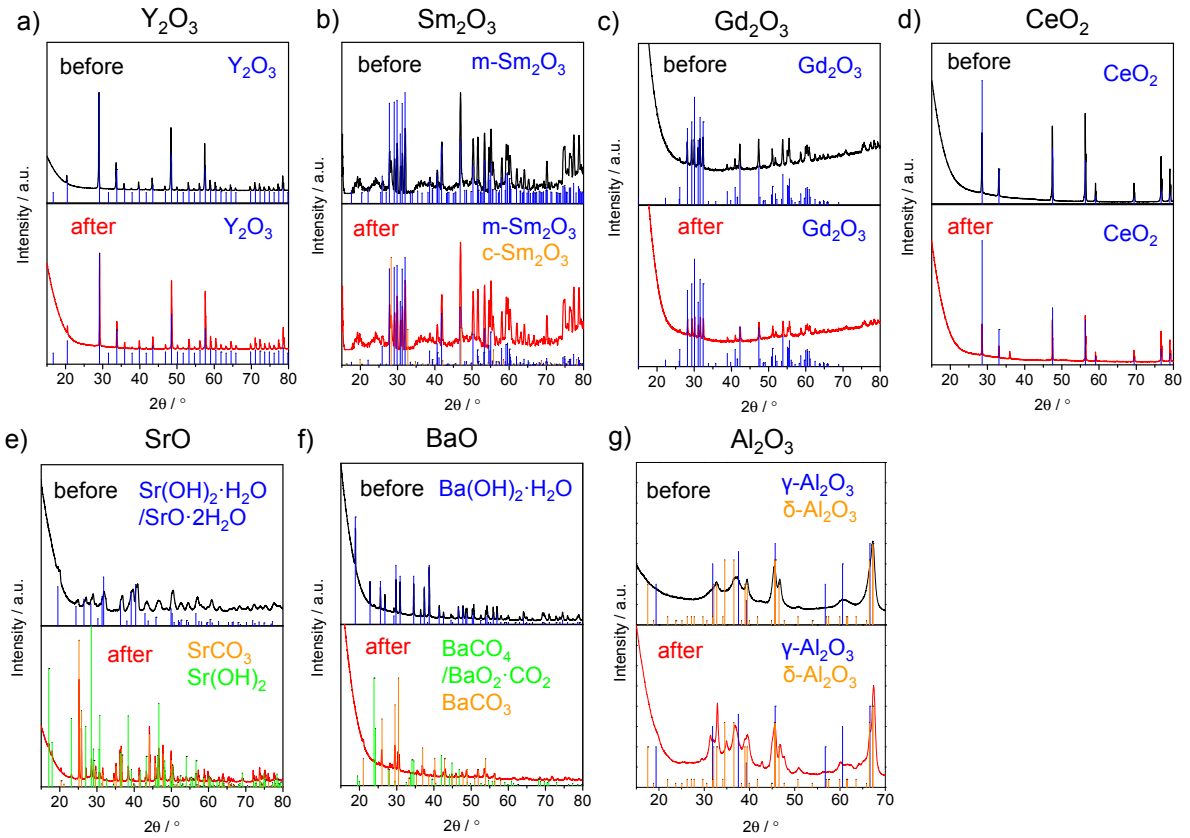

Fig. A3.4: XRD patterns of pure (a) Y_2O_3, (b) Sm_2O_3, (c) Gd_2O_3, (d) CeO_2, (e) SrO, (f) BaO and (g) Al_2O_3 treated at 800 °C before and after OCM. For Y_2O_3, Sm_2O_3, Gd_2O_3, CeO_2 and (g) Al_2O_3, only metal oxide crystal phase were detected before OCM and retains the same after OCM. However, hydroxide phase was detected in SrO and BaO samples before OCM. And after OCM, both exhibit the presence of carbonate phase.

Oxide-supported carbonate catalysts

XRD was measured for catalysts before and after OCM reaction in order to detect crystal phase composition. The results of Rb_2CO_3 on oxide catalysts are shown in Fig. A3.5.

For Rb_2CO_3-Y_2O_3, Rb_2CO_3-Sm_2O_3 and Rb_2CO_3-Gd_2O_3 catalysts, metal oxide Y_2O_3 (PDF No. 00-041-1105), Sm_2O_3 (PDF No. 01-084-1878) and Gd_2O_3 (PDF No. 00-042-1465) are the only crystalline phases detected in the fresh catalysts. These crystalline phases keep nearly no change after OCM except a new Sm_2O_3 (PDF No. 00-043-1029) phase appear possibly due to structure reconstruction. No new species, such as mix oxides were found. Surprisingly, Rb_2CO_3 or Rb_2O was not detected by XRD, which is similar to the observation of Tong et al.[147] when impregnating Na_2CO_3 on a few of rare earth metal oxide. The possible explanation is that the carbonate species appear as very tiny crystallites or amorphous forms on the surface of metal oxide supports which is not detectable by XRD.

For Rb_2CO_3-CeO_2, differently, not only CeO_2 (PDF No. 01-081-0792) but also Rb_2CO_3 (PDF No. 00-035-0972) phase were detected as broad peaks in fresh catalysts. The reason could be that Rb_2CO_3 rarely disperses into CeO_2 bulk and tends to form large crystallites on the surface during the impregnation process, which is in agreement with the SEM observation. However, Rb_2CO_3 phase seems to disappear after OCM reaction probably because of carbonate melting and decomposition under OCM temperature.

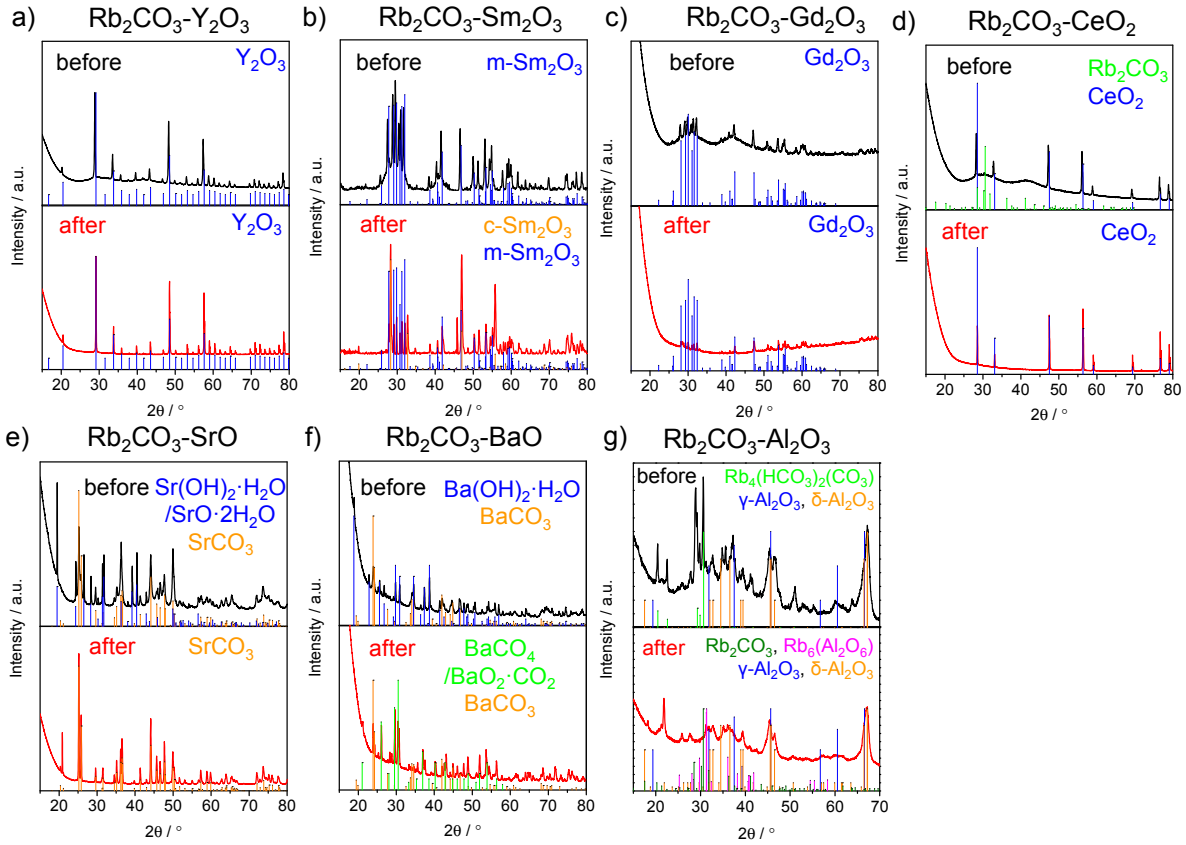

Fig. A3.5: XRD patterns of Rb_2CO_3 on (a) Y_2O_3, (b) Sm_2O_3, (c) Gd_2O_3, (d) CeO_2, (e) SrO, (f) BaO and (g) Al_2O_3 support before and after OCM. For Rb_2CO_3 on Y_2O_3, Sm_2O_3 and Gd_2O_3, only metal oxide phases were detected before OCM and retained after OCM. Rb_2CO_3 was not observed by XRD, indicating that the carbonate existed as very tiny crystallite. For Rb_2CO_3 on CeO_2, however, broad peak was detected for the carbonate phase. For Rb_2CO_3 on SrO and BaO, hydroxide and carbonate phases were detected as the water and CO_2 species may be incorporated through impregnation and drying process. After OCM reaction, Rb_2CO_3 phase was not detected for all spent catalysts. For Rb_2CO_3 on Al_2O_3, aluminate phase appears after OCM reaction.

For Rb_2CO_3-SrO and Rb_2CO_3-BaO, the crystal phase composition is more complex. For example, $Sr(OH)_2{\cdot}H_2O/SrO{\cdot}2H_2O$ (PDF No. 00-028-1222) and $SrCO_3$ (PDF No. 01-084-1778) appear in the fresh catalysts. Hydroxide phase is already present for pure SrO support due to its high affinity to H_2O species during pretreatment. But for the existence of $SrCO_3$, it may form through CO_3^{2-} species transfer from the impregnated Rb_2CO_3 to Sr^{2+} or by CO_2 adsorption on SrO during preparation process. After OCM, the only Sr-containing phase is $SrCO_3$ due to its high thermal stability (also shown later in TGA analysis). Similarly, XRD signal of Rb_2CO_3-BaO before OCM can be assigned to $Ba(OH)_2{\cdot}H_2O$ (PDF No. 00-026-0154) and $BaCO_3$ (PDF No. 00-005-0378). After OCM, Ba peroxide phase appears except $BaCO_3$, which may be derived from decomposition of carbonate species.[202]

Furthermore, the assigned crystal phase composition for all catalysts before and after OCM reaction is summarized in Table A3.1. Broadly speaking, Sm_2O_3, Y_2O_3, Gd_2O_3 and CeO_2 phase in catalysts keep no change after OCM reaction. SrO and BaO form hydroxide and carbonate in fresh catalysts whereas only carbonate phase retains after OCM. Besides, for Al_2O_3 supported catalysts, aluminate phase appears after OCM reaction. Rb_2CO_3 or Cs_2CO_3 is rarely detected in fresh catalysts, which indicates that they disperse well as fairly small crystallite, corresponding to homogeneous dispersion of the respective element in EDX mapping (Fig. A3.3). After OCM reaction, there is still no certain detection of Rb_2CO_3 or Cs_2CO_3 as well as its decomposition product Rb_2O or Cs_2O. Honestly, it is plausible to

evaluate the existence of carbonate species only by XRD detection when the carbonate exists in forms of tiny crystallite or amorphous phase.

Table A3.1: Summary of crystalline phases identified by XRD evaluation. Phases with uncertain assignment written in *Italic*.

metal oxide support	pure		Rb_2CO_3 on support		Cs_2CO_3 on support		$Mg(OAc)_2$ on support	
	before	after	before	after	before	after	before	after
Y_2O_3	Y_2O_3	Y_2O_3	Y_2O_3	Y_2O_3	Y_2O_3	Y_2O_3	Y_2O_3	Y_2O_3
Sm_2O_3	Sm_2O_3	Sm_2O_3	Sm_2O_3	Sm_2O_3 Sm_2O_3	Sm_2O_3	Sm_2O_3 Sm_2O_3	Sm_2O_3	Sm_2O_3
Gd_2O_3	Gd_2O_3	Gd_2O_3	Gd_2O_3	Gd_2O_3	Gd_2O_3	Gd_2O_3	Gd_2O_3	Gd_2O_3
CeO_2	CeO_2	CeO_2	CeO_2 *Rb_2CO_3*	CeO_2	CeO_2 $CsHCO_3$	CeO_2 *Cs_2CO_3*	CeO_2	CeO_2
SrO	$Sr(OH)_2 \cdot H_2O$ /SrO $\cdot 2H_2O$	$SrCO_3$ $Sr(OH)_2$	$Sr(OH)_2 \cdot H_2O$ /SrO $\cdot 2H_2O$ $SrCO_3$	$SrCO_3$	$Sr(OH)_2 \cdot H_2O$ /SrO $\cdot 2H_2O$ $SrCO_3$	$SrCO_3$	$Sr(OH)_2 \cdot H_2O$ $SrCO_3$	$SrCO_3$
BaO	$Ba(OH)_2 \cdot H_2O$	$BaCO_3$ $BaCO_4$/ BaO_2 $\cdot CO_2$	$Ba(OH)_2 \cdot H_2O$ $BaCO_3$	$BaCO_3$ $BaCO_4$/ BaO_2 $\cdot CO_2$	$Ba(OH)_2 \cdot H_2O$ $BaCO_3$	$BaCO_3$ $BaCO_4$/ BaO_2 $\cdot CO_2$	$Ba(OH)_2 \cdot H_2O$ $BaCO_3$	$BaCO_3$ $BaCO_4$/ BaO_2 $\cdot CO_2$
Al_2O_3	Al_2O_3	Al_2O_3	$Rb_4(HCO_3)_2(CO_3) \cdot H_2O$ Al_2O_3	*$Rb_6Al_2O_6$* *Rb_2CO_3* *$\cdot H_2O$* Al_2O_3	Al_2O_3	$CsAlO_2$ SiO_2 Al_2O_3	Al_2O_3	$MgAl_2O_4$ Al_2O_3

A3.3.5 Thermogravimetric analysis coupled with mass spectrometry (TGA-MS)

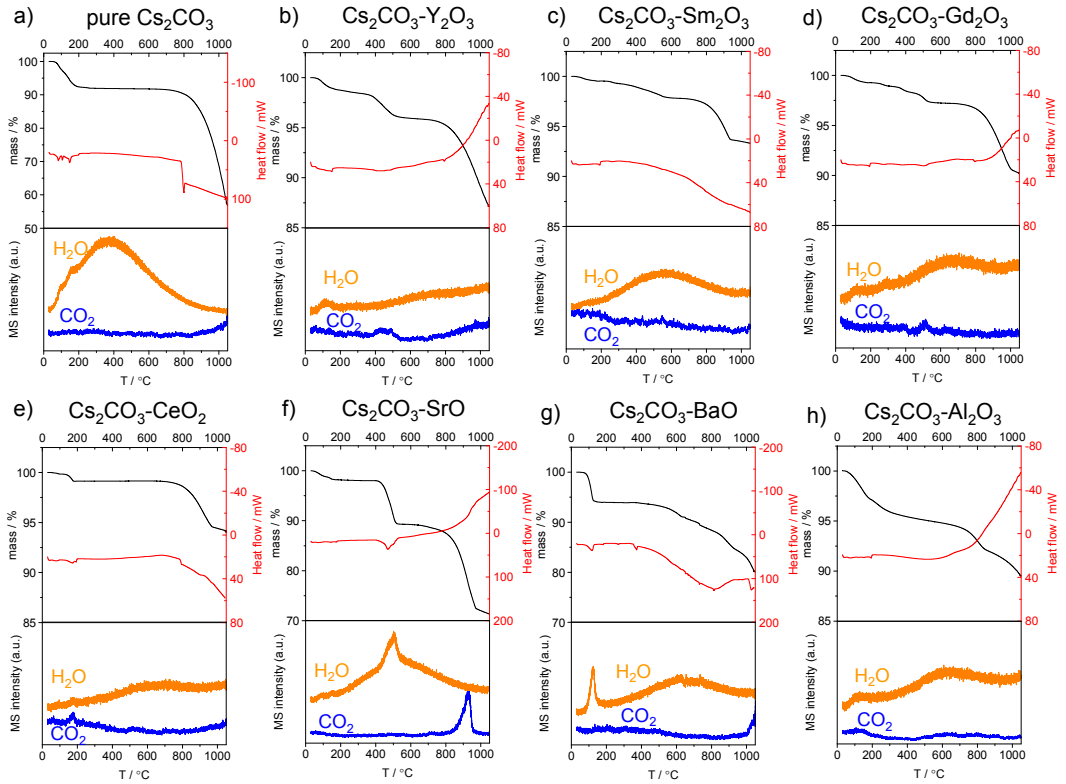

Fig. A3.6: TGA-MS results of (a) pure Cs_2CO_3 and Cs_2CO_3 on (b) Y_2O_3, (c) Sm_2O_3, (d) Gd_2O_3, (e) CeO_2, (f) SrO, (g) BaO and (h) Al_2O_3 support.

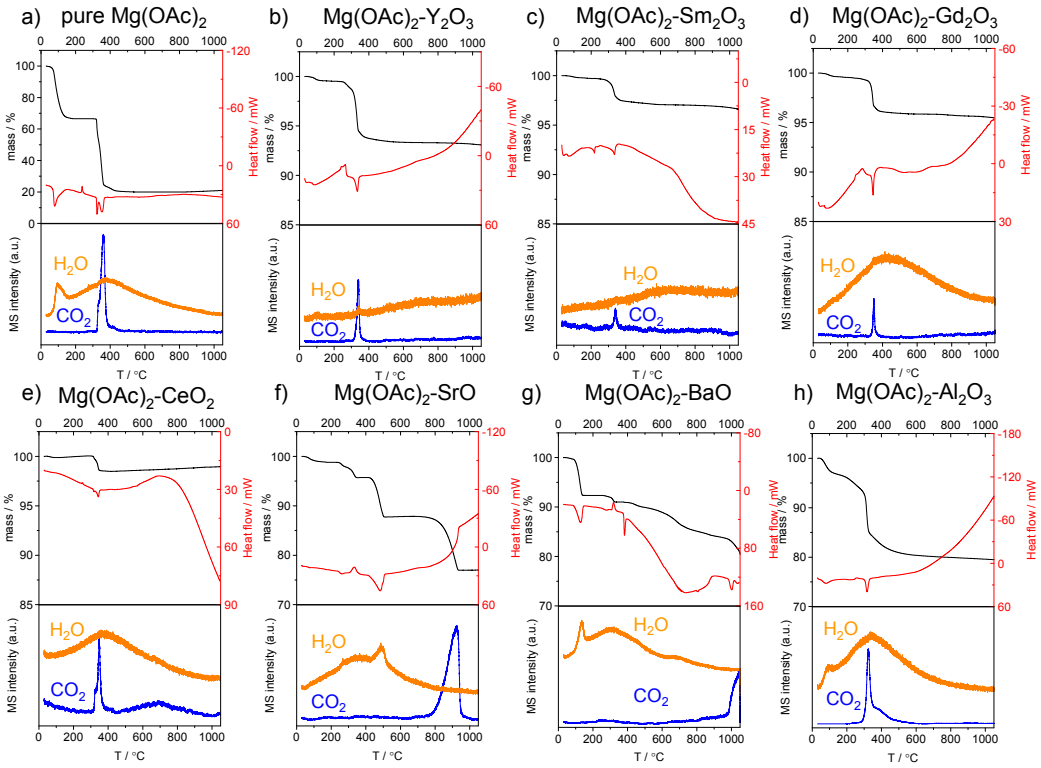

Fig. A3.7: TGA-MS results of (a) pure $Mg(OAc)_2$ and pure $Mg(OAc)_2$ on (b) Y_2O_3, (c) Sm_2O_3, (d) Gd_2O_3, (e) CeO_2, (f) SrO, (g) BaO and (h) Al_2O_3 support.

A3.4 Carbonate-supported carbonate catalysts

A3.4.1 Morphology

$Sm_2(CO_3)_3$ supported catalysts

The morphology of pure $Sm_2(CO_3)_3$, Rb_2CO_3 and Cs_2CO_3 on $Sm_2(CO_3)_3$ catalysts before and after OCM reaction was characterized and shown in Fig. A3.8.

As shown in Fig. A3.8 a, pure $Sm_2(CO_3)_3$ is composed of aggregated thin sheets. After impregnation of Rb_2CO_3 and Cs_2CO_3 (Fig. A3.8 b and c), they exhibit similar sheet-like morphology but the surface of sheets seems to be partially covered possibly by impregnated species. After OCM, significant morphological change is observed. Pure $Sm_2(CO_3)_3$ still retains major morphology, but the edge of sheet collapses along with appearance of the particulate outline which could be observed from the magnification inset. For Rb_2CO_3 and Cs_2CO_3 on $Sm_2(CO_3)_3$, the pristine sheet-like morphology is completely transformed into a network structure consisting of conjunct small particle with 100 ~ 200 nm. Nevertheless, the formed network is probably derived from the previous sheet-like morphology as the network structure roughly follows the outline of the aggregated sheets. This implies that $Sm_2(CO_3)_3$ may undergo decomposition at OCM reaction temperature and induce the change of the bulk morphology .

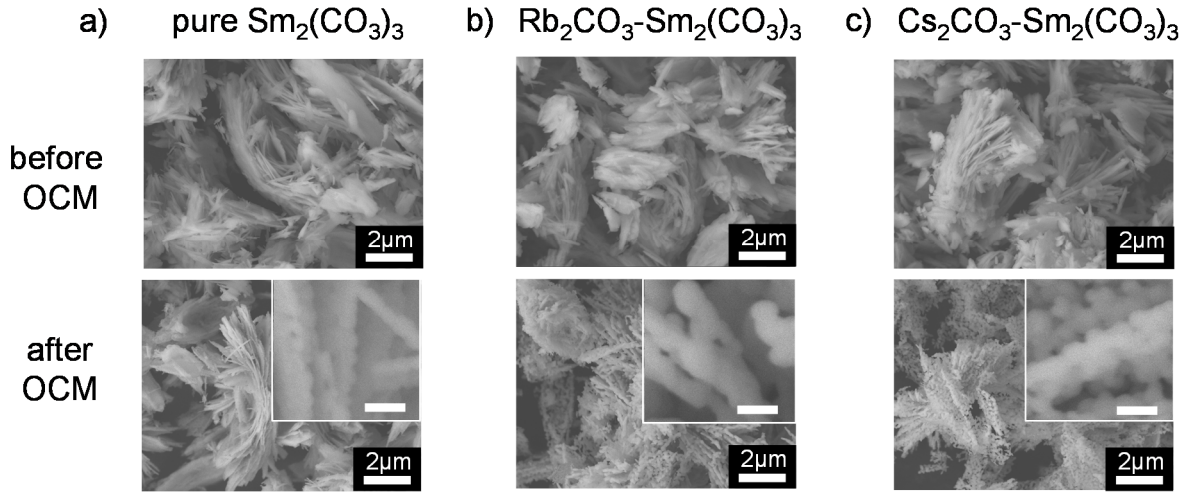

Fig. A3.8: SEM images of (a) pure $Sm_2(CO_3)_3$, (b) Rb_2CO_3-$Sm_2(CO_3)_3$ and (c) Cs_2CO_3-$Sm_2(CO_3)_3$ before and after OCM. The scale bar of inset is 200 nm. The pure $Sm_2(CO_3)_3$ consists of aggregated thin sheets. The sheets are partially covered in after impregnation of Rb_2CO_3 and Cs_2CO_3. After OCM, the sheet-like morphology of pure $Sm_2(CO_3)_3$ somehow retains, but with the formation of nanoparticles. For Rb_2CO_3 and Cs_2CO_3 on $Sm_2(CO_3)_3$, further apparent transformation from sheets to conjunct nanoparticles are observed, indicating the possible occurrence of carbonate decomposition during OCM reaction.

$SrCO_3$ supported catalysts

The morphology of pure $SrCO_3$, Rb_2CO_3 and Cs_2CO_3 on $SrCO_3$ catalysts before and after OCM reaction was also characterized.

As shown in Fig. A3.9, pure $SrCO_3$ are composed of large grains with micrometer size, surrounded by quantities of tiny particles. After OCM reaction, the grains become more pronounced with apparent crystal-like edges. Similar morphology is observed for Rb_2CO_3 and Cs_2CO_3 on $SrCO_3$. After OCM reaction, their morphology changes relatively less compared to the significant morphological variance appearing in $Sm_2(CO_3)_3$ supported carbonate (Fig.

A3.8) after reaction. This suggests that $SrCO_3$ exhibits higher stability than $Sm_2(CO_3)_3$ during OCM reaction.

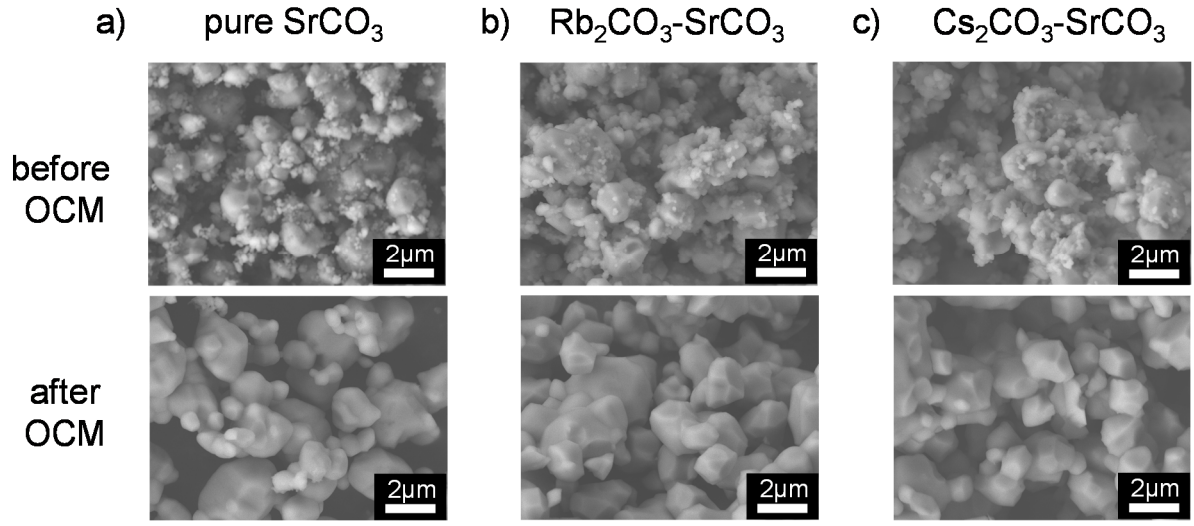

Fig. A3.9: SEM images of (a) pure $SrCO_3$, (b) Rb_2CO_3-$SrCO_3$ and (c) Cs_2CO_3-$SrCO_3$ catalysts before and after OCM . The pure $SrCO_3$ and fresh catalysts is composed of larger grains with micrometer size scale, surrounded by quantities of tiny particles. After OCM, the grains grow slightly larger with apparent crystal-like outline.

A3.4.2 Crystalline phase (XRD)

$Sm_2(CO_3)_3$ supported catalysts

Crystal phase composition of pure $Sm_2(CO_3)_3$ and its supported catalysts were characterized by XRD and shown in Fig. A3.10. Qualitatively, pure $Sm_2(CO_3)_3$ exhibits a rather sophisticated peak composition, which are mainly attributed to $Sm_2(CO_3)_3 \cdot 2.85H_2O$ (PDF No. 00-031-1201) and monoclinic-Sm_2O_3 (PDF No. 01-084-1878). Other peaks cannot be clearly assigned to defined crystal phase. Sm_2O_3 species may come from the slight decomposition of $Sm_2(CO_3)_3$ hydrate during the pretreatment process in vacuum at 150 °C.[203, 204] Similar crystal phase composition was also found in Rb_2CO_3 and Cs_2CO_3 on $Sm_2(CO_3)_3$ fresh catalysts. No significant Rb_2CO_3 and Cs_2CO_3 crystal phases are detected, possibly because they are present as very tiny crystallites or amorphous forms on the surface of support (as discussed in section 3.3.2).

However, for pure $Sm_2(CO_3)_3$, Rb_2CO_3 and Cs_2CO_3 on $Sm_2(CO_3)_3$, only one consistent crystal phase, cubic-Sm_2O_3 (PDF No. 00-043-1029), appeared after OCM reaction rather than the mixed phase composition before reaction. It reveals that $Sm_2(CO_3)_3$ decomposes at OCM reaction temperature and produces Sm_2O_3 as product. Note that the formed Sm_2O_3 cubic phase in the used catalyst is different from the Sm_2O_3 monoclinic phase in fresh catalyst. It implies that structural transition occurs during OCM reaction and the cubic-Sm_2O_3 may be the preferred oxide phase afterwards, which is in agreement with that cubic crystal phase is the only observed phase in XRD pattern for Sm_2O_3 around 800 °C.[205]

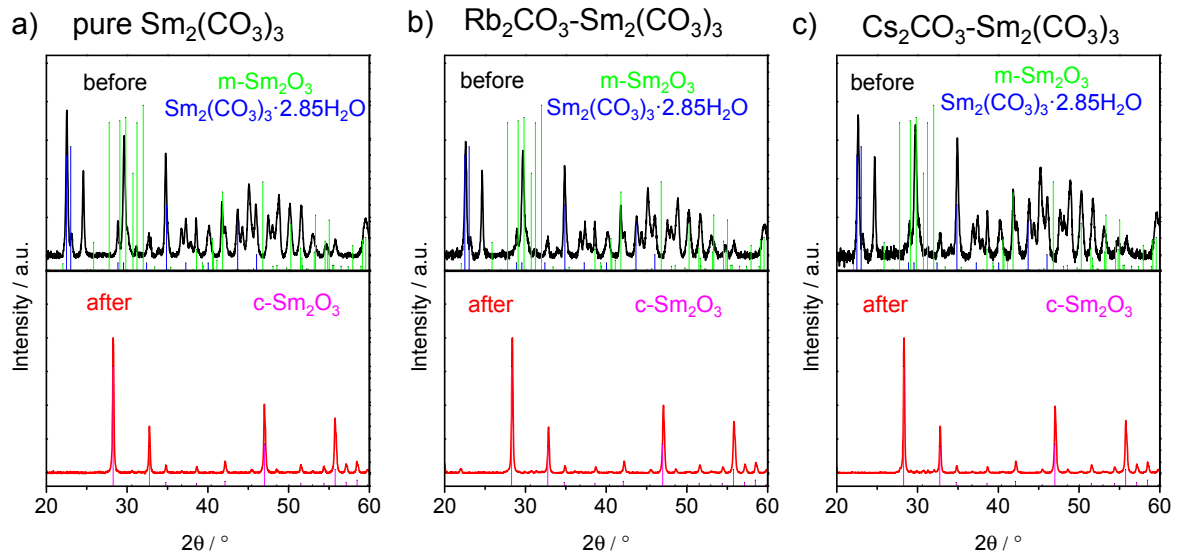

Fig. A3.10: XRD pattern of (a) pure $Sm_2(CO_3)_3$, (b) Rb_2CO_3-$Sm_2(CO_3)_3$ and (c) Cs_2CO_3-$Sm_2(CO_3)_3$ before and after OCM. Sm carbonate crystal phase is detected for pure $Sm_2(CO_3)_3$ and its supported fresh catalysts. But only Sm oxide appears after OCM reaction, suggesting the decomposition of Sm carbonate takes place during OCM. Interestingly, a newly-formed Sm_2O_3 phase is detected. It implies the latter Sm_2O_3 phase may be the preferred oxide phase after reconstruction during OCM reaction.

$SrCO_3$ supported catalysts

Crystal phase composition of pure $SrCO_3$ and its supported catalysts was determined by XRD, as shown in Fig. A3.11. For pure $SrCO_3$, Rb_2CO_3 and Cs_2CO_3 on $SrCO_3$, only $SrCO_3$ (PDF No. 01-084-1778) was detected consistently as the present crystal phase. After OCM reaction, $SrCO_3$ phase is still intact and became more pronounced. It is worth mentioning that no new crystal phase like SrO could be detected. This observation is different from the case of $Sm_2(CO_3)_3$ supported catalysts, where only Sm_2O_3 exists after OCM reaction (Fig. A3.10).

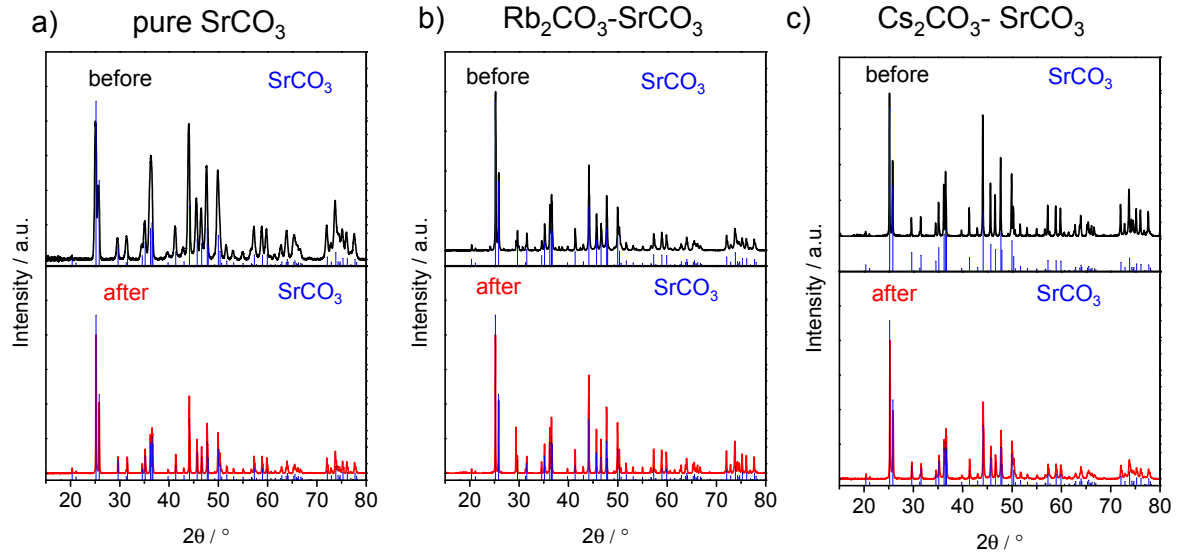

Fig. A3.11: XRD patterns of of (a) pure $SrCO_3$, (b) Rb_2CO_3-$SrCO_3$ and (c) Cs_2CO_3-$SrCO_3$ catalysts before and after OCM. $SrCO_3$ is the only detected crystal phase for pure $SrCO_3$ and its supported catalysts before and after OCM, revealing $SrCO_3$ could keep stable during OCM.

A3.5 Li/MgO and Mn-Na_2WO_4/SiO_2 catalysts

As a comparison to oxide-supported and carbonate-supported carbonate catalysts, typical OCM catalysts, Li/MgO and Mn-Na_2WO_4/SiO_2, were also prepared and characterized with regard to crystalline phase and chemical species.

A.3.5.1 Crystalline phase

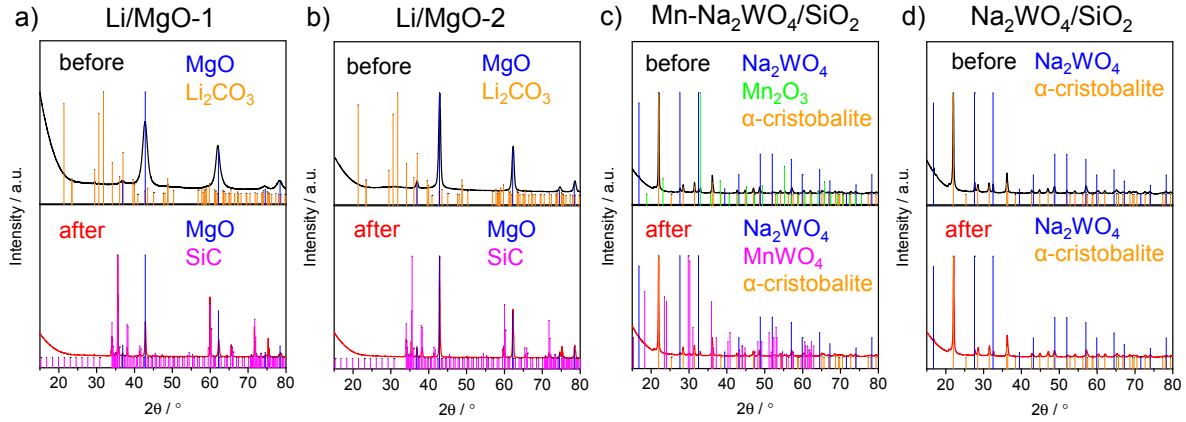

Fig. A3.12: XRD pattern of (a) Li/MgO-1, (b) Li/MgO-2, (c) Mn-Na_2WO_4/SiO_2 and (d) Na_2WO_4/SiO_2 before and after OCM. Li_2CO_3 phase appears in fresh catalysts but disappears after OCM reaction for both Li/MgO catalysts. Mn-Na_2WO_4/SiO_2 exhibits phase composition of α-cristobalite, Mn_2O_3 and Na_2WO_4 before reaction, while $MnWO_4$ seems to appear instead of Mn_2O_3 after reaction. Only Na_2WO_4 and α-cristobalite were observed for Na_2WO_4/SiO_2 before and after reaction.

As a reference, the prepared Li/MgO and Mn-Na_2WO_4/SiO_2 catalysts were characterized by XRD, as shown in Fig. A3.12.

For both Li/MgO fresh catalysts, MgO (PDF No. 01-074-1225) and Li_2CO_3 (PDF No. 01-087-0728) crystal phase were observed in XRD patterns. After OCM reaction, however, Li_2CO_3 phase can be no longer observed and MgO phase still retains in XRD pattern. Additional SiC crystal phase is derived from the remainder inert SiC for OCM catalytic test which is difficult to be completely removed by sieving process. Hence, it reveals that carbonate species present in fresh Li/MgO catalysts could not be preserved during OCM reaction.

For Mn-Na_2WO_4/SiO_2 catalyst, crystalline SiO_2 α-cristobalite (PDF No. 00-039-1425), Mn_2O_3 (PDF No. 00-41-1442) and Na_2WO_4 (PDF No. 00-12-0772) were detected in XRD, which is similar to the previous report for Mn-Na_2WO_4/SiO_2 catalyst system.[61] For Na_2WO_4/SiO_2 catalyst, not surprisingly, α-cristobalite and Na_2WO_4 were detected in XRD. After OCM reaction, not too much changes about crystal phase composition were detected for both catalysts. Besides, no obvious crystalline phase attributed to carbonate can be observed.

A3.5.2 Chemical species

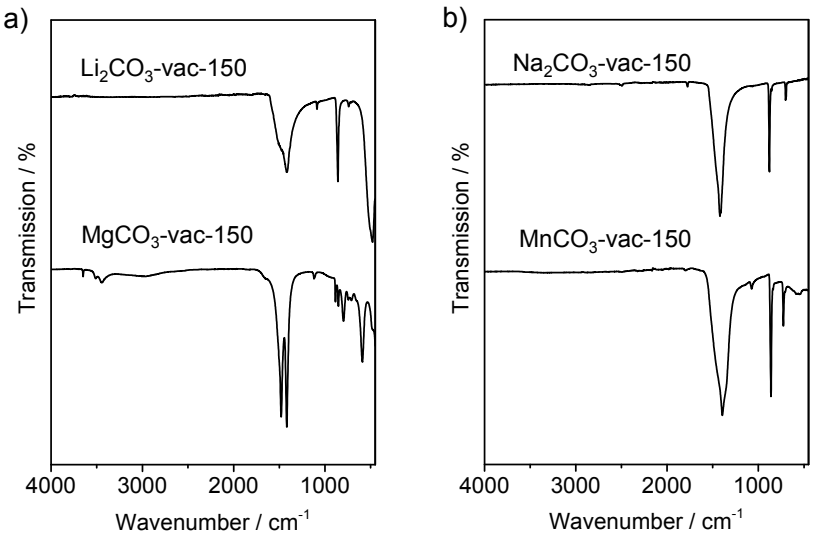

Fig. A3.13: IR spectra of Li_2CO_3, $MgCO_3$, Na_2CO_3 and $MnCO_3$ after treatment in vacuum at 150 °C for 5 h.

A4. OCM performance and performance-descriptors of oxide-supported and carbonate-supported catalysts

A4.2 Oxide-supported carbonate catalysts

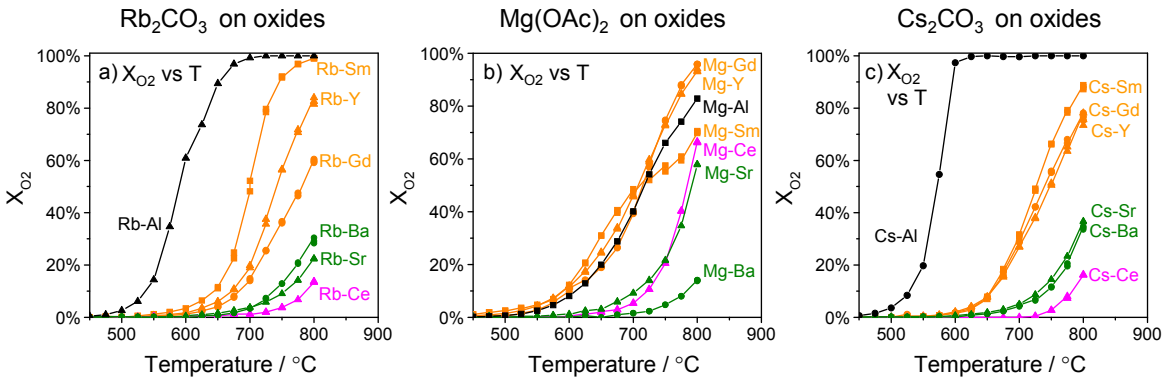

Fig. A4.1: O_2 conversion for (a) Rb_2CO_3, (b) $Mg(OAc)_2$ and (c) Cs_2CO_3 on oxides. In general, O_2 conversion trend of all catalysts is similar to the trend of CH_4 conversion.

A4.3 Carbonate-supported carbonate catalysts

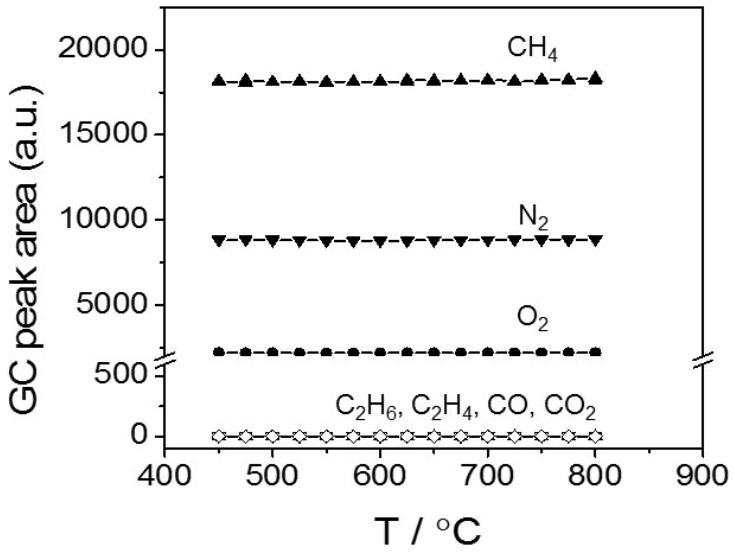

Fig. A4.2: GC peak area of each species involved in OCM reaction for blank reactor over whole reaction temperature range.

Comparison of experimental results between "Carbonate-supported" and "Inert-supported", "Carbonate thermdyn not stable" and "Carbonate thermdyn stable" group with statistical values as well as comparison between "oxides as support" and "carbonates as support"

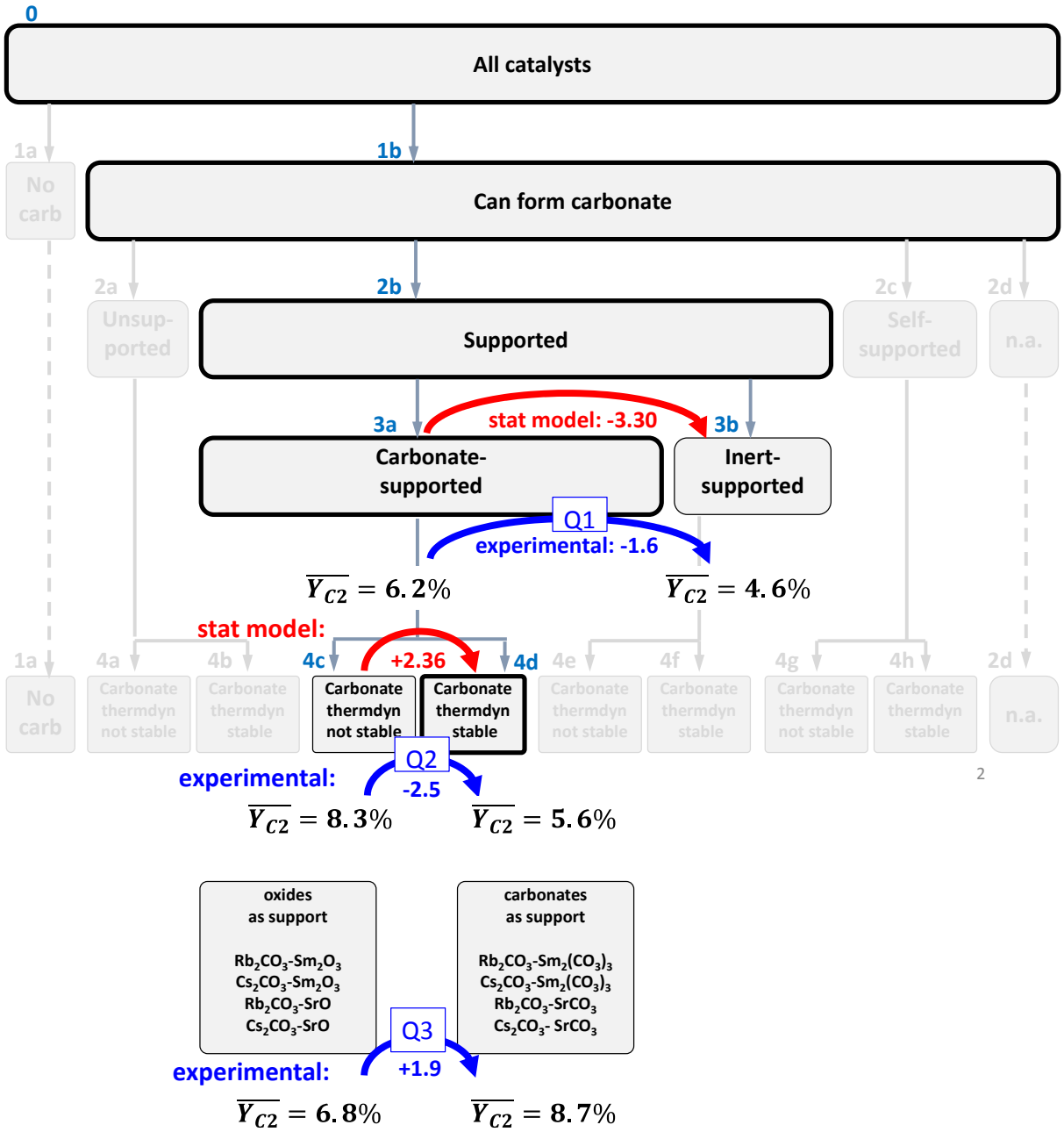

Fig. A4.3: Q1 and Q2: Comparison of experimental C_2 yield difference at 800 °C between "Carbonate-supported" and "Inert-supported" group, between "Carbonate thermdyn not stable" and "Carbonate thermdyn stable" group with results from statistical analysis. Q3: Comparison of experimental C_2 yield difference at 800 °C of catalysts using oxides or carbonates as support with same cation. The results from experimental are labelled with blue color while the results of statistical analysis are labelled in red color.

In order to solve the proposed three questions in section 1.5.2, OCM performance in terms of C_2 yield at 800 °C for designed catalysts belonging to different defined property groups was extracted and averaged.

At level 3 in Fig. A4.3, it depicts regression coefficient from statistical analysis and experimental difference of average of C_2 yield between "Carbonate-supported" and "Inert-supported" group, in order to validate the effect of support cation which can form a carbonate

or not on OCM performance. Similar to the results evaluated by statistical analysis, catalysts measured at typical OCM temperature 800 °C in this work in the “Carbonate-supported” group exhibit higher average of C_2 yield than catalysts in the “Inert-supported” group. It validates this property group classification by the criterion of whether support cation can form a carbonate or not. This reveals that catalyst support cation that is able to form a carbonate would be beneficial to its OCM performance.

At level 4 in Fig. A4.3, it depicts regression coefficient from statistical analysis and experimental difference of average of C_2 yield between “Carbonate thermdyn not stable” and “Carbonate thermdyn stable” group, in order to validate the effect of cations which can form a thermodynamically stable carbonate or not at OCM temperature on catalytic performance. Catalysts measured at typical OCM temperature 800 °C in this work in the “Carbonate thermdyn stable” group exhibit lower average of C_2 yield than catalysts in the “Carbonate thermdyn not stable” group, which is in contrary to the results evaluated by statistical analysis. This means that the property group classification by the criterion of cation which can form a stable carbonate or not at OCM temperature could not be validated by the experimental results of designed catalysts in this work. More detailed and precise criterion regarding to carbonate stability should be considered to improve the statistical analysis. In addition, one important conclusion from experimental work in this thesis is that carbonate with intermediate but not high stability is essential to control OCM performance. This also in a way explains why the statistical analysis results by simply focusing on stable carbonate at OCM temperatures could not be validated by experimental.

At bottom part of in Fig. A4.3, it depicts experimental difference of average of C_2 yield between catalysts using oxides or carbonates with same cation as support materials. Catalysts using “carbonates as support” exhibit higher average of C_2 yield than catalysts using “oxides as support”. This reveals that using carbonate as catalyst support would enhance OCM performance rather than oxide as support given that other components of catalysts stay the same.

A5. Correlations between catalyst properties and OCM performance

A5.2 Correlation between performance and carbonate stability

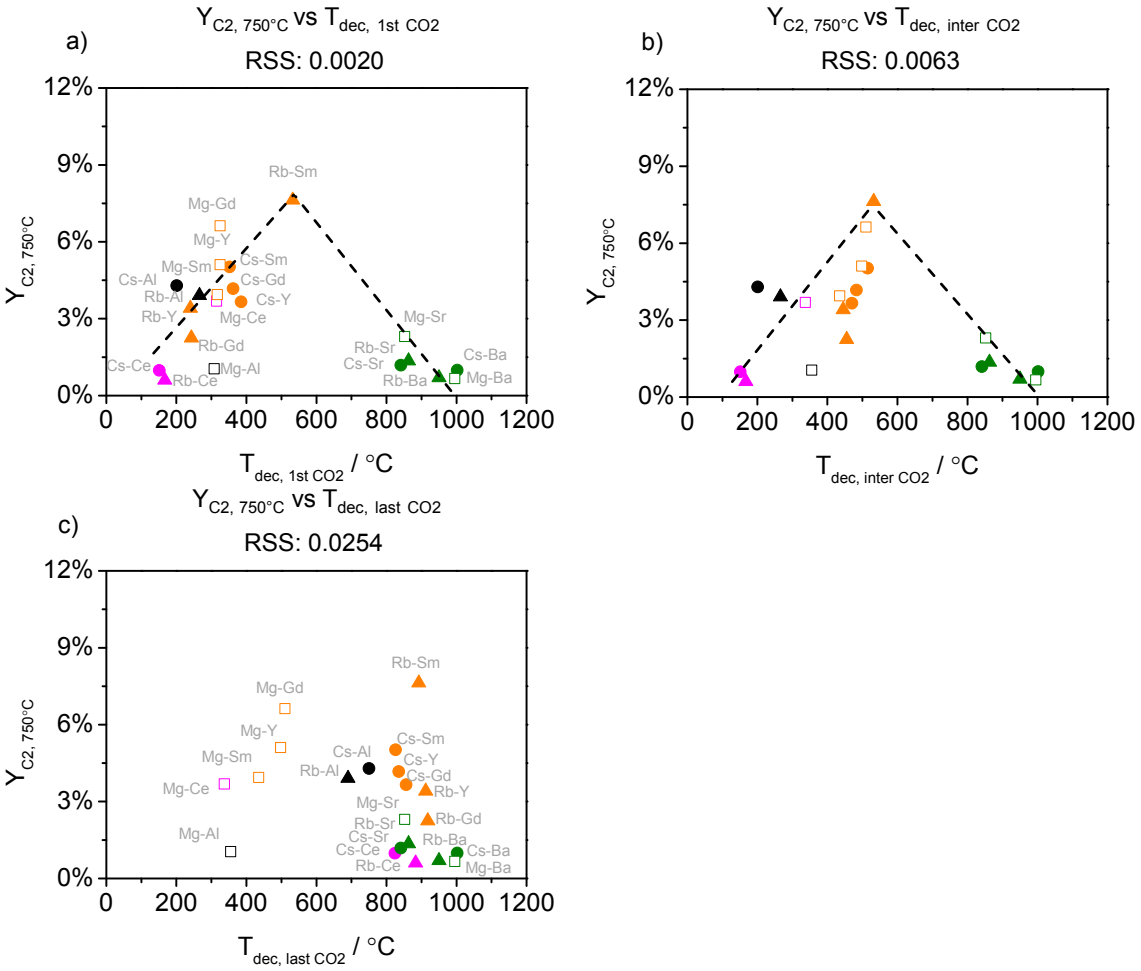

Fig. A5.1: C_2 yield at 750 °C vs. (a) $T_{dec,\ 1st\ H2O}$ or (b) $T_{dec,\ last\ H2O}$ of Rb_2CO_3 (triangle), Cs_2CO_3 (dot) and $Mg(OAc)_2$ (square) on Y_2O_3, Sm_2O_3 and Gd_2O_3 (orange), CeO_2 (pink), SrO and BaO (green) and Al_2O_3 (black).

A5.3 Correlation between performance and H_2O-relating property

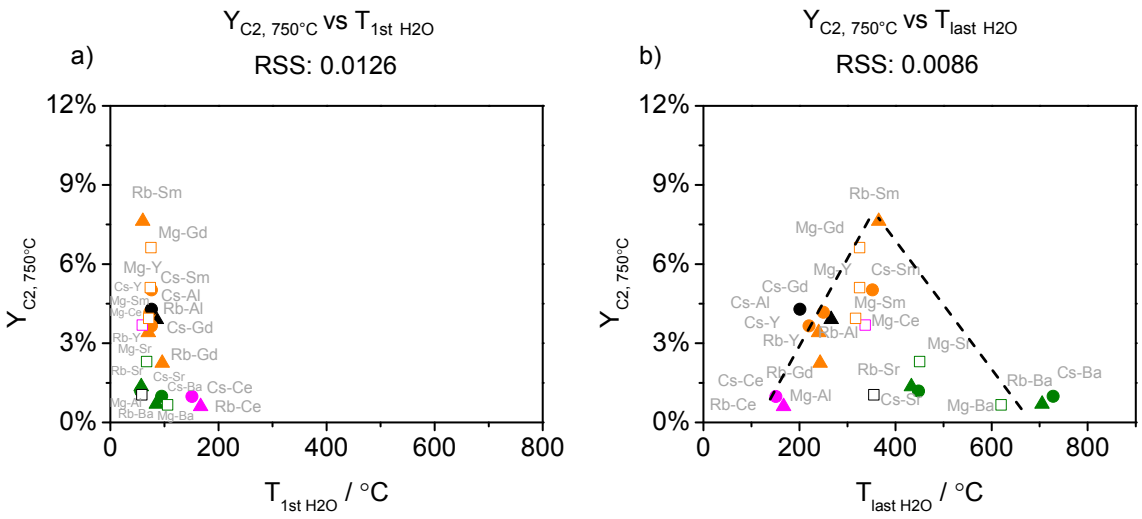

Fig. A5.2: Correlation between C_2 yield at 750 °C and (a) $T_{1st\ H2O}$ or (b) $T_{last\ CO2}$ of Rb_2CO_3 (triangle), Cs_2CO_3 (dot) and $Mg(OAc)_2$ (square) on Y_2O_3, Sm_2O_3 and Gd_2O_3 (orange), CeO_2 (pink), SrO and BaO (green), Al_2O_3 (black).

A5.4 Correlation between performance and IR bond position

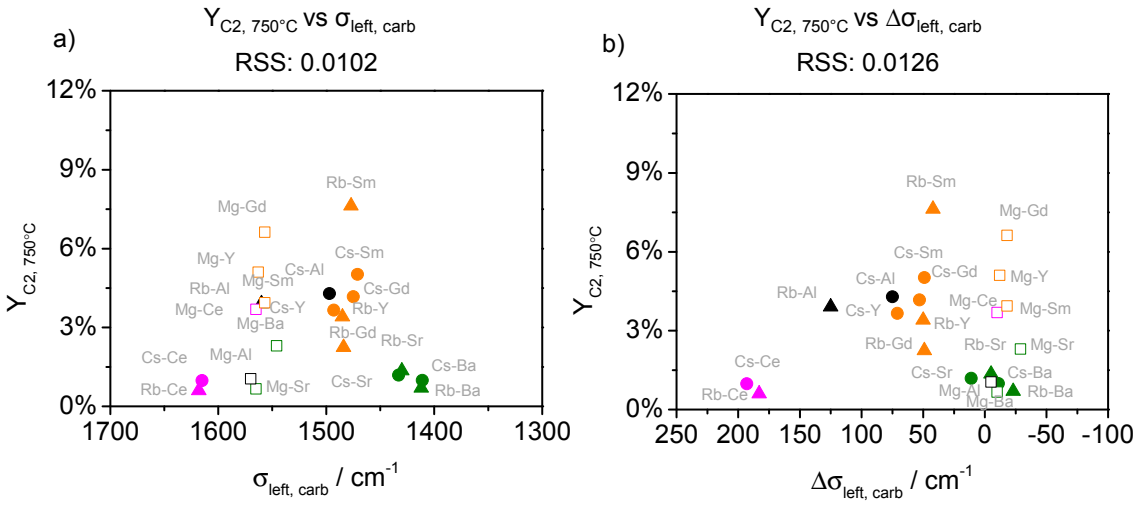

Fig. A5.3: Correlation between C_2 yield at 750 °C and (a) $\sigma_{left,\ carb}$ or (b) $\Delta\sigma_{left,\ carb}$ of Rb_2CO_3 (triangle), Cs_2CO_3 (dot) and $Mg(OAc)_2$ (square) on Y_2O_3, Sm_2O_3 and Gd_2O_3 (orange), CeO_2 (pink), SrO and BaO (green), Al_2O_3 (black).

A5.5 Discussion on descriptors

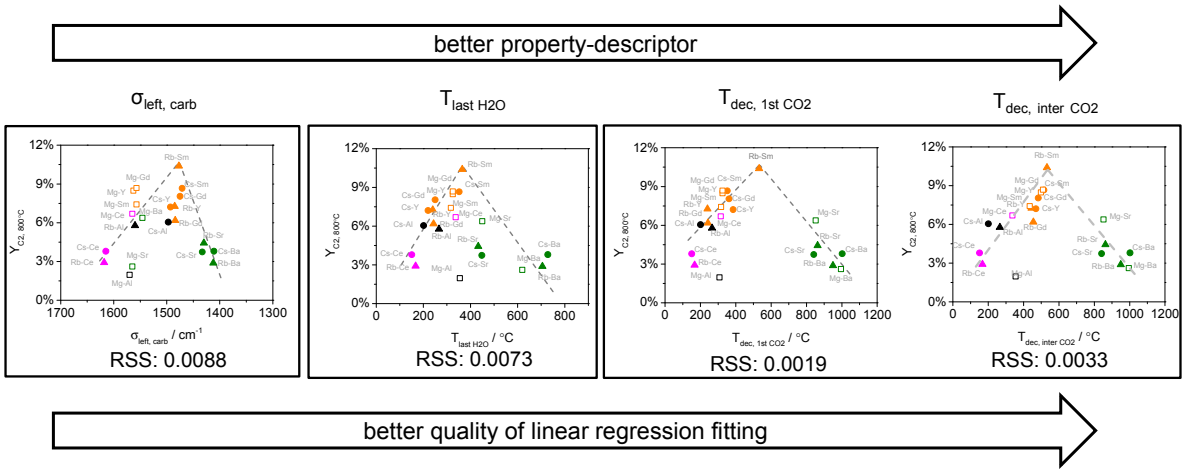

Fig. A5.4: Evaluation of linear regression fitting between C_2 yield at 800 °C and each property-descriptor generated from IR and TGA-MS results. Descriptors derived from IR, TGA-MS (H_2O-relating) to TGA-MS (CO_2-relating) are increasingly close to the practical reaction condition, and the quality of corresponding correlation with catalytic performance is increasingly higher.

A5.6 Carbonate concept extended to typical Li/MgO and Mn-Na_2WO_4/SiO_2 catalysts

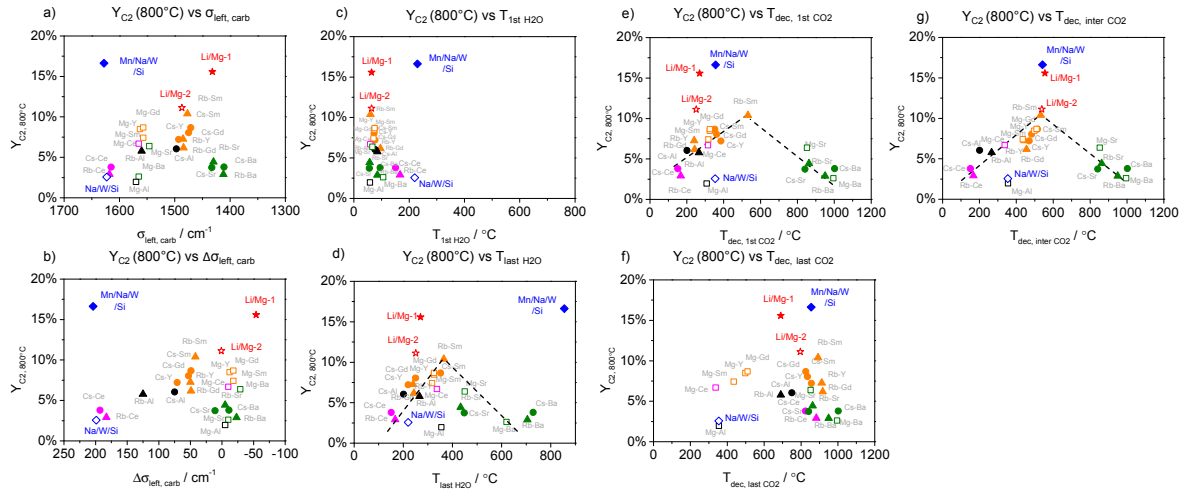

Fig. A5.5: The location of Li/MgO-1 (red solid star), Li/MgO-2 (red hollow star), Mn-Na_2WO_4/SiO_2 (blue solid diamond) and Na_2WO_4/SiO_2 (blue hollow diamond) catalyst in correlations between C_2 yield at 800 °C and (a) $\sigma_{left, carb}$, (b) $\Delta\sigma_{left, carb}$, (c) $T_{1st\ H2O}$, (d) $T_{last\ H2O}$, (e) $T_{dec, 1st\ CO2}$, (f) $T_{dec, last\ CO2}$ and (g) $T_{dec, inter\ CO2}$.

The effect of CO_2 in feed for carbonate-supported catalysts

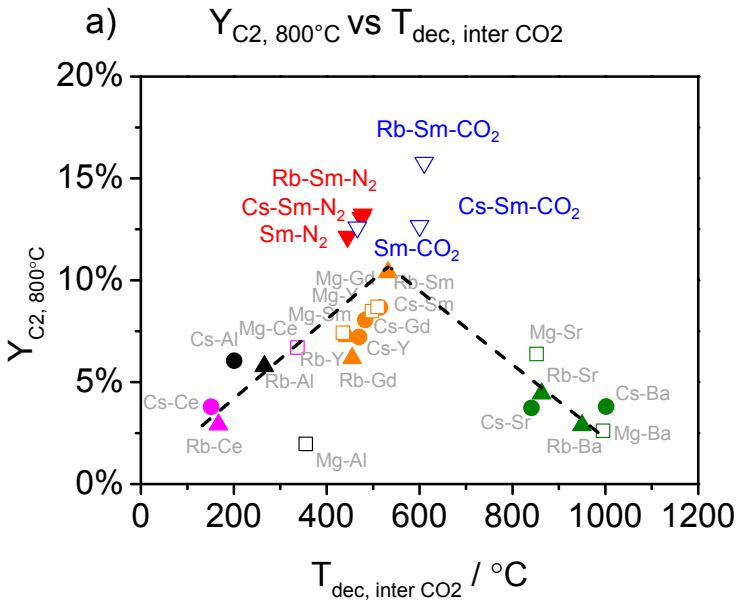

Fig. A5.6: The location of pure $Sm_2(CO_3)_3$, Rb_2CO_3 and Cs_2CO_3 on $Sm_2(CO_3)_3$ catalysts tested in N_2 (red solid triangle) and in CO_2 (blue hollow triangle) OCM feed in the volcano-like correlation (black line) between C_2 yield at 800 °C and $T_{dec,\ inter\ CO2}$ built by oxide-supported catalysts.

Generally, the decomposition/formation equilibrium of carbonate is affected by CO_2 in gas atmosphere. This effect is already proved by TGA test in CO_2 atmosphere for pure $Sm_2(CO_3)_3$, Rb_2CO_3 and Cs_2CO_3 on $Sm_2(CO_3)_3$ catalysts compared the test in Ar atmosphere (Fig. 3.16). The reason to use Ar as inert atmosphere is to simulate the actual OCM reaction condition where N_2 is usually employed as diluent gas. Obvious shift to higher temperatures is observed for all cases indicating that CO_2 atmosphere could stabilize the existing carbonate species in catalysts. Considering that intermediate carbonate species could be important to influence catalytic performance, the property-descriptor $T_{dec,\ inter\ CO2}$ for all three catalysts are derived by the defined criterion. Afterwards, their catalytic performance was independently tested in N_2 OCM feed and CO_2 OCM feed. The comparison in between is shown in Fig. 4.8. Performance-descriptor of $Y_{C2,\ 800°C}$ is derived for catalysts tested in N_2 and CO_2 OCM feed, respectively, and afterward, they are correlated with the corresponding property-descriptor of $T_{dec,\ inter\ CO2}$ as shown in Fig. A5.6, in order to elucidate the effect of CO_2 on OCM performance.

In general, carbonate-supported catalysts tested in CO_2 OCM feed exhibit higher values of $T_{dec,\ inter\ CO2}$ and $Y_{C2,\ 800°C}$ simultaneously than the values of same catalysts tested in N_2 OCM feed. This observation indicates two aspects. On one hand, higher $T_{dec,\ inter\ CO2}$ value could be explained by the stabilization effect of CO_2 atmosphere on intermediate stable carbonate species, which is proposed to be critical for OCM reaction. One the other hand, CO_2 atmosphere ensures the presence of intermediate compound at higher temperature. Under this higher temperature, the process of CO_3^{2-} species transfer and subsequent decomposition via the intermediate compound could also happen and be accelerated to some extent. The beneficial influence of this process on OCM performance is enlarged and in consequence, C_2 yield at 800 °C is increased.

A6. Mechanistic and basicity concepts in OCM catalysis

A.6.1 Possible interaction between carbonate and cations

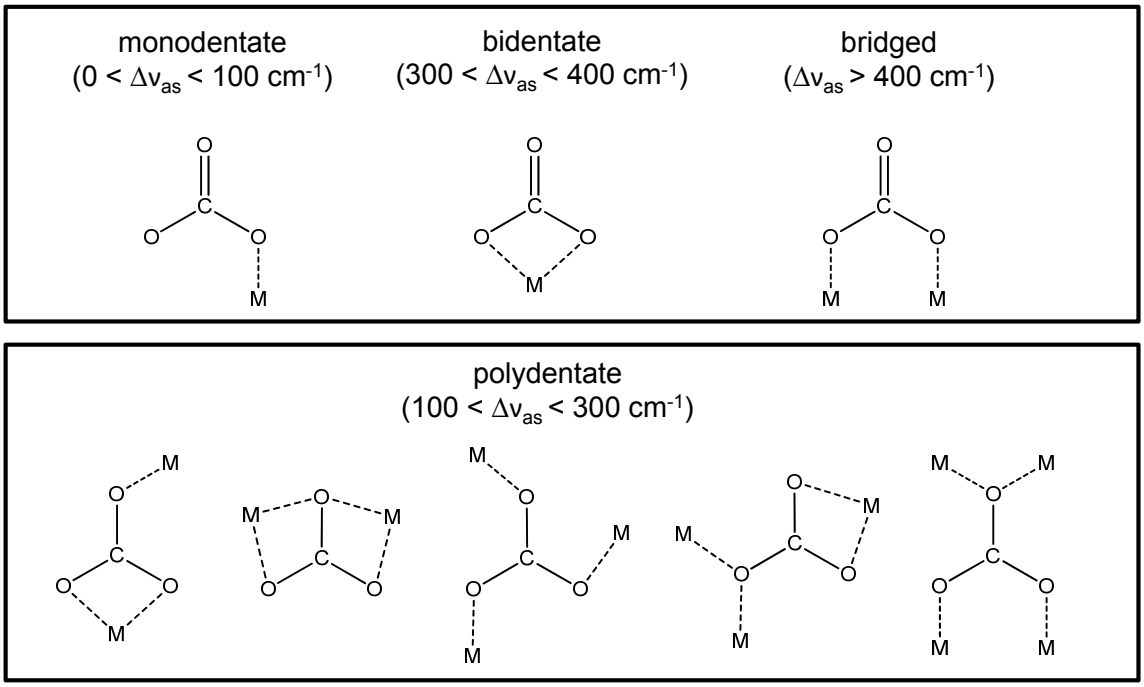

Fig. A6.1: Proposed structure of coordination between CO_3^{2-} and cations adapted from Busca's paper.[172] For pure Rb_2CO_3 and Cs_2CO_3, Rb^+, Cs^+ is speculated to coordinate with CO_3^{2-} in the monodentate type. Differently, for Rb_2CO_3 and Cs_2CO_3 on oxides, polydentate coordination between cations and CO_3^{2-} is considered to be the dominate type, where three carbonate oxygens are all bonded to cations.

Table A6.1: Splitting value of asymmetric stretching vibration of CO_3^{2-} measured by FT-IR for pure and oxides supported Rb_2CO_3 and Cs_2CO_3. For pure carbonate, the coordination type between Rb^+, Cs^+ and CO_3^{2-} is speculated to be monodentate. For Rb_2CO_3 and Cs_2CO_3 on SrO and BaO, the coordination type between the cation and CO_3^{2-} is considered to be monodentate type as well. Differently, for Rb_2CO_3 and Cs_2CO_3 on Sm_2O_3, Gd_2O_3, Y_2O_3, CeO_2 and Al_2O_3, the coordination type could be polydentate.

Catalyst composition	Δv_{as} from IR (cm^{-1})	Speculated coordination
pure Rb_2CO_3	98	monodentate
Rb_2CO_3-BaO	0	n.a.
Rb_2CO_3-SrO	0	n.a.
Rb_2CO_3-Sm_2O_3	134	polydentate
Rb_2CO_3-Gd_2O_3	154	polydentate
Rb_2CO_3-Y_2O_3	148	polydentate
Rb_2CO_3-CeO_2	228	polydentate
Rb_2CO_3-Al_2O_3	162	polydentate
pure Cs_2CO_3	96	monodentate
Cs_2CO_3-BaO	0	n.a.
Cs_2CO_3-SrO	0	n.a.
Cs_2CO_3-Sm_2O_3	150	polydentate
Cs_2CO_3-Gd_2O_3	129	polydentate
Cs_2CO_3-Y_2O_3	129	polydentate
Cs_2CO_3-CeO_2	269	polydentate
Cs_2CO_3-Al_2O_3	101	polydentate

List of Publications

1. Huan Wang, Roman Schmack, Benjamin Paul, Matthias Albrecht, Sergey Sokolov, Stefan Rümmler, Evgenii V. Kondratenko, and Ralph Kraehnert, Porous silicon carbide as a support for Mn/Na/W/SiC catalyst in the oxidative coupling of methane, *Applied Catalysis A: General*, 2017, 537, 33-39.
2. Nathaniel D. Leonard, Stephan Wagner, Fang Luo, Julian Steinberg, Wen Ju, Natascha Weidler, Huan Wang, Ulrike I. Kramm, and Peter Strasser, Deconvolution of Utilization, Site Density, and Turnover Frequency of Fe-Nitrogen-Carbon Oxygen Reduction Reaction Catalysts Prepared with Secondary N-Precursors, *ACS Catalysis*, 2018, 3, 1640-1647.
3. Yanyan Sun, Ilya Sinev, Wen Ju, Arno Bergmann, Sören Dresp, Stefanie Kühl, Camillo Spöri, Henrike Schmies, Huan Wang, Denis Bernsmeier, Benjamin Paul, Roman Schmack, Ralph Kraehnert, Beatriz Roldan Cuenya, and Peter Strasser, Efficient Electrochemical Hydrogen Peroxide Production from Molecular Oxygen on Nitrogen-Doped Mesoporous Carbon Catalysts, *ACS Catalysis*, 2018, 8, 2844-2856.